SNOW COVER PROPERTIES AND SOIL MOISTURE DERIVED FROM GPS SIGNALS

DISSERTATION ZUR ERLANGUNG DES DOKTORGRADES
AN DER FAKULTÄT FÜR GEOWISSENSCHAFTEN
DER LUDWIG-MAXIMILIANS-UNIVERSITÄT MÜNCHEN

Vorgelegt von: Dipl.-Geogr. Franziska Koch

Eingereicht am: 10.11.2016

1. Gutachter:	Prof. Dr. Wolfram Mauser
2. Gutachter:	Prof. Dr. Alexander Löw
Gutachterliche Stellungnahme:	Dr. Jürg Schweizer (WSL Institut für Schnee- und Lawinenforschung SLF)
Tag der Disputation:	01.02.2017

The best ideas for this thesis were born outside in nature.

ACKNOWLEDGEMENTS

Finally, I am about to finish the last parts of this thesis and start looking back on very interesting and unique times. Having the opportunity to combine my passion for mountains and snow with the topic of this work motivated me a lot. Besides my main research fields, physical geography and remote sensing, I had the chance to apply and get introduced to various topics in physics, electrical engineering, snow and soil sciences, and geodesy. Moreover, I was able to acquire several technical skills such as programming, data aggregation & processing, and sensor development. I was lucky to have many experts around me from whom I learned a lot. This work would not have been possible without the support of numerous people who I would like to thank:

At first, a very special thank goes to my supervisor Prof. Dr. Wolfram Mauser for all the support he gave me throughout the years. From the very beginning he shared his enthusiasm for this work and I admire his talent in developing new and extraordinary research ideas and his quick grasp and encouraging comments during fruitful discussions. I will never forget his support and great experience, especially during the first moments of the sensor construction. I am very grateful for the confidence he put in me, which enabled me to develop distinct ideas and working strategies.

I want to express my profound gratitude to my co-supervisor Dr. Monika Prasch for the very friendly atmosphere and her helpful scientific support with highly valuable discussions and ideas associated with this thesis. She always had an open ear for me and motivated me again and again. I have definitely benefited a great deal from her experience, not only during this dissertation. Thank you!

I would like to sincerely thank my second reviewer Prof. Dr. Alexander Löw, Dr. Jürg Schweizer being an external reviewer of this thesis, and the entire doctoral commission for their time and interest.

As this is a cumulative thesis, I am deeply grateful to all of my co-authors for their ideas and suggestions to improve the manuscripts.

Finance was provided by (1) the German Research Foundation (DFG) during the project ‘Kontinuierliche Messung der Schneedeckenentwicklung mit GPS-Empfangsgeräten zur Bestimmung des Schneespeichers im Hochgebirge’ and (2) the European Space Agency (ESA) during the project ‘SnowSense - Integrated Service for Runoff and Hydropower Assessment and Forecast related to Snow Cover Dynamics in Remote Areas’, both being gratefully acknowledged.

During the run-time of these projects, I had the unique chance to collaborate with several people and project partners which gave me the great opportunity to have a look ‘outside the box’. My gratitude includes the mentioned persons working at the following institutes and companies:

- WSL Institute for Snow and Avalanche Research SLF: Particular thanks deserves Dr. Jürg Schweizer who gave me the opportunity to install the GPS sensors for the snow measurements at the well-equipped high Alpine SLF test site Weissfluhjoch near Davos, Switzerland, and that he gave me the possibility to use the infrastructure and the reference data at the test field. It proved as an ideal place for my studies. Moreover, I would like to thank him for inviting me to several short-term research stays at the institute – I enjoyed them very much and learned a lot during these times. I am deeply grateful that I had the special chance to work together with Dr. Lino Schmid, especially during the time of the first two papers included in this thesis. We had a great time writing, solving equations and discussing – I really learned a lot from you and thank you also for the numerous inspiring Graubündener Rötelis. Many thanks go to Marc Ruesch for the field work and to the ‘Hauswart’ staff for restarting the sensors at the test site. Thanks also to all people I met at the SLF for making the stays in Davos so pleasant.

- Vista Remote Sensing GmbH: I would like to sincerely thank Dr. Heike Bach and the SnowSense project team including Florian Appel and Philipp Klug for the good and fruitful cooperation and sharing the passion on this project. Furthermore, many thanks go to Tobias Ruf for carrying out the PROMET soil moisture simulations and to Dr. Markus Muerth for interesting discussions on the broad field of soil sciences.
- ANavS (Advanced Navigation Solutions) GmbH: During the project SnowSense I had the great opportunity to work together with Dr. Patrick Henkel – we had a very productive and successful time in developing the GNSS snow measurement model based on carrier phase measurements and I will never forget the almost endless nocturnal programming sessions.
- German Weather Service (DWD) Munich: Thank you to Thomas Schuhmacher and Torben Lüttschwager that it was possible to install the sensors for the soil moisture measurements at the DWD test site in Munich.
- Commission for Geodesy and Glaciology of the Bavarian Academy of Sciences and Humanities: I am thankful for the exchange of ideas with Dr. Ludwig Braun, Dr. Wasti Weber, Dr. Achim Heilig and Dr. Christof Völksen.
- Alfred-Wegener-Institut Helmholtz Zentrum für Polar- und Meeresforschung: Thanks to Prof. Dr. Olaf Eisen for his valuable comments on the second paper.

A special mention goes to Thomas Ramsauer, my student assistant, who accompanied me during four years of my work. It was absolutely positive to have such a talented helping hand for soldering, installing the sensors and measuring in the field etc. I cannot imagine a better ‘Hiwi’.

I am also more than grateful to my mentors Prof. Dr. Bettina Reichenbacher and Prof. Dr. Miriam Dühnforth of the LMUexcellent Mentoring Programme GeoSciences for their support and interest in my progress during the time I had the chance to be their mentee.

I very much enjoyed working in the friendly and productive atmosphere of the Chair of Geography and Geographical Remote Sensing at the Department of Geography. Therefore, I want to express many thanks to all my office-mates, colleagues and PhD-fellows - I had a great time in the office and during several encouraging refreshing breaks, e.g. on the balcony, with you. I am glad that I became friends with many of you and that we also had great times out of university with skiing, rock climbing, cycling or just hanging out.

Particular thanks in regard to this thesis are dedicated to Dr. Roswitha Stolz for brainstorming and numerous fruitful discussions – this helped me a lot! I want to sincerely thank Dr. Florian Schlenz for introducing me into the field of soil moisture measurements – you are a real expert in this field - and thanks to Dr. Ingo Keding for the technical support at the very beginning of the sensor application board development. Many thanks goes to Dr. Thomas Feistl, Hans Grambichler, Jonas Meier, Birgitta Putzenlechner, Dr. Christian Römelsberger, and Michael Weber for several discussions or the proof-reading of specific chapters! Dr. Barbara Winter and Graeme Summers deserve my cordial thanks for their time checking through the manuscript and correcting my English.

A very deep thank you goes to all my friends and my family and of course to the mountains and the snow for giving me a good life balance.

Last but not least, I would like to cordially thank my parents Liselotte and Roland Koch for their unlimited interest, their enormous support and their great understanding during the entire time of this thesis. Without them this would not have been possible.

SUMMARY

Continuous environmental monitoring of hydrological parameters is nowadays essential, and even irreplaceable, in order to attain a better understanding of our Earth's climate system, the hydrologic cycle, and the hydrologic storages. Both, the dynamic seasonal snow and soil storages are rather short-term water storages compared to groundwater, glaciers or oceans, with the latter three having much longer retention times. Snow and soil parameters are, due to their high dynamics, important inputs for climate and hydrological simulations. Precise knowledge on them should help to reduce uncertainties in climate change scenarios, extreme event forecasting, and water and energy supply strategies, e.g. for drinking water and agricultural production. However, it is an extremely demanding task to get continuous environmental data, and to apply sensors which are potentially usable at almost any location on the Earth. Prominent problems of recent in situ and remote sensing techniques are for example, that they do not fulfil the required temporal or spatial resolution, they can be destructive, labour-intense, too expensive to be installed at numerous places, or are not applicable in remote and complex terrain. To overcome some of these shortcomings, further research on potential methods, techniques and sensors is important and promising.

This thesis investigates an innovative Global Navigation Satellite System (GNSS) approach, which is completely different to standard positioning or navigation applications. The overall aim of this approach was to develop a novel, continuous, non-destructive and globally applicable low-cost system based on the freely available Global Positioning System (GPS) L1-band signals. The approach was to collect data on environmental properties like hydrological snow and soil storages using GPS signal strength and carrier phases combined with dielectric properties. In particular, the focus was on the measurement of the three bulk snow cover properties snow water equivalent (SWE), snow height (HS), and liquid water content in snow (LWC), as well as soil moisture (SM).

To achieve the development of this novel approach, the thesis was built up in the following four main steps:

1) ***LWC retrieval based on GPS C/N_0 attenuation***

   In autumn 2012, the first experimental prototype GPS sensor was installed at the high Alpine SLF test site Weissfluhjoch (WFJ) (2.540 m a.s.l.) near Davos in Switzerland. The GPS carrier-to-noise power density ratio (C/N_0), which expresses the signal strength, was tracked with an antenna positioned under the snow cover. During wet snow periods, the signal strength was reduced markedly due to intense attenuation caused by liquid water. For better comparability, C/N_0 was normalized for each elevation- and azimuth-angle and for each of the up to 32 GPS satellites for every time step based on snow-free reference values. By combining the normalized signal strength with models of the complex permittivity of snow and by applying externally measured HS data along with a reliable assumption of the dry snow density, it was possible to quantitatively measure bulk volumetric LWC, especially for the spring melt periods. This approach was the first successful means for recording LWC using continuous and non-destructive low-cost GPS sensors. LWC showed high agreement with meteorological and snow hydrological measurements, and with several measurements with capacity probes in snow pits (*Chapter 2*). Moreover, the GPS derived LWC values were, compared to other studies in literature, validated with a high accuracy (0.4 to 0.7 percent points (pp)) with data from a L-band upward-looking ground-penetrating radar (upGPR). The latter data were supplied by a research group from the WSL Institute for Snow and Avalanche Research Institute SLF, who performed these measurements at the WFJ test site (*Chapter 3*).

2) ***Derivation of HS, SWE and LWC by combining GPS C/N_0 with upGPR TWT***

   In a subsequent step and in close collaboration with the SLF, HS and SWE were derived additionally to LWC by combining (a) GPS signal strength received at a ground-based GPS antenna located beneath the

snowpack with (b) time delay of electromagnetic waves travelling through a snowpack which was recorded by the upGPR system mentioned above. The latter was buried in the ground and measured the two-way travel time (TWT) of electromagnetic waves through the snowpack, which are markedly reflected at the air-snow interface. The snow cover properties HS, SWE and LWC derived solely by this upGPR-GPS combination were corroborated with a high correlation against conventionally measured in situ data. For example, the root-mean-square deviation (RMSD) between the upGPR-GPS combination and the closest situated HS sensor ranged from 3.3 and 6.6 cm, and 31 to 48 mm between the sensor combination and a snow pillow. A big advantage of this combination is that HS, SWE and LWC were derived non-destructively from beneath the snowpack. This is a big step towards improving avalanche forecasting and could potentially be applied in avalanche-prone slopes (*Chapter 3*).

3) ***Derivation of SWE for dry-snow conditions based on GPS carrier phases***

In autumn 2015, a second generation prototype GPS sensor setup was installed at the test site WFJ. This made it possible to analyse the GPS carrier phases in addition to GPS C/N_0. A novel snow-specific GNSS approach was developed to derive SWE from carrier phase measurements, for which two static GPS antennas, one positioned above and one below the snowpack, were used. Before the first snowfall, the baseline between both antennas was determined in millimetre accuracy using Real Time Kinematic (RTK) positioning. As snow reduces the velocity of electromagnetic waves, the idea of this approach was to determine zenith time delay information derived by carrier phase measurements as the latter change with a snowpack on top of one antenna. By using an elevation mapping function, plus an assumption of signal wave velocity in dry snow and the particular refraction angles being proportional to the dielectric snow properties, it was possible to calculate SWE from the time delay in the GPS signals. This work was performed in close collaboration with ANavS GmbH and Vista Remote Sensing GmbH within the ARTES-IAP Demo Project SnowSense co-funded by ESA. This approach already works very well for dry-snow conditions, however, for wet-snow conditions (as of November 2016) it still requires further development with regard to a more stable carrier phase processing. The GPS SWE results for dry snow are in high correlation with the conventionally measured, continuous snow pillow recordings with a RMSD of 11 mm. This is also true comparing the GPS SWE results with manual snow pit measurements with a RMSD of 23 mm (*Chapter 4*).

4) ***Transfer to other environmental properties: Soil moisture retrieval based on GPS C/N_0***

The GPS signal strength attenuation approach described under the first point was transferred from the derivation of snow cover properties to the derivation of SM. This should demonstrate a potential transferability to other environmental properties. This approach was investigated at a bare soil field at a test site of the German Weather Service (DWD) in Munich for a period of almost 1.5 years (January 2014 – June 2015). The C/N_0 changes due to the evolution of SM were recorded at GPS antennas installed at a soil depth of 10 cm. Similar to the LWC approach, a dielectric mixing model for moist soils and the dry soil density were taken into account. With this method, the SM of the entire upper soil column, which represents the direct interface between air and soil, was retrieved. SM was quantitatively measured with high correlation with other in situ methods such as frequency domain (FD) and gravitational probes at certain sampling depths and volumes. The accuracy was clearly below 0.04 $m^3\ m^{-3}$, which is considered as a high agreement and is often the benchmark for SM retrievals from microwave remote sensing products. To get an accurate validation of the entire first 10 cm, this soil layer was modelled in addition with the physically-based land-surface model PROMET. The SM accuracy of 0.025 $m^3\ m^{-3}$ between the GPS method and the simulation is very good (*Chapter 5*).

In summary, this thesis thus encompasses successful and highly promising steps towards the development of a new continuous, non-destructive, globally applicable low-cost environmental monitoring system using GPS signals. The validation of snow cover properties as well as SM showed high accuracy with reference data. A big success is that SM and SWE, in case of dry snow, were derived solely using GPS L1-band signals; no further

sensors were necessary. However, for the derivation of snow cover properties in case of wet snow, it is presently still necessary to combine GPS with other sensors (e.g., HS laser sensor or upGPR). Regarding the SWE derivation due to carrier phase time delay this GPS only approach is currently restricted to dry snow, because wet snow makes phase processing difficult (as of November 2016). This issue is currently being investigated. A successful solution of this work would lead to the derivation of all three snow cover properties HS, SWE and LWC using solely GPS L1-band signals. In *Section 6.2* an outlook is given on a potential implementation of combining (a) GPS C/N_0 with (b) carrier phase time delay in case of wet snow. In addition, as presented in *Section 6.3*, further research could be on the sensor improvement, the implementation at different areas and further methods and analysis, and as a potential transfer to further environmental characteristics such as plant biomass. As this sensor setup is a point measurement, it would be also a useful improvement, to undertake further steps towards an increase in spatial distribution of information, e.g. by installing numerous sensors in an entire network or to combine this GPS approach with other remote sensing and hydrologic modelling approaches. Moreover, this GPS approach could be extended to other GNSS systems, such as the upcoming European Galileo system.

ZUSAMMENFASSUNG

Heutzutage ist ein kontinuierliches Monitoring hydrologischer Parameter für ein besseres Verständnis des Klimas, des hydrologischen Kreislaufs sowie der hydrologischen Speicher notwendig und nicht mehr wegzudenken. Die Verweilzeit des Wassers in den hydrologischen Schnee- und Bodenspeichern ist im Vergleich zu Grundwasser-, Gletscher- und Ozeanspeichern eher kurz. Aufgrund ihrer hohen Dynamik, sind Schnee- und Bodenparameter wichtige Eingangsdaten für Klimamodelle und hydrologische Simulationen. Sie helfen Unsicherheiten hinsichtlich Klimawandelszenarien zu reduzieren, sowie Vorhersagen von Extremereignissen und der Wasserverfügbarkeit, z.B. für Trinkwasser und die Landwirtschaft, zu unterstützen. Allerdings ist es eine große Herausforderung, kontinuierliche Daten von Umweltparametern zu generieren bzw. auf Sensoren zurückzugreifen, die nahezu überall auf der Welt angewendet werden können. Schwachstellen derzeitiger in situ- und Fernerkundungstechniken können z.B. sein, dass sie arbeitsaufwendig, destruktiv oder für einen breiten Einsatz zu teuer sind. Zudem erfüllen sie oftmals nicht die nötige zeitliche oder räumliche Auflösung bzw. können nicht in entlegenen Gegenden oder in komplexem Terrain angewandt werden. Um solche Unzulänglichkeiten zu verbessern, ist mehr Forschung hinsichtlich neuer Methoden, Technologien und Sensoren wichtig und vielversprechend.

In dieser Doktorarbeit wird ein innovativer Ansatz unter Zuhilfenahme des Globalen Navigationssystems (GNSS) untersucht, der sich von standardmäßigen Positionierungs- und Navigationsanwendungen unterscheidet. Das übergeordnete Ziel war es, einen Ansatz mit kostengünstigen Sensoren des Globalen Positionierungssystems (GPS) zu entwickeln, der kontinuierliche, nicht-destruktive Messungen ermöglicht und potentiell global angewendet werden kann. Die Messungen basieren dabei auf Mikrowellensignale des freiverfügbaren GPS L1-Bandes, womit Umweltdaten zur Charakterisierung des Schnee- und Bodenspeichers erhoben werden können. Im Speziellen wurde der Fokus auf die Messung der Schneedeckeneigenschaften, Schneewasseräquivalent (SWE), Schneehöhe (HS) und der volumetrischen Feuchte des Schnees (LWC) sowie der Bodenfeuchte (SM) gelegt. Dazu wurden als GPS Rohdaten die Signalstärken und die Trägerphasen verwendet und mit den dielektrischen Eigenschaften von Schnee und Boden kombiniert.

Um diesen neuen Ansatzes zu entwickeln, wurde die Doktorarbeit anhand der folgenden vier Punkte aufgebaut:

1) Messung von LWC anhand der Abschwächung von GPS C/N_0

Im Herbst 2012 wurde ein erster experimentell entwickelter GPS Sensor-Prototyp auf dem hochalpinen SLF Messfeld Weissfluhjoch (WFJ) (2.540 m ü. NN) in der Näher von Davos in der Schweiz, installiert. Das GPS Träger-Rausch-Leistungsverhältnis (C/N_0), das die Signalstärke ausdrückt, wurde von GPS Antennen aufgenommen, die am Boden unter der Schneedecke ausgelegt wurden. Aufgrund des Flüssigwassers, wurde die Signalstärke während Zeiten mit feuchten Schneeverhältnissen deutlich reduziert. Die C/N_0-Daten wurden für jeden Zeitschritt anhand einer schneefreien Referenz normiert. Die normierten C/N_0-Werte wurden dabei je Zeitschritt, Elevations- und Azimuthwinkel für alle aktiven, insgesamt bis zu 32 GPS Satelliten berechnet. Während der Frühjahrsperioden konnte der volumetrische Feuchtegehalt des gesamten Schneepakets quantitativ bestimmt werden, indem die normalisierte Signalstärke mit Modellen zur komplexen Permittivität und mit extern gemessener Schneehöhe sowie einer realistischen Annahme der trockenen Schneedichte kombiniert wurde. Dies ist das erste kostengünstige GPS-Verfahren, um LWC kontinuierlich und nicht-destruktiv zu ermitteln. Der zeitliche Verlauf der LWC-Werte zeigte eine hohe Übereinstimmung mit kontinuierlichen meteorologischen und schneehydrologischen Messungen, ebenso, wie die an einigen Tagen in Schneeprofilen durchgeführten Messungen mit Kapazitätssonden (*Kapitel 2*). Zudem wurden LWC-Daten zur Verfügung gestellt, die von einem Forscherteam des WSL Instituts für Schnee- und Lawi-

nenforschung SLF mit einem nach oben gerichteten L-Band Bodenradar (upGPR) unter Einbeziehung extern gemessener HS-Daten kontinuierlich auf dem Testfeld gemessen wurden. Die Übereinstimmung der beiden LWC Messungen ist (verglichen mit anderen Studien in der Literatur) mit 0.4 bis 0.7 pp (Prozentpunkten) hoch (*Kapitel 3*).

2) ***Kombination von GPS C/N_0 mit upGPR TWT zur Messung von HS, SWE und LWC***
In einem weiteren Schritt und in enger Zusammenarbeit mit dem SLF wurden neben dem LWC auch HS und SWE bestimmt. Dies wurde durch die Kombination von (a) der GPS Signalstärke und (b) der Zeitverzögerung elektromagnetischer Wellen durch Schnee, die mit dem zuvor genannten upGPR gemessen wurden, ermöglicht. Das upGPR wurde im Boden vergraben und hat die Zweiwegelaufzeit (TWT) elektromagnetischer Wellen durch ein Schneepaket gemessen, die an der Grenzschicht Atmosphäre – Schneeoberfläche signifikant reflektiert wurden. Die Schneedeckenparameter HS, SWE und LWC, die durch die Kombination der zwei Sensoren abgeleitet wurden, weisen eine hohe Korrelation zu konventionell gemessenen in situ Daten auf. Die Wurzel aus der mittleren quadratischen Abweichung (RMSD) von HS, gemessen mit GPS, und dem nahegelegensten in situ Sensor lag zwischen 3.3 und 6.6 cm und die Übereinstimmung von SWE mit einem Schneekissen lag zwischen 31 und 48 mm, was als sehr gut einzustufen ist. Ein großer Vorteil dieser Sensorkombination ist, dass alle Schneedeckenparameter nichtdestruktiv und unterhalb der Schneedecke ermittelt werden können. Dies ist ein großer Schritt hinsichtlich einer potentiellen Verbesserung der Lawinenvorhersage und eignet sich potentiell dazu in Lawinenhängen eingesetzt werden zu können (*Kapitel 3*).

3) ***Messung von SWE anhand der GPS Trägerphasen unter trockenen Schneebedingungen***
Im Herbst 2015 wurde ein weiter entwickelter GPS Sensor-Prototyp am Testfeld WFJ installiert, mit der neben GPS C/N_0 auch die GPS Trägerphasen analysiert werden konnten. Um SWE zu bestimmen, wurde ein spezieller schneespezifischer GNSS Ansatz, basierend auf GPS Trägerphasenmessungen, entwickelt. Eine Antenne wurde dabei über der Schneedecke angebracht und die andere am Boden ausgelegt, die somit während der Schneeperiode mit Schnee bedeckt war. Vor dem ersten Schneefall wurde der Abstand zwischen beiden Antennen mit Millimetergenauigkeit anhand eines kinematischen Echtzeit- (RTK) Positionierungsalgorithmus bestimmt. Schnee reduziert die Geschwindigkeit von elektromagnetischen Wellen. Sobald Schnee auf der unteren Antenne liegt, wurde die Zeitverzögerung der GPS Signale im Schnee in Zenitrichtung zwischen den Antennen anhand von Trägerphasenmessungen ermittelt. Die aufgrund des Schnees resultierende Zeitverzögerung wurde unter Berücksichtigung der Geometrie und den dielektrischen Eigenschaften von trockenem Schnee, in SWE umgewandelt. Dabei definieren die dielektrischen Eigenschaften die Wellengeschwindigkeit und die Refraktion. Diese Arbeiten wurden in enger Zusammenarbeit mit den Firmen ANavS GmbH und Vista Geowissenschaftliche Fernerkundung GmbH im Rahmen des von der ESA geförderten ARTES-IAP Demo Projektes SnowSense durchgeführt. Dieser Ansatz funktioniert sehr gut für trockenen Schnee; für nassen Schnee muss er jedoch noch hinsichtlich einer stabileren Phasenauswertung verbessert werden (Stand November 2016). Die Ergebnisse für trockenen Schnee zeigen eine hohe Korrelation mit konventionell gemessenen SWE Daten. Der RMSD zwischen den kontinuierlichen SWE GPS- und Schneekissen-Daten ist mit einem RMSD von 11 mm sehr hoch. Dies gilt ebenso für den RMSD von 23 mm zwischen SWE GPS-Daten und den ein- bis zweiwöchentlich manuell in Schneeprofilen gemessenen SWE Daten (*Kapitel 4*).

4) ***Übertragung auf andere Umweltparameter: Messung der Bodenfeuchte mit GPS C/N_0***
Der LWC-Ansatz hinsichtlich der Signalstärkeabschwächung, wie im ersten Punkt beschrieben, wurde in einem weiteren Ansatz auf die Messung der Bodenfeuchte angewendet, was auch die generelle Möglichkeit der Übertragung auf andere Umweltparameter demonstrieren soll. Dies wurde auf einem nicht mit Vegetation bedeckten Boden auf dem Bodenmessfeld des Deutschen Wetterdienstes (DWD) in München untersucht. Die Zeitspanne betrug ca. 1.5 Jahren (Januar 2014 – Juni 2015). Die GPS Signalstärkeänderung aufgrund von Bodenfeuchteänderungen wurde mit Antennen ermittelt, die in einer Tiefe von 10 cm

vergraben wurden. Ähnlich zu dem LWC-Ansatz für Schnee, wurden normalisierte C/N_0-Werte gebildet, die mit einem dielektrischen Bodenfeuchtemodell kombiniert wurden. Damit wurde die Bodenfeuchte der gesamten oberen Bodenschicht bestimmt, die die direkte Austauschschicht zwischen Atmosphäre und Boden darstellt. Quantitativ stimmt die GPS Bodenfeuchte mit Messungen der klassischen Gravitationsmethode und der sogenannten ‚Frequency Domain' (FD) Methode, aufgenommen in verschiedenen Bodentiefen und für verschiedene Probenvolumina, sehr gut überein. Die Genauigkeit lag jeweils deutlich unter 0.04 m^3 m^3, welches einen typischen Bezugspunkt für die Güte von mithilfe Mikrowellenfernerkundung ermittelten Bodenfeuchteprodukten darstellt. Um zusätzlich eine Validierung der GPS SM der ersten 10 cm durchzuführen, wurde diese Bodenschicht mit dem physikalisch basierten Landoberflächenmodell PROMET modelliert. Die Übereinstimmung lag hier bei 0.025 m^3 m^3 und ist als sehr hoch einzustufen (*Kapitel 5*).

Zusammengefasst stellt diese Doktorarbeit erfolgreiche und sehr vielversprechende Schritte in Richtung der Entwicklung eines neuen kostengünstigen und potentiell global einsetzbaren Umweltmesssystems dar, welches kontinuierlich und nicht-destruktiv, unter Verwendung von GPS L1-Band Signalen, misst. Sowohl die mit GPS gemessenen Schneedeckenparameter als auch die Bodenfeuchte zeigen eine sehr hohe Übereinstimmung mit den Referenzdaten. Ein großer Erfolg ist, dass sowohl die Bodenfeuchte als auch SWE unter trockenen Schneebedingungen nur anhand von GPS Signalen abgeleitet werden konnte, ohne weitere Sensoren miteinzubeziehen. Für die GPS-Messungen der Schneedeckenparameter unter feuchten Schneebedingungen ist es momentan allerdings nach wie vor notwendig, sie mit anderen Sensoren (z.B. HS Laser Sensor oder upGPR) zu kombinieren. Der SWE-Ansatz, basierend auf Trägerphasen, ist auf trockenen Schnee beschränkt und zeigt noch Schwierigkeiten bei der Verarbeitung der Phase unter feuchten Schneebedingungen (Stand November 2016). Dies ist allerdings Gegenstand laufender Arbeiten. Eine erfolgreiche Lösung dieser Aufgabe würde dazu führen, dass somit alle drei Schneedeckenparameter, HS, SWE und LWC, nur unter Verwendung von GPS L1-Band Daten, abgeleitet werden könnten. Eine mögliche Durchführung dieser Kombination von (a) GPS C/N_0 und (b) der anhand der Trägerphasen ermittelten Laufzeitverzögerung unter feuchten Schneebedingungen, ist als Ausblick in *Kapitel 6.2* behandelt. Wie in *Kapitel 6.3* dargestellt, können weitere Forschungs-und Entwicklungsarbeiten eine Verbesserung des Sensors an sich, die Implementierung in anderen Regionen, darauf aufbauende Methoden und Analysen, sowie der Transfer zu weiteren Umweltcharakteristika, wie z.B. die Pflanzenbiomasse, beinhalten. Da es sich bei dem momentanen Ansatz um eine Punktmessung handelt, könnten zudem weitere Arbeiten in Richtung räumlich verteilter Messungen unternommen werden. Dies könnte z.B. durch kostengünstige GPS-Sensornetzwerke oder durch eine Kombination mit anderen Fernerkundungs- bzw. Modellierungsansätzen gelöst werden. Zudem könnte dieser GPS Ansatz auch unter Berücksichtigung weiterer GNSS-Systeme, wie z.B. das neue Europäische Galileo System, erweitert werden.

CONTENTS

ACKNOWLEDGEMENTS IV
SUMMARY VI
ZUSAMMENFASSUNG IX
CONTENTS XII
LIST OF FIGURES XVI
LIST OF TABLES XIX
LIST OF ABBREVIATIONS XX
LIST OF SYMBOLS XXIII
1. INTRODUCTION 1
1.1 Motivation and research questions 1
1.2 Definition and measurement methods of snow cover properties and soil moisture 4
1.2.1 Snow cover properties 4
1.2.2 Soil moisture 7
1.2.3 Challenges and limitations 8
1.3 Physical basis on electromagnetic waves and dielectric properties of snow and soil 8
1.3.1 Propagation, reflection and refraction of electromagnetic waves 9
1.3.2 Attenuation and penetration depth in the microwave domain 10
1.3.3 Microwave dielectric properties of snow and soil 10
1.4 Overview on GNSS and their applications on environmental properties 12
1.4.1 GNSS and GPS 12
1.4.2 GNSS measurements for environmental monitoring 13
1.5 GPS sensors, raw data and test sites 15
1.5.1 GPS sensors and raw data 15
1.5.2 Test site Weissfluhjoch 16
1.5.3 Test site Munich 18
1.6 Thesis outline 19
1.6.1 Research objectives 19
1.6.2 Chapter outline 20
1.6.3 Scientific publications 21
2. MEASURING SNOW LIQUID WATER CONTENT WITH LOW-COST GPS RECEIVERS 23
Abstract 23
2.1 Introduction 23
2.2 Measurement setup 25

2.3 GPS raw data and processing of normalized C/N_0 values 27
2.3.1 GPS raw data 27
2.3.2 Normalized C/N_0 values 28
2.4 Interaction of GPS signals with the snowpack 29
2.4.1 Overview of processes and influences on GPS signals 29
2.4.2 Atmospheric influence and variability 30
2.4.3 Refraction and snow depth correction 30
2.4.4 Reflection at the snow surface 31
2.4.5 Attenuation within the snowpack 32
2.5 Calculation of liquid water content based on the complex permittivity 32
2.5.1 Real and imaginary part of the complex permittivity 32
2.5.2 Retrieval algorithm 33
2.6 Results 34
2.6.1 Bulk volumetric liquid water content derived with the three different formulations 34
2.6.2 Comparison with reference measurements in snow pits 35
2.6.3 Comparison with meteorological and snow-hydrological data 36
2.7 Discussion 38
2.7.1 Advantages and limits 38
2.7.2 Uncertainty estimates for the calculation of the bulk volumetric liquid water content 39
2.7.3 Comparison with other measurements 39
2.8 Conclusion and outlook 40
Acknowledgments 41
3. A NOVEL SENSOR COMBINATION (UPGPR–GPS) TO CONTINUOUSLY AND NONDESTRUCTIVELY DERIVE SNOW COVER PROPERTIES 42
Abstract 42
3.1 Introduction 42
3.2 Methods 43
3.2.1 Weissfluhjoch study site and accompanying data 43
3.2.2 upGPR 44
3.2.3 GPS 45
3.2.4 Combination of both methods 45
3.3. Results 45
3.3.1 Comparison of both methods 45
3.3.2 Combination of both methods 47
3.4. Discussion 48
3.4.1 Comparison of both methods 48
3.4.2 Combination of both methods 49
3.5 Conclusions 49
Acknowledgments 50

4. SNOW WATER EQUIVALENT OF DRY SNOW DERIVED FROM GNSS CARRIER PHASES 51
Abstract 51
4.1 Introduction 51
4.2 Modelling of carrier phases with snow cover 53
4.3 Method for SWE derivation 54
4.3.1 Fixing of initial ambiguities 55
4.3.2 Initialization of ambiguities of newly tracked satellites 57
4.3.3 Re-adjustment of ambiguities 58
4.3.4 Fixed phase residuals 58
4.3.5 Filtering of snow parameter estimate 60
4.3.6 Calculation of SWE 61
4.4 Results and Discussion 61
4.5 Conclusions 64
Acknowledgements 64
5. SOIL MOISTURE RETRIEVAL BASED ON GPS SIGNAL STRENGTH ATTENUATION 65
Abstract 65
5.1 Introduction 65
5.2 Measurement setup and data 67
5.2.1 GPS measurements at the DWD test site Munich 67
5.2.2 Accompanying in situ data 68
5.2.3 Land-surface model PROMET 68
5.2.4 Soil moisture sampling volumes and vertical ranges of different methods 69
5.3 Soil moisture derivation with GPS 70
5.3.1 GPS data processing 70
5.3.2 GPS signal strength attenuation 71
5.3.3 Dobson four-component dielectric mixing model 72
5.3.4 Calculation of soil moisture and sensitivity 74
5.4 Results 74
5.4.1 Time series of soil moisture and hydrological data 74
5.4.2 Comparison of the different soil moisture methods 77
5.5 Discussion 78
5.5.1 Conformities and discrepancies between the different soil moisture methods 78
5.5.2 Advantages and limitations of GPS soil moisture measurements 79
5.5.3 Sensitivity analysis of GPS soil moisture measurements 81
5.6 Conclusions 82
Acknowledgements 83
6. CONCLUSIONS AND OUTLOOK 84
6.1 Conclusions 84

6.2 Combination of GPS C/N_0 and carrier phase time delay for wet snow 86
6.3 Further research and development perspectives 88
APPENDIX XXVI
REFERENCES XXXVIII

LIST OF FIGURES

Figure 1.1: Behavior of the real and imaginary part of the complex permittivity of water in the entire microwave range for temperatures of 0 to 100°C. The red and blue arrows illustrate the effect of increasing temperature [*Chaplin*, 2016, modified]. The GPS L1-band frequency at 1.57542 GHz is marked as green line. 11

Figure 1.2: Overview of the SLF test site Weissflhjoch, near Davos, Switzerland in the Parsenn skiing area (photo taken by L. Schmid). The area where the GPS sensors are installed is situated approximately in the middle of the test field. 17

Figure 1.3: (a) Areal overview of the circular DWD test site which is situated in the North-western part of the City of Munich [*Google Earth*, 2016]. The vegetation-free soil measurement field is marked. (b) Part of the soil measurement field which was used for the soil moisture measurements (5 November 2013). The location of the surface antenna GPS1 and the approximate location of the buried antennas GPS2 & GPS3 and the weather-proofed box are marked. 18

Figure 1.4: Overview of the research objectives OJ1-OJ6 regarding setup, data input and processing. The derivation of the snow and soil properties, are indicated by different colours and are classified also according to the six thesis chapters. The direction of development is indicated..... 20

Figure 2.1: Overview of the location of the water-proof box with the Fastrax IT430 receivers, the hut where the PC was located and the Hirschmann GPS7M antennas of GPS1, GPS2 and GPS3 at the Weissfluhjoch test site on a snow-free reference day (26 September 2012)..... 26

Figure 2.2: Sky plot as a polar plot of all GPS satellites recorded simultaneously by the three GPS receivers at the Weissfluhjoch test site for one sidereal day. The angular coordinates describe the azimuth angle and the polar axis the elevation angle. C/N_0 values below an elevation angle of 10° were masked out for the calculation (these areas are marked grey)..... 27

Figure 2.3: Sky plot as a polar plot for the GPS satellite PRN 1 for one sidereal day with the classification of the C/N_0 values with 16 elevation and 16 azimuth classes. The classes assigned with values for PRN 1 are colored blue. C/N_0 values below an elevation angle of 10° were masked out for the calculation (these areas are marked grey). 28

Figure 2.4: Overview of influences on the measured GPS intensity and radiation path length through snow, as well as the angle changes due to the reflection, refraction and attenuation processes. Only the direct signal paths are shown (in red); several multipath effects at and multiple bounces between the air/snow and snow/ground interfaces are neglected..... 30

Figure 2.5: Permittivity vs. liquid water content (LWC) calculated with the three formulations and their mean for the real part ε_s' and the imaginary part ε_s''. The dry snow density was set to 370 kg/m³. 33

Figure 2.6: Normalized GPS C/N_0 values (dB) taken as the mean of the two GPS receivers under the snow cover (GPS2 and GPS3) at the Weissfluhjoch test site for the period 7 April–6 July 2013. 34

Figure 2.7: Bulk volumetric LWC of the snowpack above the antennas of GPS2 and GPS3 at the Weissfluhjoch test site for the period 7 April–6 July 2013, calculated with the normalized GPS C/N_0 data. The LWC was calculated with three different formulations (Roth, Denoth and Tiuri). Furthermore, the mean of the three curves, as well as reference measurements with the Snow Fork, the Denoth meter and the estimate from manually observed snow profiles are shown. 35

Figure 2.8: (a) Snow depth, (b) air and snow surface temperature and (c) lysimeter meltwater outflow, as well as the bulk volumetric LWC (mean of the three approaches, as in Figure 2.7) derived from normalized GPS C/N_0 measurements at the Weissfluhjoch test site during the time period 7 April–6 July 2013. Vertical dashed lines between six sub-periods (denoted I to VI). 36

Figure 2.9: (a) Snow depth, (b) air and snow surface temperature and (c) lysimeter meltwater outflow, as well as the bulk volumetric LWC derived from normalized GPS C/N_0 measurements at the Weissfluhjoch test site during the time period 14–21 April 2013. Daily peaks of the lysimeter outflow and the LWC are marked with the dashed lines in corresponding colors. 38

Figure 3.1: Overview of the study site Weissfluhjoch and the location of the measurement instruments and the profile line. The upGPR and the two GPS antennas as well as the snow scale and the snow pillow are buried in the ground below the snow cover. Ultrasonic 1 and 2 and the laser gauge are mounted on poles above the snow cover. The distances between the measuring devices are shown at the top. 44

Figure 3.2: Comparison of snow properties derived from upGPR and GPS with conventional measurements for the time periods 15 February to 12 July 2013 and 10 February to 20 June 2014. The colored backgrounds illustrate in white dry snow and in blue wet snow conditions. Light blue shows when snow height was at least 1m; dark blue when it was below 1m. Red backgrounds indicate when there were no upGPR data in 2013 and when the GPS receivers were no longer covered with snow in 2014. (a, b) Bulk volumetric liquid water content derived separately with upGPR and GPS using externally measured snow height data (laser). The markers show the average liquid water content of the snowpack measured in a snow pit with the Denoth sensor and the Snow Fork. (c, d) Snow height derived with the combination of upGPR and GPS, conventionally measured snow height at three different locations as well as manually measured snow height by probing directly above the upGPR. In addition, the snow height measured with the upGPR as described in *Schmid et al.* [2014] without GPS or external information is shown. (e, f) Snow water equivalent derived with the combination of upGPR and GPS, compared with the snow pillow, the snow scale, and manual measurements in a snow pit. 46

Figure 3.3: Diurnal variations of the bulk volumetric liquid water content in comparison with temperature and snow height data, exemplarily shown for the time period 29 May to 16 June 2013. (a) Evolution of the liquid water content in snow with daily fluctuations (upGPR and GPS), low-pass filtered with a moving average over 24 h without daily fluctuations ($upGPR_{mw24}$ and GPS_{mw24}), and the difference of LWC and the low-pass filtered trend representing the daily fluctuations ($upGPR_{df}$ and GPS_{df}). (b) Air temperature (TA) and snow surface temperature (TSS). (c) Snow height (HS) measured with the laser sensor and height of new snow (HN) as manually measured daily at 8 a.m. 47

Figure 4.1: GNSS setup for derivation of SWE. 53

Figure 4.2: Flow chart for individual processing steps aiming to derive SWE. The steps in blue/dashed boxes are specific to snow. 55

Figure 4.3: Carrier phase residuals for each GPS satellite recorded over one day (a) snow-free conditions (11 Oct 2015) with small fixed phase residuals around zero. Carrier phase residuals and arcs for each GPS satellite recorded over one day (b) for dry-snow conditions with a SWE of approx. 200 mm w.e. (13 Jan 2016), (c) for dry-snow conditions with a SWE of approx. 400 mm w.e. (5 Feb 2016), and (d) for dry-snow conditions with a SWE of approx. 600 mm w.e. (31 Mar 2016). 58

Figure 4.4: (a) Fixed phase residuals with arcs, exemplary shown for four reference satellites, recorded over approximately a time period of five hours on 17 January 2016. (b) Corresponding refracted elevation in dry snow of those four satellites. 59

Figure 4.5: Snow parameter determination: scaling of phase noise by mapping function and speed correction factor. 60

Figure 4.6: Snow water equivalent derived by GNSS carrier phase residuals compared to measurements recorded with a snow pillow and to manual snow pit measurements; all data from the test site Weissfluhjoch during the dry-snow season 2015-2016. 62

Figure 4.7: Linear regression between in each case two of the three SWE methods GNSS, snow pillow and manual. Black solid line indicates 1:1 line. 63

Figure 5.1: Soil measurement field at the DWD test site Munich. The locations of GPS1, GPS2 and GPS3 as well as the locations of the other soil moisture measurements (ECH_2O, ThetaProbe and gravimetric core probes) are marked. 67

Figure 5.2: (a) Vertical location and measurements range in the soil column of the different methods to derive soil moisture. (b) Validation of ThetaProbe soil moisture readings by comparison with gravimetric measurements at the DWD test site Munich at numerous field campaigns during the measurement period January 1, 2014 - June 10, 2015. 69

Figure 5.3: Overview of influences on the measured GPS intensity and radiation path length through the soil column, as well as the angle changes due to reflection, refraction and attenuation processes according to *Koch et al.* [2014]. Only the direct signal paths are shown for one satellite at a specific elevation (in red). 71

Figure 5.4: (a) Soil temperature at a soil depth of 5 cm and precipitation measured at the DWD test site Munich as well as (b) soil moisture measured by GPS, ECH_2O, ThetaProbe and gravitationally as well as modelled with PROMET at the DWD test site Munich during the measurement period January 1, 2014 - June 10, 2015. The winter time with potential snow cover and soil frost is excluded. 75

Figure 5.5: Comparison of soil moisture values (a) measured by ThetaProbe vs. measured by GPS, (b) measured by ECH_2O vs. measured by GPS, (c) modelled with PROMET vs. measured by GPS, (d) measured by ThetaProbe vs. measured by ECH_2O, (e) measured by ThetaProbe vs. modelled with PROMET and (f) measured by ECH_2O, vs. modelled with PROMET at the DWD test site Munich during the measurement period January 1, 2014 - June 10, 2015. 76

Figure 5.6: Comparison of soil moisture derived by GPS with the difference between (a) GPS and ThetaProbe, (b) GPS and ECH_2O, and (c) between GPS and PROMET as well as with the regression residuals between (d) GPS and ThetaProbe, (e) GPS and ECH_2O, and (f) between GPS and PROMET. The linear regression equations to calculate the residuals for each method compared to GPS were taken from the information given in Figure 5.5(a)-(c), respectively. 78

Figure 5.7: Soil moisture derived from GPS containing different assumptions on (a) an increase or decrease of the specific soil surface A_s, which is an indicator for different soil texture assumptions by ± 10 and ± 20, (b) a fix soil temperature assumption of 15°C and (c) a soil density over- and underestimation of $\pm 10\%$ and $\pm 20\%$ compared to the original parameterized calculations at the DWD test site Munich during the measurement period January 1, 2014 - June 10, 2015. 82

Figure 6.1: Schematic overview of a potential processing chain for dry and wet-snow conditions combining GPS C/N_0 and carrier phase. In this example a priori knowledge (option (b)) is used to solve the derivation of SWE, HS and LWC in case of wet snow. 87

LIST OF TABLES

Table 1.1: Overview on GPS sensor components and their amount installed at the test sites WFJ and MUC. In the Appendix related pictures are shown. 15

Table 1.2: Overview of journals in which the papers of this thesis are published or are submitted to (Journal Citation Report 2015 [*Thomson Reuters*, 2016]). 22

Table 2.1: Real ε_s' and imaginary part ε_s'' of the complex permittivity of snow, corresponding reflectivity r^2 and the attenuation coefficients α for varying values of LWC; LWC is the mean of the three approaches for the real part (Equations (2.13), (2.14) and (2.16)). 33

Table 2.2: Difference between the GPS-derived LWC and reference measurements (Denoth meter, Snow Fork and snow profile estimates). The absolute mean difference and the adjusted correlation coefficient are given. 36

Table 3.1: Root-mean-square deviations for bulk volumetric liquid water content ($RMSD_{LWC}$), snow height ($RMSD_{HS}$) and snow water equivalent ($RMSD_{SWE}$) for the season 2012-2013 (above diagonal, regular) and 2013-2014 (below diagonal, italic). Important results are shown in bold. 48

Table 4.1: Statistics overview of the comparison of SWE derived by GNSS and measured by snow pillow and weekly to bi-weekly manually measured in snow pits at the test site Weissfluhjoch for the dry-snow winter period 2015-2016. 62

Table 5.1: Values for the real and imaginary part of the complex permittivity of air ε_a, dry soil ε_{ds} according to the soil properties of the observed soil and bound water ε_{bw} [*Dobson et al.*, 1985]. 73

Table 5.2: Values for the real and imaginary part of the complex permittivity of free bulk water ε_{fw} at different soil temperatures. 73

Table 5.3: Statistics overview of the soil moisture retrieval from GPS, ECH_2O, ThetaProbe and gravimetric samples as well as the modelled soil moisture with PROMET at the DWD test site Munich during the measurement period January 1, 2014 - June 10, 2015. 77

Table 5.4: Statistics overview of the correlation coefficient and the RMSE comparing ThetaProbe, ECH_2O, PROMET and GPS. The upper triangular part (regular) represents the correlation coefficient and the lower triangular part (*italic*) represents the RMSE. 77

LIST OF ABBREVIATIONS

Abbreviation	Description
ALOS	Advanced Land Observing Satellite
AMSR-E	Advanced Microwave Scanning Radiometer-EOS
AMSU	Advanced Microwave Sounding Unit
ANavS	Advanced Navigation Solutions
ASAR	Advanced Synthetic Aperture Radar
a.s.l.	above sea level
C/A	Coarse Acquisition
C/N_0	Carrier-to-Noise power density ratio
CYGNSS	CYclone Global Navigation Satellite System
DD	Double Differences
DFG	German Research Foundation (Deutsche ForschungsGemeinschaft)
DWD	German Weather Service (Deutscher WetterDienst)
ERS	European Remote Sensing Satellite
ESA	European Space Agency
FD	Frequency Domain
GEROS-ISS	GNSS REflectometry, Radio Occultation and Scatterometry sensors onboard of the International Space Station
GLONASS	GLObalnaja NAwigazionnaja Sputnikowaja Sistema, Russian Satellite Navigation System
GLOWA	Global Change and the Hydrological Cycle (GLObaler WAndel des Wasserkreislaufs)
GNSS	Global Navigation Satellite System
GNSS-R	GNSS Reflectometry
GPS	Global Positioning System, American Satellite Navigation System
GRACE	GRavity Recovery and Climate Experiment
HN	Height of New snow
HS	Snow Height
HY	HYpothesis
ICESat	Ice, Cloud and land Elevation Satellite
IEEE	Institution of Electrical and Electronics Engineers

ISMN	International Soil Moisture Network
LiDAR	Light Detection And Ranging
LMU	Ludwig-Maximilians-Universität München
LWC	Liquid Water Content in snow
MODIS	MODerate resolution Imaging Spectrometer
MUC	MUniCh
NASA	National Aeronautics and Space Administration
NAVSTAR-GPS	NAVigational Satellite Timing And Ranging Global Positioning System
NMEA	National Marine Electronics Association
NOAA	National Oceanic and Atmospheric Administration
NSE	Nash-Sutcliffe Efficiency coefficient
OJ	ObJective
OSP	One Socket Protocol
QuickScat	Quick Scatterometer
QZSS	Quasi-Zenith Satellite System
PALSAR	Phased Array type L-band Synthetic Aperture Radar
pp	percent point
PRN	Pseudo Random Noise
PROMET	PROcesses of Mass and Energy Transfer
RA	Research Answer
RDP	Research and Development Perspectives
RHOD	Dry snow density
RINEX	Receiver INdependent EXchange
RMSD	Root-Mean-Square Deviation
RMSE	Root-Mean-Square Error
RQ	Research Question
RTK	Real Time Kinematic
SLF	Institute for Snow and Avalanche Research (Institut für Schnee- und LawinenForschung)
SSE	Sum of Squared Error
SWE	Snow Water Equivalent
SNF	Swiss National Science Foundation
SM	Soil Moisture

SMAP	Soil Moisture Active Passive
SMOS	Soil Moisture and Ocean Salinity
TA	Air Temperature
TanDEM-X	TerraSAR-X add-on for Digital Elevation Measurement
TDR	Time Domain Reflectometry
TechDemoSat-1	Technology Demonstration Satellite-1
TSS	Snow Surface Temperature
TWT	Two-Way Travel time
upFMCW	upward-looking Frequency Modulated Continuous Wave
upGPR	upward-looking Ground-Penetrating Radar
UTM	Universal Transverse Mercator
w.e.	water equivalent
WFJ	WeissFluhJoch
WSL	Eidg. Forschungsanstalt für Wald, Schnee und Landschaft

LIST OF SYMBOLS

Symbol	Description	Units
α	Attenuation coefficient	-
A_s	Specific soil surface	$m^2\ g^{-1}$
b	Baseline	m
c	Synchronization correction	m
c_0	Free-space speed of light	$m\ s^{-1}$
γ	Speed correction factor	-
d	Distance; vertical snow height / soil depth	m
d_s	Snow height at radiation path length / snow parameter	m
d_δ	Maximum bound water layer of uniform thickness	Å
δ_p	Penetration depth	m
ε	Phase noise	m
ε_0	Electric constant (vacuum permittivity)	$F\ m^{-1}$
ε'	Real part of complex relative permittivity	-
ε''	Imaginary part of complex relative permittivity	-
ε_a	Complex relative permittivity of water	-
ε_i	Complex relative permittivity of ice	-
ε_r	Complex relative permittivity	-
ε_s	Complex relative permittivity of snow / soil	-
ε_{ds}	Complex relative permittivity of dry snow / soil	-
ε_{ws}	Complex relative permittivity of wet snow / soil	-
ε_w	Complex relative permittivity of water	-
ε_{bw}	Complex relative permittivity of bound water	-
ε_{fw}	Complex relative permittivity of free water	-
ε_{w0}	Static dielectric constant of water	-
$\varepsilon_{w\infty}$	High frequency limit of the permittivity of water	-
e	Euler's number	-
$\vec{e}$	line of sight vector	-
E	Electric field	$kg{\cdot}m{\cdot}s^{-3}{\cdot}A^{-1}$

$E_{\perp}^{i}$	Field component of the incident wave perpendicular to the plane of incidence	kg·m·s^{-3}·A^{-1}
$E_{\parallel}^{i}$	Field component of the incident wave parallel to the plane of incidence	kg·m·s^{-3}·A^{-1}
$E_{\perp}^{r}$	Field component of the reflected wave perpendicular to the plane of incidence	kg·m·s^{-3}·A^{-1}
$E_{\parallel}^{r}$	Field component of the reflected wave parallel to the plane of incidence	kg·m·s^{-3}·A^{-1}
E_{a}	Elevation (without refraction)	°
E_{s}	Elevation of refracted signal in snow	°
f	Frequency	Hz
H	Magnetic field	N·m^{-1}·A^{-1}
I_o	Incident intensity; peak intensity	W m^{-2}
I_a	Attenuated intensity within the snowpack / soil	W m^{-2}
I_{m1}	Measured intensity above the snowpack / soil	W m^{-2}
$I_{m2,3}$	Measured intensity underneath the snowpack / within the soil	W m^{-2}
I_r	Reflected intensity at the snow / soil surface	W m^{-2}
I_t	Transmitted intensity into the snowpack / soil	W m^{-2}
J	Current density	A m^{-2}
λ	Wavelength	m
λ_{a}	Wavelength in air	m
λ_{s}	Wavelength in snow	m
N	Integer ambiguity	-
m	Mapping function	-
m_v	Volumetric soil moisture	m^3 m^{-3}
μ_0	Magnetic constant (vacuum permeability)	V s A^{-1} m^{-1}
N	Integer ambiguity	-
n	Refraction index	-
n_{a}	Refraction index of air	-
n_{s}	Refraction index of snow / soil	-
Q	Electric charge	C
ρ	Pseudorange, code phase	m
ρ_{a}	Density of air	kg m^{-3}
ρ_{b}	Density of soil	kg m^{-3}
ρ_{i}	Density of ice	kg m^{-3}
ρ_{s}	Density of snow / specific soil density	kg m^{-3}

ρ_{ds}	Density of dry snow	kg m^{-3}
ρ_{ws}	Density of wet snow	kg m^{-3}
ρ_{w}	Density of water	kg m^{-3}
φ	Carrier phase	cycles
$r_{\perp}$	Perpendicular reflection coefficient	-
$r_{\parallel}$	Parallel reflection coefficient	-
σ	Standard deviation of x	units of x
σ_{bulk}	Conductivity of the soil paste	mS cm^{-1}
σ_G	Conductivity in the Gouy layer	mS cm^{-1}
σ_{m_v}	Conductivity of water	mS cm^{-1}
t	Time	s
τ	Time constant	s
τ_w	Relaxation time of pure water	s
ϑ_0	Angle of incidence	°
ϑ_{elev}	Elevation angle	°
ϑ_{refr}	Refraction angle	°
θ	angle	°
θ_w	Liquid water content in snow	%
v	Velocity	m s^{-1}
v_{a}	Velocity in air	m s^{-1}
v_{s}	Velocity in snow	m s^{-1}
V_a	Volume fraction of air in soil	g cm^{-3}
V_{bw}	Volume fraction of bound water in soil	g cm^{-3}
V_{fw}	Volume fraction of free water in soil	g cm^{-3}
γ	Speed correction factor	-
χ	Upper bound of squared residuals	m²
z	Direction	-
Z_{s}	Wave impedance for snow	Ω
Z_v	Free-space wave impedance	Ω

1. INTRODUCTION

1.1 Motivation and research questions

Responsibilities and tasks of applied hydrology are of rising importance. Continuous environmental monitoring of hydrological parameters is irreplaceable for a better understanding of our Earth's climate system, the hydrologic cycle and the hydrologic storages. This includes for example the big challenges extreme event and hazard prevention, water supply for agricultural production and drinking water as well as economic and ecological management of navigation, tourism and energy. These topics were extensively investigated for example in the integrated project GLOWA-Danube and in continuing studies for the Upper Danube basin for the past and recent climate situation and for future climate scenarios [*GLOWA-Danube*, 2009; *Ludwig et al.*, 2003; *Mauser and Prasch*, 2015].

As an example, *Koch et al.* [2011a and 2011b] found out that for the Alpine Upper Danube basin a large portion of runoff and hydropower generation is influenced by the amount and temporal release of the seasonal snow cover. Within this catchment, the highest portion of snow melt, with up to approximately 40% of the total runoff, occurs in the Alps and Alpine forelands. Particularly, the energy generation of run-of-the-river power plants is influenced by the temporal occurrence of snow melt. Additionally, reservoir power plants are affected by snow cover driven reservoir filling stages. This illustrates that a precise knowledge on the amount and melting occurrence of snow is largely important for planning and managing energy generation. Bringing this example to a broader context by taking into account the needs of future generations and considering climate change impacts, a better and enlarged monitoring of the environment, encompassing e.g. the snow and soil storages, is highly needed as an adaptation strategy [*ICPDR*, 2013]. The hydrological snow storage and soil storage are rather short-term, compared to groundwater, glaciers or oceans which underlie a longer retention time. Both are due to their high dynamics extremely important as input variables for climate and hydrological simulations.

In general, seasonal snow is a key parameter in fresh-water resources management and an essential component within the Earth's climate system [*Barnett et al.*, 2005; *DeWalle and Rango*, 2008; *Vaughan et al.*, 2013]. Snow cover dynamics in alpine head-watersheds play a significant role on the water supply under current and future climate conditions [*Prasch et al.*, 2013; *Weber et al.*, 2016], but are also globally of high importance. Depending on the season, the worldwide snow cover of land lies between 16 and 57 Mio. km² [*Baumgartner and Liebscher*, 1996]. During the Northern Hemisphere's winter period, more than 50% of the landmass can be covered with snow [*Foster and Rango*, 1982]. In the Northern Hemisphere, snow plays an important role as temporal water storage for most areas of the Eurasian and Northern American continents between the Arctic Circle and the Northern Tropics. Worldwide, approximately one-third of water originating from snow melt serves for crop growth [*Steppuhn*, 1981] and is in numerous regions a necessary source and control parameter for irrigation and general water availability [*Immerzeel et al.*, 2009; *Mankin et al.*, 2015; *Rango*, 1980]. Moreover, the amount of snow and the snow melt may also influence the dynamics in soil moisture in affected regions.

Soil moisture in general is one of the most relevant variables for water management, plant growth, e.g., in agriculture, or for the emergence of floods and is a key variable in the global energy and water cycle [*Dirmeyer*, 2000; *Jung et al.*, 2010]. Especially in the upper most centimetres of the soil, soil moisture is highly dynamic and acts as direct link between the terrestrial and atmospheric interface. Similar to the hydrological snow storage, the soil storage is coupled with the climate system and hydrological processes like precipitation, evapotranspiration, infiltration and as surface runoff, interflow or groundwater recharge. Therefore, continuous and spatially distributed knowledge about this variable is highly needed for global and regional climate and land surface simulations and to improve the forecasting of water availability [*Dorigo et al.*, 2011; *Koster et al.*, 2004;

Seneviratne et al., 2010]. As mentioned above, soil moisture serves as water source for plants. In times of climate change and an increasing world populations this is highly relevant for agricultural production and food security [*Godfray et al.*, 2010; *Mauser et al.*, 2015] and is also discussed in current debates on water resources management and the food water energy nexus [*Dobriyal et al.*, 2012; *Ringler et al.*, 2013].

In summary, an improvement in snow and soil monitoring is necessary to reduce uncertainties in the simulation of climate change, and to improve diverse hydrological applications. However, until now, continuous model inputs and proper validations of snow cover properties and soil moisture are scarce. Environmental monitoring is still not sufficient and current remote sensing and ground-based snow measurements often lack the required temporal and spatial resolution or are not applicable in remote and complex terrain. Furthermore, numerous sensors and measurements techniques are quite expensive, weather-dependant, error-prone or labour-intense.

Therefore, the overall motivation of this thesis is to improve environmental monitoring with high temporal resolution, of hydrological snow and soil storages. Envisaging a potentially ideal in situ sensor for such applications, it should be easy to install with low maintenance, it should measure non-destructively and should also be suitable for applications in remote or difficult to access areas. The potential sensor should be low-cost, e.g. compared to high-end geodetic sensors, making the installation at numerous locations for basin-wide applications potentially possible.

This thesis introduces an innovative Global Navigation Satellite System (GNSS) technique to derive essential data for continuous snow and soil monitoring. In particular, this approach focuses on the three snow cover properties snow height (HS), snow water equivalent (SWE), and liquid water content in snow (LWC) as well as soil moisture (SM). The measurements are based on simple low-cost Global Positioning System (GPS) receivers and antennas recording the freely available L1-band signals at 1.57542 GHz. However, these GPS sensors were used in a completely different way than for standard applications, like positioning or navigation approaches. Moreover, this novel GPS approach is different to current microwave remote sensing approaches, where the information of the Earth's surface is mainly based on scattering at the medium's surface by applying active sensor systems or based on emission through the medium by applying passive sensor systems. The main idea of this thesis is that the electromagnetic waves, broadcast by the GPS satellites, pass through media like snow or soil and are tracked within or underneath the observed medium to deliver information about the investigated medium. Thereby mainly signal strength attenuation and time delay of electromagnetic waves through a medium are investigated. In the following, the three **research questions** (**RQ**) of this thesis are presented. Additionally, the corresponding **hypotheses** (**HY**) are formulated:

RQ1. ***Is it possible to derive information on environmental parameters with low-cost GPS sensors by analysing GPS signals passing through a medium like snow or soil?***

HY1: With commercially available low-cost GPS sensors, the freely broadcasted L1-band can be tracked encompassing numerous signal information in their sensor specific raw data protocol like information on position, carrier phase and carrier frequency, Doppler shift and signal strength. In general, by applying the physical fundamentals of the interrelation of electromagnetic waves with dielectric materials, information on environmental properties can be measured by passing through a medium considering signal attenuation within the medium and time delay of the signals through the medium. Already many remote sensing Earth observation missions, which successfully derived environmental parameters like soil moisture and snow cover properties, have been carried out in the L-band frequency range. As the GPS L1-band is also broadcast in the L-band domain, it should be possible to use the GPS signals for the derivation of environmental properties as well.

RQ2. ***Which snow cover properties can be derived? Which GPS raw data information is necessary, how should the GPS sensors be located, and is external information required?***

HY2.1: Dry snow is a mixture of air and ice. If the snow becomes wet, droplets of liquid water occur in the snow pores due to melting processes or rain water. In the microwave range, water has, compared to

other material of the Earth's surface, significantly different dielectric properties leading to clear signal strength attenuation of the signals received at an antenna beneath the observed media. The signal strength is recorded by the carrier-to-noise-power density ratio (C/N_0) of each GPS satellite at each time step and elevation. Combined with dielectric mixing models and information on its vertical extent, the GPS signal strength attenuation in wet snow can be used to retrieve quantitative information on the bulk volumetric LWC.

HY2.2: Following physical laws and considering dielectric mixing models of snow, the snow properties LWC, SWE and HS can be retrieved simultaneously. Therefore, signal attenuation and information on the travel time of signals in snow have to be combined. HS and SWE are related by the dry snow density, which can either be assumed or measured. During wet-snow conditions, when liquid water is present, the wave velocity is further reduced, which leads to the problem that SWE and HS might be overestimated. This could, however, be corrected by including signal strength information on LWC.

HY2.3: The GPS carrier phase measurements give information on the travel time of GPS signals between satellites and receivers. The velocity of electromagnetic waves travelling through snow is markedly reduced, compared to the velocity in the air, which is roughly the speed of light. To get information on this, one GPS antenna should be installed above the snow cover and one should be placed on the ground level below the snowpack. Both GPS receivers simultaneously record carrier phases. With a specific RTK (Real Time Kinematic) positioning approach the baseline between both antennas can be calculated for snow-free conditions. During periods with snow cover, the calculated distance between the two antennas, expressed as carrier phase residuals, increases virtually due to the delay of the GPS signals passing through snow. This time delay information can then be transformed to the snowpack quantity, expressed as SWE. During wet-snow conditions, in addition C/N_0 data should be used to correct the SWE and to derive HS and LWC as well.

RQ3. ***Is it possible to transfer the derivation of snow cover properties to soil properties?***

HY3: In principle, the physical fundamentals of the behaviour of electromagnetic waves in snow and in soil are the same. However, their dielectric characteristics are different and soil has a higher density than snow. Soil is a mixture of air, soil particles with a specific texture and bound and free water in the soil pores. Analogous to the signal strength attenuation in wet snow, the GPS signals attenuate due to liquid water in the observed soil column. For this approach at least one antenna has to be placed at a certain soil depth. The maximum installation depth whether or not the GPS signal can still be tracked depends on the soil texture, density and SM. From this information and combined with a dielectric mixing model, SM can be derived quantitatively.

The presented research questions and hypothesis are investigated in detail within the scientific papers of this cumulative thesis in the *Chapters 2* to *5*. In *Chapter 6* the answers to the research questions are summarized and an outlook on potential further work is given.

Before going more into detail, the state of the art on this topic is described. In *Section 1.2*, the three investigated snow cover properties, and soil moisture are defined, and an overview on possible ground based and remote sensing methods, encompassing their challenges and potential limitations, is presented. The physical basis of electromagnetic waves and their interrelations with materials with different dielectric properties such as air, water, snow and soil is demonstrated in *Section 1.3*. An overview on GNSS as well as the state of the art of GNSS measurements of environmental properties is following in *Section 1.4*. In *Section 1.5*, the used GPS sensors and the partly self-constructed components, the applied raw data, and the test sites Weissfluhjoch (WFJ) for the snow observations, and the Munich (MUC) for the soil moisture monitoring are described. *Section 1.6* provides the formulation of the six main research objectives, which should help to solve the research questions and finally lead to the thesis outline, structured by objectives, chapters and scientific papers, respectively.

1.2 Definition and measurement methods of snow cover properties and soil moisture

The investigated snow cover properties and the soil moisture are shorty defined in this section. Moreover, comprehensive information on the state of the art regarding snow cover properties and soil moisture measurements are presented and their challenges and limitations are pointed out.

1.2.1 Snow cover properties

Snow is one of the most difficult weather elements to be measured in an accurate, consistent manner [National Weather Service, 2013]. In the early and mid-20th century, first in situ snow measurements were carried out for scientific research [*Colbeck*, 1987]. This encompassed snow hydrological purposes [*Garstka*, 1958; *US Army Corps of Engineers*, 1956] and avalanche protection [*SLF*, 2015a]. In the last decades, snow monitoring of various snow cover properties with ground-based in situ and remote sensing methods has increased largely and became operationally for various hydrological, climatological and hazard prevention applications. In this thesis the snow cover properties HS, SWE and LWC are investigated, which are as already mentioned to be of major interest to describe hydrological and climate processes and which play an important role in risk assessment. In the following, these terms are defined and an overview on current ground-based and remote sensing methods regarding HS, SWE and LWC for dry and wet-snow conditions is given.

Definition of HS, SWE and LWC

Snow is a granular material of crystalline ice that was formed as flakes in the clouds. During snowfall the flakes are further shaped due to the atmospheric conditions and can be deposited on the Earth's surface as seasonal or permanent snow cover. Deposited snow on the ground is a highly porous, sintered material and undergoes a steady transformation, known as metamorphism, according to temperature, radiation and wind [*Fierz et al.*, 2009]. In general, the snow cover is characterized by several properties like its amount, depth, wetness, and density and several stratigraphic characteristics such as grain size, grain shape and hardness.

HS: The snow height describes the entire thickness of a dry or wet snowpack and is given in cm; the height of new snow (HN) is defined as freshly fallen snow which has accumulated during a defined observation period of e.g. 24 h on top of HS from the day before [*Fierz et al.*, 2009]. Information on HS and HN and temperature, wind and stratigraphy, are essential parameters in avalanche research [*Schweizer et al.*, 2003].

SWE: The snow water equivalent represents the quantity of water that would be released upon complete melting of a dry or wet snowpack [*Fierz et al.*, 2009]. As SWE is a measure for the amount of snow, it is highly requested by hydrologists [*DeWalle and Rango*, 2008]. SWE is the product of HS and the snow density and is given in mm water equivalent (w.e.). Therefore, HS and SWE are closely related, especially for dry-snow conditions. During melting conditions, they can differ significantly due to a markedly increase of the wet snow density. Dry snow density can either be measured in snow pits or can be estimated [e.g., *Jonas et al.*, 2009].

LWC: The liquid water content in snow is the factor that determines whether a snowpack is dry or wet. If the snowpack is dry, it contains only air and ice particles. If it turns wet, also droplets of liquid water arise between the ice particles. The transition from dry to wet snow occurs either in case the snowpack starts to melt due to intense short- and longwave radiation or if it is infiltrated by rain. In return, the snowpack can only refreeze partly to almost dry conditions; an irreducible liquid water content remains [*Mitterer*, 2012]. Qualitatively, snow wetness can be expressed by the five conditions dry, moist, wet, very wet and soaked/slush [*Fierz et al.*, 2009; *Perla and Martinelli*, 1978]. The bulk volumetric LWC can be derived by several empirical formulas as well as dielectric mixing models (see *Section 2.5*). LWC is closely linked to the melt-water outflow of a snowpack. Moreover, due to water infiltration, the snowpack may lose its strength which might lead to wet snow avalanche formation [*Mitterer et al.*, 2011b].

Ground-based snow measurements

Ground-based measurements of snow are limited to a certain location, but serve as a necessary input for different applications. Measurements of HS are the most common snow measurements. Although SWE is a highly demanded variable, especially by hydrologists, there is still a great lack in ground-based SWE measurements and LWC is even totally underrepresented by measurements.

HS: Since several decades, HS is conventionally and operationally measured, either routinely by manual surveys with rulers and snow sticks or continuously with laser or ultrasonic sensors. The new snow height (HN) accumulated during one day can either be measured manually with a snowboard which has to be cleared every day at the same time or as the increase in HS with other continuous measurement instruments during a defined time period. In general, HS measurements are the most accurate snow measurements. New measurements techniques encompass e.g., terrestrial laser scanning [e.g., *Grünewald et al.*, 2010; *Prokop*, 2008] or microwave radar systems such as an upward-looking ground-penetrating radar (upGPR) which are installed below the snow cover [e.g., *Heilig et al.*, 2009; *Schmid et al.*, 2014]. The new systems have in common that they are also applicable for slopes, but are not conventionally applicable and quite expensive which makes a usage at numerous locations like sensor networks unrealistic. Regarding recent investigations in ground based GNSS reflectometry (GNSS-R) it is referred to *Section 1.4.2*.

SWE: Compared to HS, it is more difficult and less accurate to measure SWE. The most accurate measurements are done manually. At snow profile surveys, SWE measurements are performed by weighing the snow mass in cylindrical probes with a defined volume, but only at a few locations in the mountains, like at the SLF test site WFJ, these manual measurements are performed on a bi-weekly mode [*Marty and Meister*, 2012]. Only at a few locations, SWE is measured continuously with instruments that rely on weighing systems. These are mainly permanently installed snow pillows or snow scales. However, both systems are limited to levelled terrain and could be influenced by bridging effects within the snowpack, especially when the snow transits from dry to wet [*Johnson and Marks*, 2004]. Further, estimates on SWE can be carried out by precipitation or runoff measurements, which, however, neglect evaporation losses. The meltwater outflow of a snowpack can be registered, e.g., with a special snow lysimeter [*Kattelmann*, 1984], though this method is only possible during melting conditions. The amount of solid precipitation can be measured by precipitation gauges or laser distrometers, but the measurement of solid precipitation is more error prone than for liquid precipitation [*Tabler et al.*, 1990]. Especially wind can cause 40 to 80% errors in solid precipitation measurements compared to liquid precipitation were the errors due to wind range between 3 to 20% [*Goodison et al.*, 1998].

LWC: Measurements of LWC are even more difficult. This is due to non-linear processes like water infiltration and flow within the snowpack, which are moreover variable in space and time. Until now, no satisfying operational method exists to continuously and non-destructively monitor LWC. Manual snow wetness observations in snow pits provide only a rough estimate which are based on a wetness index [*Fierz et al.*, 2009; *Perla and Martinelli*, 1978]. An overview of several in situ snow wetness measurements with devices is given by *Boyne and Fisk* [1987], *Mitterer* [2012] and *Techel and Pielmeier* [2011]. They include techniques like hot (melting), cold (freezing) or alcohol calorimetry and dilution methods and dielectric measurements. The dielectric properties of wet snow can, e.g., be measured within snow pits by the devices Denoth meter [*Denoth*, 1989; *Denoth et al.*, 1984] and the Finnish Snow Fork [*Sihvola and Tiuri*, 1986]. However, they have in common that they are destructive, cumbersome, laborious, show only a snap-shot in time, and can only be applied at accessible locations. Approaches of time-domain reflectometry (TDR) [e.g., *Schneebeli et al.*, 1998; *Waldner et al.*, 2001] were able to monitor the snow wetness continuously and non-invasively; but, this technique is also error-prone as these instruments need to be placed within the snowpack and influence thereafter the water flow. With radar systems, a wetting front within the snowpack and the bulk volumetric LWC can be monitored also at avalanche starting zones [*Schmid et al.*, 2014]. But, as already pointed out, radar measurements are expensive and they need further external measurements to derive LWC.

Remote sensing of snow properties

Compared to ground-based measurements, remote sensing approaches have the advantage to deliver data with high spatial coverage, also for locations which are remote and not easy to access. However, they often lack the necessary temporal or spatial resolution, e.g., regarding snow melting processes or are not applicable in steep terrain due to geometric issues. A comprehensive overview on snow remote sensing is given e.g., by *Hall and Martinec* [1985], *Rees* [2005] and *Tedesco* [2014]. With multispectral and hyperspectral sensors, the snow cover extent or single snow cover properties like albedo or grain size can be detected by indexing methods [*Dozier and Painter*, 2004; *Painter et al.*, 2009]. Regarding all spaceborne techniques, in particular active and passive microwave remote sensing approaches are applied for the detection of snow cover properties. Their information relies on the dielectric characteristics of the observed medium snow [*Mätzler et al.*, 1984].

HS/SWE: As a first step, most approaches aim to derive HS and then, take density estimates into account, to calculate SWE [*Tedesco*, 2014]. HS and SWE approaches work quite well under dry-snow conditions but are still unreliable or uncertain as the snow becomes wet. The reason for this is that the occurrence of water causes distinct change in the dielectric properties. Passive microwave approaches investigate microwaves emitted from the snowpack. The brightness temperature measured at the sensor is dependent on wetness, volumetric scattering, grain size and the frequency of the microwave signal. Until now, several brightness temperature algorithms for HS and SWE detection exist in the literature [e.g., *Chang et al.*, 1987; *Hallikainen*, 1984; *Mätzler*, 1987; 1994; *Pulliainen and Hallikainen*, 2001; *Rango et al.*, 1979; *Tedesco and Kim*, 2006; *Tsang et al.*, 1992]. However, several sources of errors might occur due to uncertainties in estimating the correct grain size or considering liquid water [*Foster et al.*, 2005; *Rees et al.*, 2006; *Tedesco et al.*, 2010]. The same brightness temperatures might express different snow cover property combinations describing the ill-posed nature of the retrieval problem. Therefore, passive microwave approaches are dependent on a priori knowledge to properly depict HS and SWE. Active microwaves techniques use the backscattered signal from an active sensor. Ku-band scatterometers (e.g., QuickScat) seem to be most suitable for HS retrievals [*Hallikainen et al.*, 2003]. But also X, C, or even L-band sensors (e.g., SIR-C, X-SAR, Envisat ASAR, CryoSat-2, SMOS, Sentinel-1) have recently been applied [e.g., *Bernier and Fortin*, 1998; *Bernier et al.*, 1999; *Maaß et al.*, 2013; *Shi and Dozier*, 2000]. In addition, several interferometric approaches (e.g., ERS-1/2, TanDEM-X, TerraSAR-X) have been proposed [e.g., *Guneriussen et al.*, 2001; *Rott et al.*, 2003]. In some studies, active and passive microwave techniques were combined to achieve more precise solutions [e.g., *Hallikainen et al.*, 2003; *Tedesco and Miller*, 2007]. Besides microwave remote sensing, global SWE estimates have been achieved e.g., with gravity data from the GRACE satellites [*Niu et al.*, 2007]. Moreover, the new LiDAR ICESat-2 satellite, which should be launched in 2017, looks promising to generate global HS maps. Looking at small scales, changes in HS can be derived with photogrammetry or airborne laser scanning and LiDAR (Light Detection and Ranging) techniques with high accuracy [e.g., *Deems et al.*, 2013; *Hopkinson et al.*, 2004]. SWE can be gained with airborne gamma radiation measurements [e.g., *Carroll and Carroll*, 1989; *Fritzsche*, 1983]. However, these techniques can only be carried out for small catchments and are not operationally in use because they are expensive, weather-dependant, labour-intense. As they can only be applied occasionally these data show only a snap-shot in time.

LWC: Wet snow can be detected with optical and thermal sensors (e.g., MODIS, LANDSAT) [e.g., *Hall et al.*, 2006 and 2013]. Moreover, all active and passive microwave sensors (see above) directly detect changes of the dielectric properties of snow due to an increase of water in snow [e.g., *Abdalati and Steffen*, 1995; *Loew et al.*, 2002; *Nagler and Rott*, 2000; *Takala et al.*, 2009; *Tedesco*, 2009]. Regarding active microwaves, the backscattering coefficient decreases significantly as the snow becomes wet whereas, regarding passive microwaves, the brightness temperature increases [*Stiles and Ulaby*, 1980]. Most of these remote sensing approaches for wet snow detection are used to generate large scale (e.g., Greenland or Antarctica) or global snow melting maps. The melt-onset and daily melt-freeze cycles can easily be detected, but no quantitative assumption on the LWC using microwave remote sensing can be made [*Tedesco*, 2014].

1.2.2 Soil moisture

The intense monitoring of SM has started in the early last century with agricultural crop growing as its main focus driver. This aspect is nowadays an even more important factor in managing today's global food security. In the last decades, the scope of SM monitoring has moved also towards climate and hydrological aspects. Currently numerous ground-based in situ measurements and microwave remote sensing approaches are operationally in use and worldwide databases on SM are built up.

Definition of soil moisture

SM describes the quantity of water in the soil. It may be expressed as volumetric water content with regard to the volume or as gravimetric content with regard to the mass of a soil column. The SM range of a specific soil largely depends on its soil texture, soil density and mineral composition. It has an influence on the capacities of water storage, percolation and capillary rise. The minimum SM that can be accessed by plants is often expressed as wilting point and the maximum SM content which can be hold in the pores as field capacity. The resulting overall SM range available for plants is the so called usable field capacity [*Scheffer and Schachtschabel*, 2002].

Ground-based soil moisture measurements

In situ soil moisture can either be measured directly or indirectly. The gravimetric method is the only direct method where defined soil samples are weighed before and after drying. The mass changes are directly linked to the SM content of the observed soil sample. Time domain reflectometry (TDR) and frequency domain (FD) are indirect methods applying electromagnetic techniques which measure the dielectric properties of the soil in connection with its water content. TDR uses the time information of a reflected waveform to calculate the SM content, whereas FD is classified as a capacitance technique. Both methods can be utilized as permanently installed probes in sensor networks and are able to log SM at different soil depths. However, they often have to be calibrated and the original soil column might be disturbed by the installation. Moreover, the SM readings might be affected by air or water gaps around the sensor prongs [*Walker et al.*, 2004]. In the last years, ground-penetrating radar systems have also been applied to derive SM non-invasively based on dielectric soil properties [e.g., *Klenk*, 2012]. The matric potential of soil water can be measured with tensiometers and resistance blocks, which are mainly applied for agricultural applications. Since recently, in situ SM can also be derived by applying cosmic-ray neutrons [*Zreda et al.*, 2008] as an integral over a few 100 m. Further, approaches based on neutron probes [*Vachaud et al.*, 1977] can be used. But these techniques are, in particular due to intense calibration, high costs and high maintenance, not operationally applicable, yet. A comprehensive overview of different in situ soil moisture measurement techniques is given, e.g., in *Robinson et al.* [2008], *Scheffer and Schachtschabel* [2002] and *Walker et al.* [2004]. Besides, many SM techniques applied in a number of different networks around the globe are summarized in the International Soil Moisture Network (ISMN) [*Dorigo et al.*, 2011].

GNSS-R approaches for SM monitoring exist and are similar to those retrieving HS. They are also shortly described in *Section 1.4.2*.

Remote sensing of soil moisture

In the last decades, active and passive microwave remote sensing techniques have been developed and were applied successfully for soil moisture monitoring on different scales [e.g., *Dobson and Ulaby*, 1986; *Loew et al.*, 2006; *Mauser et al.*, 1995; *Njoku et al.*, 2003; *Ulaby et al.*, 1996; *Wagner et al.*, 2007]. *Brocca et al.* [2011] and *Peng et al.* [2015], for example, evaluated different satellite based SM products and with respect to spatial downscaling of satellite soil moisture. Moreover, *Peng et al.* [2016] developed a method applying besides microwave data also visible and infrared satellite observations and using a specific vegetation temperature condition index. With all these remote sensing methods it is possible to derive surface SM as an integral of the moisture in the upper few centimetres of the soil depending on the dielectric characteristics, which vary with

varying SM content. The spaceborne sensors used for active microwave SM monitoring encompass, e.g., Sentinel-1, ERS-1/2, Envisat ASAR, RADARSAT-1/2, ALOS PALSAR. Since several decades, also numerous studies based on passive microwave approaches to measure SM have been carried out [e.g., *Eagleman and Lin*, 1976; *Wang et al.*, 1990; *Wigneron et al.*, 2003]. One of the first spaceborne passive microwave radiometer missions was AMSU in 1978, followed by several others like AMSR-E since 2002. In 2009, the Soil Moisture and Ocean Salinity (SMOS) satellite operated by ESA [*Barré et al.*, 2008; *Kerr et al.*, 2010] and in January 2015, the Soil Moisture Active Passive (SMAP) satellite operated by NASA was launched [*Entekhabi et al.*, 2010]. Both recent passive satellite missions operate in the microwave L-band, which is most suitable for soil moisture observations [*Kerr et al.*, 2001].

1.2.3 Challenges and limitations

Environmental monitoring of snow cover properties and soil moisture is still a challenge and in many areas there is a lack of continuous and reliable measurements. Besides many advantages, practically all current measurement methods have their limitations.

Ground-based measurements give an appropriate picture of the situation at a certain location and deliver measurements with high temporal resolution. However, they are often restricted in their spatial coverage, especially when applied at single stations, representing information for large areas. Regarding this, without a dense sensor network, representativeness for larger areas is limited. Soil moisture can vary locally and vertically, depending on local soil texture variations and climate factors. Regarding snow covered regions the snow cover properties vary significantly at different expositions, slope gradients or altitudes. Moreover, several in situ sensors installed on poles are not applicable, e.g. in complex or steep avalanche prone terrain as they would be destroyed in case of extreme events. Due to high maintenance and too high costs of the sensors, e.g., snow pillows, some environmental properties like SWE are measured only at a few locations worldwide. Manual measurements are often precise, but they show only a snap-shot in time and are time consuming and labour intense. If a snowpack or a soil column should be investigated in its vertical extent, snow pits or a hole in the soil have to be dug, which might destroy the original snow or soil layering. Moreover, some regions are too remote or are too risky to access routinely by labourers.

Regarding remote sensing applications with optical and infrared sensors, problems arise from possible cloud cover. Microwave remote sensing is weather-independent but relies on complex data processing. Passive microwave sensors cover large areas and deliver good estimates for large scale soil moisture or snow cover applications; however, their spatial resolution with up to several km² is too low to apply it in complex, especially alpine terrain. And in particular active microwave approaches are limited due to foreshortening, shadowing and layover effects which reduce their applicability in complex terrain and especially in alpine regions, where a low spatial resolution and mixed pixels can distort the information for certain regions and altitude levels [*Strozzi et al.*, 1997, *Wiesmann et al*., 2007].

Generally, a reasonable combination of several methods encompassing ground-based measurements and remote sensing techniques and combinations with modelling approaches might be most promising to avoid errors and to achieve the highest benefit in environmental monitoring [*Tedesco*, 2014] and of course, further development and research in the field of environmental monitoring as presented in this thesis, is promising and advisable.

1.3 Physical basis on electromagnetic waves and dielectric properties of snow and soil

The GPS approach presented in this thesis is based on the interrelation of electromagnetic waves with media like snow and soil. The physical fundamentals are presented in the following.

1.3.1 Propagation, reflection and refraction of electromagnetic waves

A significant point in the history of physics was the formulation of the Maxwell's equations describing the relation of the electric field E, the magnetic field H, the electric charge Q, the current density J, the magnetic permeability $\mu^*$and the dielectric permittivity ε^* [*Ulaby and Ravaioli*, 2015; *Woodhouse*, 2005]. In this section, the main formulations which are relevant for the scope of this thesis are described.

The one-dimensional propagation of the electromagnetic waves is defined by

$$\frac{\partial^2 E}{\partial z^2} = \mu^* \varepsilon^* \frac{\partial^2 E}{\partial t^2}, \tag{1.1}$$

where E is the electrical field, z the direction and t the time variable. The magnetic permeability ($\mu^* = \mu_0 \cdot \mu$) is the product of the magnetic permeability μ_0 of free space and the relative magnetic permittivity μ which is 1 for nonmagnetic materials like snow or soil. Analogously, the dielectric permittivity ($\varepsilon^* = \varepsilon_0 \cdot \varepsilon$) is the product of the dielectric permittivity of free space ε_0 and the relative dielectric permittivity ε in Equation (1.1). The latter is medium-specific and is considered complex ($\varepsilon = \varepsilon' + i\varepsilon''$) with a real part ε′and an imaginary part ε′′. In general, dielectric properties are often described as a complex function of the frequency of the applied electromagnetic field. The real part ε′ of the complex permittivity is thereby related to the stored energy. The imaginary part ε′′ is related to the loss of energy within a medium and is also called dielectric loss factor [*Ulaby et al.*, 2014].

The phase velocity v of electromagnetic waves can be derived after Maxwell's equations:

$$v = \frac{1}{\sqrt{\mu^* \varepsilon^*}} \tag{1.2}$$

Investigating a low-loss dielectric material ($\varepsilon''/\varepsilon' \ll 1$) [*Woodhouse*, 2005], where conductivity can be neglected, the phase velocity within a nonmagnetic material can be simplified [*Bradford et al.*, 2009] to

$$v = \frac{c_0}{\sqrt{\varepsilon'}} \tag{1.3}$$

where the speed of light in free space is

$$c_0 = \frac{1}{\sqrt{\mu_0 \varepsilon_0}} \cong 3 \times 10^8 \text{ m s}^{-1} \tag{1.4}$$

The distance d the electromagnetic wave travelled through a medium in a certain time t is defined as

$$d = vt \tag{1.5}$$

In general, the incident, reflected and transmitted waves at an interface between two media follow the Fresnel equations of reflection and transmission and the law of conservation of power. At boundaries between two different media, electromagnetic waves might be reflected at and transmitted through their interface. The amount of reflected energy is dependent on the relationship between the wave impedance Z_i of media 1 and 2, which defines the reflection coefficient

$$r = \frac{Z_2 - Z_1}{Z_2 + Z_1} = \frac{(\varepsilon_2' + i\,\varepsilon_2'') - (\varepsilon_1' + i\,\varepsilon_1'')}{(\varepsilon_2' + i\,\varepsilon_2'') + (\varepsilon_1' + i\,\varepsilon_1'')} \tag{1.6}$$

in case the magnetic permeability does not change and at normal incidence. The calculation of the amount of reflected energy for oblique incident angles is described in *Section 2.4.4*.

The refraction index n is defined as the square-root of the relative dielectric permittivity

$$n = \sqrt{\varepsilon}. \tag{1.7}$$

After Snell's Law the angles of incidence θ_1 and refraction θ_2 are related as follows to the refraction coefficients n_1 and n_2 of two different media:

$$\frac{n_1}{n_2} = \frac{\sin\theta_2}{\sin\theta_1} \tag{1.8}$$

1.3.2 Attenuation and penetration depth in the microwave domain

Travelling through a lossy dielectric medium, even if it is low-loss dielectric, electromagnetic waves loose energy. This is called attenuation. The decay of the incident intensity I_0 is exponential for the distance d:

$$I(d) = I_0 \exp(-\alpha d) \tag{1.9}$$

The attenuation coefficient α for a specific frequency f is defined as

$$\alpha = \sqrt{\frac{\mu_0}{\varepsilon'\varepsilon_0}}\,\varepsilon''\varepsilon_0 2\pi f \tag{1.10}$$

Thereafter, attenuation is related to the complex permittivity where the imaginary part describes the energy losses and also is related to the penetration depth of the electromagnetic waves within a medium. The penetration depth δ_p is the inverse of the attenuation

$$\delta_p = \frac{1}{\alpha} = \frac{\sqrt{\frac{\varepsilon'\varepsilon_0}{\mu_0}}}{\varepsilon''\varepsilon_0 2\pi f} \tag{1.11}$$

and is defined as the distance at which the power of the incident electromagnetic wave is reduced by the factor e.

The microwave domain encompasses the frequency range from 0.3 to 300 GHz in the electromagnetic spectrum. This refers to wavelengths of 1 m to 1 mm [*Ulaby et al.*, 2014]. The microwave frequencies are classified in several bands, whereof the L-band is defined by IEEE to be situated at 1 to 2 GHz. This corresponds to wavelengths from 30 to 15 cm. L-band has the advantage that it is almost weather-independent [*Hofmann-Wellenhof et al.*, 2008] and undergoes, compared to the shorter wavelengths of the Ku-, X- and C-bands, a higher penetration depth into the Earth's surface. As this is multiple as long as the size of snow grains, the waves can easily penetrate into the snow cover or soil. For dry snow the penetration depth can be hundreds of meters, whereas for wet snow it is reduced to the (sub-)meter level, depending on the LWC [*Mätzler*, 2002]. For extremely dry soils the penetration depth may reach several meters [*Woodhouse*, 2005], however, if the soil is moist the penetration depth is reduced to a few centimetres [*Ulaby et al.*, 2014].

In this study, the GPS L1-band at 1.57542 GHz referring to a wavelength of $\lambda \cong 19$ cm is used. In the *Sections 2.4*, *3.2*, *4.2* and *5.3*, the propagation of L-band microwaves and the interrelation of the reflection, refraction and attenuation processes due to dielectric behaviour are described more in detail for the investigated snow cover properties and soil moisture measurements.

1.3.3 Microwave dielectric properties of snow and soil

In the microwave range the interactions between the electromagnetic waves and a certain material are expressed as dipolar processes describing the rotation and vibration of polar molecules. The response of a dielectric material to an applied electromagnetic field is not instantaneous and might lead to a phase difference and amplitude decline which is expressed in the real and imaginary part of the complex permittivity of a certain medium. Already on the way through the Earth's ionosphere and atmosphere, several effects on microwaves like reflection and refraction as well as energy loss due to attenuation may occur [*Hofmann-Wellenhof et al.*, 2008; *Woodhouse*, 2005]. However, these effects are negligible compared to the interaction with the Earth's surface

materials like snow or soil which are investigated in this study. Snow and soil are a mixture of different materials where each of them has characteristic dielectric properties depending on frequency and temperature.

Dry snow is a two-phase mixture of air and ice. The real part of the complex permittivity of air ε_a' is 1 and the imaginary part ε_a'' is 0. This means that for dry snow, only the dielectric properties of ice in combination with the density of the snowpack are significant. The real part of the dielectric constant of ice is $\varepsilon_i' = 3.18$ [*Bradford et al.*, 2009] and the imaginary part is negligible at 0°C in the lower GHz range [*Artemov and Volkov*, 2014; *Sihvola and Tiuri*, 1986]. In case the snow becomes wet, water is added as a third phase. Water, however, has very prominent dielectric properties and depending on its volumetric content in the snowpack, it highly influences its dielectric behaviour [*Mätzler*, 1987; *Stiles and Ulaby*, 1982].

Free liquid water follows the dielectric response of polar molecules where the movements occur at GHz frequencies. The complex permittivity of water ε_w can be described by the Debye model [*Hasted*, 1972]

$$\varepsilon_w = \varepsilon_{w\infty} + \frac{\varepsilon_{w0} - \varepsilon_{w\infty}}{1 + i(2\pi f \tau_w)} \tag{1.12}$$

where $\varepsilon_{w\infty}$ is the dielectric constant at high frequencies, ε_{w0} the static dielectric constant of water and τ_w the relaxation time constant. These constants are temperature dependent and the complex permittivity of water changes with temperature [*Chaplin*, 2016]. Figure 1.1 illustrates the temperature and frequency dependence of the complex permittivity of water for the entire microwave range. For the GPS L1-band frequency at 1.57542 GHz the real part of the complex permittivity of water at 0°C is around 88 and the imaginary part slightly above 10. For higher temperatures, both, the real and imaginary part increases.

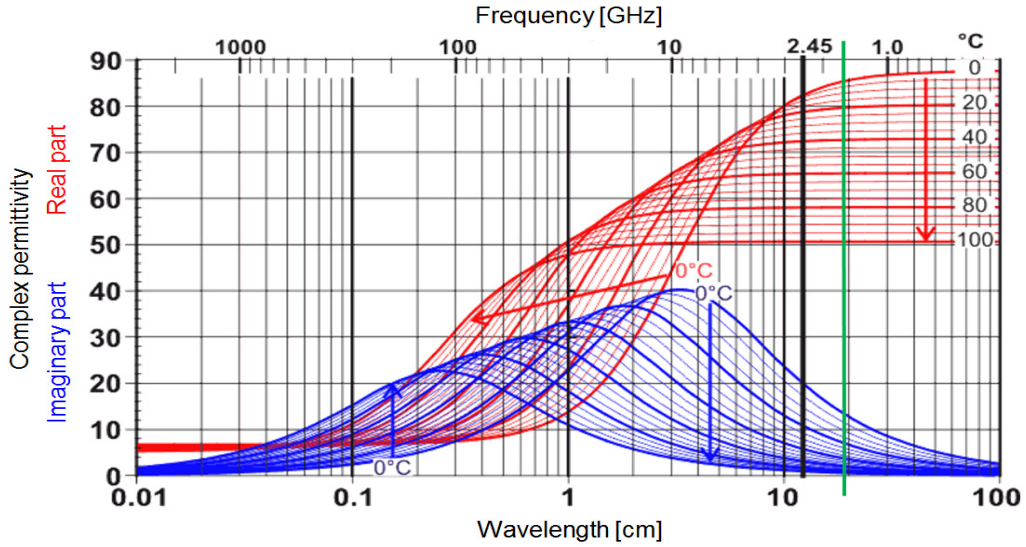

Figure 1.1: Behavior of the real and imaginary part of the complex permittivity of water in the entire microwave range for temperatures of 0 to 100°C. The red and blue arrows illustrate the effect of increasing temperature [*Chaplin*, 2016, modified]. The GPS L1-band frequency at 1.57542 GHz is marked as green line.

In literature, the dielectric properties of snow are either estimated empirically [e.g., *Denoth*, 1989; *Sihvola and Tiuri*, 1986; *Tiuri et al.*, 1984]) or by three-phase mixing models [e.g., *Lundberg and Thunehed*, 2000; *Perla*, 1991; *Roth et al.*, 1990]. All approaches show that the proportion of water highly influences the dielectric properties of snow. For LWC values between 0 and 8%, the real part of the complex permittivity ranges between 1.7 and 3.5 to 4 depending on the applied dielectric model. The imaginary values range between 0 and 0.3. For more details on the calculations of the real and imaginary part of the complex permittivity of snow it is referred to *Section 2.5.1*.

Soil, if it is not frozen, is a mixture of air, soil particles, bound water and free water. The dielectric properties of air and free water were described above. Similar as for snow, the water content plays a significant role to define

the dielectric properties of the soil. Molecular movements in bound water are similar to free water, however, they occur in the MHz range and remain constant in the GHz range [*Chaplin*, 2016]. According to *Dobson et al.* [1985], the real part is most likely set to 35 and the imaginary part of the complex permittivity of bound water to 15. The dielectric properties of soil particles are dependent on soil texture classified as sand, silt and clay, and their mineral composition, e.g., if they originate from limestone or granite. They mainly lay in the range of 2 to 10 for the real part, whereas the imaginary part is negligible. Completely dry soil lays in the range of 2 to 4 for the real part of the complex permittivity and is dependent on layering and porosity of the soil particles [*Ulaby et al.*, 2014]. The dielectric properties of soils, if dry or wet have been described widely in literature with several empirical or semi-empirical model [e.g., *Hallikainen et al.*, 1985; *Roth et al.*, 1990; *Topp et al.*, 1980; *Wang and Schmugge*, 1980] and the physically based four-component model [*Dobson et al.*, 1985]. The latter is described in detail in *Section 5.3.3*.

1.4 Overview on GNSS and their applications on environmental properties

In this section, the Global Satellite System (GPS) as part of the Global Navigation Satellite System (GNSS) and possible environmental measurement techniques using GNSS are introduced.

1.4.1 GNSS and GPS

The U.S. NAVigational Satellite Timing And Ranging Global Positioning System (NAVSTAR GPS) is a weather independent and space-based navigation system and belongs to the Global Navigation Satellite System. Satellite navigation systems were built up since the 1970s in the United States and Russia for precise positioning for military applications and were fully operational since the mid-1990s. Later plenty of further applications, ranging from geodetic, navigational, mapping and scientific applications, came up, too. Nowadays, GNSS is a system of satellites for navigation applications with global coverage. At present, it encompasses the operational U.S. NAVSTAR GPS and the Russian GLONASS. By 2020, the European Galileo and the Chinese BeiDou/COMPASS system, which will be expanded into the global Compass BeiDou-3 navigation system, are planned to be fully operational and will be added to the GNSS in its entire extend [*Hofmann-Wellenhof et al.*, 2008; *Jin et al.*, 2014].

For this approach, the NAVSTAR GPS system (in the following just named GPS) was used. However, the techniques described in the following would also potentially be applicable with the other GNSS systems. In total, the GPS system encompasses up to 32 GPS satellites, arranged in six orbits with an equatorial inclination of 55° and with an altitude of ~20200 km above the Earth. The ground repeat period is one sidereal day (~ 23 h 56 min). This leads to a global coverage of at least four to ten simultaneously observable satellites above an elevation mask of 10° at any time [*Hofmann-Wellenhof et al.*, 2008].

The GPS signals are broadcast in the L-band microwave range and are right-handed circular polarized. All GPS satellites transmit two signals, the civilian L1-band (1.57542 GHz) and the non-civilian L2-band (1.2276 GHz), which are phase modulated on two different frequencies. Moreover, satellites of the recent generation can also transmit a further civilian signal, the L5-band (1.17645 GHz). The civilian C/A (coarse acquisition) code for a standard positioning service is modulated on the L1-band, whereas the non-civilian P-code is placed on the L1- and L2-band for a highly precise positioning service reaching a millimetre range. The standard observable is the pseudorange which is derived from run-time observations between each GPS satellite and the GPS receiver. In total, at least four satellites with measured pseudoranges are needed to determine position, velocity or attitude, which are applied in the fields of surveying and navigation. The pseudorange can result either from the coded satellite signals as code pseudorange or from measurements of the carrier phase as phase pseudorange. Though the latter leads to a much higher accuracy in positioning, the carrier phase is ambiguous and difficult to process [*Hofmann-Wellenhof et al.*, 2008]. The signal power of the received GPS signals is expressed as the carrier-to-

noise power density ratio (C/N_0), whereof the noise is assumed to be white and Gaussian distributed. C/N_0 is a bandwidth-independent index that relates the carrier power to the noise per 1 Hz bandwidth taking ten times the decadic logarithm and is expressed in dBHz. In general, for the most geodesists the broadcast GNSS signal strength is only a quality flag measure which was not applied for positioning and navigation applications. Normally, the C/N_0 values range between 44 to 50 dBHz; values below 34 dBHz are characterized as weak [*Hofmann-Wellenhof et al.*, 2008]. The received GPS data can either be logged with a receiver dependent raw data format or by the standard NMEA (National Marine Electronics Association) or RINEX (Receiver INdependent EXchange) output format. Raw GPS protocols contain information on carrier phase, carrier frequency, Doppler shift and C/N_0 for each visible satellite with a certain pseudo random noise (PRN) number at a certain elevation and azimuth angle for each time step. Further, some receivers provide positioning and navigation solutions and information on satellite orbit data expressed as almanac data [*Hofmann-Wellenhof et al.*, 2008].

Until now, numerous GPS receiver types exist. The spectrum ranges from highly precise and quite expensive military and geodetic receivers, differential GPS systems and simple low-cost GPS systems, which are for example installed in smartphones or in car navigation systems. Even though the low-cost receivers are only able to record the L1-band and are more imprecise regarding clock errors and phase tracking, it is also possible to reach very high accuracies (~ 1 cm) in static and kinematic positioning applications by applying specifically adapted RTK positioning algorithms [*Borre and Strang*, 2012; *Henkel*, 2015; *Henkel and Iafrancesco*, 2014].

1.4.2 GNSS measurements for environmental monitoring

Besides numerous real-time navigational and surveying applications, environmental monitoring with GNSS is on the advance. Highly precise positioning algorithms allow the monitoring of short- and long-term geodynamical phenomena like movements, e.g., in the fields seismology, geology and glaciology. Thereby, investigations of volcanic eruptions, fault motions or earthquakes may resolve the geodetic signature or even predict hazards in advance [e.g., *Blewitt et al.*, 2009; *Larson*, 2013; *Ohta and Iguchi*, 2015; *Shi et al.*, 2010]. Moreover, GNSS is increasingly used for meteorological observations using tomography techniques [e.g., *Bartelt et al.*, 2012; *Bender et al.*, 2011; *Bosy et al.*, 2010; *Lutz*, 2008].

The explicit derivation of environmental properties, such as snow cover properties or soil moisture, is investigated by the following three techniques using C/N_0 and carrier phase. In the following, these methods are shortly defined:

- GNSS reflectometry: With this approach, reflections of GNSS signals on the Earth surface are analysed [*Jin et al.*, 2014]. Comparing direct and indirect signals, the GNSS receivers act as an interferometer, whereby the observed GPS C/N_0 signal frequency, mainly recorded by L2-band, depends on the height of the antenna above the Earth, the GPS wavelength and the environmental properties.
- GNSS signal attenuation: With this approach the attenuation of GNSS signals through a medium depending on its thickness and permittivity is investigated, whereof especially the moisture content of a media can be derived.
- GNSS signal time delay: Based on a fix baseline between two antennas, the time delay of the GNSS signals through a medium can be resolved by processing carrier phases with a specific RTK positioning approach. With this method, especially the amount of the media which was passed by the GNSS signals can be expressed.

In the following the state of the art of these three methods is presented, whereof the last two techniques were mainly developed in this thesis.

GNSS reflectometry: In the last two decades, GNSS reflectometry (GNSS-R) increased as a new Earth observation remote sensing technology which was first suggested by *Martin-Neira* [1993] in the 1990s. GNSS-R

involves, measurements e.g., on snow, sea ice, ocean surface roughness, soil moisture and vegetation biomass by reflections from the Earth of GNSS signal strength either from a ground-based station or from aircraft or spacecraft platforms [*Jin et al.*, 2014]. Due to the consideration of oblique angles below 30 degrees of satellite elevation, a larger area or so called footprint compared to the direct vicinity of the antenna is investigated. The spatial scale of GNSS-R approaches reaches up to 1.000 m² which is intermediate between point-based in situ measurements and remote sensing satellite data [*Larson*, 2016]. Depending on the snow height, soil moisture content or plant water content, the reflections occur at a shallower or a deeper soil level and leads to different reflection patterns. An overview of numerous GNSS reflectometry approaches is provided by *Botteron et al.* [2013], *Cardellach et al.* [2011] and *Jin et al.* [2014]. Several investigations were undertaken to detect particularly HS based on multipath analysis and by using C/N_0 information [*Gutmann et al.*, 2012; *Jacobson*, 2010; *Larson and Small*, 2016; *Larson et al.*, 2009; *McCreight et al.*, 2014; *Nievinski and Larson*, 2014a; b; *Ozeki and Heki*, 2012; *Rodriguez-Alvarez et al.*, 2012b]. SM for both, bare and vegetated soils, was also investigated by numerous approaches [*Chew et al.*, 2015; *Katzberg et al.*, 2006; *Larson et al.*, 2008; *Privette III et al.*, 2016; *Rodriguez-Alvarez et al.*, 2009; *Rodriguez-Alvarez et al.*, 2011; *Vey et al.*, 2016; *Zavorotny et al.*, 2010]. Besides, few GNSS-R approaches on forests [*Ferrazzoli et al.*, 2011; *Wu and Jin*, 2014] and several approaches on agricultural and vegetation biomass [*Egido et al.*, 2012; *Pierdicca et al.*, 2013; *Small et al.*, 2010] were investigated, too. GNSS-R studies especially for SM and biomass estimation based on aircraft are investigated e.g. by *Egido et al.* [2014], *Motte et al.* [2016] and *Pei et al.* [2014]. Reflected GNSS signals were also recorded with the European GEROS-ISS sensor on-board of the International Space Station for large scales [*Wickert et al.*, 2014]. Moreover, observations of reflected GNSS signals with a specific sensor onboard of the low Earth orbiting TechDemoSat-1 have been used recently for global soil moisture maps [*Chew et al.*, 2016]. For the future, the new NASA CYGNSS mission (launch, November 2016, as of November 2016) of 8 GPS bi-static radar receivers to be deployed on separate micro-satellites have a high potential for further global GNSS-R observations for large scale land applications [*Rose et al.*, 2014].

GNSS signal attenuation: Until now, GNSS approaches, investigating changes in signal strength are very rare in literature, and were not used for quantitative studies. Regarding snow studies, *Schleppe and Lachapelle* [2008] analysed a significant GPS signal attenuation and a decrease in position accuracy and precision due to pseudorange quality deterioration within avalanche deposited snow, but they could not qualitatively measure snow properties. Regarding other fields, the existence of ice loadings on GPS antennas [*O Keefe et al.*, 2000] and the effect of vegetation water content [*Rodriguez-Alvarez et al.*, 2012a] were observed by signal attenuation approaches. As a clear advancement and as a highly innovative approach, successful analysis on LWC and SM had recently been developed by *Koch et al.* [2014] and *Schmid et al.* [2015]. This is presented for the snow cover properties in the *Chapters 2* and *3* and by *Koch et al.* [2016] for soil moisture, presented in *Chapter 5*. With these studies, it was possible for the first time, to continuously, non-destructively and quantitatively derive environmental properties with low-cost GNSS sensors. The objectives of these studies are introduced in *Section 1.6*, for detailed information it is referred to the relevant chapters.

GNSS signal time delay: Further, another highly innovative GNSS approach was recently developed which uses signal time delay to retrieve SWE within a snowpack. Two static GPS receivers were used to determine the carrier phases differentially, indicating time delay in snow, whereby changes in carrier phases are related to changes in SWE. This method is also presented in this thesis and is submitted to a peer-reviewed journal; its current status is presented in *Chapter 4*. With this novel method it is possible to successfully derive SWE for dry-snow conditions by solely using GPS carrier phase measurements. However, further research is needed on the carrier phase processing during wet-snow conditions. As a vision for wet-snow conditions, the combination of time delay of GPS signals through a snowpack with the above mentioned signal strength attenuation approach would lead to the derivation of HS, SWE and LWC by solely using GPS signals. This is shortly presented as an outlook in *Section 6.2*

1.5 GPS sensors, raw data and test sites

In this section the used GPS sensors and further components and the applied raw data are described. Besides, the test sites Weissfluhjoch (WFJ) for the snow measurements and Munich (MUC) for the soil measurements are presented.

1.5.1 GPS sensors and raw data

For the development of a first experimental prototype GPS sensor, highly suitable components were chosen. Important points were their robustness, low-power consumption, and suitability for extreme meteorological conditions. On the one hand, suitable low-cost GPS antennas, receivers and fanless PCs, weather-proofed boxes, and cables were acquired. On the other hand, several components were self-constructed, including an antenna radome, GPS reset boxes and application boards for the GPS receivers. In Table 1.1, the specific sensor components which were used for the two GPS setups at the test sites WFJ and MUC are listed.

Table 1.1: Overview on GPS sensor components and their amount installed at the test sites WFJ and MUC. In the Appendix related pictures are shown.

Sensor component	WFJ	MUC	Appendix
Fastrax IT430 GPS receiver with application board and SiRF IV chip [*Fastrax*, 2011]; operation temperature range: -40 to 85°C	3	3	A.1
Self-constructed GPS application board with USB-to-serial interface and voltage regulation	3	3	A.1
Large weather-proofed box (~ 100 x 40 x 30 cm³) to store receivers and PC	1	1	A.2, B.1
Small weather-proofed box (~ 20 x 10 x 5 cm³) to store receivers	1	-	A.3
Hirschmann GPS7M magnetic mount antenna [*Hirschmann*, 2014] with a coax cable length of 3 m	3	3	A.3, A.4, B.2, B.3
Tallysman TW2140 magnetic mount antenna [*Tallysman*, 2016] with a coax cable length of 5 m, ground plate (since autumn 2013)	3	-	A.5
Antenna radome to protect the antenna above the snow from snow cover and weather influences	1	-	A.6
Spo-book fanless PC to store data and to connect and control the receivers with the software SiRFLive; ideal for harsh environmental conditions: operation temperature / relative humidity ranges: –40 to 70°C / 0 to 95%	1	1	A.7, A.8
Self-constructed reset box for the GPS receivers	1	1	A.9
70 m of Ethernet and power cables and cables for reset (WFJ) and 25 m power cable (MUC). All cables were protected against animal bites.	1	1	A.10

One GPS system encompasses a fanless PC and three receivers and three antennas. At the SLF test site WFJ one of these GPS sensor systems is running since autumn 2012 and at the DWD test site MUC another one was running from January 2014 until June 2015. At the test site WFJ, a stable internet connection enabled permanent data access and at the test site MUC, it was possible to collect the data each week with an external device. To get a better impression on the sensor components, several pictures are shown in *Appendix A* for the test site WFJ and in *Appendix B* for the test site MUC.

Figure C.1 in *Appendix C* illustrates, exemplarily for the test site WFJ, the installation plan of all GPS sensor components listed above. The receiver for the antenna installed at the pole was placed in the smaller weather-proofed box, whereas the other two receivers connected with the ground antennas and the fan-less PC were stored in the larger box. The reset box, the switch for the internet connection and the power outlet were situated in a sheltered hut nearby this test site. In general, the installation plan for the test site MUC is quite similar.

Differences are that no internet was available at the test site MUC and as the distance between all antennas was less than 3 m, all receivers could be placed in one weather-proofed box.

Since autumn 2015, additionally a second generation prototype GPS sensor was installed at the test site WFJ. This sensor was provided by the company ANavS GmbH within the frame of the ESA-funded Artes-IAP project SnowSense. It encompasses two u-blox LEA-6T GPS receivers and two u-blox ANN-MS GPS patch antennas with a cable length of 5 m [*u-blox*, 2016] and a processing and storage unit. The receivers were connected to a low-power consuming cheap single-board computer, which controlled the receivers and managed the data storage (*Appendix A.11* and *A.12*).

For this thesis, the following raw data messages received by Fastrax IT430 were of interest. They were considered in the receiver specific One Socket Protocol (OSP) and were extracted for every visible satellite at each time step of a 1 Hz measurement [*Hofmann-Wellenhof et al.*, 2008; *House and Park*, 2009]:

- TOW (GPS time of week) and GPS week number: Time and date information.
- PRN (pseudo random noise) number: GPS satellite number.
- Elevation and azimuth: Orbital angle annotation of each GPS satellites in relation to the receiver.
- Carrier-to-noise-power density ratio (C/N_0): Bandwidth-independent index number that relates the power received from the satellites to the receiver's noise per 1 Hz bandwidth. This parameter is used to quantify the signal power of the received signal.

Moreover, from the further developed second generation ANavS GPS sensor, the following information were additionally used [*Hofmann-Wellenhof et al.*, 2008]:

- Code phase (pseudorange) (ρ): Distance information between GPS satellites and GPS receiver with an accuracy in the meter level, which can be potentially improved by specific processing techniques.
- Carrier phase (φ): Has a periodic nature and can be used (in combination with code phase information) to determine the distance between GPS satellites and GPS receiver with an accuracy in the centimetre to millimetre level. However, carrier phase measurements are ambiguous by integer numbers of full waves and are more difficult to process than the code phases.
- Orbit data: Two-hourly updated information on precise ephemerides data of each PRN

The application and processing of the GPS raw data for the derivation of the snow cover properties and the soil moisture are described in detail in the *Sections 2.3, 3.2.3, 4.2-4.3* and *5.3.1*.

1.5.2 Test site Weissfluhjoch

The snow cover property measurements were performed at the high Alpine SLF test site WFJ (46°49'47"N, 9°48'34"E, 2540 m a.s.l.) above Davos, Switzerland in the Plessur Alps. The flat site is situated in the small, south-west facing valley Dorftälli in the Parsenn skiing area, whereof the peak Weissfluh is the highest mountain (2834 m a.s.l.). The extension of the test site is approximately 25 m by 25 m. Figure 1.2 gives an overview of the test site during the snow covered period. *Appendix A.13* to *A.18* show further pictures of the site during summer and winter.

The high-alpine climate is characterized by a mean annual temperature of -2.5°C and a mean annual precipitation sum of about 1200 mm. The dominating wind direction is north-west and 75% of precipitation is accumulated as snow. On average, the first permanent snow cover date is 18 October (range from 6 September to 25 November) and the mean melt out date is 9 July (range from 3 June to 15 August) [*Marty and Meister*, 2012; *SLF*, 2015b]. Geologically, the region is situated in the outermost west of the Eastern Alps with Penninic facies and the overthrusted Eastern Alpine facies including dolomitic material (Aroser Dolomite), which is predominant for the peaks [*Hsü and Briegel*, 2013; *Spicher et al.*, 2004]. The test site lays in the alpine grassland zone [*Meurer*, 1984; *Reisigl and Keller*, 1987], however, it is partly covered with gravel.

Figure 1.2: Overview of the SLF test site Weissflhjoch, near Davos, Switzerland in the Parsenn skiing area (photo taken by L. Schmid). The area where the GPS sensors are installed is situated approximately in the middle of the test field.

The test site WFJ has good accessibility, internet connection, and is connected to the public electricity grid. It is fully equipped with numerous sensors recording meteorological and snow cover properties [*Marty and Meister*, 2012; *SLF*, 2015a]. Some recordings started already in 1936 and as a special issue, this site holds globally unrivalled time series measurements. Besides ongoing operational measurements, also several sensor prototypes were tested at this site and important snow science experiments have been carried out [*SLF*, 2015b]. This test site is an ideal location for GPS applications in high alpine areas due to its wide and open terrain. At any time, it has high satellite coverage because of an unobstructed line of sight between the GPS receivers and the GPS satellites. In autumn 2012, three GPS sensors were installed. One antenna (GPS1) was mounted facing-up on a 5 m high pole in the middle of the test site and was always situated above the snow cover. The other two antennas (GPS2 & GPS3) were installed, also facing-up, on the ground level and were buried underneath the snowpack during the entire snow period. *Appendix A.3* and *A.5* give an impression on the setup of GPS2 and GPS3. *Appendix A.4* and *A.6* depicts the GPS1 antenna on the pole. In autumn 2015, the advanced ANavS sensors were installed, whereof one antenna was mounted on the same pole as the first system and the second antenna was brought out next to the others on the ground level. *Appendix A.12* shows an antenna of the advanced prototype GPS senor. For more details on the measurement setups, see *Sections 2.2, 3.2.1* and *4.1*, respectively.

This test site is ideal to validate new prototype sensors as their results can be compared with numerous meteorological and snow measurements of conventional sensors. The snow surface temperature (TSS) and all relevant meteorological parameters were measured continuously in a fine temporal resolution. The measurements of HS were recorded by two ultrasonic and one laser sensor, SWE by a snow scale and a snow pillow (*Appendix A.19* and *A.20*) and the meltwater outflow by a 5-m² snow lysimeter (*Appendix A.21*). The temporal resolution of these snow measurements was 30 minutes. Additionally, HN was measured with a snowboard every day at 8 a.m. At a bi-weekly rhythm, manual measurements in snow pits (*Appendix A.22*) were taken and at a few dates LWC measurements with a Denoth meter and a Snow Fork (*Appendix A.23*). Moreover, measurements of a L-band upward-looking ground-penetrating radar (*Appendix A.24*), operating at 1.6 GHz, were used to compare and combine the GPS measurements. Figure D.1 in *Appendix D* gives an overview of the location of all sensors applied in this study, either for reference measurements or for combination with the GPS measurements. Additionally, Table D.1 in *Appendix D* lists of the measurements and sensors and their (aggregated) temporal resolution used in this study.

1.5.3 Test site Munich

The soil moisture measurements were performed at the inner-city meteorological observation site of the German Weather Service (DWD) in Munich (48°16'43" N, 11°32'37" E, 518 m a.s.l.) in Southern Germany. This site is easy to access and is located close to the university, which made frequent maintenance possible. Munich is characterized by a temperate and humid climate of Central Europe with monthly average temperatures ranging from -2°C in winter to 17°C in summer. The prevailing wind direction is west. The mean annual precipitation in Munich reaches 930 mm with a summer precipitation peak [*Mauser and Prasch*, 2015]. Snow cover typically lasts for several weeks in winter, but with a decreasing trend in coverage duration and amount due to climate change [*Weber et al.*, 2010]. The test site is well equipped with standard DWD meteorological measurement instruments recording e.g. precipitation, wind, temperature and cloud cover.

The GPS measurements were performed at a standard DWD soil measurement field (see Figure 1.3), wherein the soil temperature at several depths is continuously measured by the DWD. This soil measurement field has an extent of approximately 10 m² and is not covered by vegetation. Therefore, it is highly suitable specifically for the SM derivation of bare soil. Within a radius of approximately 20 m, the test site is free from surrounding obstacles like houses or trees and allows relatively undisturbed GPS measurements for a city location. The soil texture of the soil measurement field is sandy loam. As the test site is situated on top of the Munich gravel plain north of the Northern Calcareous Alps, limestone is the dominant rock type leading to chromic luvisols. The groundwater table in this region is lower than 2.5 m below the surface and, due to the small clay content capillary rise plays a negligible role.

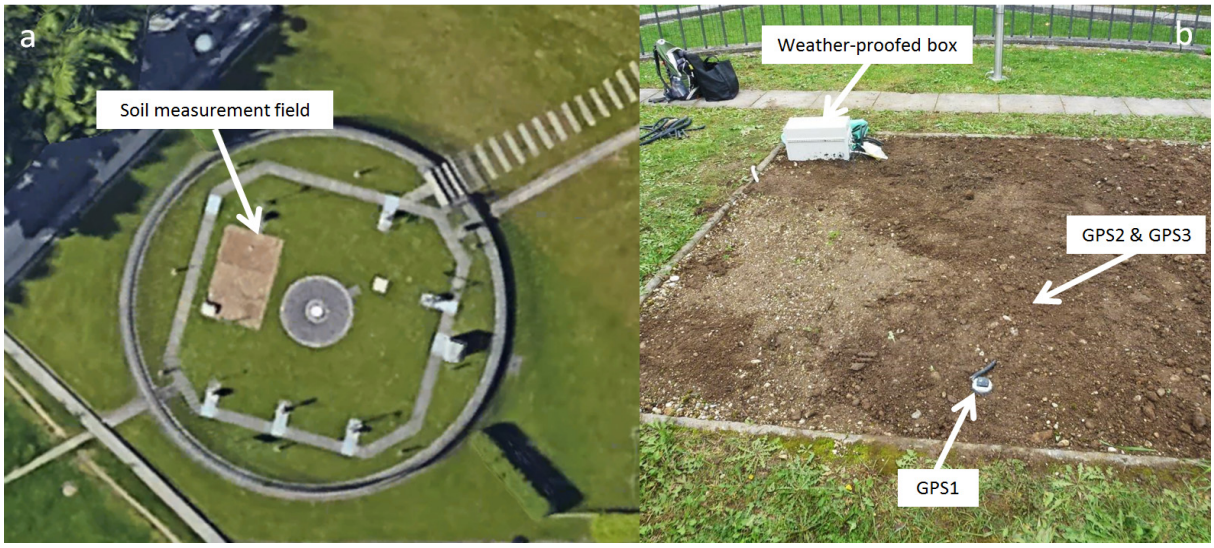

Figure 1.3: (a) Areal overview of the circular DWD test site which is situated in the North-western part of the City of Munich [*Google Earth*, 2016]. The vegetation-free soil measurement field is marked. (b) Part of the soil measurement field which was used for the soil moisture measurements (5 November 2013). The location of the surface antenna GPS1 and the approximate location of the buried antennas GPS2 & GPS3 and the weather-proofed box are marked.

In total, three GPS receivers were installed. One antenna (GPS1) was placed on top of the soil and the other two antennas (GPS2 & GPS3) were placed within the soil column at a soil depth of 10 cm (*Appendix B.2* and *B.3*). Regarding meteorological measurements, precipitation, air temperature and soil temperature at a depth of 5 cm were used. As reference, FD ECH$_2$O probes (Decagon Devices, U.S.; *Appendix B.4* and *B.5*) to continuously measure SM at soil depths at 5 cm and 10 cm were installed. Surface SM was additionally measured by ThetaProbe ML2x FD probes (Delta-T Devices, U.K.; *Appendix B.6*) and standard manual gravimetric probes in a weekly to bi-weekly rhythm. Additionally, the SM for a layer depth of 10 cm and all relevant hydrological parameters percolation were modelled by the physically based, hydrologic land-surface PROcesses of Mass and Energy Transfer (PROMET) model [*Mauser and Schädlich*, 1998; *Mauser and Bach*, 2009].

1.6 Thesis outline

The following describes the research objectives and gives rise to the structure of this thesis, it's chapters and scientific publications.

1.6.1 Research objectives

It is a highly demanding task to provide continuous environmental data with a sensor system which is potentially applicable at almost any place on Earth. The main goal of this thesis is to develop a new continuous, non-destructive and globally applicable low-cost measurement system based on GPS L1-band signals to derive, in a first step the snow cover properties HS, SWE and LWC, and in a second step SM. To answer the three research questions introduced in *Section 1.1*, several strategic development and validation steps have to be passed. Accordingly, this thesis is structured around the following **research objectives** (**OJ**), showing a continuous progress in data analysis, algorithm development, and application:

OJ1. ***Construction and installation of a suitable GPS sensor system***

a) Definition of GPS sensor requirements, with the aim to develop a low-cost GPS sensor system which should be able to continuously measure snow cover properties and SM in a non-destructive manner, and in harsh environmental conditions.
b) Construction and installation of a suitable GPS sensor system to measure snow cover properties at the SLF test site WFJ.
c) Installation of a suitable GPS sensor system for SM measurements at the DWD test site MUC.

OJ2. ***LWC of wet snow derived by GPS C/N_0***

a) C/N_0 algorithm development retrieving normalized C/N_0 values based on a snow-free reference.
b) Derivation of the bulk volumetric LWC based on GPS signal strength attenuation, and HS using a conventional sensor.
c) Verification of the temporal LWC evolution and daily melt-freeze cycles detected by GPS in comparison with temperature, HS and snow lysimeter readings and several capacity measurements.
d) Validation of GPS derived data by comparison with upGPR measurements.

OJ3. ***HS, SWE and LWC derived by combining GPS C/N_0 and upGPR TWT***

a) Combination of the GPS C/N_0 algorithm with time information of L-band electromagnetic waves travelling through the snowpack, which were recorded by an upGPR sensor. The latter records the two-way travel time (TWT) of waves, which are reflected at the air-snow boundary.
b) Derivation of the three snow cover properties HS, SWE and LWC from beneath the snowpack.
c) Validation of the data derived by the upGPR-GPS combination with conventionally measured data.

OJ4. ***SWE of dry snow derived by GPS carrier phase***

a) Development of GPS carrier phases algorithm and assuming a reduced signal propagation in snow to extract snow-specific time delay.
b) Derivation of SWE under dry-snow conditions based on changes in the time delay of GPS signals through the snowpack.
c) Validation with conventional SWE measurements.

OJ5. ***Method transfer to other environmental properties: Soil moisture derived by GPS C/N_0***

a) Development of C/N_0 algorithm to derive SM based on GPS signal strength attenuation in the soil.
b) Validation with SM measured gravimetrically and by FD sensors.
c) Validation with the land-surface model PROMET for the same integral surface soil layer.

OJ6. ***HS, SWE and LWC derived solely by combining GPS C/N_0 and GPS carrier phase***

a) Combination of GPS C/N_0 attenuation within snow and time delay of GPS signals through a snowpack to derive the snow cover properties HS, SWE and LWC for dry and wet snow.

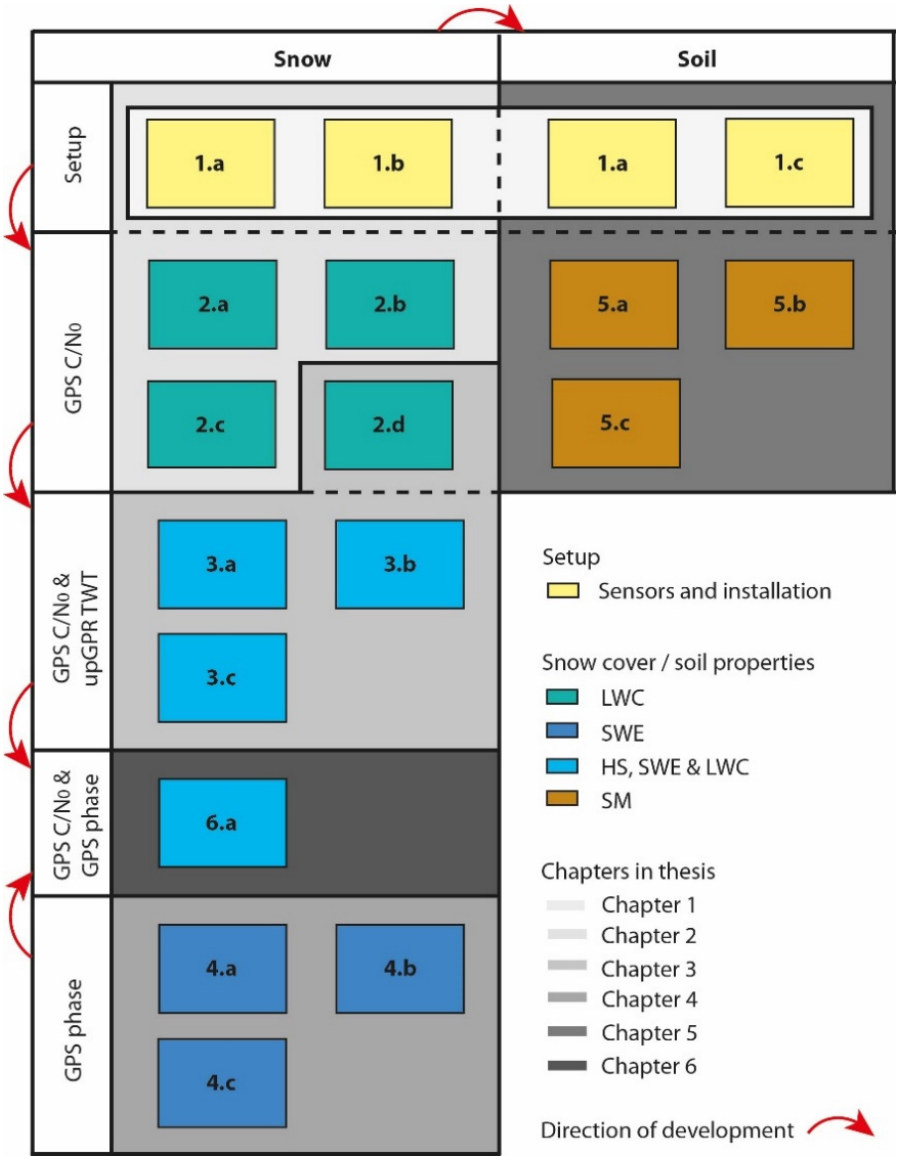

Figure 1.4: Overview of the research objectives OJ1-OJ6 regarding setup, data input and processing. The derivation of the snow and soil properties, are indicated by different colours and are classified also according to the six thesis chapters. The direction of development is indicated.

The overview given in Figure 1.4 summarizes the research objectives in a scheme. The objectives OJ1-OJ6 are classified according to the thesis chapters, the snow properties LWC, SWE and HS and the soil property SM. Moreover, they are classified after the analysis categories setup and the different raw data inputs GPS C/N_0, GPS phase, the combinations GPS C/N_0 and upGPR TWT as well as GPS C/N_0 and GPS carrier phase. The research development direction is indicated step by step with red arrows. On the one hand it shows the development within the snow property derivation applying signal strength and time delay information and on the other hand the transfer to SM as another environmental property.

1.6.2 Chapter outline

Chapter 1 introduces the overall motivation and the research questions of this thesis, different snow and SM measurement methods, the physical fundamentals, and gives an overview on GNSS. This first chapter also contains parts of OJ1 regarding the applied GPS sensors and the test sites which are presented in *Section 1.5*. The further outline of this thesis is as follows (see Figure 1.4): ***Chapter 2*** introduces the new GPS method to continuously and non-destructively derive LWC in snow through GPS signal strength attenuation and externally measured HS. The results are compared with meteorological and snow hydrological data (OJ1 and OJ2). In

Chapter 3, at first, the bulk LWC derived by GPS is compared and validated with LWC measurements by an upGPR (OJ2). Secondly, the GPS signal strength and the time delay information derived by upGPR TWT are combined and lead to the derivation of HS, SWE and LWC (OJ3). ***Chapter 4*** describes the methodology to derive SWE for dry-snow conditions solely by GPS carrier phase. The results were validated with conventional snow pillow and manual snow pit measurements (OJ4). In ***Chapter 5***, the signal strength attenuation approach presented for snow LWC is transferred to the derivation of SM. The GPS SM validation was carried out by several in situ SM measurements and PROMET model results (OJ6). In ***Chapter 6***, the conclusions and an outlook on future work are given, including potential further steps on the combination of C/N_0 and carrier phase to derive HS, SWE and LWC for dry and wet snow solely by GPS signals (OJ5).

Appendix A and ***B*** encompasses several illustrations of the measurement setup at the two test sites WFJ and MUC. The GPS installation plan and an overview of all measurements at the test site WFJ are shown in ***Appendix C*** and ***D***, respectively. ***Appendix E*** presents a conference proceeding on the first results on GPS signal strength reduction caused by melt-freeze cycles in spring.

1.6.3 Scientific publications

In total, this cumulative thesis encompasses four manuscripts, three of them have already been published in peer-reviewed journals and one has recently been submitted to a peer-reviewed journal. Each manuscript is reprinted in one single chapter and contains the chapter specific objectives.

Chapter 2*:** Publication in the journal ***Sensors

Koch, F., Prasch, M., Schmid, L., Schweizer, J. and Mauser W. (2014): Measuring snow liquid water content with low-cost GPS receivers. Sensors, 14(11), 20975-20999.

Chapter 3*:** Publication in the journal ***Geophysical Research Letters. This publication was performed in close collaboration with the WSL Institute for Snow and Avalanche Research SLF.

**** L. Schmid and F. Koch contributed equally to this work.***

Schmid*, L., Koch*, F., Heilig, A., Prasch, M., Eisen, O., Mauser, W. and Schweizer, J. (2015): A novel sensor combination (upGPR-GPS) to continuously and nondestructively derive snow cover properties. Geophysical Research Letters, 42(9), 3397–3405.

Chapter 4*:** Submitted to the journal ***IEEE Transactions on Geoscience and Remote Sensing. This publication was performed in close collaboration with ANavS GmbH and Vista Remote Sensing GmbH.

**** P. Henkel and F. Koch contributed equally to this work.***

Henkel*, P., Koch*, F., Appel, F., Bach, H., Prasch, M., Schmid, L., Schweizer, J. and Mauser, W. (2017): Snow water equivalent of dry snow derived from GNSS carrier phases. IEEE Transactions on Geoscience and Remote Sensing, Volume, Issue, Pages.

Chapter 5*:** Publication in the journal ***Water

Koch, F., Schlenz, F., Prasch, M., Appel, F., Ruf, T. and Mauser W. (2016): Soil moisture retrieval based on GPS signal strength attenuation, Water, 8(7), 276.

The findings of the first two publications were investigated during the project ‘Kontinuierliche Messung der Schneedeckenentwicklung mit GPS-Empfangsgeräten zur Bestimmung des Schneespeichers im Hochgebirge’ (DFG MA 875/12-1; project period: 07/2011 – 0572015) funded by the German Research Foundation. The findings of the third publication were investigated during the ARTES-IAP Demo Project SnowSense (http://artes-apps.esa.int/projects/snowsense-dp) co-funded by the European Space Agency (ESA 4000113149/14/NL/AD; project period: 02/2015 – 02/2018). The findings of the forth publication were investigated during the period of both projects.

The journals' impact factors and rankings are listed in Table 1.2.

Table 1.2: Overview of journals in which the papers of this thesis are published or are submitted to (Journal Citation Report 2015 [*Thomson Reuters*, 2016]).

	Sensors	**Geophysical Research Letters**	**IEEE Transactions on Geo-science and Remote Sensing**	**Water**
Impact Factor	2.245	4.196	3.360	1.428
5-year Impact Factor	2.474	4.406	3.863	1.751
Category	Instruments & Instrumentation	Geosciences, Multidisciplinary	Remote Sensing	Water Resources
Journal ranking (category)	10 / 56	9 / 175	4 / 28	39 / 83
Status	published	published	submitted	published

2. MEASURING SNOW LIQUID WATER CONTENT WITH LOW-COST GPS RECEIVERS

This chapter is published in the journal ***Sensors***:

Koch, F., Prasch, M., Schmid, L., Schweizer, J. and Mauser W. (2014): Measuring snow liquid water content with low-cost GPS receivers. Sensors, 14(11), 20975-20999; doi: 10.3390/s141120975.

Abstract

The amount of liquid water in snow characterizes the wetness of a snowpack. Its temporal evolution plays an important role for wet-snow avalanche prediction, as well as the onset of meltwater release and water availability estimations within a river basin. However, it is still a challenge and a not yet satisfyingly solved issue to measure the liquid water content (LWC) in snow with conventional *in situ* and remote sensing techniques. We propose a new approach based on the attenuation of microwave radiation in the L-band emitted by the satellites of the Global Positioning System (GPS). For this purpose, we performed a continuous low-cost GPS measurement experiment at the Weissfluhjoch test site in Switzerland, during the snow melt period in 2013. As a measure of signal strength, we analyzed the carrier-to-noise power density ratio (C/N_0) and developed a procedure to normalize these data. The bulk volumetric LWC was determined based on assumptions for attenuation, reflection and refraction of radiation in wet snow. The onset of melt, as well as daily melt-freeze cycles were clearly detected. The temporal evolution of the LWC was closely related to the meteorological and snow-hydrological data. Due to its non-destructive setup, its cost-efficiency and global availability, this approach has the potential to be implemented in distributed sensor networks for avalanche prediction or basin-wide melt onset measurements.

2.1 Introduction

Seasonal snow is a very important reservoir component in the hydrological cycle, which releases temporarily delayed fresh water to the forelands. Downstream water suppliers are highly dependent on snow meltwater release from the alpine head-watersheds, which provides drinking and irrigation water, especially when mostly needed during the summer time. The average snow water equivalent (SWE) describes the total amount of snow stored within a certain catchment. However, this measure does not provide information on the state of snow melting. The liquid water content (LWC) θ_w in snow describes the snow wetness of a snowpack. It is an indicator for snow melt and snow stability. A clear increase in liquid water leads to an onset of meltwater runoff within a catchment. This is relevant information, e.g., for flood predictions during intense melting due to intense solar radiation or rain-on-snow events. Temporal and quantitative meltwater delivery predictions are therefore highly demanded by decision makers in the field of water management dealing, e.g., with catchment runoff and flood forecasts [*Prasch et al.*, 2013; *Strasser and Mauser*, 2001; *Weber et al.*, 2010], hydropower generation, as well as reservoir management [*Koch et al.*, 2011a; *Koch et al.*, 2011b] and, thereafter, optimization of

hydropower production. Moreover, information on the LWC of a snowpack is important information for wet-snow avalanche forecasting, since infiltrating water affects the mechanical strength and hence the stability of the snowpack [*Baggi and Schweizer*, 2009; *Kattelmann*, 1987; *Mitterer et al.*, 2011b].

In general, snow wetness is difficult to measure *in situ*, as well as to derive from satellite-based remote sensing measurements. Moreover, to consider the spatiotemporal evolution of meltwater runoff and snow stability, there is a need for continuous, non-destructive monitoring of the LWC in snow. Changes in the LWC can quickly change snowpack properties and meltwater outflow [*Heilig et al.*, 2009; *Mitterer et al.*, 2011b]. They represent non-linear processes, which are difficult to detect or forecast. Manual snow wetness observations in snow pits only provide a rough estimate and are based on a wetness index [*Fierz et al.*, 2009]. An overview of several *in situ* snow wetness measurements is given by *Boyne and Fisk* [1987] and *Techel and Pielmeier* [2011]. Most *in situ* techniques are based on centrifugal, dielectric, dilution and calorimetric measurement methods. Instruments that measure the permittivity of wet snow are, e.g., the Denoth meter [*Denoth*, 1989; *Denoth et al.*, 1984] and the Finnish Snow Fork [*Sihvola and Tiuri*, 1986]. They have in common that they are destructive, time consuming, laborious and can only be applied at accessible locations. Approaches of time-domain reflectometry (TDR) (e.g., [*Schneebeli et al.*, 1998]) were able to monitor the snow wetness continuously and non-invasively; however, this technique is also not applicable, e.g., in avalanche-prone areas. With upward-looking frequency modulated continuous wave (upFMCW) and ground-penetrating radar (upGPR) systems, the bulk volumetric LWC can be derived also at avalanche starting zones [e.g., *Okorn et al.*, 2014; *Schmid et al.*, 2014]. However, upward looking radar systems are limited in application to a single point and are expensive, power intensive and laborious to install.

The radiative properties of a snowpack in the range of L-band microwave radiation are mainly determined by the dielectric constant. Due to the high dielectric constant of water compared to dry snow, wet snow causes characteristic changes in microwave backscattering and penetration depth or emission rate regarding active or passive microwaves, respectively. Several microwave remote sensing approaches and their combinations were investigated for snow wetness detection [e.g., *Appel et al.*, 2005; *Hallikainen*, 1989; *Mätzler et al.*, 1997; *Rott and Davis*, 1993; *J Shi and Dozier*, 1995; *Stiles and Ulaby*, 1980]. However, remote sensing applications are difficult to apply in alpine terrain, due to the low spatial resolution and complex topography (mountain shadowing and foreshortening effects). Because of the satellite's long repetition times, snow wetness parameters can only be detected every few days, depending on the swath width. Consequently, satellite remote sensing can currently not observe daily melt-freeze cycles. Moreover, regarding contemporary passive microwave systems, spatial resolutions up to 25 km² are very coarse and not applicable for mountainous regions. In sum, microwave applications in alpine terrain lack the required temporal resolution to observe the spatiotemporal dynamics of important melt processes. Though various *in situ* measurements at the point scale and remote sensing approaches at a large scale have been investigated, it remains challenging to continuously and non-destructively determine LWC in snow with high spatial resolution.

Due to its global and continuous availability, new remote sensing applications based on the Global Navigation Satellite System (GNSS), such as the American GPS, the Russian GLONASS, the future European Galileo and the Chinese Beidou/COMPASS systems, have become increasingly popular. Several investigations were undertaken to detect snow depth or snow water equivalent based on multipath analysis of the carrier-to-noise power density ratio or carrier phase data [*Gutmann et al.*, 2012; *Jacobson*, 2010; *Larson et al.*, 2009; *Ozeki and Heki*, 2012; *Rodriguez-Alvarez et al.*, 2012b]. An overview is provided by *Botteron et al.* [2013] and *Jin et al.* [2011]. These GNSS reflectometry techniques are mainly based on the analysis of reflections at the Earth surface in comparison to direct signals received at an antenna above the ground. Changes in snow depth [*Jin and Najibi*, 2014; *Larson et al.*, 2009], vegetation [*Wu and Jin*, 2014] or soil moisture [*Zavorotny et al.*, 2010] lead to changes in the reflected signals and signal polarization. Besides observations in the microwave range, surface reflectivity for snow surface monitoring is also applied at other wavelength spectral domains, like the near-

infrared [*Leroux et al.*, 1998; *Salminen et al.*, 2009]. A detailed study on the reflectivity and polarization of GNSS signals was carried out by *Najibi and Jin* [2013]. Besides snow depth estimates, *Jin and Najibi* [2014] found that snow surface temperatures are detectable with dual-frequency GPS signals on behalf of reflected signals from the pseudorange and carrier phase. In general, these methods describe *in situ* measurements on a small scale covering an area of the GPS footprint according to the Fresnel ellipsoids, which depend on the antenna installation height above the reflecting surface and the elevation angle. According to *Larson and Nievinski* [2013], the footprint can be up to hundreds of square meters. *Schleppe and Lachapelle* [2008] showed with low-cost GPS receivers a clear signal attenuation within avalanche deposited snow and a decrease in position accuracy and precision due to pseudorange quality deterioration. Besides, ice loading on GPS antennas [*O Keefe et al.*, 2000] and the effect of vegetation water content [*Rodriguez-Alvarez et al.*, 2012a] were observed by signal attenuation approaches. However, to our knowledge, the existing GNSS snow studies were limited to flat terrain, and no studies regarding the snow wetness (LWC) have been carried out to date.

The aim of this study is to analyze whether the bulk volumetric LWC of an entire snowpack can be derived non-destructively at a high temporal resolution from GPS signal strength losses. We used low-cost GPS receivers and antennas, which are, in principle, globally applicable. The measurement devices are low power consuming; the data analysis is not time consuming and labor-intensive; and the measurements are taken in a continuous mode. After providing an overview of our new experimental low-cost GPS measurement setup at the Weissfluhjoch test site (2540 m a.s.l., Eastern Swiss Alps) (*Section 2.2*), we will describe the GPS data processing in *Section 2.3*. Signal changes due to atmospheric variability, reflection and refraction at the snow-atmosphere interface, as well as attenuation within the snowpack are considered in *Section 2.4*. In *Section 2.5*, the method to calculate the LWC based on signal attenuation is demonstrated and subsequently applied to the melt period in spring, 2013 (*Section 2.6*). The GPS data are shown in comparison with single reference measurements, as well as continuous meteorological and snow-hydrological data. The results are discussed in *Section 2.7*, and finally, *Section 2.8* provides the conclusions and an outlook.

2.2 Measurement setup

The flat test site, Weissfluhjoch (46°49'47" N, 9°48'34" E), is located above Davos (Eastern Swiss Alps) at an elevation of 2540 m a.s.l in a small, south-west facing valley. The site is well-equipped with numerous sensors to continuously record meteorological and snow properties [*Marty and Meister*, 2012]. It is an ideal location for GPS applications in high alpine areas, as it has a high satellite coverage, due to its almost unobstructed line of sight between the GPS receivers and the GPS satellites.

On 26 September 2012, before the first snowfall in autumn occurred, we installed three low-cost Fastrax IT430 GPS receivers with SiRF IV chips [*Fastrax*, 2011], named GPS1, GPS2 and GPS3 (Figure 2.1). Each of the receivers was connected with low-cost Hirschmann GPS7M magnetic mount antennas [*Hirschmann*, 2014]. The cost of each receiver and antenna pair (without data logging, data transmission, power supply, *etc*.) is approximately 150 USD. The antenna of GPS1 was mounted facing-up at a 4-m high pole approximately in the middle of the test site, to always be situated above the snow cover. Due to its small size of 3.9 cm × 3.9 cm and almost permanent wind influence at this exposed point, there was no or only negligible snow deposition on top of this antenna. Because GPS1 stayed snow-free, it delivered information on atmospheric influences on the GPS signals. The antennas GPS2 and GPS3 were installed also facing-up on the ground nearby GPS1. They stayed buried underneath the snowpack during the entire snow-covered period. The horizontal distance between GPS2 and GPS3 was approximately 1 m. The cable length between the receivers and the antennas was 3 m. Figure 2.1 illustrates the location of all three GPS antennas at the test site Weissfluhjoch on a snow-free day. The GPS antennas were connected to the receivers, which were stored in a weather-proof box, via 3-m coax cables. Between the weather-proof box and the data acquisition on a PC in the nearby hut, 70 m of power and data cable

were installed. The GPS receivers recorded the raw data each second, which resulted in a total data volume of approximately 700 MB/day.

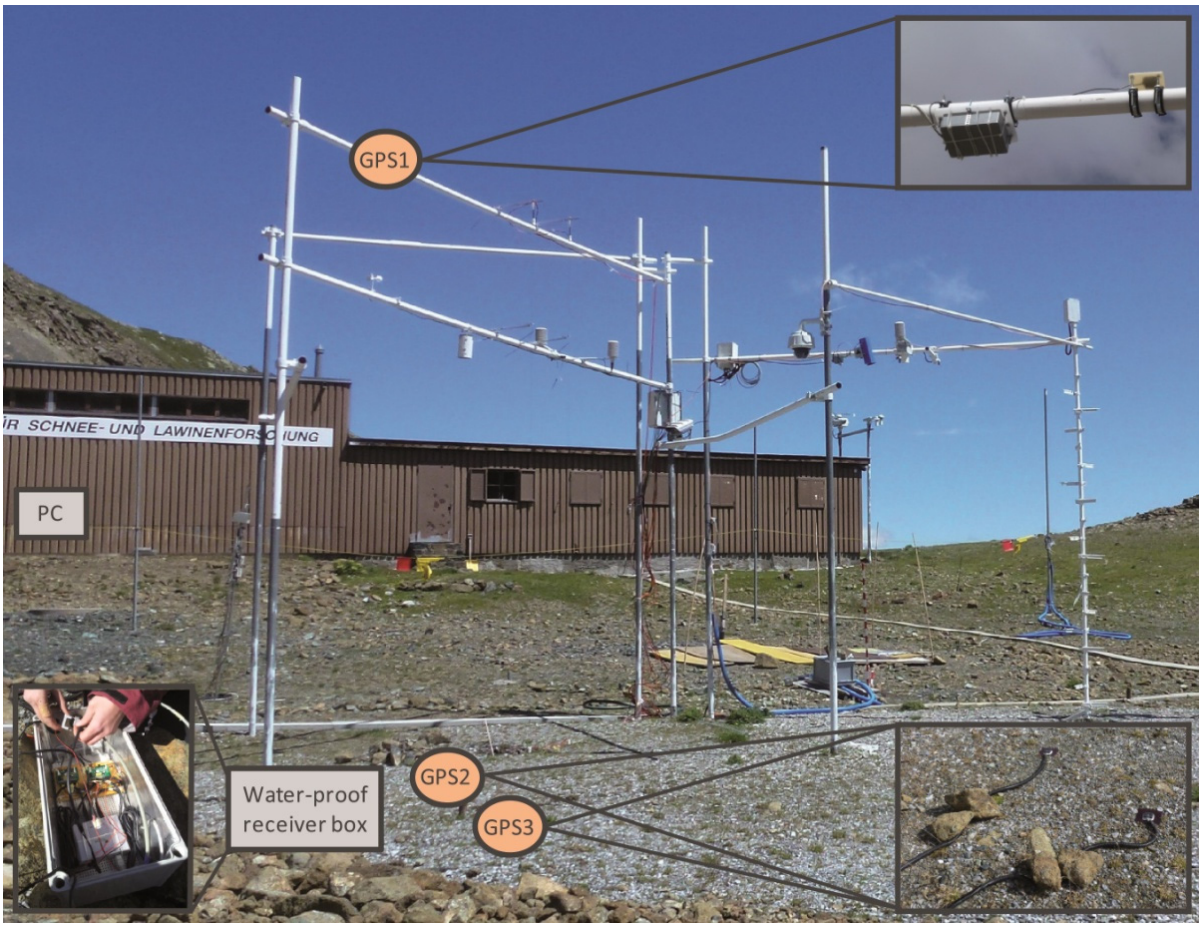

Figure 2.1: Overview of the location of the water-proof box with the Fastrax IT430 receivers, the hut where the PC was located and the Hirschmann GPS7M antennas of GPS1, GPS2 and GPS3 at the Weissfluhjoch test site on a snow-free reference day (26 September 2012).

For validation, continuously measured meteorological and snow-hydrological data were analyzed, including air and snow surface temperature, snow depth measurements from a laser sensor and meltwater outflow at a snow lysimeter. The comprehensive set of meteorological and snow-hydrological measurements was aggregated to a resolution of half an hour. On eleven days, conventional manual snow profiles according to *Fierz et al.* [2009] were recorded near the GPS system setup. In addition, the LWC was measured using the dielectric devices, Denoth meter and Snow Fork. The Denoth meter data were collected on six and the Snow Fork data on four dates during the considered spring period, on some days even at two different times. Both measurements were taken in the snow pit for each layer, and for analysis, the weighted mean for the entire snow depth was calculated. The snow profiles included an estimate of snow wetness for each layer (Wetness Index 1 to 5). To make this information comparable to the bulk volumetric LWC derived from the GPS recordings, we converted the wetness index of each layer to an approximate volumetric LWC (Wetness Index 1 to 5 corresponding to θ_w of 0, 1.5, 5.5, 11.5 and >15%, respectively). The bulk volumetric LWC for the entire snowpack was calculated as the weighted mean of the LWC of each layer. The test site was continuously covered with snow from 27 October 2012, to 11 July 2013; the snow cover remained predominantly dry until mid-April. For the derivation of liquid water in snow, a three-months spring period (7 April–6 July 2013) was chosen as a representative demonstration period. The first week of this period is one week before the snow melt started and represents almost dry conditions, whereas during the rest of this period, the snowpack was mainly moist or wet.

2.3 GPS raw data and processing of normalized C/N_0 values

2.3.1 GPS raw data

The applied low-cost Fastrax IT430 GPS receivers track the L1 C/A code only. The freely available GPS broadcast is transmitted via microwaves at the L1-band at a frequency *f* of 1.57542 GHz [*Hofmann-Wellenhof et al.*, 2008]. The main field of application for low-cost GPS L1-band receivers is navigation, with its focus on positioning data. However, for deriving the LWC in snow, the received signal strength is of interest. As a measure, the signal strength is expressed as the carrier-to-noise power density ratio (C/N_0). C/N_0 is a bandwidth-independent index and is used for assessing signal quality. It quantifies the signal power of the received signal of tracked satellites [*Hofmann-Wellenhof et al.*, 2008].

Daily variations of the receiver noise due to temperature changes at the receiver and the cables were neglected, and the receiver noise was kept constant for the further modeling of the GPS input data. During the measurement period, GPS2 and GPS3 were always underneath the snow cover with a snow temperature at the bottom of the snowpack constantly at about 0 °C. At the upper antenna (GPS1), slight daily variations might occur, which were, however, neglected for the scope of this study. The ratio C/N_0 is determined for each satellite that is in sight of the receiver at a certain time. At the Weissfluhjoch test site eleven GPS satellites can be tracked on average with the applied Fastrax IT430 receivers. In total, the system operates 32 GPS satellites grouped in six orbits with an equatorial inclination of 55 degrees. During a sidereal day (~23 h 56 min), all GPS satellites can be tracked for several hours at the test site, Weissfluhjoch.

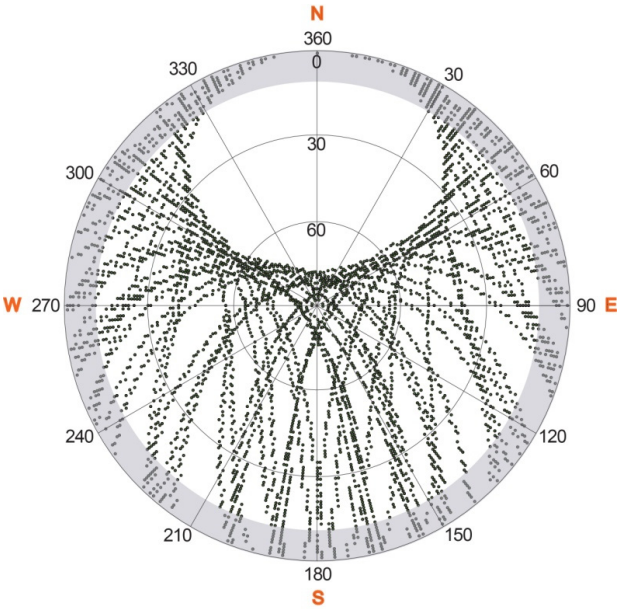

Figure 2.2: Sky plot as a polar plot of all GPS satellites recorded simultaneously by the three GPS receivers at the Weissfluhjoch test site for one sidereal day. The angular coordinates describe the azimuth angle and the polar axis the elevation angle. C/N_0 values below an elevation angle of 10° were masked out for the calculation (these areas are marked grey).

For the study period (7 April–6 July 2013), the C/N_0 data, logged in a receiver-dependent raw data protocol, were extracted for each of the 32 satellites at each time step of one second; in addition, the corresponding satellite number (pseudo random noise, PRN), the time, as well as the satellite elevation and azimuth information were recorded. Due to a failure of GPS satellite PRN 27, there were no data available from this satellite during the observation period. The sky plot in Figure 2.2 displays the trajectory of all GPS satellites on their sky paths and illustrates the hemispherical coverage during one sidereal day at the test site, Weissfluhjoch. This pattern of trajectories is repeated every sidereal day and is identical for GPS1, GPS2 and GPS3. Due to the orbital arrangement of the satellite tracks, the northern azimuth angles have less coverage, because the test site is situated at northern latitudes. For further data processing, C/N_0 values below an elevation angle of 10 degrees

were masked out, because only weak signals were recorded below this elevation angle, or no signals were received, due to a slight hemispherical obstruction of the GPS satellites by surrounding slopes. The location of the flat hut (see Figure 2.1) in the north-eastern sector at an approximate distance of 40 m from the GPS receivers had negligible influence on the line of sight between GPS receivers and GPS satellites. All three receivers maintained lock on all GPS satellites (except PRN 27) every day, even when the maximum snow depth and LWC values were reached.

2.3.2 Normalized C/N_0 values

Besides environmental and atmospheric influences and the characteristics of receiver and antenna, the value of the recorded carrier-to-noise power density ratio (C/N_0) depends on the elevation and azimuth angles of the received signals, as well as on the specific GPS satellite that emitted them. Due to different GPS satellite ages and other satellite characteristics, the peak field strength and, thereafter, also, the magnitude of the received C/N_0 values differ slightly for each GPS satellite. Due to angle-dependent antenna sensitivity patterns, the received signal varies with different azimuth and elevation angles. Furthermore, multipath effects can cause changes in the received signals, especially at near grazing incidence. To account for all of these influences, several azimuth and elevation classes were defined to normalize the C/N_0 values for each time step with respect to elevation- and azimuth-angle and satellite characteristics. In total, 16 elevation angle classes (in steps of five degrees between 10 and 90 degrees) and 16 azimuth angle classes for the entire azimuth range (in steps of 22.5 degrees) for all 32 GPS satellites were assigned, accounting for a total of 8192 classes. However, due to the hemispherical satellite distribution with less satellite tracks in the northern direction (see Figure 2.2), not all classes are covered by C/N_0 values. Figure 2.3 shows exemplarily the C/N_0 class distribution for GPS satellite PRN 1 for one sidereal day. One single class is covered only once by approximately 10 min. The mean class value is represented by the mean of all C/N_0 values recorded during the satellite passage over this class.

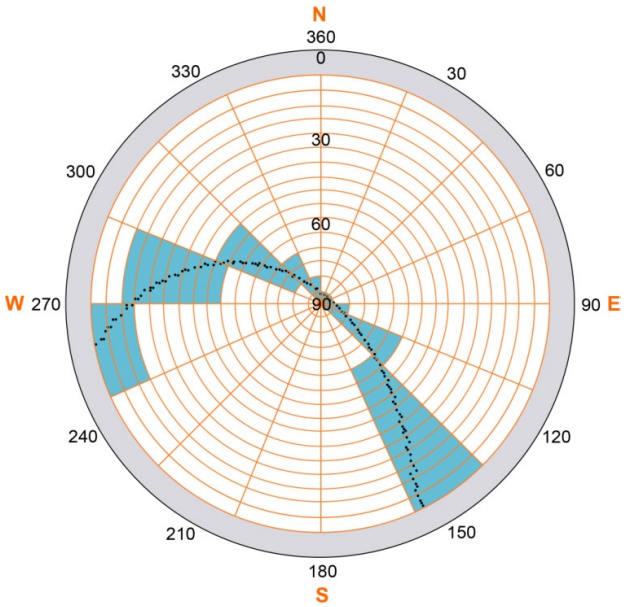

Figure 2.3: Sky plot as a polar plot for the GPS satellite PRN 1 for one sidereal day with the classification of the C/N_0 values with 16 elevation and 16 azimuth classes. The classes assigned with values for PRN 1 are colored blue. C/N_0 values below an elevation angle of 10° were masked out for the calculation (these areas are marked grey).

To make the C/N_0 values comparable individually for each GPS antenna, it was necessary to define a snow-free reference day encompassing the period of a sidereal day. Therefore, a representative sidereal reference day without a snow cover and stable and dry tropospheric conditions was chosen, which is, for this study, the UTC time period 09:00, 21 July 2013–08:56, 22 July 2013. It is assumed that for this time period, all C/N_0 values were influenced by low atmospheric attenuation and ionospheric fluctuations. This means that all recorded C/N_0

values during the entire time period theoretically represent the same signal strength. Thereafter, all values in each of the 8192 classes for this reference day express the normalized GPS C/N_0 value 1.0. Then, all C/N_0 values at each time step of each class were compared to the reference C/N_0 value in the corresponding class. With this approach, also sub-daily variations of the C/N_0 pattern, which are repeated every sidereal day, are considered and normalized. The data of all normalized C/N_0 values calculated for each class with one-second resolution were aggregated to 30 min. Besides the temporal aggregation, the normalized GPS C/N_0 values express also a spatial aggregation of GPS data recorded from different satellites at different elevation and azimuth angles covering different Fresnel zones around the antennas.

GPS1 as a snow-free reference measurement showed slight temporal fluctuations due to different atmospheric conditions for each time step, which impact also GPS2 and GPS3. During the snow-covered period, GPS2 and GPS3 were also influenced by the snow cover. The normalized half-hourly GPS C/N_0 data of GPS1, GPS2 and GPS3 served as input for the further calculation of the LWC. Due to their almost identical location, GPS2 and GPS3 recorded the C/N_0 values in parallel. For the observed three-month spring period, the coefficient of determination (R^2) and the Nash-Sutcliffe efficiency coefficient (NSE) showed a very good agreement, with R^2 = 0.96 and NSE = 1.00. For further data processing, for each time step, the average of the normalized GPS C/N_0 from GPS2 and GPS3 was taken. The normalized C/N_0 of GPS1 is denoted as I_{m1}, and the normalized C/N_0 of the mean of GPS2 and GPS3 is denoted as $I_{m2,3}$.

2.4 Interaction of GPS signals with the snowpack

2.4.1 Overview of processes and influences on GPS signals

Several processes influence the GPS L1-band microwave signals on their way from the GPS satellites to the GPS receivers underneath the snow cover. These include reflection and refraction at the snow-air interface, as well as attenuation within the snowpack, which encompasses absorption and scattering [*Bernier*, 1987; *Woodhouse*, 2005]. These processes are mainly dependent on changes of the complex permittivity of a medium. For this study, ε_s describes the complex relative permittivity of snow, which is given as:

$$\varepsilon_s = \varepsilon_s' + i\,\varepsilon_s'' \tag{2.1}$$

where ε_s' is the real part and ε_s'' the imaginary part of the permittivity. An overview of received intensity and signal strength losses, as well as angle changes due to reflection, refraction and attenuation processes is given in Figure 2.4. The measured intensity $I_{m2,3}$ underneath the snow cover at GPS2 and GPS3 can be described with:

$$I_{m2,3} = I_t - I_a = I_{m1} - I_r - I_a \tag{2.2}$$

where I_{m1} is the received intensity at GPS1 above the snow cover, I_r is the reflected intensity at the snow-air interface, I_t is the transmitted intensity into the snowpack and I_a is the intensity loss due to signal attenuation within the snowpack.

In general, signal losses in the atmosphere are much smaller than signal influences at the snow-atmosphere interface and within the snowpack. Comparing dry and wet snowpack conditions, a dry snowpack has less influence on the signals than wet snow. According to *Mätzler* [2002], the penetration depth, defined as the distance at which the power is reduced to $1/e$ of its original value [*Woodhouse*, 2005], of L-band microwaves in dry snow is up to 400 m, whereas at an LWC of approximately 1%, it decreases to ~2.5 m and at approximately 5% to ~0.5 m. The main reason is signal attenuation within the snowpack due to liquid water [*Stiles and Ulaby*, 1980]. Due to the fact that water has a high complex permittivity compared to air and ice [*Bernier*, 1987; *Sihvola et al.*, 1985], the received signal power is remarkably lower for wet than for dry snow. The degree of refraction and reflection at the snow-atmosphere interface is also influenced by the LWC, but has a lower effect than losses due to attenuation within the snowpack. Due to a longer wavelength of GPS

microwave radiation (L1-band: λ = 19 cm) compared to the approximately 10- to 20-times smaller size of snow grains, the effects of snow microstructure can be neglected in the range of L-band microwaves. In the following, the consideration of signal attenuation (including scattering and absorption), refraction and reflection in the processing chain are shortly described.

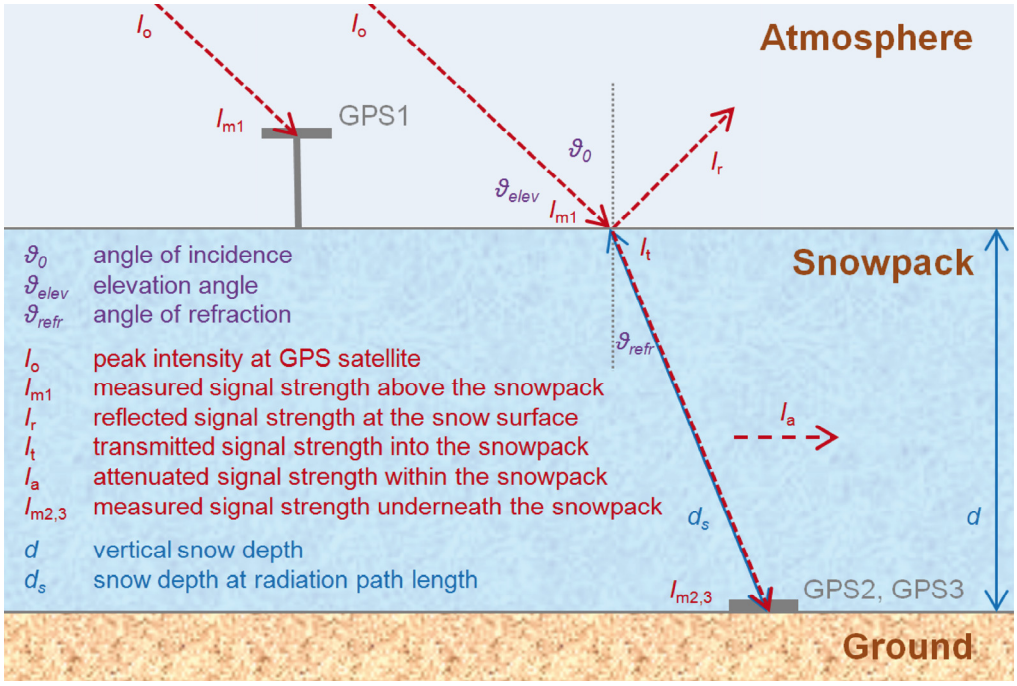

Figure 2.4: Overview of influences on the measured GPS intensity and radiation path length through snow, as well as the angle changes due to the reflection, refraction and attenuation processes. Only the direct signal paths are shown (in red); several multipath effects at and multiple bounces between the air/snow and snow/ground interfaces are neglected.

For the sake of simplicity, we neglected within our low-cost approach several multipath effects with coherent reflections at and bounces between the air/snow and snow/ground interfaces, which have only minor effects on the calculation of the LWC, as the latter is mainly based on the signal attenuation within the snowpack.

2.4.2 Atmospheric influence and variability

The incident radiation, also called peak intensity I_0, which is sent directly from the GPS satellites, first undergoes losses by passing the atmosphere. These losses occur because of signal attenuation, reflection and refraction processes, e.g., at electrons, small particles and water vapor molecules in the ionosphere and troposphere, and can vary from day to day, due to different atmospheric and ionospheric conditions. These processes affect the incoming radiation at all three GPS receivers above and underneath the snow cover in the same way. For each time step, the intensity I_{m1} derived from GPS1 represents theoretically also the intensity that would be measured at GPS2 und GPS3 without the influence of the snowpack.

The normalized GPS C/N_0 values received at GPS1 contain information about these atmospheric signal strength variations for each time step compared to the chosen reference day with good weather and stable ionospheric conditions. For all further calculations, the normalized GPS C/N_0 values derived from GPS1 with its atmospheric variability information were used as input values to calculate the reflection, refraction and attenuation processes within the snowpack and at its surface.

2.4.3 Refraction and snow depth correction

The calculation of the refraction influence on the GPS signals, expressed as the angle of refraction $\vartheta_{\mathrm{refr}}$ and the refraction index n_{s}, depends on the angle of incidence and the snow wetness. The mean angle of incidence at the

GPS antennas at the Weissfluhjoch test site received from all GPS satellites considering all possible elevation angles between 10° and 90° is ϑ_0 = 48° (which corresponds to a GPS elevation angle of $\vartheta_{\mathrm{elev}}$ = 42°). Due to:

$$d_{\mathrm{s}} = \frac{d}{\cos \vartheta_{\mathrm{refr}}} \tag{2.3}$$

this oblique incident radiation travels a longer distance $\mathrm{d_s}$ through the snow than the vertical distance that represents the snow depth d measured with the laser sensor. Refraction due to a change from one to another medium, such as at the snow-atmosphere interface, causes a change of the angle of incidence and, thereafter, also in $\mathrm{d_s}$. The refraction coefficient ns of snow is described with:

$$n_{\mathrm{s}} = \sqrt{\varepsilon'_{\mathrm{s}}} \tag{2.4}$$

Because the refraction coefficient of the atmosphere can be approximated with 1.0, the angle of refraction $\vartheta_{\mathrm{refr}}$ at the snow-atmosphere interface is expressed using Snell's Law as:

$$n \sin \vartheta_{\mathrm{refr}} = \frac{\sin \vartheta_0}{n_{\mathrm{s}}} \tag{2.5}$$

The wetter the snow, the larger the value of $\varepsilon'_{\mathrm{s}}$ and, consequently, the higher the refraction. As a result, this means that d_{s} decreases and gets closer to the measured snow depth d.

2.4.4 Reflection at the snow surface

Due to reflection at the snow-atmosphere interface, less than the entire intensity I_{m1} penetrates into the snowpack. As the incident radiation is circular polarized, the mean reflected intensity I_{r} at one circumference ($\alpha = [0\ 2\pi]$) is given by:

$$I_r = \frac{\int_0^{2\pi} \sqrt{(r_\perp \sqrt{I_{\mathrm{m1}}} \sin \alpha)^2 + (r_\parallel \sqrt{I_{\mathrm{m1}}} \cos \alpha)^2}^2 \, d\alpha}{2\pi} = \frac{r_\perp^2 + r_\parallel^2}{2} I_{\mathrm{m1}} \tag{2.6}$$

with $r_\perp$ and $r_\parallel$ as the perpendicular and parallel reflection coefficients, respectively:

$$r_\perp = \frac{E_\perp^r}{E_\perp^i} = \frac{Z_{\mathrm{s}} \cos \vartheta_0 - Z_{\mathrm{v}} \cos \vartheta_{\mathrm{refr}}}{Z_{\mathrm{s}} \cos \vartheta_0 + Z_{\mathrm{v}} \cos \vartheta_{\mathrm{refr}}} \tag{2.7}$$

$$r_\parallel = \frac{E_\parallel^r}{E_\parallel^i} = \frac{Z_{\mathrm{v}} \cos \vartheta_0 - Z_{\mathrm{s}} \cos \vartheta_{\mathrm{refr}}}{Z_{\mathrm{v}} \cos \vartheta_0 + Z_{\mathrm{s}} \cos \vartheta_{\mathrm{refr}}} \tag{2.8}$$

with:

$$Z_{\mathrm{s}} = \sqrt{\frac{\mu_0}{\varepsilon_0 \, (\varepsilon'_{\mathrm{s}} + i \, \varepsilon''_{\mathrm{s}})}} \tag{2.9}$$

as the wave impedance for snow and:

$$Z_{\mathrm{v}} = \sqrt{\frac{\mu_0}{\varepsilon_0}} \tag{2.10}$$

as the free-space wave impedance (approximately corresponding to the wave impedance of the atmosphere), where μ_0 is the magnetic constant and ε_0 the electric field constant. $E_\perp^i$ and $E_\parallel^i$ are the field components of the incident wave perpendicular and parallel to the plane of incidence, respectively, and $E_\perp^r$ and $E_\parallel^r$ the field components of the reflected wave perpendicular and parallel to the plane of incidence, respectively.

2.4.5 Attenuation within the snowpack

The attenuation coefficient α of a medium like snow is defined as:

$$\alpha = \sqrt{\frac{\mu_0}{\varepsilon'_s \varepsilon_0}}\, \varepsilon''_s \varepsilon_0\, 2\pi f \tag{2.11}$$

and can additionally be described for a homogenous medium, as we assumed it for snow, by applying Beer-Lambert's law [*Otto*, 2011]:

$$\alpha = -\frac{\ln\left(\frac{I_t - I_a}{I_t}\right)}{d_s} = -\frac{\ln\left(\frac{I_{m2,3}}{I_{m1} - I_r}\right)}{d_s} \tag{2.12}$$

with I_{m1} and $I_{m2,3}$ as input data and d_s and I_r calculated with Equations (3) and (6), respectively. The attenuation within the snowpack increases with increasing snow wetness.

2.5 Calculation of liquid water content based on the complex permittivity

2.5.1 Real and imaginary part of the complex permittivity

Considering reflection, refraction and attenuation processes in the atmosphere, at the snow-atmosphere interface and within the snowpack, the bulk volumetric LWC based on the complex permittivity can be calculated by mixing formulas for wet snow. The complex permittivity of wet snow as a three-phase mixture of air, ice and water is dominated by its volumetric LWC. In general, wet snow has a significantly higher complex permittivity than dry snow [*Sihvola et al.*, 1985; *Tiuri et al.*, 1984]. Permittivity can either be estimated with an empirical relation [*Denoth*, 1989; *Tiuri et al.*, 1984] or three-phase mixing models [e.g., *Perla*, 1991; *Roth et al.*, 1990]. Most formulas for wet snow determination are valid within the pendular regime with an LWC below 8% to 10%.

Real part: Three approaches exist to determine the real part of the complex permittivity for wet snow [*Lundberg and Thunehed*, 2000] in the frequency range of the GPS signals: the empirical equations of *Sihvola and Tiuri* [1986] and *Denoth* [1989] and the three-phase mixing formula from *Roth et al.* [1990]. With regard to the latter, *Lundberg and Thunehed* [2000] found an empirical relationship for their measurements and showed similar results in calculating the LWC. The real part depends on both the snow wetness and the dry snow density [*Lundberg and Thunehed*, 2000; *Sihvola and Tiuri*, 1986]. The liquid water content (LWC) θ_w is given as percent per volume.

(1) Empirical formula from *Sihvola and Tiuri* [1986] after *Tiuri et al.* [1984]:

$$\varepsilon'_s = 1 + 1.7 \times 10^{-3}\, \rho_{ds} + 7.0 \times 10^{-7}\, \rho_{ds}^2 + 8.7\, \times 10^{-2} \theta_w + 7.0 \times 10^{-3} \theta_w^2 \tag{2.13}$$

with ρ_{ds} as the dry-snow density in kg/m³.

(2) Empirical formula from *Denoth* [1989]:

$$\varepsilon'_s = 1 + 1.92 \times 10^{-3} \rho_{ws} + 4.4 \times 10^{-7} \rho_{ws}^2 + 1.87 \times 10^{-1} \theta_w + 4.5\, \times 10^{-3} \theta_w^2 \tag{2.14}$$

with ρ_{ws} as the wet-snow density defined as:

$$\rho_{ws} = \rho_{ds} + 0.01\, \theta_w \rho_w \tag{2.15}$$

with ρ_w = 1000 kg/m³ as the density of water.

(3) Three-phase mixing formula from *Roth et al.* [1990]:

$$\varepsilon'_s = \left(0.01\, \theta_w \varepsilon'^{\,0.5}_w + \frac{\rho_{ds}}{\rho_i}\, \varepsilon'^{0.5}_i + \left(1 - \frac{\rho_{ds}}{\rho_i} - 0.01\, \theta_w\right) \varepsilon'^{\,0.5}_a\right)^2 \tag{2.16}$$

with the permittivity of air $\varepsilon'_a = 1.0$, of ice $\varepsilon'_i = 3.18$ and of water $\varepsilon'_w = 88$ at 0°C and a frequency of 1 GHz [*Bradford et al.*, 2009; *Mitterer et al.*, 2011b]. For this study, the dry-snow density was assumed with $\rho_{ds} = 370$ kg/m³, which was the bulk dry-snow density just before the first melting in the measurement period in spring, 2013, at the test site, Weissfluhjoch; the density of ice is $\rho_i = 917$ kg/m³.

Imaginary part: The imaginary part ε''_s of the complex permittivity for wet snow is directly related to the snow wetness and can be given according to *Sihvola and Tiuri* [1986] after *Tiuri et al.* [1984] and *Bradford et al.* [2009] as:

$$\varepsilon''_s = \frac{f}{10^9 \mathrm{Hz}}(1.0 \times 10^{-3}\theta_w + 8.0 \times 10^{-5}\theta_w^2)\varepsilon''_w \tag{2.17}$$

with $\varepsilon''_w = 9.8$ as the imaginary part of the complex permittivity of water at 0°C and a frequency of 1 GHz [*Sihvola and Tiuri*, 1986].

In the range of microwave radiation from 1 MHz–2 GHz [*Bradford et al.*, 2009], the real part of the complex permittivity of wet snow is frequency independent, so that these equations can be applied without corrections. However, the imaginary part depends on frequency in this microwave range. Figure 2.5 illustrates the dependence of the permittivity on the LWC for the different formulations (Equations (2.13), (2.14), (2.16) and (2.17)). The higher the LWC, the higher is the deviation between the different formulations.

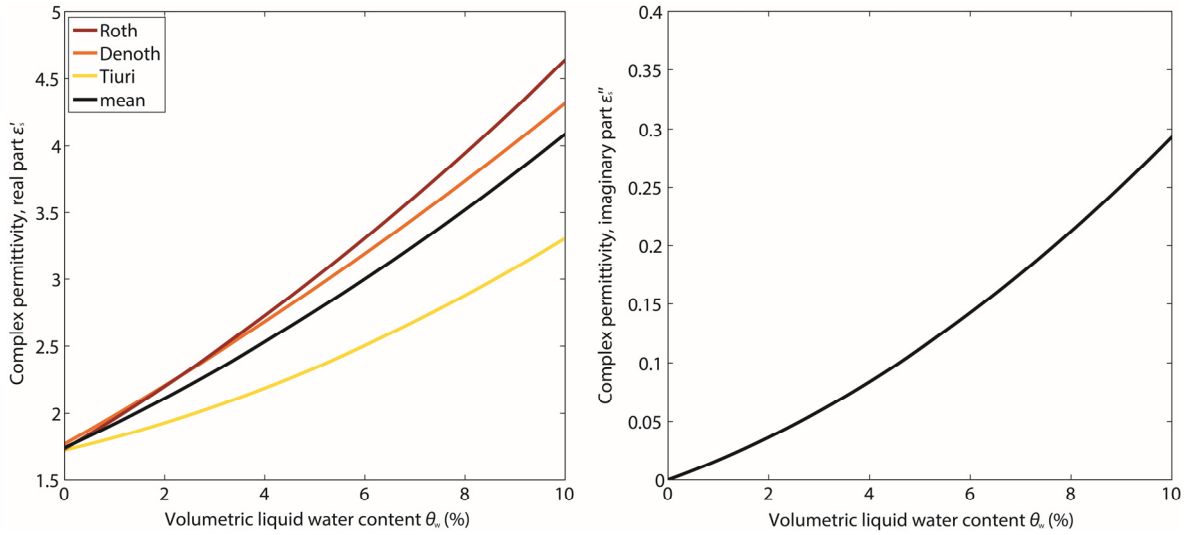

Figure 2.5: Permittivity *vs*. liquid water content (LWC) calculated with the three formulations and their mean for the real part ε'_s and the imaginary part ε''_s. The dry snow density was set to 370 kg/m³.

Table 2.1: Real ε'_s and imaginary part ε''_s of the complex permittivity of snow, corresponding reflectivity r^2 and the attenuation coefficients α for varying values of LWC; LWC is the mean of the three approaches for the real part (Equations (2.13), (2.14) and (2.16)).

Volumetric Liquid Water Content θ_w	Permittivity, Real Part ε_s'	Permittivity, Imaginary Part ε_s''	Reflectivity r^2	Attenuation Coefficient α
0%	1.74	0.00	0.03	0.01
2%	2.10	0.04	0.03	0.83
4%	2.50	0.08	0.05	1.79
6%	2.96	0.14	0.07	2.75
8%	3.46	0.21	0.09	3.79

2.5.2 Retrieval algorithm

The input data for Equations (2.2)–(2.17) are the normalized GPS C/N$_0$ data I_{m1} and $I_{m2,3}$ and the snow depth d measured by a laser sensor nearby the GPS receivers every 30 min. With a root-finding algorithm, the two attenuation Equations (2.11) and (2.12) were set equal under consideration of the three different cases for the

equations for the real part ε_s' of the complex permittivity of snow (Equations (2.13), (2.14) and (2.16)). The imaginary part ε_s'' was calculated after Equation (2.17). The permittivity was assumed to be temperature-independent, so no external temperature measurement was required as input. In summary, the only unknown of this approach is the LWC, which can be calculated as described above by the externally measured snow depth and the recorded GPS data for each time step assuming a constant value of the dry snow density (370 kg/m³), which means that it was held fixed at this nominal value. Table 2.1 illustrates how the reflectivity and the attenuation coefficient increase with increasing LWC; in particular, the attenuation coefficient strongly increases.

2.6 Results

The LWC of the snowpack covering the antennas GPS2 and GPS3 at the Weissfluhjoch test site was calculated for the three-months spring period (7 April–6 July 2013) in half-hourly temporal resolution. The system worked well apart from one break-down of 50 h from 19–21 June due to a power failure at the test site.

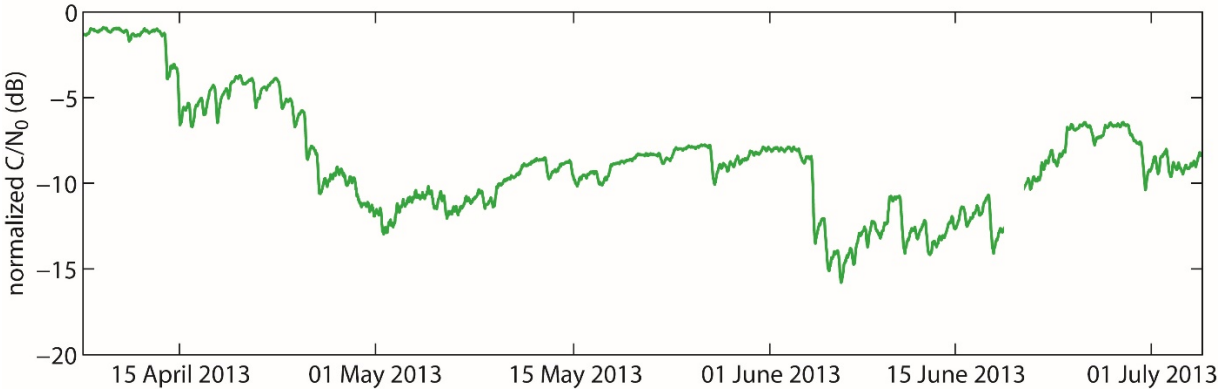

Figure 2.6: Normalized GPS C/N_0 values (dB) taken as the mean of the two GPS receivers under the snow cover (GPS2 and GPS3) at the Weissfluhjoch test site for the period 7 April–6 July 2013.

2.6.1 Bulk volumetric liquid water content derived with the three different formulations

Figure 2.6 shows the evolution of the normalized GPS C/N_0 values in decibels taken as the mean of GPS2 and GPS3, which were buried under the snowpack during the entire spring period. These values serve besides the snow depth as main input data for the calculation of the LWC. Higher normalized GPS C/N_0 (~ −1 dB) values represent dry snow, whereas lower values (< −3 dB) represent moist to wet snow. A value of about 0 dB would represent snow-free conditions. The LWC was calculated as described above with the snow depth and the normalized GPS C/N_0 values as input for each time step of 30 min. For the real part of the complex permittivity, the three approaches, in the following named Tiuri (Equation (2.13)), Denoth (Equation (2.14)) and Roth (Equation (2.16)), as well as their mean value were applied for each time step.

The bulk volumetric LWC calculated as the mean of all three equations for the entire observation period covered a range from 0% to 6.3%. The minimum LWC determined with the three equations was 0%, and the maximum varied between 6% and 6.9%, with the lowest values calculated with Tiuri and the highest with Roth. In general, the differences in LWC between the different approaches increase with increasing LWC. The largest difference between the three mixing formulas was 0.9 percent points (pp). Figure 2.7 illustrates the temporal evolution of the bulk volumetric LWC calculated with the three mixing formulas for wet snow for the real part, as well as their mean value during the study period. In general, the evolution is fairly similar. At the beginning of the period, the snow was almost dry with a bulk volumetric LWC clearly below 0.5%. Around mid-April, the LWC started to increase and reached a first maximum of approximately 4% in the first week of May. Until the beginning of June, the values decreased to approximately 1.7% with a sharp increase in the first week of June up

to a second peak, comparable to the level of the first maximum, *i.e.*, approximately 4%. The further increase until the beginning of July up to the maximum values was interrupted by three smaller minima around 2.5% to 3%. Moreover, all curves show small daily fluctuations of the bulk volumetric LWC indicating daily melt-freeze cycles, which we will focus on in more detail later. The differences due to the different formulations for calculating the LWC were quite small. In the following, to simplify comparisons, we will refer to the mean of the bulk volumetric LWC calculated from the three different formulations.

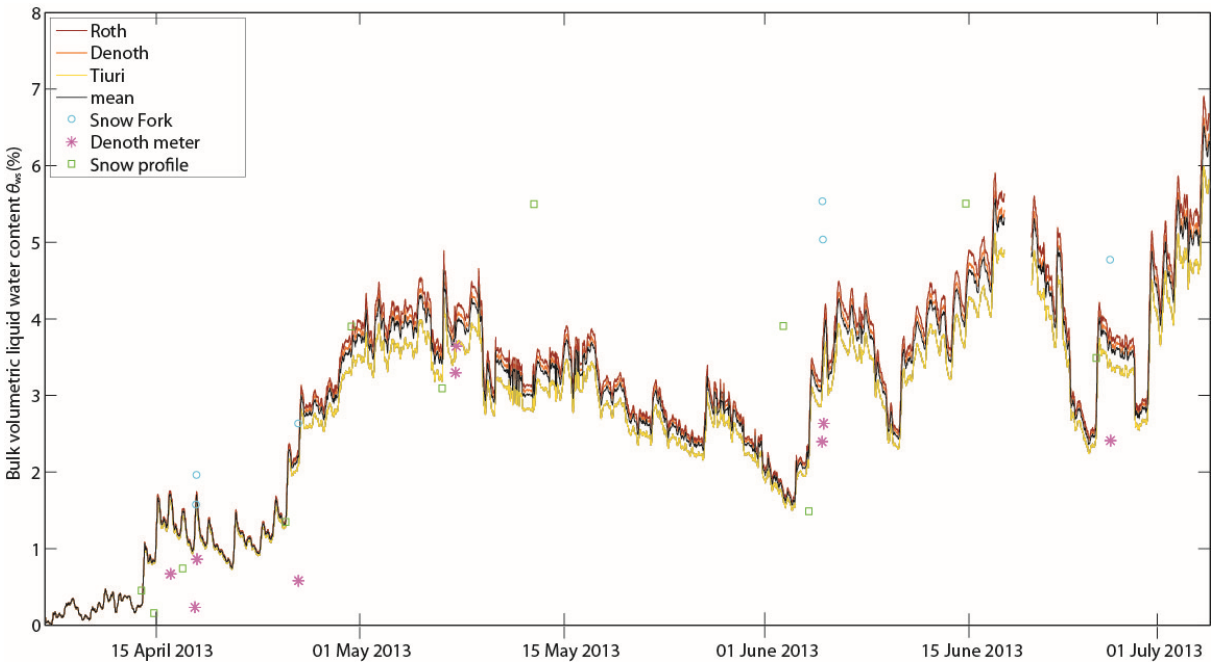

Figure 2.7: Bulk volumetric LWC of the snowpack above the antennas of GPS2 and GPS3 at the Weissfluhjoch test site for the period 7 April–6 July 2013, calculated with the normalized GPS C/N_0 data. The LWC was calculated with three different formulations (Roth, Denoth and Tiuri). Furthermore, the mean of the three curves, as well as reference measurements with the Snow Fork, the Denoth meter and the estimate from manually observed snow profiles are shown.

2.6.2 Comparison with reference measurements in snow pits

In addition to the GPS-derived LWC, Figure 2.7 includes single destructive reference measurements taken in snow pits nearby. These include measurements with a Denoth meter, a Snow Fork and wetness estimates for each stratigraphic layer according to *Fierz et al.* [2009]. The wetness values determined with the Denoth meter and the Snow Fork did not match well with the GPS measurements. The under- and over-estimation compared to GPS-derived values was up to 2 pp. Moreover, values obtained with the Snow Fork were up to 3 pp higher than with the Denoth meter for the same date. However, this discrepancy is in accordance with previous findings by *Techel and Pielmeier* [2011], *Mitterer et al.* [2011b] and *Schmid et al.* [2014]. Overall, Figure 2.7 suggests that the values of the bulk volumetric LWC derived from the normalized GPS C/N_0 data are approximately within the range of the values measured with the Denoth meter and the Snow Fork. During the first four weeks of the study period when the LWC was below 2%, the bulk values derived from the manually observed wetness index were slightly below the normalized GPS C/N_0 curves. They agreed quite well at the end of the study period, but they clearly deviated in mid-May and at the beginning of June, when the LWC was generally high. The root-mean-square deviation (RMSD) between the GPS-derived LWC and the reference measurements was about 1 pp (Table 2.2). The correlation between GPS-derived LWC and reference measurements was lowest for the snow profile estimates (adjusted $R^2 = 0.55$).

Table 2.2: Difference between the GPS-derived LWC and reference measurements (Denoth meter, Snow Fork and snow profile estimates). The absolute mean difference and the adjusted correlation coefficient are given.

	Denoth Meter	Snow Fork	Snow Profile
number of measurements	9	6	11
RMSD (pp)	1.0	1.2	1.2
adjusted R^2	0.90	0.91	0.55

2.6.3 Comparison with meteorological and snow-hydrological data

Figure 2.8 shows the evolution of the measured snow depth, air and snow surface temperatures and the meltwater outflow for a 5 m² lysimeter, as well as the bulk volumetric LWC derived from the normalized GPS C/N_0 measurements (only the mean is shown) at the Weissfluhjoch test site for the entire study period. In the following, the evolution is described by considering six sub-periods with different snow melt conditions.

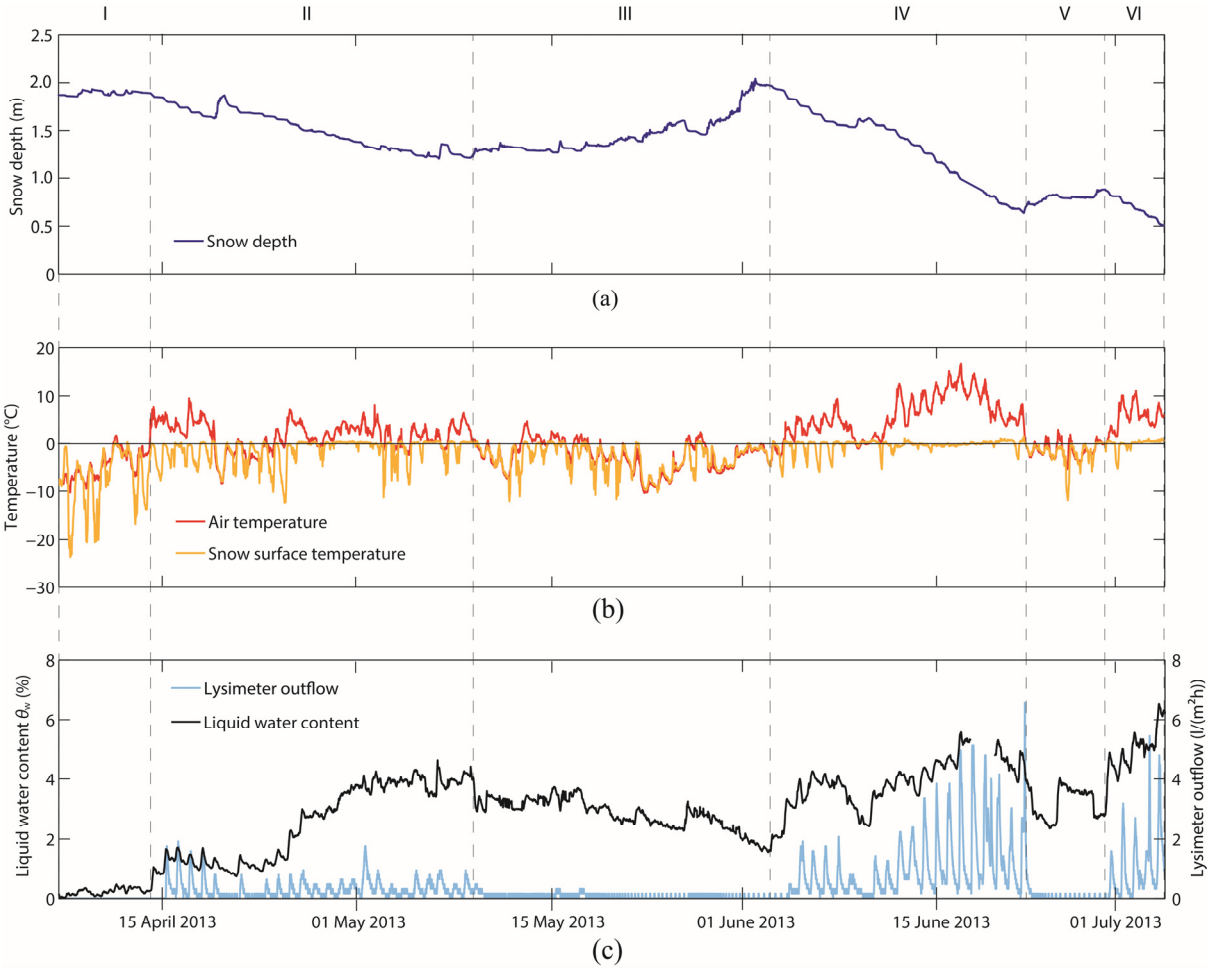

Figure 2.8: (a) Snow depth, (b) air and snow surface temperature and (c) lysimeter meltwater outflow, as well as the bulk volumetric LWC (mean of the three approaches, as in Figure 2.7) derived from normalized GPS C/N_0 measurements at the Weissfluhjoch test site during the time period 7 April–6 July 2013. Vertical dashed lines between six sub-periods (denoted I to VI).

Sub-period I (7–13 April 2013): This sub-period is characterized by almost dry-snow conditions. Due to cold air and snow surface temperatures, no discharge was registered at the lysimeter, and the bulk volumetric LWC was between 0 and 0.5%.

Sub-period II (14 April–8 May 2013): Due to melting, the snow depth decreased from 1.9 to 1.4 m. The air temperature, especially during mid-day, was mostly above 0°C, and the snow surface temperature reached mostly 0°C at its daily maximum, indicating snow melting processes. The LWC started to increase markedly on 14 April, one day before the start of the first lysimeter meltwater outflow, which indicates that the wetting front

arrived at the bottom of the snowpack. The bulk volumetric LWC increased to approximately 4%, and the maximum daily discharge amounted to 1 to 2 l/(m²h).

Sub-period III (9 May–4 June 2013): Temperatures below 0°C and several snowfalls causing the snow depth to increase to almost 2 m again characterized the third sub-period. These conditions resulted in an absence of meltwater outflow and a clear decrease in the bulk volumetric LWC. However, even though meltwater outflow stopped, the GPS-derived measurements suggested that approximately 2% of liquid water was still present in the snowpack at the end of this sub-period.

Sub-period IV (5–22 June 2013): The air temperature was almost always above 0°C, reaching a maximum of up to 15°C. Consequently, the snow surface temperature ranged, especially in the second week, around 0°C. These melting conditions led to a strong decrease in snow depth and to an increase of the LWC of up to 5.5% and a peak discharge of up to 6.5 l/(m²h). The increase in discharge was temporally highly correlated with the increase in air temperature and LWC.

Sub-period V (23–29 June 2013): In contrast to the previous sub-period, temperatures were lower and no meltwater-outflow was registered. This sub-period was characterized by two small snowfalls, which resulted in a significant decrease in the bulk volumetric LWC, in particular during the snowfalls.

Sub-period VI (30 June–6 July 2013): Temperatures rose again, leading to a clear decrease in snow depth and an increase in meltwater outflow. The bulk volumetric LWC increased in parallel. After 6 July, the snow depth was spatially too variable to calculate reliable values of LWC. Furthermore, the snow wetness reached a higher bulk volumetric LWC than expected within the pendular regime, for which the applied mixing formulas are valid. The snow finally disappeared on 11 July, only five days after the end of this sub-period.

From the above descriptions, it becomes clear that the meteorological and snow-hydrological evolution had a great influence on the evolution of both the measured LWC and the lysimeter meltwater outflow; and that, in general, the temporal evolution of GPS-derived LWC agreed well qualitatively with meteorological, as well as the snow-hydrological data.

The daily evolution of GPS-derived LWC clearly showed the daily melt-freeze cycles typically observed during the snowmelt period. Figure 2.9 exemplarily shows the temporal evolution of measured snow depth, air and snow surface temperature and lysimeter meltwater outflow, as well as the LWC derived from the normalized GPS C/N_0 measurements for eight days (14–21 April). During this period, the snow depth decreased in the first six days from 1.89 to 1.65 m. On the seventh day, it increased to 1.85 m during a snowfall and decreased again to 1.68 m on the eighth day. Snow depth decreased especially during mid-day when the snow surface temperature reached 0°C and was stable at nighttime, in accordance with temperatures below 0°C. During the first six days, the air temperature was almost always above 0°C, and the snow surface temperature reached 0 °C during the daytime. During these days with melt activity, the bulk volumetric LWC showed a daily course, reaching a maximum in the afternoon. Furthermore, a time-lagged daily discharge maximum was observed. While reaching the maximum LWC, also the maximum percolation rate was reached within the snowpack. After the meltwater passed through the entire snowpack, it arrived at the bottom of the snowpack at the lysimeter with a delay of approximately 0.5 to 1.5 h after the daily LWC maximum was reached. During the end of the night and the early morning, the minima were reached due to refreezing processes. On 20 April, a dry snowfall was recorded, and the temperatures dropped to approximately 0°C. Subsequently, no discharge was registered, and the LWC decreased. On the last day, a clear daily melt-freeze cycle can be observed again.

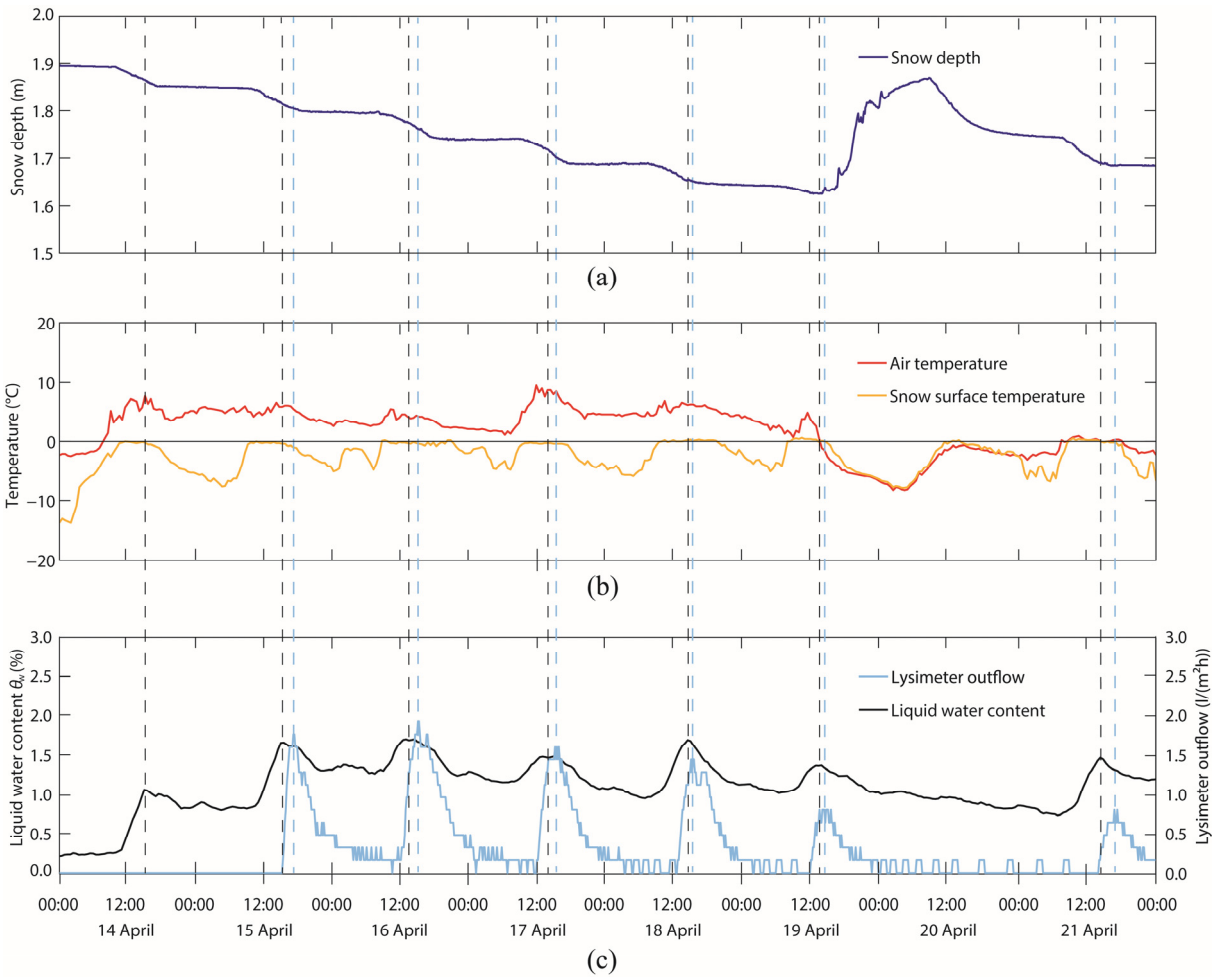

Figure 2.9: (a) Snow depth, (b) air and snow surface temperature and (c) lysimeter meltwater outflow, as well as the bulk volumetric LWC derived from normalized GPS C/N$_0$ measurements at the Weissfluhjoch test site during the time period 14–21 April 2013. Daily peaks of the lysimeter outflow and the LWC are marked with the dashed lines in corresponding colors.

2.7 Discussion

2.7.1 Advantages and limits

This new experimental low-cost GPS measurement system is capable of detecting bulk volumetric LWC continuously and non-destructively over an entire melting period. This means changes in the LWC, such as daily melt-freeze cycles, can be traced with half-hourly resolution. This highly temporally resolved and non-destructive information on the evolution of the LWC was so far only reached with radar systems [*Okorn et al.*, 2014; *Schmid et al.*, 2014]. Other *in situ* measurements, like dielectric probes or manual measurements, are all labor-intense, time consuming and invasive, which means that snow profiles have to be dug to derive snow pit information. Even though the LWC derived by GPS sensors can only deliver bulk values without information on the snow stratigraphy, the GPS data provide valuable information for hydrological applications, e.g., to detect the melt-onset with high temporal resolution. These GPS measurement systems have the clear advantage that they can be installed at large numbers, due to their cost efficiency, with low-cost devices and freely available GPS raw data. Sensor networks with large numbers of sensor members could be installed, monitoring on a large scale, e.g., melting processes of an entire hydrological catchment, or on a small scale, e.g., an avalanche prone slope, which is heterogeneously covered by snow. Nevertheless, for the LWC calculations, additional snow depth measurements are necessary. This could probably be overcome in the future by determining the snow

depth by applying additional GPS measurements and algorithms [e.g., *Gutmann et al.*, 2012; *Larson et al.*, 2009].

2.7.2 Uncertainty estimates for the calculation of the bulk volumetric liquid water content

For the GPS-derived LWC based on intensity losses, three common approaches exist to determine the real part of the complex permittivity for wet snow in the frequency range of the GPS signals. However, Figure 2.7 does not give an answer to which of the applied equations after *Sihvola and Tiuri* [1986] (Equation (2.13)), *Denoth* [1989] (Equation (2.14)) and *Roth et al.* [1990] (Equation (2.16)) is the most realistic, though this is not subject of this study. Even if the curves of the bulk volumetric LWC lay close together, the choice of the mixing formula for wet snow may carry uncertainties in the derivation, especially if the wetness is high. For comparison with other data, the mean of the three quite common approaches was taken.

Besides differences in the results by applying the different empirical mixing formulas, further uncertainties remain. In addition to the normalized GPS C/N_0 data, snow depth and the dry snow density are input parameters that may also be erroneous, e.g., due to spatial variations in snow depth, which may have implications on different Fresnel zones around the GPS antenna. Though the laser sensor is installed quite close to the GPS measurement setup, snow depth at the location of the GPS receivers can certainly deviate by a few centimeters. An overestimation in snow depth leads to an underestimation of the LWC and *vice versa*; the higher this error is, the lower is the snow depth. If, for example, the LWC is 4%, an overestimation of 10 cm in snow depth leads to θ_w = 3.8% (*i.e.*, an underestimation by 5.6%) at a measured snow depth of 1.54 m at the laser sensor; if the measured snow depth is only 0.64 m, the same error in snow depth results in an underestimation of θ_w by 13%. A possible effect of snow depth variability could, e.g., be reduced if the snow depth sensor would have been directly mounted above the GPS instruments, which was technically not feasible. However, errors in snow depth larger than about ±10 cm are rather unlikely at the test field, as further snow depth sensors and manual measurements showed.

The dry snow density was 370 kg/m³ before the snow became wet and was held constant over the entire melting period, as suggested by *Mitterer et al.* [2011b]. Deviations in dry snow density, for example due to settling during the melting period, have little effect on the calculation of the LWC. For example, for an LWC of 4.0%, a deviation in snow density of ±20% leads to an increase or decrease of the LWC to only 4.1 or 3.9%, respectively. To avoid uncertainties caused by the density assumption, it would only be possible to continuously derive the wet snow density, e.g., using independent measurements, which, however, could cause further measurement uncertainties.

Moreover, additional uncertainties may occur due to multiple reflection paths at and between the air/snow and snow/ground interfaces or at the flat hut or other poles at the test site and, in particular, affect the GPS antenna above the snow cover (GPS1). However, these effects are minor, compared to the considered reflection, refraction and attenuation processes at and within the snowpack, and these are neglected within this simple low-cost approach.

2.7.3 Comparison with other measurements

Few quantitative reference measurements were available. The bulk volumetric LWC derived by the non-destructive normalized GPS C/N_0 measurements could only be compared to the few destructive measurements conducted with either the Denoth meter [*Denoth*, 1989] or the Snow Fork [*Sihvola and Tiuri*, 1986] or to the wetness estimates for each stratigraphic layer according to *Fierz et al.* [2009]. First, the destructive methods cannot be carried out at exactly the same location, including the problem that the snow wetness can spatially be variable. Second, they are all destructive methods, and due to the fact that the snow pit wall is exposed to atmospheric influences, the snow wetness can change rapidly and, hence, influence the measurements. Third, these reference measurements are quite labor-intense and, due to their destructiveness, were only performed on a

few dates, so they are only a snapshot without showing the temporal evolution of the LWC. Forth, the manual measurements and observations within the snow pit are often subjective and can only be interpolated with limited accuracy for the entire snowpack. Fifth, the two dielectric methods show large discrepancies, which was already observed by *Techel and Pielmeier* [2011], *Mitterer et al.* [2011b] and *Schmid et al.* [2014].

Overall, we showed that the bulk volumetric LWC derived from GPS data was highly sensitive to the daily meteorological and snow-hydrological evolution and can plausibly be explained by them. Due to their frequent repetition and sensitivity, the measured C/N_0 values from GPS signals can be used to resolve the evolution of the entire period and daily melt-freeze cycles and their impact on snow LWC. The daily evolution of the LWC derived from the GPS measurements was in good qualitative agreement with the daily evolution of the meteorological and snow-hydrological data, but we were at this point of our research unable to provide a proper quantitative validation, as appropriate *in situ* or remote sensing methods were not readily available.

2.8 Conclusion and outlook

We presented a new approach to continuously determine snow liquid water content (LWC) with simple low-cost GPS receivers based on the attenuation in wet snow of the GPS signal strength broadcasted via L1-band microwaves. With this new experimental measurement approach, it was possible to directly derive from measured normalized GPS C/N_0 data the bulk volumetric LWC of a seasonal snowpack continuously and non-destructively. Intensity losses due to reflection, refraction and attenuation processes within the atmosphere and the snowpack, as well as at the snow-atmosphere interface were considered.

The LWC was calculated with three common and plausible mixing formulas based on the real permittivity of wet snow at the high elevation Weissfluhjoch test site above Davos, Switzerland, over an entire melt period in spring, 2013. The GPS-derived temporal evolution of LWC was compared with single destructive reference measurements and continuous meteorological and snow-hydrological data. The LWC showed qualitatively a high temporal coincidence with the evolution of air and snow surface temperatures, snow depth and meltwater outflow during the entire observation period. Furthermore, the melt onset and daily melt-freeze cycles were clearly detected.

In summary, the comparison of the evolution of the meteorological and snow-hydrological data with the bulk volumetric LWC derived with GPS data showed that a wealth of information on the dynamics of snow LWC is contained in the measurements. The normalized GPS C/N_0 values reacted very sensitively to an increase or decrease of the LWC within the snowpack, e.g., during melting and refreezing conditions, and provide an indication for meltwater outflow. However, it has to be clearly stated that with the available *in situ* reference measurements, it was not possible to quantitatively validate the measured snow LWC. Therefore, in a next step, the bulk volumetric LWC derived by normalized GPS C/N_0 data should be compared with other continuous and non-destructive measurement methods for the same time period. A promising method for this task may be an upward-looking ground-penetrating radar system.

The main advantages of this approach are that the measurement devices are low cost and low power consuming and that data analysis is not time consuming and labor intensive. The GPS signals are freely, globally and continuously available, and through the development of dedicated GPS receivers for smart internet appliances, like smartphones, the market offers a wide range of highly-sensitive, cheap, small, robust and low-power devices. This means that the measurement principle can be applied on a global basis (provided power and telemetry is available) to acquire information on LWC at a high temporal resolution without destroying the snow cover. It is possible to join large numbers of these receivers to sensor networks, which, once installed within a hydrological catchment, could be used, e.g., to deliver data for predicting snow melt and runoff in their spatial distribution and at different elevation levels. This could help to validate and temporally complement remote

sensing applications supporting continuous runoff predictions for flood or hydropower services. Moreover, due to the small size of the instruments and the non-destructive measurement setup, it is possible to install the GPS antennas also in steep slopes. This has the potential to, e.g., support avalanche forecasting through continuous information on snow wetness directly from avalanche-prone slopes, where, to date, this information is hardly available. Analyzing signal strength losses of normalized GPS C/N_0 data caused by wet snow has therefore a high potential for continuously monitoring the LWC, e.g., in basin-wide sensor networks for hydrological applications or for avalanche predictions.

Acknowledgments

F.K. was supported by the German Research Foundation (DFG MA 875/12-1) and L.S. by the Swiss National Science Foundation (SNF 200020_144390). We are grateful for the constructive comments by four anonymous reviewers that greatly helped to improve the manuscript.

3. A NOVEL SENSOR COMBINATION (upGPR–GPS) TO CONTINUOUSLY AND NONDESTRUCTIVELY DERIVE SNOW COVER PROPERTIES

This chapter is published in the journal ***Geophysical Research Letters***:

L. Schmid and F. Koch contributed equally.

Schmid*, L., Koch*, F., Heilig, A., Prasch, M., Eisen, O., Mauser, W. and Schweizer, J. (2015): A novel sensor combination (upGPR-GPS) to continuously and nondestructively derive snow cover properties. Geophysical Research Letters, 42(9), 3397–3405; doi: 10.1002/2015GL063732.

Abstract

Monitoring seasonal snow cover properties is critical for properly managing natural hazards such as snow avalanches or snowmelt floods. However, measurements often cannot be conducted in difficult terrain or lack the high temporal resolution needed to account for rapid changes in the snowpack, e.g., liquid water content (LWC). To monitor essential snowpack properties, we installed an upward looking ground-penetrating radar (upGPR) and a low-cost GPS system below the snow cover and observed in parallel its evolution during two winter seasons. Applying external snow height (HS) information, both systems provided consistent LWC estimates in snow, based on independent approaches, namely measurements of travel time and attenuation of electromagnetic waves. By combining upGPR and GPS, we now obtain a self-contained approach instead of having to rely on external information such as HS. This allows for the first time determining LWC, HS, and snow water equivalent (SWE) nondestructively and continuously potentially also in avalanche-prone slopes.

3.1 Introduction

The snow cover is not only an important component of the climate system [*Vaughan et al*., 2013] and a vital reservoir of freshwater but also can contribute to natural disasters such as floods and snow avalanches. For hazard mitigation, continuous information on snow height (HS), snow water equivalent (SWE), and liquid water content (LWC) of snow are highly demanded. HS and SWE are important parameters describing the total amount of snow. The evolution of LWC, or the wetness of the snowpack, is an indicator for snowmelt and snow stability. Melting at the snow surface affects the albedo that is a very important parameter for modeling the climate system. The temporal evolution of these snow cover properties is essential for, e.g., snow avalanche [*Baggi and Schweizer*, 2009; *Mitterer et al.*, 2011a] or flood forecasts [*Bacchi and Ranzi*, 2003; *Jasper et al.*, 2002]. In situ snowpack and meteorology observations are highly demanded input variables for snowpack modeling [*Bartelt and Lehning*, 2002; *Brun et al.*, 1992; *Brun et al.*, 1989; *Lehning et al.*, 2002a; *Lehning et al.*, 2002b] as well as global climate simulations [*Barnett et al.*, 2005; *Lemke et al.*, 2007; *Loth et al.*, 1993] and

hydrological models and water use applications [*Koch et al.*, 2011b; *Martinec and Rango*, 1986; *Mauser and Bach*, 2009; *Prasch et al.*, 2013; *Strasser and Mauser*, 2001; *Warscher et al.*, 2013].

Several satellite and ground-based measurements exist to monitor snow properties but are often difficult to apply in high mountain regions and particularly when the snow becomes wet. This is especially the case for avalanche-prone slopes, where up to date, it is impossible to continuously and nondestructively measure HS, SWE, and LWC. Current remote sensing techniques apply visible and infrared as well as active and passive microwaves, in particular to monitor changes over large areas in the polar regions (e.g., tundra and sea ice) [e.g., *Bartsch et al.*, 2007; *Dozier and Painter*, 2004; *Frei et al.*, 2012; *Langlois et al.*, 2007; *Pulliainen and Hallikainen*, 2001; *J Shi et al.*, 1994; *Stiles and Ulaby*, 1980; *M Tedesco et al.*, 2013]. However, their applicability is inappropriate for steep slopes in mountainous terrain due to layover and foreshortening effects. Moreover, their temporal or spatial resolution inhibits reliable monitoring of rapid changes in, e.g., LWC in the snow cover. Ground-based measurements are scarce and often not applicable in complex and remote terrain. Though laser or ultrasonic sensors measure HS continuously, they need to be installed on poles which can easily be destroyed in steep slopes due to snow movements or avalanches. Snow pillows or snow scales can provide SWE but are only applicable in level terrain. Furthermore, these measurement systems are susceptible to bridging effects and therefore, erroneous measurements may occur, particularly when the snow changes from dry to wet [*Johnson and Marks*, 2004]. Studies exploiting the Global Navigation Satellite System (GNSS) raw data, such as Global Positioning System (GPS) reflectometry, have demonstrated that HS or SWE can be continuously monitored but are presently also limited to flat terrain and are installed on poles [*Jacobson*, 2010; *Larson et al.*, 2009; *McCreight et al.*, 2014; *Najibi and Jin*, 2013; *Ozeki and Heki*, 2012]. Measurements of LWC with dielectric probes like the Denoth sensor [*Denoth*, 1994] or the Finnish Snow Fork [*Sihvola and Tiuri*, 1986] have in common that they are destructive, labor intense, error prone, and miss the subdaily temporal dynamics of melt and refreeze processes. Moreover, due to safety concerns, they are, as well as other manual observations (e.g., following *Fierz et al.* [2009]), not applicable in avalanche-prone terrain.

Two promising methods for continuously and nondestructively measuring snow properties, which are also potentially applicable in complex terrain, are (1) radar systems like an upward looking ground-penetrating radar (upGPR) [*Heilig et al.*, 2010; *Mitterer et al.*, 2011b; *Schmid et al.*, 2014] or an upward looking frequency modulated continuous-wave radar [*Gubler and Hiller*, 1984; *Okorn et al.*, 2014] and (2) a system of small and easy to apply low-cost GPS receivers [*Koch et al.*, 2014]. For this study, we made use of an upGPR and compared and combined the measurements with a GPS system. Both systems are buried underneath the snowpack, continuously record its properties, and work in a similar frequency range, namely the microwave L band. They rely on independent methods: upGPR on velocity and GPS on signal attenuation of the electromagnetic waves [*Bradford et al.*, 2009]. Combined with external HS information, these two methods are among the first systems that can reliably determine bulk LWC of snow nondestructively [*Koch et al.*, 2014; *Schmid et al.*, 2014].

The aim of this study is to compare the LWC derivations of both systems and to combine the two methods (upGPR and GPS) in order to continuously and nondestructively derive – with this novel sensor combination – the essential snow properties LWC, HS, and SWE, even without additional external information and also during wet snow conditions.

3.2 Methods

3.2.1 Weissfluhjoch study site and accompanying data

The upGPR [*Schmid et al.*, 2014] and GPS [*Koch et al.*, 2014] measurements were performed at the flat study site Weissfluhjoch (Davos, Switzerland) at 2540masl. Meteorological and snow cover properties are recorded

with numerous sensors [*Marty and Meister*, 2012; *Mitterer et al.*, 2011b]. We made use of a laser gauge and two ultrasonic sensors to measure HS and a snow scale and a snow pillow to measure SWE. Manual snow profiles, in accordance to *Fierz et al.* [2009], were performed on a biweekly basis within 2–8 m of the location where the upGPR was buried [*Schmid et al.*, 2014]. In addition to the conventional snow profile, we recorded LWC using a capacity probe [*Denoth*, 1994] and during the winter season 2012–2013, also the Finnish Snow Fork [*Sihvola and Tiuri*, 1986]. SWE was determined by measuring snow density in the pit multiplied by HS. Furthermore, HS was directly measured above the upGPR by using an avalanche probe. The height of new snow (HN) accumulated during a standard observing period of 24 h was measured every morning at approximately 8 A.M. as described in *Fierz et al.* [2009]. The location of the upGPR, the GPS antennas, the profile line, the other measuring devices used in this study as well as the distances between the sensors are shown in Figure 3.1.

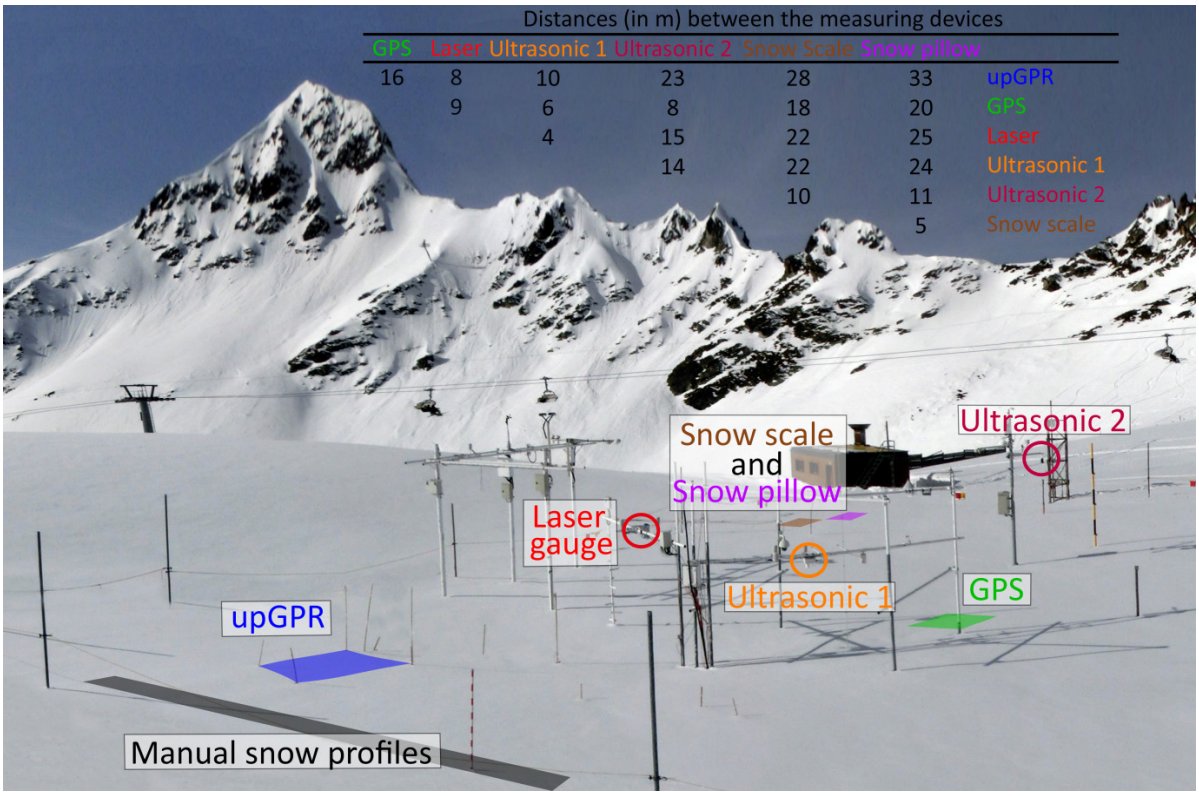

Figure 3.1: Overview of the study site Weissfluhjoch and the location of the measurement instruments and the profile line. The upGPR and the two GPS antennas as well as the snow scale and the snow pillow are buried in the ground below the snow cover. Ultrasonic 1 and 2 and the laser gauge are mounted on poles above the snow cover. The distances between the measuring devices are shown at the top.

3.2.2 upGPR

The radar instrumentation as well as the radar data processing is described in [*Schmid et al.*, 2014]. In this study, we made use of the 1.6 GHz data set. We determined the two-way travel time of the snow surface reflection using the semiautomated picking algorithm [*Schmid et al.*, 2014, p. 512]. HS was calculated according to *Schmid et al.* [2014, Equation (1)] assuming a constant speed of the electromagnetic wave of 0.23 m ns^{-1} as suggested by [*Mitterer et al.*, 2011b], which is the speed in dry snow with a density (ρ_{ds}) of 357 kg m^{-3} [*Schmid et al.*, 2014]. HS can only be determined under dry snow conditions. If an external HS measurement is available, the real part of the bulk relative effective dielectric permittivity [*Schmid et al.*, 2014, Equation (6)] and the LWC can be derived after *Roth et al.* [1990] with the parameters defined in *Schmid et al.* [2014, Equation (5)] assuming a constant value of ρ_{ds} (357 kg m^{-3}).

3.2.3 GPS

The nondestructive low-cost GPS measurement setup and the GPS data processing are described in *Koch et al.* [2014]. For redundancy, two GPS antennas were buried underneath the snowpack. The freely available GPS L1 band information is transmitted at a frequency of 1.57542 GHz. The calculation of LWC is based on GPS signal strength losses in snow. The LWC model described in *Koch et al.* [2014] considers attenuation, reflection, and refraction processes at the snow surface and within the snowpack and requires an external HS measurement as well as the same assumption for dry snow density ($\rho_{\mathrm{ds}} = 357$ kg m^{-3}). Whereas *Koch et al.* [2014] only considered the mean elevation angle, we now calculated the reflection and refraction for each single elevation angle. Furthermore, to be independent of an above-ground installation, we only used GPS receivers beneath the snow cover for this study, as atmospheric influences are negligible for calculating LWC. LWC is per definition zero for dry snow conditions. However, the values derived from the GPS measurements showed a slight offset, possibly due to elusive further losses by multiple reflections. Because we knew from the upGPR measurements the date of the first wetting of the snowpack [*Schmid et al.*, 2014, p. 514] and hence the duration of the dry snow period, we compensated the offset such that the GPS-derived values of LWC were zero on average during dry snow conditions. For the calculation of the attenuation and reflection processes [*Koch et al.*, 2014, Equations (2.6)-(2.12)], we considered the complex permittivity of snow. To be consistent with the radar measurements, the real part was also calculated after *Roth et al.* [1990] and the imaginary part after *Tiuri et al.* [1984] [*Koch et al.*, 2014, Equations (2.16) and (2.17)]. The values of LWC derived separately from the two GPS antennas underneath the snowpack agreed very well as indicated by a root-mean-square deviation (RMSD) of 0.2 percentage points (pp). In the following, the mean of these two recordings will be used.

3.2.4 Combination of both methods

With both systems, operating in the microwave L band, the bulk volumetric LWC can be determined from beneath the snowpack—based on two independent physical approaches applying two-way reflectometry for the upGPR [*Schmid et al.*, 2014] and signal attenuation for the GPS [*Koch et al.*, 2014]. However, both systems required external information on HS and ρ_{ds} to derive LWC. Basically, the following equation with three unknowns had to be solved by both systems:

$$\mathrm{LWC} = f(\mathrm{HS}, \rho_{\mathrm{ds}}) \tag{3.1}$$

As mentioned above, a constant value for ρ_{ds} (= 357 kg m^{-3}) can be assumed. By combining the two methods, upGPR and GPS, we obtained two equations with two unknowns; and thus, the equations can be solved and HS and LWC can be derived. Knowing ρ_{ds}, HS, and LWC, we can also determine SWE:

$$\mathrm{SWE} = (\rho_{\mathrm{ds}} + a\,\mathrm{LWC}\,\rho_{\mathrm{w}})\,\mathrm{HS} \tag{3.2}$$

with ρ_{w} the density of water and $a = 3.08$ as proposed in *Schmid et al.* [2014].

3.3. Results

3.3.1 Comparison of both methods

For the winter seasons 2012–2013 and 2013–2014, the bulk volumetric LWC was derived separately from the upGPR and GPS data relying on additional external HS data of a nearby laser sensor. Figure 3.2a and 3.2b show the temporal evolution of LWC during the two winter seasons covering dry and wet snow conditions. After 14 April 2013 and 1 April 2014, the snow considerably changed from dry to wet. At 17 June 2013, both systems stopped due to a power failure at the study site; after 19 June 2013, only data from the GPS were available. During wet snow conditions and with a snow height of at least 1m, the two values of LWC (and their temporal

evolution) derived separately from upGPR and GPS data agreed very well as indicated by a RMSD of 0.4 to 0.7 pp (Table 3.1). However, at the end of the snow-covered period, as HS decreased below 1 m and became more variable due to fast melting, the curves started to deviate. Comparing the LWC values obtained with the Denoth sensor and the Snow Fork with those from upGPR and GPS, resulted in a RMSD for the Denoth sensor between 0.3 and 0.9 pp and for the Snow Fork between 1.5 and 2.2 pp. The agreement between the two dielectric devices was weak with 2.1 pp.

Diurnal variations of LWC derived separately from upGPR and GPS are shown in Figure 3.3, exemplarily for late spring 2013. During periods of fair weather and hence melting, the daily fluctuations were prominent but did not exceed 2%. When the air temperature was below 0°C or during snowfall (e.g., 29 May to 3 June), the variations were clearly less pronounced. Even though the absolute values of LWC derived from upGPR and GPS differed slightly, the temporal agreement with regard to daily melt and refreeze processes was high.

Figure 3.2: Comparison of snow properties derived from upGPR and GPS with conventional measurements for the time periods 15 February to 12 July 2013 and 10 February to 20 June 2014. The colored backgrounds illustrate in white dry snow and in blue wet snow conditions. Light blue shows when snow height was at least 1m; dark blue when it was below 1m. Red backgrounds indicate when there were no upGPR data in 2013 and when the GPS receivers were no longer covered with snow in 2014. (a, b) Bulk volumetric liquid water content derived separately with upGPR and GPS using externally measured snow height data (laser). The markers show the average liquid water content of the snowpack measured in a snow pit with the Denoth sensor and the Snow Fork. (c, d) Snow height derived with the combination of upGPR and GPS, conventionally measured snow height at three different locations as well as manually measured snow height by probing directly above the upGPR. In addition, the snow height measured with the upGPR as described in *Schmid et al.* [2014] without GPS or external information is shown. (e, f) Snow water equivalent derived with the combination of upGPR and GPS, compared with the snow pillow, the snow scale, and manual measurements in a snow pit.

3.3.2 Combination of both methods

Combining the upGPR and GPS data, HS was derived for the two winter seasons and compared to three conventional and continuous HS measurements (a laser gauge and two ultrasonic sensors) as well as several manual measurements (probing above the upGPR) (Figure 3.2c and 3.2d). In addition, HS derived with upGPR as described in *Schmid et al.* [2014] without GPS or external information is shown. In Table 3.1, the RMSD between all methods is listed for wet snow conditions when HS was at least 1m. Overall, the correlation between the devices was better in spring 2014 (mean RMSD = 7.9 cm) than in 2013 (mean RMSD = 10 cm). The mean RMSD between the upGPR-GPS combination and the conventional methods was 9.8 cm in spring 2013 (6.5% of the mean HS ($\overline{HS}$) of 150 cm) and 6.3 cm in spring 2014 (4.3% of $\overline{HS}$ of 146 cm). For comparison, the mean RMSD between the conventional methods was 10.2 cm in spring 2013 and 8.9 cm in spring 2014. The RMSD between the upGPR-GPS combination and the laser sensor (which is the nearest sensor to the upGPR and the GPS) was 6.6 cm in 2013 (4.4% of $\overline{HS}$) and 3.3 cm in 2014 (2.3% of $\overline{HS}$). The RMSD between laser and ultrasonic 1 was in a similar range (3.3 cm in 2013 and 5.2 cm in 2014), although they were closer together. Deriving HS from upGPR data only leads to a distinct overestimation during wet snow conditions of on average 27 cm in 2013 and 16 cm in 2014.

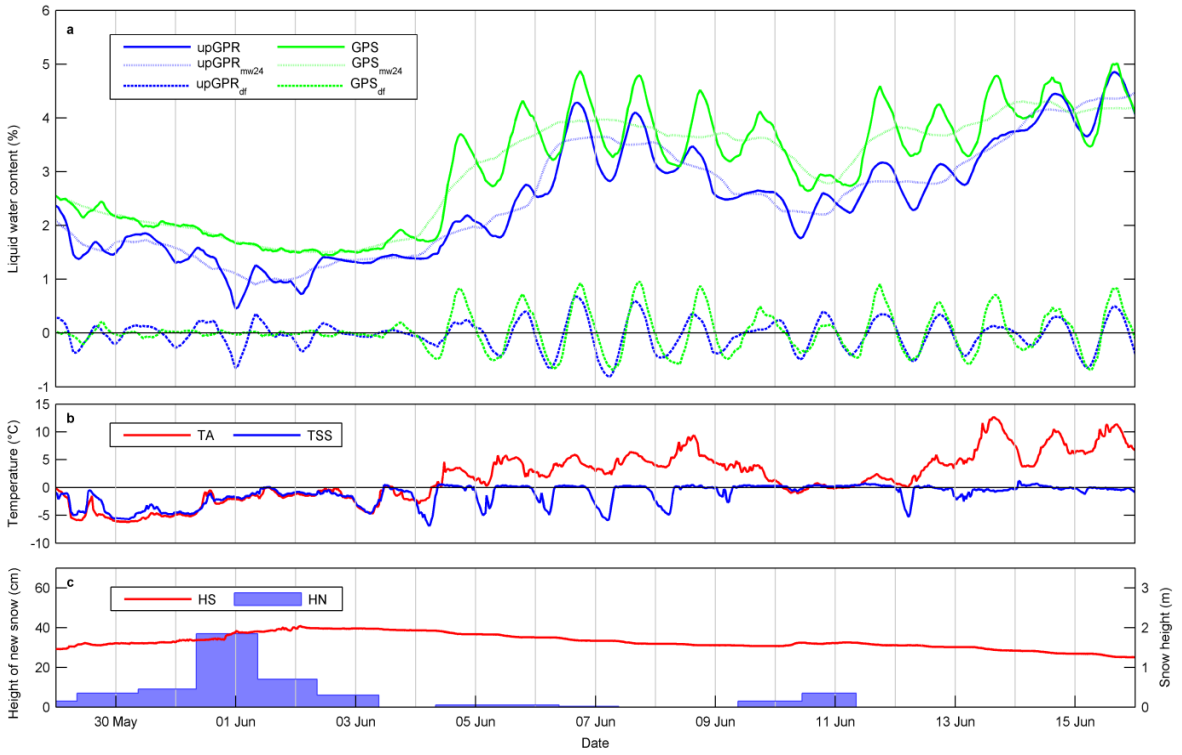

Figure 3.3: Diurnal variations of the bulk volumetric liquid water content in comparison with temperature and snow height data, exemplarily shown for the time period 29 May to 16 June 2013. (a) Evolution of the liquid water content in snow with daily fluctuations (upGPR and GPS), low-pass filtered with a moving average over 24 h without daily fluctuations ($upGPR_{mw24}$ and GPS_{mw24}), and the difference of LWC and the low-pass filtered trend representing the daily fluctuations ($upGPR_{df}$ and GPS_{df}). (b) Air temperature (TA) and snow surface temperature (TSS). (c) Snow height (HS) measured with the laser sensor and height of new snow (HN) as manually measured daily at 8 a.m.

Figure 3.2e and 3.2f show the SWE derived with the upGPR-GPS combination in comparison with snow pillow and snow scale as well as the manual measurements from the snow pits. Especially in 2013 during the dry-to-wet transition, snow scale and snow pillow deviated considerably. In general, the agreement between the conventional measurements was poorer (mean RMSD of 127 mm w.e. in 2013 and 78 mm w.e. in 2014, Table 3.1) than compared to the upGPR-GPS combination with a mean RMSD of 69 mm w.e. in 2013 (10.6% of mean SWE ($\overline{SWE}$) of 650 mm w.e.) and 52 mm w.e. in 2014 (9.8% of $\overline{SWE}$ of 532 mm w.e.). Even though the snow pillow is situated furthest away from the upGPR and GPS, the agreement was best in both years.

Table 3.1: Root-mean-square deviations for bulk volumetric liquid water content ($RMSD_{LWC}$), snow height ($RMSD_{HS}$) and snow water equivalent ($RMSD_{SWE}$) for the season 2012-2013 (above diagonal, regular) and 2013-2014 (below diagonal, italic). Important results are shown in bold.

$RMSD_{LWC}$ (pp)

	upGPR	GPS	Denoth meter	Snow Fork
upGPR	-	**0.7**	0.9	2.2
GPS	***0.4***	-	0.9	1.5
Denoth meter	*0.4*	*0.3*	-	2.1

$RMSD_{HS}$ (cm)

	upGPR	upGPR & PS	Laser	Ultrasonic 1	Ultrasonic 2	Manual
upGPR	-	27.6	26.8	24.5	39.0	18.4
upGPR & GPS	*14.0*	-	**6.6**	7.1	13.7	11.7
Laser	*14.8*	***3.3***	-	3.3	13.8	5.8
Ultrasonic 1	*10.4*	*5.3*	*5.2*	-	15.3	4.8
Ultrasonic 2	*26.1*	*13.5*	*12.6*	*17.3*	-	18.1
Manual	*12.8*	*3.1*	*1.0*	*6.4*	*11.1*	-

$RMSD_{SWE}$ (mm w.e.)

	upGPR & GPS	Snow pillow	Snow scale	Manual
upGPR & GPS	-	48	77	82
Snow pillow	*31*	-	112	121
Snow scale	*83*	*55*	-	149
Manual	*43*	*65*	*114*	-

3.4. Discussion

3.4.1 Comparison of both methods

We separately derived the bulk volumetric LWC fromthe upGPR and the GPS data. Both systems recorded data with sensors installed below the snow cover but required externally measured HS and an estimate for ρ_d to derive LWC. The few measurements with the dielectric devices (eight Denoth and five Snow Fork samples in 2013 and three Denoth samples in 2014) revealed values of LWC in a similar range as derived with upGPR and GPS. The RMSD between all measurements and the Snow Fork was quite large with 1.5–2.2 pp; values measured by the Snow Fork were larger than measured by the other methods. This discrepancy was already reported by *Mitterer et al.* [2011b], *Schmid et al.* [2014], and *Techel and Pielmeier* [2011]. In general, the comparison of upGPR and GPS with the dielectric devices is questionable. The latter are destructive, gives only a snap shot in time and is conducted within a snow pit where conditions might change rapidly due to external influences [*Koch et al.*, 2014; *Mitterer et al.*, 2011b; *Schmid et al.*, 2014].

For the first time, it was possible to compare and validate the two methods that both provide bulk LWC in a continuous and nondestructive manner. The comparison between upGPR and GPS showed a high level of agreement with regard to the temporal evolution and the range of LWC values over the entire spring periods 2013 and 2014 (Table 3.1). Moreover, both systems showed diurnal variations due to melt and refreeze processes—again in good temporal agreement. Differences in LWC between the two methods might occur because HS at the location of the laser sensor differs from HS above the upGPR or the GPS antennas. Considerable differences in LWC between upGPR and GPS were observed only at the end of the snow-covered period (June 2014), when HS decreased below 1m accompanied with a clear increase in LWC. On the one hand,

as the calculation of LWC strongly depends on HS, possible differences in HS between the upGPR and GPS locations and the HS sensor location may be more pronounced shortly before the melt out of the instruments and will have a relatively large effect. In addition, very deep concave furrows of 10 cm were observed on the surface, such that not even the surface was well defined. On the other hand, the LWC directly upon upGPR and GPS can easily vary due to rapid melting processes within the ripe snowpack (end of June 2013 and beginning of June 2014). Moreover, the formulas applied for the complex permittivity are only valid up to a LWC of approximately 8% [*Lundberg and Thunehed*, 2000; *Mitterer et al.*, 2011b]. However, these deviations were only observed at the very end of the snow covered season; overall, the agreement between both systems was very good.

3.4.2 Combination of both methods

Combining upGPR and GPS allowed deriving the snow properties LWC, HS, and SWE without using any other external information. As main advantages, this combination is installed below the snow cover and works nondestructively, operates independently from poles and stakes, avoids possible bridging effects within the snow cover, and can therefore potentially be applied in slopes to support avalanche and flood warnings in remote areas. Because the GPS receivers are cheap, the costs of this sensor combination are only negligibly higher than for the upGPR alone. To eliminate a possible error due to spatial variability within the snowpack, especially during melt conditions, both instruments can be installed at the same place at the ground surface, which means that they can observe the same snowpack properties simultaneously.

As illustrated in Figure 3.2c and 3.2d, HS derived from the upGPR-GPS combination is in very good agreement with the HS laser measurement during dry and wet snow conditions. Laser, ultrasonic 1, and manual measurements were recorded closest to the upGPR and GPS locations. The RMSD between these measurements and the HS derived from the upGPR-GPS combination are all well below the mean RMSD of all conventional methods. These results suggest that the combined upGPR and GPS approach is suited to determine HS, even during wet snow conditions. Compared to upGPR without external information alone, the RMSD improved from on average 27 cm (2013) and 16 cm (2014) to 9.8 cm and 6.3 cm (Table 3.1).

Regarding SWE (Figure 3.2e and 3.2f), the agreement between snow pillow and snow scale was surprisingly poor despite the fact, that they were situated only 5 m apart from each other. The deviations, especially obvious during the first wetting period in 2013 (1 April–6 May) might be due to bridging effects [*Johnson and Marks*, 2004]. Overall, not being influenced by bridging effects and measuring nondestructively, the SWE and its evolution derived from only upGPR and the combination of upGPR and GPS seemed more reliable. Values of SWE derived from upGPR and GPS were mostly higher than those from snow pillow and snow scale but lower than from manual measurements. These findings can be explained by the observation of increasing HS at the study site from the snow pillow location to the manual snow profiles (Figure 3.1). The combined approach upGPR and GPS overestimated SWE during and shortly after intense snowfalls, as the bulk density decreased due to the low density of new snow (≈100 kg m^{-3}) (e.g., end of March 2014). Exemplarily for a HS of 1.5 m and a LWC of 4%, an overestimation/underestimation of the bulk density of ±10% leads to an overestimation/ underestimation of SWE of ±7%.

3.5 Conclusions

We derived the bulk volumetric LWC with (1) an upGPR and (2) low-cost GPS receivers buried below the snow cover during two winter seasons. The independently estimated LWC and its evolution agreed very well—suggesting that each of the two methods provides reliable values of LWC. The observation of daily melt-freeze cycles with high temporal resolution may improve runoff calculations within hydrological catchments, which are, e.g., important for hydropower and reservoir management.

We then combined the data from upGPR and GPS to continuously and nondestructively derive LWC, HS, and SWE without the need for additional external information (i.e., HS) from above snow instrumentation; this was not possible before. HS and SWE agreed well with conventional measurements. The novel combination allows to monitor essential snow cover properties from below the snow cover—which potentially can be applied in complex and remote terrain, e.g., in avalanche-prone slopes. We suggest to routinely upgrade all upGPR or other below snowpack techniques with low-cost GPS receivers, as the additional costs and manual effort for the installation are negligible compared with other costs like those of a radar system. The upGPR-GPS combination has the potential to improve avalanche forecasting and flood predictions. It could, moreover, provide an additional proxy for surface melt for comparison with surface energy balance models, which depend on several parameters like albedo. As the combination can estimate SWE with high temporal resolution, our approach may also be suited for large-scale applications, e.g., for catchment-wide estimation of runoff and hydroelectric power generation potential, as well as provide valuable ground truth data for remote sensing applications, e.g., in the field of glacier and sea ice studies. Therefore, we recommend widespread applications.

Acknowledgments

Lino Schmid was supported by the Swiss National Science Foundation (SNF 200020_144390), Franziska Koch and Achim Heilig by the German Research Foundation (DFG MA 875/12-1 and EI 672/6, respectively). The data presented in this manuscript can be made available on request. The Editor thanks two anonymous reviewers for their assistance in evaluating this paper.

4. SNOW WATER EQUIVALENT OF DRY SNOW DERIVED FROM GNSS CARRIER PHASES

This manuscript was submitted to the journal ***IEEE Transactions on Geoscience and Remote Sensing***:

**** P. Henkel and F. Koch contributed equally.***

Henkel*, P., Koch*, F., Appel, F., Bach, H., Prasch, M., Schmid, L., Schweizer, J., and Mauser, W. (2017): Snow water equivalent of dry snow derived from GNSS carrier phases. IEEE Transactions on Geoscience and Remote Sensing, Volume, Issue, Pages.

Abstract

Snow water equivalent (SWE) is a key variable for various hydrological applications. It is defined as the depth of water that would result upon complete melting of a mass of snow. However, until now, continuous measurements of SWE are either scarce, expensive, labour-intense or lack temporal or spatial resolution especially in mountainous and remote regions. We derive SWE for dry-snow conditions using carrier phase measurements from Global Navigation Satellite System (GNSS) receivers. Two static GNSS receivers are used, whereby one antenna is placed below the snow and the other antenna on a pole above the snow. The carrier phase measurements of both receivers are combined in double differences (DD) to eliminate atmospheric errors and clock offsets. Each DD carrier phase measurement depends on the relative position between both antennas, on an integer ambiguity due to the periodic nature of the carrier phase signal, and on the SWE projected into the direction of incidence. The relative positions of the antennas are determined under snow-free conditions with millimetre accuracy using Real Time Kinematic (RTK) positioning. Subsequently, SWE and carrier phase integer ambiguities are jointly estimated with an integer least-squares estimator. We tested our method at an Alpine test site in Switzerland during the dry-snow season 2015-2016. The SWE derived solely by GNSS shows very high correlation with conventionally measured snow pillow (RMSE: 11 mm) and manual snow pit data. This method can be applied to dense low-cost GNSS receiver networks to improve the spatial and temporal information on snow cover properties.

4.1 Introduction

The Earth's water resources are stored to a great extent in permanent or seasonal snow cover. The amount of water stored in the snowpack expressed as snow water equivalent (SWE) is a key variable in water resources management and an essential component within the Earth's climate system [*Vaughan et al*., 2013]. The amount of snow and its melting determines quantitatively and temporally the river runoff of numerous mountain catchments. The snow cover is hence a naturally regulated storage which is relevant for many hydrological applications such as hydropower production, navigation, water supply for drinking water and irrigation [*Barnett et al*., 2005; *Koch et al*., 2011; *Mauser and Prasch*, 2015]. Moreover, the release of water stored in the snowpack might contribute to avalanche formation, slush flows and floods. The latter may in particular occur during

conditions of intense melting and rain in spring; their intensity and temporal occurrence may increase under changing climatic conditions [*Bavay et al*., 2009; *Stewart*, 2009]. Continuous monitoring of the snowpack, especially SWE is therefore highly requested for hydrological modelling approaches as well as avalanche and in particular flood forecasts.

However, until now, measurements of SWE are very scarce, especially in difficult to reach and sparsely populated areas, and are often not conducted continuously. Conventionally, SWE is measured by weighing a given volume of snow cut out of the snowpack with tubes [*Fierz et al*., 2009]. This technique is so far the most reliable method, but it is destructive, as snow pits have to be dug, labour-intense, and gives only a snapshot in time. Snow pillows [*Archer and Stewart*, 1995] and snow scales, for example, measure continuously, but are quite expensive and difficult to install and are limited to flat terrain. Moreover, these methods are prone to measurement errors due to bridging effects, especially during the first wetting of snow in spring [*Johnson and Marks*, 2004]. Active and passive microwave remote sensing approaches, e.g. summarized by *Tedesco* [2014], provide spatial information, on snow height but also on SWE. However, they are often not available in high temporal resolution, may lack the required spatial resolution or are restricted due to foreshortening or layover effects, in particular in mountain regions [e.g., *Strozzi et al*., 1997]. In general, continuous and high quality measurements at numerous locations would be largely useful for the validation of Earth observation satellite data and to improve hydrological models.

Since the last decade, several approaches to derive snow cover properties from GNSS signals have been developed. These are in particular GNSS reflectometry approaches, mainly based on fix installed, high-end geodetic receivers, aiming to derive information on snow height as the signals are reflected at the air – snow interface [e.g., *Cardellach et al.*, 2011; *Jacobson*, 2010; *Jin and Najibi*, 2014; *Larson et al.*, 2009; *Rodriguez-Alvarez et al.*, 2012b]. For this technique, mainly the line-of-sight and reflected GNSS signal strength information is applied and a quite flat area of up to 1.000 m² is needed [*Larson, 2016*], whereby the antenna is situated in the middle. *Koch et al.* [2014] developed an alternative approach using low-cost GPS receivers to quantitatively derive the liquid water content in the snowpack from the attenuation of the carrier-to-noise-power density ratio C/N_0 caused by a prominent change of the dielectric properties of snow as liquid water occurs. In addition, this approach, in combination with an upward-looking ground penetrating radar system, provides snow height and SWE information under dry- and wet-snow [*Schmid et al.*, 2015]. Evaluating the two-way travel time information of the electromagnetic pulse in the same L-band frequency domain had already shown good results for snow properties, as long as the snowpack was dry, but overestimated the snow height under wet-snow conditions [*Schmid et al.*, 2014]. This deficiency was improved by the combination with the GPS system [*Schmid et al.*, 2015]. However, radar sensors are expensive and thus not attractive for dense sensor networks.

A novel and highly promising method to derive SWE with low-cost GNSS sensors, which is presented in this paper, was developed and applied within the ARTES-IAP Demo Project SnowSense (https://artes-apps.esa.int/projects/snowsense-dp), co-funded by the European Space Agency (ESA). In general, this project aims to provide highly demanded continuous and non-destructive information on snow cover properties, also in remote and difficult to access areas, e.g., for hydropower companies and flood or avalanche forecast centres. In order to make dense sensor networks possible, all sensors are low-cost encompassing two GNSS receivers and antennas, a micro-controller and data storage. One of these setups using low-cost GPS sensors (recording L1-band GPS signals) was used for this study at the high Alpine test site Weissfluhjoch near Davos, Switzerland at an elevation of 2.540 m a.s.l. Additionally, an optional self-sufficient energy component as well as a component for data transmission are available for the SnowSense GNSS sensor setup. However, regarding the latter, for this study, the infrastructure of the test site with its electric grid and its internet facility were used.

We show, exemplarily for the dry winter period 2015-2016, that with this GNSS setup, SWE can continuously be determined solely with GNSS carrier phase signals.

4.2 Modelling of carrier phases with snow cover

The snow causes a delay in both, code and carrier phase measurements, which is proportional to SWE under dry-snow conditions. However, as the code measurements are too noisy for SWE derivation, we use only GNSS carrier phase measurements.

In general, snow has the following effects on the carrier phase, which are both taken into account in our model:

- delay of GNSS signals due to reduced signal propagation speed in snow
- refraction at air-snow interface due to change in medium

The signal delay can be derived from the phase measurements and is described using a precise model of the phase measurements and an integer least-squares estimator. It is the most sophisticated part as the phase measurements are also affected by several other parameters (e.g., the receiver's and satellite's position and integer ambiguities) and since all parameters need to be determined with a total error of at most a few centimetres. The consideration of the refraction is easy as the change of satellite elevation due to refraction can be computed analytically. Regarding this approach, we are interested only in the effect of snow, i.e. receiver and satellite clock offsets and biases, orbital errors and atmospheric errors are all nuisance parameters. Therefore, we eliminate all nuisance parameters by performing double difference measurements using two low-cost GNSS antennas connected to two low-cost GNSS receivers. Thereby, one antenna is placed on a pole above the snow and one antenna on the ground as shown in Figure 4.1.

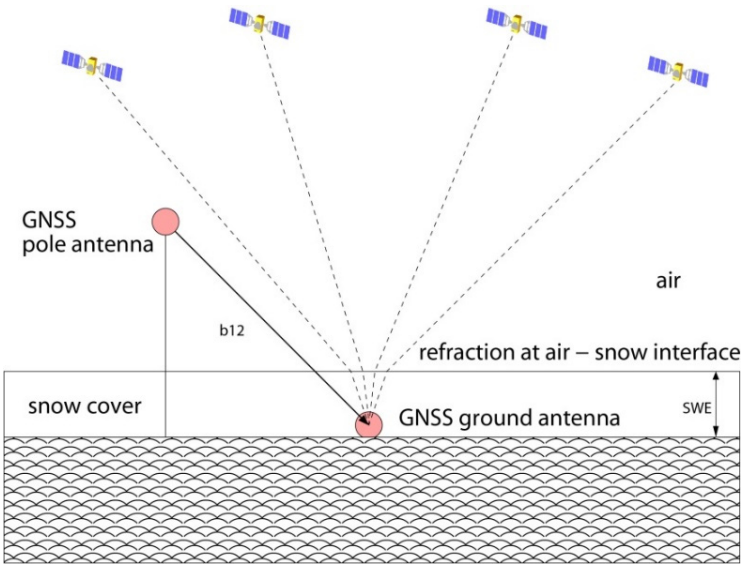

Figure 4.1: GNSS setup for derivation of SWE.

We model the double difference (DD) carrier phase measurements for receiver pair $r \in \{1,2\}$ and satellite pair $\{k, l\}$ by

$$\begin{aligned}\lambda\varphi_{12}^{kl} &= \lambda(\varphi_1^k - \varphi_2^k) - \lambda(\varphi_1^l - \varphi_2^l) \\ &= \vec{e}^{kl}\vec{b}_{12} + c_{12}^{kl} + \lambda N_{12}^{kl} + \frac{\lambda}{2}\Delta N_{12}^{kl} + \gamma m^{kl} \cdot d_s + \lambda\Delta\varphi_{\mathrm{MP},12}^{kl} + \varepsilon_{12}^{kl}\end{aligned} \tag{4.1}$$

with wavelength λ, phase measurement φ_r^k recorded in cycles, normalized line of sight vector $\vec{e}^{kl}$ between the antenna phase centres of the satellites and the receivers, baseline vector $\vec{b}_{12}$ between pole and ground antennas, synchronization correction c_{12}^k, integer ambiguity N_r^k, half-cycle slip $\frac{1}{2}\Delta N_r^k$, speed correction factor γ due to snow, mapping function m^k for projecting the vertical delay into slant delay, snow parameter d_s, phase multipath $\Delta\varphi_{\mathrm{MP},r}^k$, and phase noise ε_r^k and

$$(\cdot) = (\cdot)^k - (\cdot)^l \tag{4.2}$$

being the difference between satellites k and l.

As the phase multipath and phase noise of Equation (4.1) can hardly be separated, we map the multipath to the noise, i.e.

$$\tilde{\varepsilon}_{12}^{kl} := \lambda \Delta\varphi_{\mathrm{MP},12}^{kl} + \varepsilon_{12}^{kl}. \tag{4.3}$$

The *snow*-related term $\gamma m^{kl} \cdot d_\mathrm{s}$ is obtained from the DD phase measurements by subtraction of the estimates of the baseline term, the synchronization correction, the integer ambiguities and the cycle slips. The obtained term is typically called *carrier phase residuals*. If there is no snow, then the residuals are close to zero-mean white Gaussian noise with a standard deviation of less than 1 cm. If a snow pack exists, then the residuals are linearly proportional to both the mapping function m^{kl} and the snow parameter d_s.

The snow parameter d_s expresses a *virtual* snow height which is proportional to the time delay of a vertical GNSS signal through the snowpack. The single difference mapping function is given by

$$m^{kl} = \frac{1}{\sin(E_\mathrm{s}^k)} - \frac{1}{\sin(E_\mathrm{s}^l)}, \tag{4.4}$$

with E_s^k and E_s^l being the elevation of the refracted signal of the k-th and l-th satellite, respectively. The elevation of this refracted signal can be obtained from Snell's law as

$$E_\mathrm{s}^k = 90° - \mathrm{asin}\left(\frac{n_\mathrm{s}}{n_\mathrm{a}} \sin(90° - E_\mathrm{a}^k)\right), \tag{4.5}$$

with E_a^k being the satellite's elevation above the snow cover for exemplary the k-th satellite, and n_a and n_s being the refraction indices in the air and snow. For this approach, we set the elevation mask to 25° to eliminate satellites with excessive phase multipath and frequent losses of lock.

The speed correction factor for electromagnetic waves for dry snow is given by

$$\gamma = \frac{c_0}{v_\mathrm{s}} - 1, \tag{4.6}$$

with the speed of light c_0 and the speed of signal propagation $v_\mathrm{s} \approx 2.3 \times 10^8$ ms^{-1}, which was also applied, e.g., in *Schmid et al.* [2014 and 2015]. Moreover, v_s can be determined by using the permittivity of snow ε_s' and applying Snell's law as

$$v_s = \frac{n_\mathrm{a}}{n_\mathrm{s}} c_0 \tag{4.7}$$

with

$$n_\mathrm{s} = \sqrt{\varepsilon_\mathrm{s}'}. \tag{4.8}$$

Moreover, it has to be considered that due to Snell's law, the wavelength in air λ_a of electromagnetic waves is reduced to the wavelength λ_s in snow as

$$\lambda_\mathrm{s} = \frac{n_\mathrm{a}}{n_\mathrm{s}} \lambda_\mathrm{a}. \tag{4.9}$$

4.3 Method for SWE derivation

In this section, we describe in detail our method for the SWE derivation with GNSS. As the GNSS antennas are mounted at static points, it is sufficient to determine the 3D baseline vector only once and to re-use this known baseline for SWE derivation at every subsequent epoch. We determined the 3D baseline vector directly after the

installation of the receivers without any snow cover. Thus, the positioning can be separated from the estimation of the snow parameter. This setup without any snow cover refers to classic Real Time Kinematic (RTK) positioning, which was described by *Talbot* [1993]. An efficient implementation was developed e.g. by *Takasu and Yasuda* [2009]. The performance has been improved over the last two decades, e.g. by using multi-GNSS measurements and fixing ambiguities of multiple constellations (e.g. joint GPS/Glonass fixing [*Henkel et al.*, 2016a] and joint GPS/QZSS fixing [*Kubo et al.*, 2004]), by code multipath estimation [*Henkel et al.*, 2016b], by partial ambiguity fixing [*Teunissen*, 1995a], and/or by partial integer decorrelation [*Henkel and Günther*, 2009].

Figure 4.2 includes a flow chart for determining SWE. The steps in black solid boxes are identical to the ones of standard RTK positioning. The synchronization correction is needed for low-cost GNSS receivers and computed according to *Henkel and Cárdenas* [2014]. Cycle slips are obtained by prediction of measurements from history and by comparison of these predicted measurements with actual measurements. The steps in blue/dashed boxes are specific to snow and explained in this section.

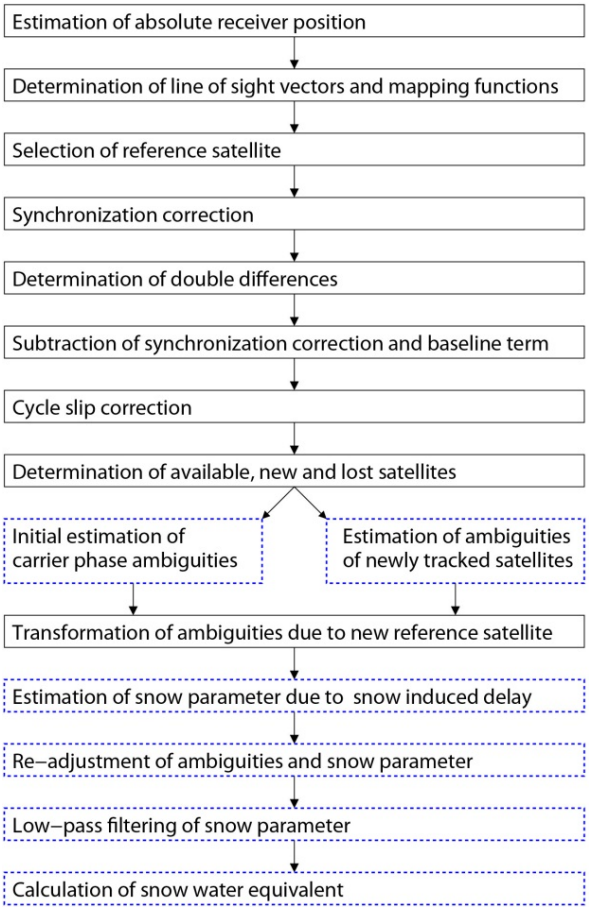

Figure 4.2: Flow chart for individual processing steps aiming to derive SWE. The steps in blue/dashed boxes are specific to snow.

4.3.1 Fixing of initial ambiguities

We correct the DD measurements for the a priori known baseline, the synchronization error and cycle slips, i.e.

$$\lambda\tilde{\varphi}_{12}^{kl} = \lambda\varphi_{12}^{kl} - \vec{e}^{kl}\vec{b}_{12} - c_{12}^{kl} - \frac{\lambda}{2}\Delta N_{12}^{kl} = \lambda N_{12}^{kl} + \gamma m^{kl} \cdot d_{\mathrm{s}} + \lambda\Delta\varphi_{\mathrm{MP},12}^{kl} + \tilde{\varepsilon}_{12}^{kl} \tag{4.10}$$

which leaves only the ambiguities N_{12}^{kl} and the snow parameter d_{s} as unknowns. The combined phase noise and multipath $\tilde{\varepsilon}_{12}^{kl}$ is typically below 2 cm.

The separation of N_{12}^{kl} and d_{s} can be performed only via the known mapping function, which changes over time with the satellite elevation. Therefore, we consider the corrected DD measurements from n epochs jointly:

$$\begin{pmatrix} \lambda\tilde{\varphi}_{12}^{kl}(t_1) \\ \vdots \\ \lambda\tilde{\varphi}_{12}^{kl}(t_n) \end{pmatrix} = H^{kl}\begin{pmatrix} N_{12}^{kl} \\ d_\mathrm{s} \end{pmatrix} + \begin{pmatrix} \tilde{\varepsilon}_{12}^{kl} \\ \vdots \\ \tilde{\varepsilon}_{12}^{kl} \end{pmatrix}, \tag{4.11}$$

with

$$H^{kl} = \begin{pmatrix} \lambda & \gamma m^{kl}(t_1) \\ \vdots & \vdots \\ \lambda & \gamma m^{kl}(t_n) \end{pmatrix}. \tag{4.12}$$

The least-squares estimates of the ambiguity and the snow parameter follow as

$$\begin{pmatrix} \widehat{N}_{12}^{kl} \\ \hat{d}_\mathrm{s} \end{pmatrix} = \arg\min_{N_{12}^{kl},\, d_\mathrm{s}} \left\| \begin{pmatrix} \lambda\tilde{\varphi}_{12}^{kl}(t_1) \\ \vdots \\ \lambda\tilde{\varphi}_{12}^{kl}(t_n) \end{pmatrix} - H^{kl}\begin{pmatrix} N_{12}^{kl} \\ d_\mathrm{s} \end{pmatrix} \right\|^2 = ((H^{kl})^\mathrm{T} H^{kl})^{-1}(H^{kl})^\mathrm{T} \begin{pmatrix} \lambda\tilde{\varphi}_{12}^{kl}(t_1) \\ \vdots \\ \lambda\tilde{\varphi}_{12}^{kl}(t_n) \end{pmatrix}. \tag{4.13}$$

The sum of squared residuals of this least-squares adjustment is given by

$$\mathrm{SSE}_{12}^{kl} = \left\| P_H^\perp \begin{pmatrix} \lambda\tilde{\varphi}_{12}^{kl}(t_1) \\ \vdots \\ \lambda\tilde{\varphi}_{12}^{kl}(t_n) \end{pmatrix} \right\|^2, \tag{4.14}$$

with $P_H^\perp$ being the projector on the space orthogonal of the space orthogonal of H. If the sum of squared residuals is sufficiently small and the ambiguity estimate is close to an integer number, the ambiguity can be fixed by rounding to the nearest integer number, i.e.

$$\breve{N}_{12}^{kl} = \left[\widehat{N}_{12}^{kl}\right]. \tag{4.15}$$

The snow parameter occurs as common variable for all double differences in Equation (4.10). Thus, the snow parameter couples the double differences of all satellites. The estimation of both, N_{12}^{kl} , $k \in \{1, \ldots., K\}$, and d_s, can be improved by a *joint* consideration of the measurements from all visible satellites and available epochs. Therefore, Equation (4.11) is expanded to

$$\begin{pmatrix} \lambda\tilde{\varphi}_{12}^{1l}(t_1) \\ \vdots \\ \lambda\tilde{\varphi}_{12}^{1l}(t_n) \\ \vdots \\ \lambda\tilde{\varphi}_{12}^{Kl}(t_1) \\ \vdots \\ \lambda\tilde{\varphi}_{12}^{Kl}(t_n) \end{pmatrix} = H\begin{pmatrix} N_{12}^{1l} \\ \vdots \\ N_{12}^{Kl} \\ \hline d_s \end{pmatrix} + \begin{pmatrix} \tilde{\varepsilon}_{12}^{1l}(t_1) \\ \vdots \\ \tilde{\varepsilon}_{12}^{1l}(t_n) \\ \vdots \\ \tilde{\varepsilon}_{12}^{Kl}(t_1) \\ \vdots \\ \tilde{\varepsilon}_{12}^{Kl}(t_n) \end{pmatrix}, \tag{4.16}$$

with

$$H = \left(\begin{array}{ccc|c} \lambda & & & \gamma m^{1l}(t_1) \\ \vdots & & & \vdots \\ \lambda & & & \gamma m^{1l}(t_n) \\ \hline & \ddots & & \vdots \\ \hline & & \lambda & \gamma m^{Kl}(t_1) \\ & & \vdots & \vdots \\ & & \lambda & \gamma m^{Kl}(t_n) \end{array}\right). \tag{4.17}$$

The least-squares solution of the DD integer ambiguities and snow parameter is given by

$$\left(\breve{N}_{12}^{1l}, \ldots, \breve{N}_{12}^{Kl}, \breve{d}_\mathrm{s}\right)^\mathrm{T} = \arg\min_{\substack{\{N_{12}^{1l}, \ldots, N_{12}^{1l}\} \in \mathbb{Z} \\ d_\mathrm{s} \in \mathbb{R}}} \left\| \lambda\tilde{\varphi}_{12} - H\begin{pmatrix} N_{12}^{1l} \\ \vdots \\ N_{12}^{Kl} \\ \hline d_\mathrm{s} \end{pmatrix} \right\|_{\Sigma^{-1}}^2 \tag{4.18}$$

where the phase measurements of all epochs and satellites are stacked as

$$\lambda\tilde{\varphi}_{12} = \left(\lambda\tilde{\varphi}_{12}^{1l}(t_1), \dots, \lambda\tilde{\varphi}_{12}^{1l}(t_n), \dots, \lambda\tilde{\varphi}_{12}^{Kl}(t_1), \dots, \lambda\tilde{\varphi}_{12}^{Kl}(t_n)\right)^{\mathrm{T}}. \tag{4.19}$$

The solution of Equation (4.18) can be obtained with an integer least-squares estimator, e.g. the LAMBDA method of *Teunissen* [1995b], which includes an integer decorrelation Z and sequential tree seach S to fix the ambiguities to integers. The i-th candidate of the search is given by

$$\breve{N}_{12}^{(i)} = \begin{pmatrix} \breve{N}_{12}^{1l} \\ \vdots \\ \breve{N}_{12}^{Kl} \end{pmatrix} = Z^{-1}S(Z\hat{N}_{12}), \tag{4.20}$$

with

$$\hat{N}_{12} = \begin{pmatrix} \hat{N}_{12}^{1l} \\ \vdots \\ \hat{N}_{12}^{Kl} \end{pmatrix}. \tag{4.21}$$

A fixing is typically considered as reliable if the sum of squared ambiguity residuals of the *second*-best candidate $\breve{N}_{12}^{(2)}$ are significantly larger than the sum of squared ambiguity residuals of the *first*-best candidate $\breve{N}_{12}^{(1)}$. This ratio test q is given by

$$q = \frac{\left\|\hat{N}_{12} - \breve{N}_{12}^{(2)}\right\|^2}{\left\|\hat{N}_{12} - \breve{N}_{12}^{(1)}\right\|^2} \gg 1, \tag{4.22}$$

and was analyszed in detail for future ambiguity resolution by *Verhagen and Teunissen* [2013]. Once the initial ambiguities are fixed, an instantaneous estimate of the snow parameter can be obtained at every epoch given by

$$\check{d}_{\mathrm{s}}(t_n) = \frac{1}{m^{\mathrm{T}}(t_n)\Sigma^{-1}(t_n)m(t_n)} \cdot m^{\mathrm{T}}(t_n)\Sigma^{-1}(t_n)\begin{pmatrix} \lambda\tilde{\varphi}_{12}^{1l}(t_n) - \breve{N}_{12}^{1l} \\ \vdots \\ \lambda\tilde{\varphi}_{12}^{Kl}(t_n) - \breve{N}_{12}^{Kl} \end{pmatrix}, \tag{4.23}$$

with

$$m(t_n) = \gamma \cdot \begin{pmatrix} m^{1l}(t_n) \\ \vdots \\ m^{Kl}(t_n) \end{pmatrix}. \tag{4.24}$$

4.3.2 Initialization of ambiguities of newly tracked satellites

The ambiguities of newly tracked satellites need to be initialized. We distinguish between initializations after *short* signal interruptions (e.g. due to loss of phase lock) and *long* signal interruptions (e.g. rise of satellite above horizon). For short signal interruptions, the ambiguities can be instantaneously fixed using the phase measurements at epoch $n-1$ and the change of the mapping function, i.e.

$$\breve{N}_{12}^{kl} = \left[\tilde{\varphi}_{12}^{kl}(t_n) - \frac{m^{kl}(t_n)}{m^{kl}(t_{n-1})}\,\tilde{\varphi}_{12}^{kl}(t_{n-1}) - \breve{N}_{12}^{kl}(t_{n-1})\right]. \tag{4.25}$$

For longer signal interruptions, the likelihood of undetected cycle slips and/or of a change in the snow parameter increases. Therefore, the ambiguities are fixed using the current snow parameter estimate, i.e.

$$\breve{N}_{12}^{kl} = \left[\frac{1}{\lambda}\left(\tilde{\varphi}_{12}^{kl} - \gamma m^{kl} \cdot \hat{d}_{\mathrm{s}}\right)\right]. \tag{4.26}$$

4.3.3 Re-adjustment of ambiguities

Tracking errors of the receivers and/or errors in the cycle slip correction might require a re-adjustment of the ambiguities. We consider two options for this re-adjustment.

The first option can be applied if a satellite is having approximately the same elevation as the reference satellite. In this case, the mapping function m^{kl} vanishes and the ambiguity of the satellite can be simply re-adjusted as

$$\breve{N}_{12}^{kl} = \left[\frac{\lambda\tilde{\varphi}_{12}^{kl}}{\lambda}\right]. \tag{4.27}$$

The second option is a least-squares re-estimation of ambiguities and snow parameter according to Equation (4.13). In general, the first option is clearly preferred since it is much more accurate. However, there are some satellite passes with an elevation maximum far below the elevation of the reference satellite. In this case, a re-adjustment can only be performed with the second option.

4.3.4 Fixed phase residuals

After the ambiguities were fixed, r_{12}^{kl} remains as

$$r_{12}^{kl} = \lambda\tilde{\varphi}_{12}^{kl} - \lambda\breve{N}_{12}^{kl} = \gamma m^{kl} \cdot \check{d}_s + \tilde{\varepsilon}_{12}^{kl}. \tag{4.28}$$

Regarding Equation (4.28), the fixed phase residuals r_{12}^{kl} encompass the *snow* term $\gamma m^{kl} \cdot \check{d}_s$ and $\tilde{\varepsilon}_{12}^{kl}$.

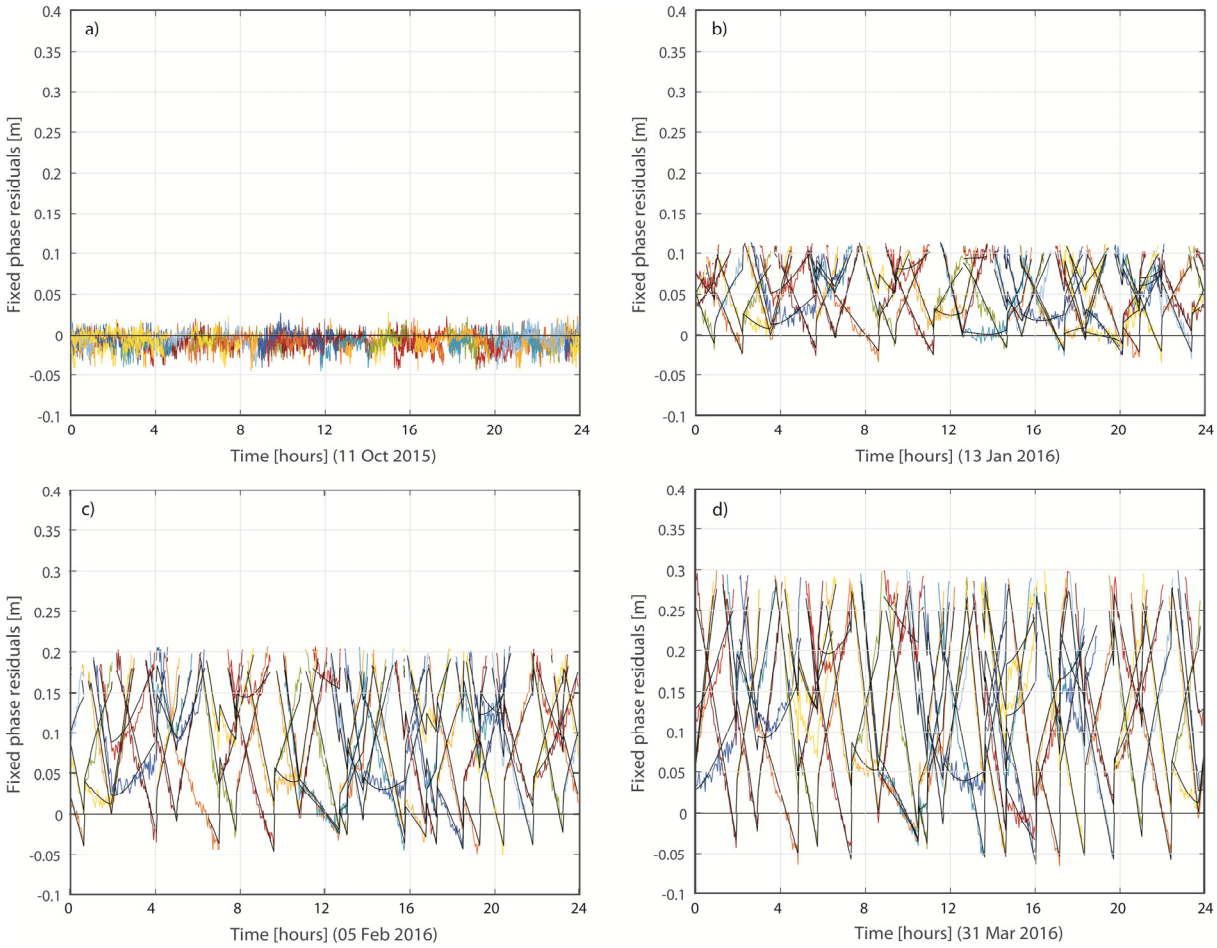

Figure 4.3: Carrier phase residuals for each GPS satellite recorded over one day (a) snow-free conditions (11 Oct 2015) with small fixed phase residuals around zero. Carrier phase residuals and arcs for each GPS satellite recorded over one day (b) for dry-snow conditions with a SWE of approx. 200 mm w.e. (13 Jan 2016), (c) for dry-snow conditions with a SWE of approx. 400 mm w.e. (5 Feb 2016), and (d) for dry-snow conditions with a SWE of approx. 600 mm w.e. (31 Mar 2016).

Figure 4.3 illustrates the carrier phase residuals of all 32 GPS satellites recorded during one day for four exemplary days with different values of SWE with approximate SWE values of 0, 200, 400 and 600 mm w.e. The starting point and the ending point of each satellite is given by the time of satellite rising and setting and, thus, is almost independent of snow cover. Each colour corresponds to one of the 32 GPS satellites.

There are three different types of dynamics in the residuals: First, short-term variations over a few seconds are caused by phase multipath. Second, mid-term variations over a few hours are caused by the change of the satellite elevation. Finally, long-term variations over several hours or days are caused by changes of the snowpack. Clearly, the second type is dominant once the SWE exceeds a certain minimum and leads to the typical arched shape.

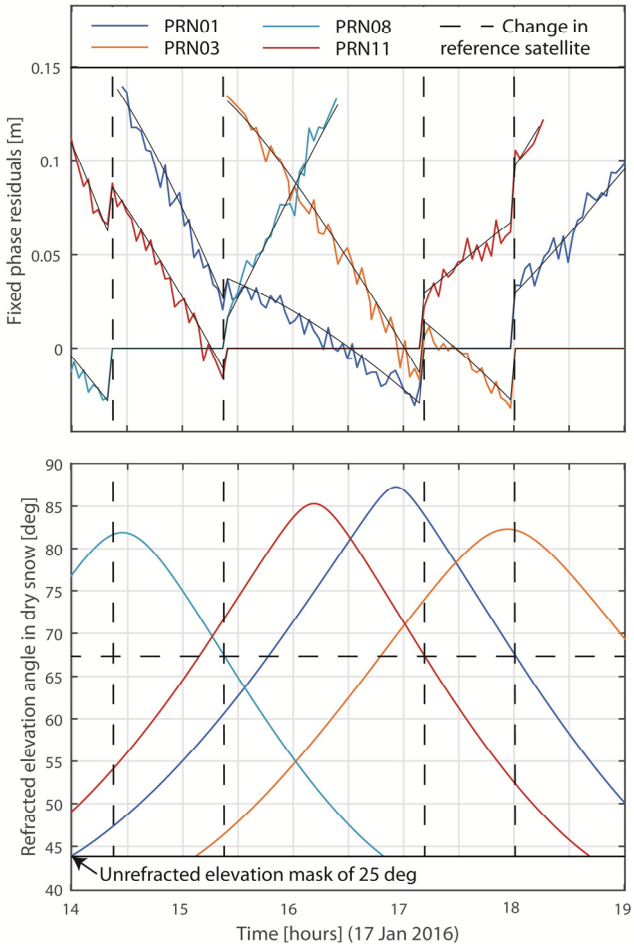

Figure 4.4: (a) Fixed phase residuals with arcs, exemplary shown for four reference satellites, recorded over approximately a time period of five hours on 17 January 2016. (b) Corresponding refracted elevation in dry snow of those four satellites.

The minimum of the carrier phase residuals is reached when the satellites reach their maximum elevation angle. The residuals of satellites serving as reference satellite are equal to zero due to the DD approach, and residuals of satellites, which have temporally even a higher elevation than the reference satellite, show negative values. An example is given in Figure 4.4 for a time period of approximately five hours for the passing of four reference satellites and their corresponding refracted elevation angles over the un-refracted mask of 25 degrees corresponding to a refracted angle of approximately 44.2 degrees. Each change of the reference satellite is indicated with a black dashed line. We require a minimum of 60 degrees for the un-refracted signal (corresponding to an elevation of approximately 67.4 degrees for the refracted signal) of a satellite to be chosen as reference satellite. Once a satellite falls below this minimum elevation, the satellite with the highest elevation is chosen as new reference satellite.

4.3.5 Filtering of snow parameter estimate

The accuracy of the least-squares snow parameter estimate can be obtained from Equation (4.23) as

$$\sigma_{\check{d}_{s(t_n)}} = \frac{1}{\sqrt{m^{\mathrm{T}}(t_n)\Sigma^{-1}(t_n)m(t_n)}}, \tag{4.29}$$

and simplifies for a single double difference measurement to

$$\sigma_{\check{d}_{s(t_n)}} = \frac{1}{\gamma m^{kl}} \cdot \sigma_{\varphi}. \tag{4.30}$$

This standard deviation of the snow parameter depends on the following factors:

- accuracy of DD carrier phase measurements ($\sigma_{\varphi} \leq 1$ cm)
- difference of mapping functions m^{kl}
- speed correction factor $\gamma = \frac{c_0}{v_s} - 1 \approx 0.3$

Figure 4.5 shows the scaling of the noise standard deviation. The scaling is lowest if the difference between the elevation of a satellite and the elevation of the reference satellite reaches its maximum. In this case, the scaling factor varies between 5 and 10 depending on the elevation of the reference satellite.

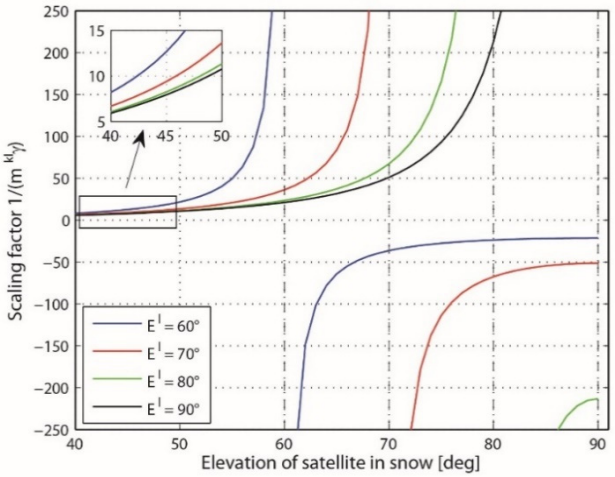

Figure 4.5: Snow parameter determination: scaling of phase noise by mapping function and speed correction factor.

The scaling factor quickly increases with smaller elevation differences between the considered satellite and the reference satellite. This large scaling factor makes the single-epoch snow parameter estimate very noisy and requires some filtering.

The fixed phase measurements can be described by some arcs parametrized by the snow parameter and mapping function. We can obtain such fitted arcs by least-squares estimation of the snow parameter based on given fixed phase measurements and mapping functions. As the phase measurements of some satellites might be corrupted by receiver tracking errors or azimuthal inhomogeneities in the snow cover, we perform the fitting for each satellite separately, i.e.

$$\lambda\check{\tilde{\varphi}}^{kl}_{12,\mathrm{fitted}} = \gamma\tilde{m}^{kl} \cdot \arg\min_{d_s} \left\| \lambda\check{\tilde{\varphi}}^{kl}_{12} - \gamma\tilde{m}^{kl} \cdot d_s \right\|^2 = \gamma\tilde{m}^{kl} \cdot \frac{1}{\gamma(\tilde{m}^{kl})^{\mathrm{T}}\tilde{m}^{kl}} (\tilde{m}^{kl})^{\mathrm{T}} \lambda\check{\tilde{\varphi}}^{kl}_{12}, \tag{4.31}$$

with the stacked fixed phase measurements of epochs t_1 and t_n

$$\lambda\check{\tilde{\varphi}}^{kl}_{12} = \begin{pmatrix} \lambda\left(\tilde{\varphi}^{kl}_{12}(t_1) - \check{\tilde{N}}^{kl}_{12}\right) \\ \vdots \\ \lambda\left(\tilde{\varphi}^{kl}_{12}(t_n) - \check{\tilde{N}}^{kl}_{12}\right) \end{pmatrix}, \tag{4.32}$$

and the stacked mapping functions

$$\tilde{m}^{kl} = \begin{pmatrix} m^{kl}(t_1) \\ \vdots \\ m^{kl}(t_n) \end{pmatrix}. \tag{4.33}$$

We use only the satellites with a good agreement of the fixed phase measurements and fitted arcs, i.e.

$$\sum_{j=1}^{n} \left\| \lambda \breve{\varphi}_{12}^{kl}(t_j) - \lambda \breve{\varphi}_{12,\text{fitted}}^{kl}(t_j) \right\|^2 \leq \chi^2, \tag{4.34}$$

with χ^2 being an upper bound on the sum of squared residuals. Additionally to the fixed phase residuals, Figure 4.3 shows the arcs for each satellite in black for days with snow cover as well as Figure 4.4 in detail for a few hours. The fitted arcs based on raw residuals and mapping functions assume a constant snow parameter for SWE derivation.

The accuracy of the snow parameter can be further improved by a *joint* consideration of the fitted arcs from the satellites with good fitting. Therefore, we replace the "raw" measurements in Equation (4.23) by the fitted arcs and consider only the subset of satellites with sufficiently accurate arc fitting, i.e.

$$\breve{d}_{\text{s,fitted}}(t_n) = \frac{1}{m_s^{\text{T}}(t_n)\sum_s^{-1}(t_n)m_s(t_n)} \cdot m_s^{\text{T}}(t_n)\sum_s^{-1}(t_n) \cdot \begin{pmatrix} \lambda \breve{\varphi}_{12,\text{fitted}}^{1l}(t_n) \\ \vdots \\ \lambda \breve{\varphi}_{12,\text{fitted}}^{Kl}(t_n) \end{pmatrix}, \tag{4.35}$$

where the lower index s denotes the subset of satellites with sufficiently small sum of squared residuals.

Finally, $\breve{d}_{\text{s,fitted}}(t_n)$ is low pass filtered to reduce jumps in case of lost or newly tracked satellites. Thus, the final snow parameter estimate is given by

$$\overline{\breve{d}}_{\text{s,fitted}}(t_n) = \frac{1}{\tau}\breve{d}_{\text{s,fitted}}(t_n) + \left(1 - \frac{1}{\tau}\right)\breve{d}_{\text{s,fitted}}(t_{n-1}), \tag{4.36}$$

with τ being the time constant of the low-pass filter. For this approach, τ was set to 4 hours.

4.3.6 Calculation of SWE

In a final step, we calculated SWE by multiplying the speed correction factor with the filtered snow parameter, expressing the *virtual* snow height, which is proportional to the time delay of the GNSS signals through the dry snowpack, by

$$\text{SWE}(t_n) = \gamma \cdot \overline{\breve{d}}_{\text{s,fitted}}(t_n) \cdot 1000 \text{ [mm w. e.]}. \tag{4.37}$$

4.4 Results and Discussion

We applied this approach for our GNSS measurement setup at the test site Weissfluhjoch for the entire dry-snow season from 1 October 2015 to 1 April 2016. After the latter date, the first significant wetting of the snowpack occurred and the snowpack was not considered as dry any more. The test site is equipped with numerous meteorological and snow sensors [*Schmid et al.*, 2015; *Marty and Meister*, 2012]. We compared our measurements to SWE data recorded with a snow pillow and to manual measurements from weekly to bi-weekly snow profiles. The temporal resolution of the GNSS output data was reduced to one SWE value per 30 minutes to be temporally comparable with the continuous SWE in situ reference measurements taken in parallel with the snow pillow. The snowpillow and the GNSS system ran continuously without any breakdown.

Figure 4.6 shows in dark blue the evolution of the GNSS-derived SWE and in light blue the SWE measured by the snow pillow. The weekly to bi-weekly manual snow profile measurements are indicated with magenta stars.

The distance between the GNSS measurements and the snow pillow is 20 m [*Schmid et al.*, 2015]. The snow profiles including the manual measurements were performed in the vicinity of the two continuous measurements. In general, all three SWE measurements provide similar results. The continuous recordings of the snow pillow and GNSS show a very similar temporal evolution and similar absolute values. Small deviations between these two measurement methods might be due to small scale spatial variability caused by slightly different precipitation amounts and/or wind conditions, even though they are located close to each other at the same test site. The manual SWE measurements fit well with the values obtained with the two continuous measurement methods. However, in general, the manually measured values are slightly lower than the continuous measurements, which might also be related to small scale spatially variable snow properties at the test site. On some days, the agreement is better than on others. The reason for the observed difference in agreement might be related to the fact that the profile location varied in the course of the winter, being sometimes closer to the location of the continuous measurements, sometimes further away.

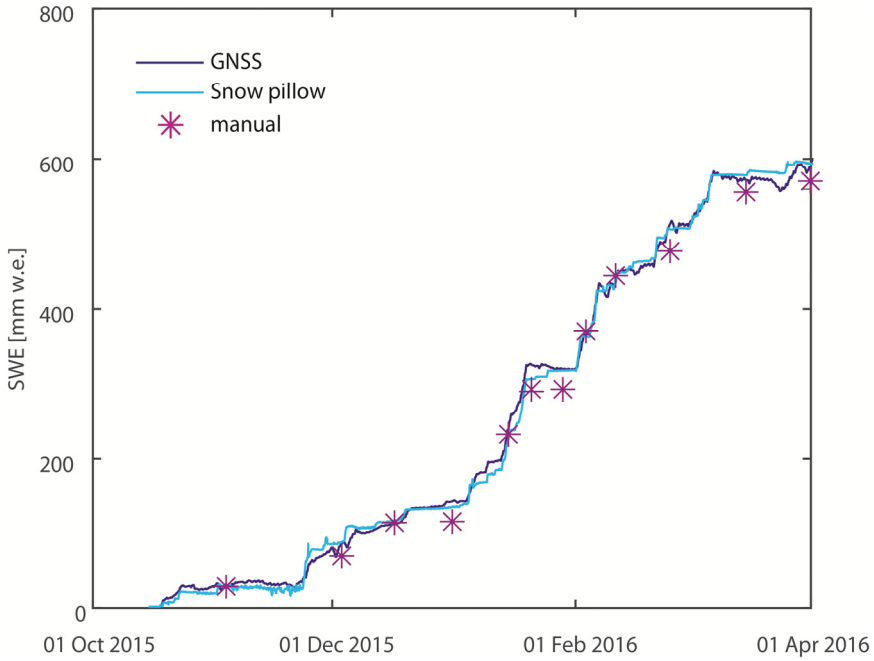

Figure 4.6: Snow water equivalent derived by GNSS carrier phase residuals compared to measurements recorded with a snow pillow and to manual snow pit measurements; all data from the test site Weissfluhjoch during the dry-snow season 2015-2016.

Table 4.1 summarizes the statistics for the comparison of the three SWE measurement methods. The methods show high agreement indicated by values of R^2 and Nash-Sutcliff-Efficiency Index (NSE) [*Nash and Sutcliffe*, 1970] close to 1. Regarding the root mean square error (RMSE), the two continuous measurements GNSS and snow pillow fit best; the RMSE is very low, approximately 11 mm. The RMSE between manual measurements and GNSS or snow pillow measurements is, in both cases about 23 to 24 mm, low as well. The high degree of agreement between the methods is also shown by the regression lines in Figure 4.7. GNSS-derived and snow pillow data are very close to the 1:1 line.

Table 4.1: Statistics overview of the comparison of SWE derived by GNSS and measured by snow pillow and weekly to bi-weekly manually measured in snow pits at the test site Weissfluhjoch for the dry-snow winter period 2015-2016.

	R^2	NSI	RMSE [mm]
GNSS – Snow pillow	0.999	0.998	10.6
GNSS - manual	0.995	0.986	23.4
Snow pillow - manual	0.997	0.985	24.0

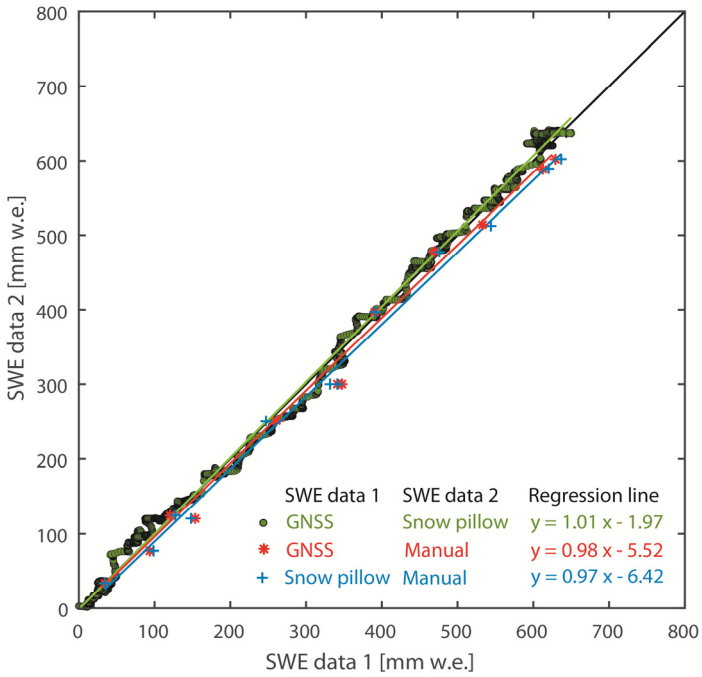

Figure 4.7: Linear regression between in each case two of the three SWE methods GNSS, snow pillow and manual. Black solid line indicates 1:1 line.

With this GNSS method it is possible to continuously and non-destructively derive SWE for dry-snow conditions. Important advantages of our GNSS approach, especially compared to snow pillow measurements, are that only low-cost GNSS sensors are used and that they only need little space for installation, whereas snow pillows are expensive and consist of 3 metres diameter bladder containing approximately 800 liters of an antifreeze solution, which needs to be installed with concrete at a flat area. Moreover, the heat-flux between the snow pillow surface might not be adequate to the heat-flux of the soil and the bottom of the snowpack [*Johnson and Schaefer*, 2002], and as already mentioned, the snow pillow measurements are potentially prone to errors due to bridging effects in the snowpack, especially during the transition of dry- to wet-snow conditions [*Johnson and Marks*, 2005]. In contrast, the GNSS system is not affected by disturbing heat fluxes or bridging effects as the signals travel non-destructively through the snow. However, as we only considered dry snow during the observed time period, no bridging effects at the snow pillow occurred. Regarding manual snow pit measurements in snow profiles, they represent the most reliable conventional method up to now, but are destructive and performed (bi-)weekly at best. In summary, our results of GNSS-derived values of SWE suggest that with this novel method it is possible to determine SWE with high accuracy and at low costs.

In general, the following points have to be considered for obtaining highly precise GNSS-derived values of SWE. First, it is important to very accurately determine the baseline between the two GNSS antennas with our RTK model under snow-free conditions. An error in distance between the antennas of only 2.5 cm would lead to an error in SWE of approx. 50 mm. Therefore, it is very important to accurately process the carrier phase data also under snow-free conditions and to filter the baseline estimate to reduce phase noise and multipath. Moreover, it is important to tightly tense the pole with the upper antenna, e.g. with ropes, so that it cannot be markedly affected by vibrations or positional changes, e.g. due to wind effects. However, if a slight shift of one antenna occurs, it is possible to re-estimate the baseline using RTK. Second, at least two GNSS satellites have to be received at both antennas. Both satellites should be above an elevation angle of 25 degrees, to exclude errors and multipath problems potentially occurring at low elevation angles. Furthermore, the highest satellite should be above an elevation angle of 60 degrees to serve as reference satellite. This is actually guaranteed on every

place on Earth at any time due to the global GNSS satellite constellations, except the receivers are situated in extremely deep and steep valleys.

Finally, this study was performed during dry-snow conditions when stable GNSS carrier phase processing is possible and provides, as shown above, highly accurate SWE values. The phase processing during wet-snow conditions is currently under development. Phase processing becomes increasingly difficult during wet-snow conditions as signal attenuation increases markedly with increasing liquid water content [*Koch et al*., 2014]. GNSS signal strength information as already applied in *Koch et al*., [2014] and *Schmid et al*., [2015] would have to be additionally considered in an integrated GNSS carrier phase and signal strength algorithm. However, this issue is beyond the scope of the study presented here, but will be considered in our future work.

4.5 Conclusions

Snow water equivalent (SWE) was continuously derived for dry-snow conditions solely based on carrier phase measurements of Global Navigation Satellite System (GNSS) receivers. Two static GNSS receivers were used to determine double differenced (DD) GNSS carrier phase measurements. A precise snow-specific model was developed for these DD measurements, which takes the delay of GNSS signals in snow due to the reduced signal propagation speed and the refraction processes, as well as the relative position between both GNSS antennas using Real Time Kinematic (RTK) positioning, and the carrier phase integer ambiguities into account. The carrier phase integer ambiguities and SWE were jointly estimated using an integer least-squares estimator. After ambiguity fixing, we analyzed the fixed phase residuals that depend on snow, phase noise and multipath. The snow-dependent part is proportional to SWE and an elevation-dependent mapping function. We applied a low-pass filter to reduce phase noise and multipath and, thereby, to improve the accuracy of SWE.

The proposed method was tested with two low-cost GPS receivers installed at the high Alpine test site at Weissfluhjoch in Switzerland during the dry-snow winter season 2015-16. The SWE measurements of a snow pillow with a temporal resolution of 30 minutes served as continuous reference. Our GNSS-derived SWE data show a high degree of agreement in absolute values and temporal evolution with this reference. The weekly to bi-weekly performed manual SWE measurements in snow pits also agree well with our GNSS-derived values.

Advantage of the proposed method are e.g. that it does not require manual measurements, is globally applicable and it does not disrupt the snow cover. The reliability of integer ambiguity fixing and the accuracy of SWE can be further improved by using multi-GNSS instead of GPS-only measurements, i.e. by additionally including Galileo, GLONASS and/or Beidou measurements. The use of low-cost sensors is sufficient, which enables dense sensor networks. Thereby, snow information with high spatial and temporal resolution can be derived for entire river basins allowing for more accurate runoff and flood prediction. The global availability of GNSS signals enables measurements also in remote locations where conventional measurements are scarce. In many regions, especially in high mountain regions and the large areas of the Tundra, Taiga and Arctic, it is very valuable to gain information on the snow accumulated during the entire dry-snow winter period. Currently, our setup is installed at various remote test sites in Newfoundland involving first demo users within the scope of the ARTES-IAP Demo Project SnowSense.

Acknowledgements

P.H., F.K. and F.A. are co-funded by the European Space Agency (ESA, 4000113149/14/NL/AD) within the ARTES-IAP Demo Project SnowSense (https://artes-apps.esa.int/projects/snowsense-dp), which is gratefully acknowledged. The authors would like to thank several staff members of the WSL Institute for Snow and Avalanche Research SLF who performed the manual snow profile measurements at the test site Weissfluhjoch.

5. SOIL MOISTURE RETRIEVAL BASED ON GPS SIGNAL STRENGTH ATTENUATION

This chapter is published in the journal ***Water***:

Koch, F., Schlenz, F., Prasch, M., Appel, F., Ruf, T. and Mauser W. (2016): Soil moisture retrieval based on GPS signal strength attenuation, Water, 8(7), 276; doi: 10.3390/w8070276.

Abstract

Soil moisture (SM) is a highly relevant variable for agriculture, the emergence of floods and a key variable in the global energy and water cycle. In the last years, several satellite missions have been launched especially to derive large-scale products of the SM dynamics on the Earth. However, in situ validation data are often scarce. We developed a new method to retrieve SM of bare soil from measurements of low-cost GPS (Global Positioning System) sensors that receive the freely available GPS L1-band signals. The experimental setup of three GPS sensors was installed at a bare soil field at the German Weather Service (DWD) in Munich for almost 1.5 years. Two GPS antennas were installed within the soil column at a depth of 10 cm and one above the soil. SM was successfully retrieved based on GPS signal strength losses through the integral soil volume. The results show high agreement with measured and modelled SM validation data. Due to its non-destructive, cheap and low power setup, GPS sensor networks could also be used for potential applications in remote areas, aiming to serve as satellite validation data and to support the fields of agriculture, water supply, flood forecasting and climate change.

5.1 Introduction

Soil moisture (SM) is a measure for the quantity of water contained in the soil. It is one of the most relevant variables for plant growth, e.g., in agriculture or for the emergence of floods and it is a key variable in the global energy and water cycle [*Dirmeyer*, 2000; *Jung et al.*, 2010; *Kerr et al.*, 2010]. As SM is largely coupled with the climate system and hydrological processes, knowledge of this variable is highly demanded for global and regional climate predictions to improve the simulation of the climate system [*Koster et al.*, 2004; *Seneviratne et al.*, 2010]. As such, it is of high importance as input for hydrological models as well as flood and drought monitoring [*Komma et al.*, 2008; *Loew et al.*, 2009a]. Especially in the top layer, SM conditions can change very quickly, e.g., due to intense precipitation and high solar radiation. Therefore, the soil of the upper few centimetres is of great importance and the decisive variable that controls the processes at the interface of air and soil processes like evaporation, surface runoff formation, as well as infiltration, percolation, capillary rise and water storage to give plants the opportunity for water uptake [*Jung et al.*, 2010; *Koster et al.*, 2004]. For plant growth, the root-zone SM is of high importance. It is linked to surface SM with a temporal delay. However, until now it is still difficult to measure surface SM accurately. As climate and hydrological model approaches make use of information on the soil, an improvement in SM monitoring can help to reduce uncertainties in the

simulation of climate change forecasting, extreme events, ecosystems as well as agriculture and food production [*Fischer et al.*, 2007; *A Loew et al.*, 2009b; *Mauser et al.*, 2015; *Seneviratne et al.*, 2010].

In the last decades, active and passive microwave remote sensing techniques have been developed and were applied successfully for SM monitoring on different scales [*Dobson and Ulaby*, 1986; *Loew et al.*, 2006; *Mauser et al.*, 1995; *Njoku et al.*, 2003; *Ulaby et al.*, 1996; *Ulaby et al.*, 2014; *Wagner et al.*, 2007]. In 2009, the Soil Moisture and Ocean Salinity (SMOS) satellite operated by ESA was launched [*Barré et al*., 2008; *Kerr et al*., 2010], and in January 2015, the Soil Moisture Active Passive (SMAP) satellite operated by NASA was launched [*Entekhabi et al*., 2010]. Both missions operate in the microwave L-band, which is most suitable for SM observations [*Kerr et al.*, 2001; *Ulaby et al.*, 1996]. Moreover, first SM retrievals have been carried out by GNSS (Global Navigation Satellite System) reflectometry approaches [*Chew et al.*, 2015; *Katzberg et al.*, 2006; *Larson et al.*, 2008; *Privette III et al.*, 2016; *Rodriguez-Alvarez et al.*, 2009; *Rodriguez-Alvarez et al.*, 2011; *Zavorotny et al.*, 2010], which analyse GNSS signals reflected from the soil. Depending on the moisture content in the soil, the reflected pattern changes, which is in principle quite similar to active microwave remote sensing. All of these remote sensing methods measure the surface SM as an integral of the SM in the upper centimetres of the soil.

Satellite SM products are validated in most cases with in situ measurements in a continuous mode or manually during field campaigns at different test sites by different research teams. As reference, in situ time domain reflectometry (TDR) or frequency domain (FD) probes and gravimetric measurements are used as well as model approaches [*Bircher et al.*, 2012; *Dall'Amico et al.*, 2012; *De Rosnay et al.*, 2006; *Delwart et al.*, 2008; *Jackson et al.*, 2011; *Panciera et al.*, 2008; *Rötzer et al.*, 2014]. A comprehensive overview on in situ SM measurements from many different networks around the globe can be obtained in the International Soil Moisture Network (ISMN) [*Dorigo et al.*, 2011]. However, the validation sensors, which measure continuously, are typically installed at a certain soil depth and mostly measure the SM only at this certain soil depth without obtaining information from the interface of air and soil. Of course, the general trend in SM can be covered like this; however, the high dynamics directly at the soil surface that can in principle be captured by satellites might be underrepresented in the measurements with these methods.

To overcome these limitations and as validation data are still scarce, we investigated a new dielectric non-destructive in situ measurement technique that is able to continuously track the bulk SM of the upper ten centimetres of the first soil layer. This approach is based on L1-band GPS signal strength changes due to changes in the permittivity of the soil, which are highly correlated with changes in the water content within the soil. As the GPS signals are broadcasted via L-band, the physical processes are comparable to passive L-band microwave remote sensing, e.g., with the SMOS mission [*Wigneron et al.*, 2007]. To be independent of vegetation influences on the GPS signals, this approach was tested on a bare soil field. In general, this GPS measurement setup and its technical background are quite similar to the retrieval of liquid water content in snow based on GPS signal strength changes that we described and validated in *Koch et al.* [2014] and *Schmid et al.* [2015]. The methodology of the low-cost GPS hardware on hydrological measurements was therefore already successfully applied in these studies.

The aim of this study is to describe how this new method can be used to derive continuous SM data from GPS signal strength losses in the L-band microwave domain and to validate them. In *Section 5.2*, we provide an overview of the low-cost GPS measurement setup at the German Weather Service (DWD) in Munich and describe the accompanying in situ SM data measured by different sensors in bare soil. As the applied FD sensors and gravimetric probes measured the SM only at a certain depth, we used the PROcesses of Mass and Energy Transfer (PROMET) model [*Mauser and Bach*, 2009] to simulate the integrated SM for the upper soil layer that is measured by the GPS sensors. In *Section 5.3*, the GPS algorithm to retrieve SM is described. The bulk SM of a soil column is based on the GPS signal strength attenuation and is related to the complex permittivity, which is described with the Dobson four-component dielectric mixing model [*Dobson et al.*, 1985]. In *Section 5.4*, SM

data derived from the different methods are presented and compared for a time period of almost 1.5 years (1 January 2014–10 June 2015) encompassing wet and dry soil periods. The conformities and discrepancies of all methods and the advantages and limitations of the GPS approach are discussed in *Section 5.5*, where we also present results from a small analysis to assess the sensitivity of the new method according to selected soil parameters. *Section 5.6* provides the conclusion.

5.2 Measurement setup and data

5.2.1 GPS measurements at the DWD test site Munich

The test site for the GPS SM measurements is situated at the meteorological observation site of the German Weather Service (DWD) in the city of Munich (48°16'43" N, 11°32'37'' E, 518 m a.s.l.) in Southern Germany. It is well equipped with all standard meteorological measurement instruments. The DWD test site is characterized by a temperate and humid climate of Central Europe with monthly average temperatures ranging from -2°C in winter to 17°C in summer. The mean annual precipitation in Munich reaches 930 mm with a summer precipitation peak [*Mauser and Prasch*, 2015]. Snow cover typically lasts for several weeks in winter, but with a decreasing trend in coverage duration and amount due to climate change [*Koch et al.*, 2011b; *Weber et al.*, 2010].

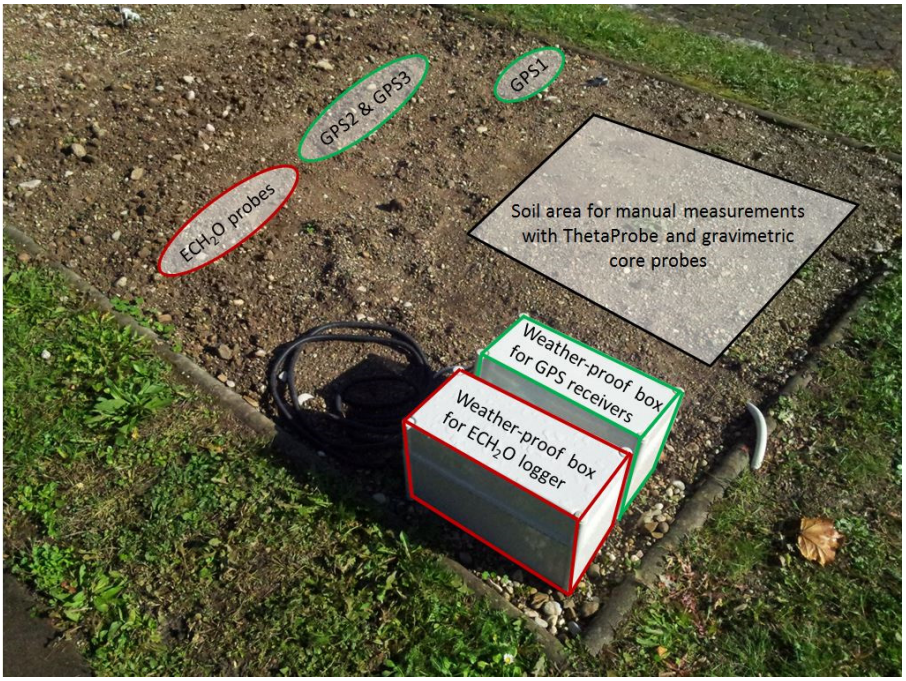

Figure 5.1: Soil measurement field at the DWD test site Munich. The locations of GPS1, GPS2 and GPS3 as well as the locations of the other soil moisture measurements (ECH_2O, ThetaProbe and gravimetric core probes) are marked.

The soil of the DWD soil measurement field was classified according to a laboratory soil texture analysis as sandy loam. The average sand and clay content at 10 cm depth are 49% and 7%, respectively. The bulk soil density ρ_b is 1.3 $g \cdot cm^{-3}$. As the test site is situated in the Munich gravel plain north of the Northern Calcareous Alps, limestone is the dominant rock type leading to chromic luvisols. The groundwater table in this region is lower than 2.5 m below the surface and due to the low clay content, capillary rise plays a negligible role.

The DWD test site Munich is suitable for soil measurements by GPS. Within a radius of approximately 20 m, the test site is free from surrounding obstacles like houses or trees and allows relatively undisturbed GPS measurements for a city location. We installed three low-cost GPS sensors at the vegetation-free DWD soil measurement field (see Figure 5.1). One sensor (GPS1) was mounted directly on top of the soil and the other two

sensors (GPS2 and GPS3) were installed at a depth of 10 cm within the soil column and were displaced horizontally to avoid being obstructed by the top one. The reason why we installed two GPS sensors in the soil is for redundancy purposes because maintenance of buried sensors is difficult under running conditions and to verify their high correlation, as stated in *Section 5.3.2*.

The measurement period was from 1 January 2014 to 10 June 2015. Apart from a system failure another two days close to the end of the measurement period (27–29 April 2015) due to power failure another two days close to the end of the measurement period (27–29 April 2015) due to power failure and a delayed reset, the GPS sensors operated without interruption in a continuous mode. However, days with snow cover and frozen soil were excluded from the analysis in this paper, as snow on top of the soil, especially when it turns wet [*Koch et al.*, 2014], and also soil frost, have a clear influence on the received GPS signal strength and can therefore influence the exact GPS SM retrieval. To avoid creeping temperature effects within the cables, a temperature threshold of 2 °C was chosen for the air as well as the soil temperature at a depth of 5 cm. In winter 2013/14, only very few days were affected by snow or soil frost; however, in winter 2014/15, there were longer snow periods where we excluded the entire winter months of December 2014 as well as January and February 2015 from this analysis.

Regarding the technical equipment, we used Fastrax IT430 GPS receivers [*Fastrax*, 2011] with integrated SiRF IV chips and stored them together with a temperature-robust and fan-less outdoor PC in a weather-proof box (see Figure 5.1). The receivers were connected via 3-m coax cables with small (3.9 cm × 3.9 cm) Hirschmann GPS7M magnetic mount antennas [*Hirschmann*, 2014]. The raw data were stored on the PC, which was driven by electric power provided by the test site. The GPS system was controlled and driven by receiver-specific GPS software. As we used low-cost GPS components, which are easily available and utilized for numerous technical applications like smartphones, cameras or car navigation, the hardware costs of one antenna and receiver pair are quite low, approximately 150 USD, excluding weather-proof boxes, data storage and power supply. Taking all components into account, the applied hardware might be in a similar price range as standard FD or TDR probes.

5.2.2 Accompanying in situ data

Besides the GPS sensors, we installed three ECH2O EC-5 and two ECH2O TM frequency domain (FD) probes (Decagon Devices, Pullman, WA, USA) to continuously measure SM at soil depths of 5 cm (three probes) and 10 cm (two probes). In the following, both sensor types will be named ECH2O probes. The measurement devices are located approximately 0.5 m apart from the buried GPS antennas within the same soil measurement field (see Figure 5.1). All ECH2O probes were installed horizontally with the prongs pointing in a horizontal direction. As suggested in *Bogena et al.* [2007], we applied a sensor-specific correction procedure based on ECH2O temperature readings to adjust the SM values for each time step. Due to battery failures, two data interruptions of the ECH2O sensors of a few days occurred (18–21 October 2014 and 1–3 March 2015). During field campaigns, which were conducted in a weekly to bi-weekly rhythm, we regularly measured surface SM with ThetaProbe ML2x FD probes (Delta-T Devices, U.K.) as well as standard manual gravimetric core probes. Further, we used hourly meteorological DWD data encompassing precipitation, air temperature and soil temperature at a depth of 5 cm as well as daily snow height data.

5.2.3 Land-surface model PROMET

The hydrologic land-surface PROcesses of Mass and Energy Transfer (PROMET) model is physically based and describes all relevant water and energy fluxes [*Mauser and Schädlich*, 1998*; Mauser and Bach*, 2009; *Mauser et al*., 2015]. We modelled at a point scale and in an hourly resolution all relevant hydrological parameters for the DWD test site Munich. PROMET was driven by meteorological input data measured at the station and provided by the DWD. The output data, especially the SM, have successfully been validated within different studies, locations and at different scales [e.g., *Loew et al.*, 2006; *Mauser and Bach*, 2009; *Prasch et al.*, 2013; *Prasch et*

al., 2011; *Strasser and Mauser*, 2001]. The soil water dynamics in PROMET are simulated with a four-layer soil model applying an explicit solution of the Richards equation for flow in unsaturated media [*Philip*, 1957]. The soil water retention model of *Brooks and Corey* [1964] is used to relate soil suction head to SM content; a detailed description is given in *Mauser and Bach* [2009] and *Muerth and Mauser* [2012]. *Muerth* [2008] evaluated the soil temperature modelling abilities of PROMET in the Upper Danube Catchment with measurements and remote-sensing data. According to *Schlenz et al.* [2012b], modelled and measured SM data were compared extensively on different scales and locations in several large scale field campaigns around Munich between 2007 and 2012 and a detailed analysis of the SM modelling abilities and uncertainties of PROMET is given. The soil water model has been validated with good results, e.g., by *Loew et al.* [2006] and *Schlenz et al.* [2012b]. The model results were inter alia used to validate passive microwave remote sensing recordings from the SMOS mission [*Dall'Amico et al.*, 2012; *Loew and Schlenz*, 2011; *Schlenz et al.*, 2012a].

For this study, the soil layers were selected to be situated at 0–5, 5–10, 10–45 and 45–145 cm depths. PROMET reports on the vertical average of each selected soil layer. The soil model parameterization parameterisation was done according to the soil texture analysis in the laboratory. For all comparisons between modelled and measured SM, the first two PROMET soil layers were used, as these correspond to the 10 cm surface soil layer that is considered with the GPS measurements. From the model output, we used SM, percolation and evaporation information.

5.2.4 Soil moisture sampling volumes and vertical ranges of different methods

Currently, several in situ SM measurement methods exist at an operational level. However, they may differ in their results as they use different techniques, are based on different sampling volumes, may disturb the original soil column or are affected by air or fluid gaps around their prongs [*Walker et al.*, 2004]. Moreover, the results might be site specific and the sensor sensitivity might vary with the SM content [*Mittelbach et al.*, 2011].

In this study, we applied the four different measurement methods ECH2O, ThetaProbe, gravimetric measurement and GPS as well as the model PROMET to derive SM at the DWD test site in Munich. As they are all based on different techniques, vary in sample volume or cover different soil layers, their comparability is restricted. Figure 5.2a gives an overview on the vertical location and measurement range in the soil column with a depth of 10 cm.

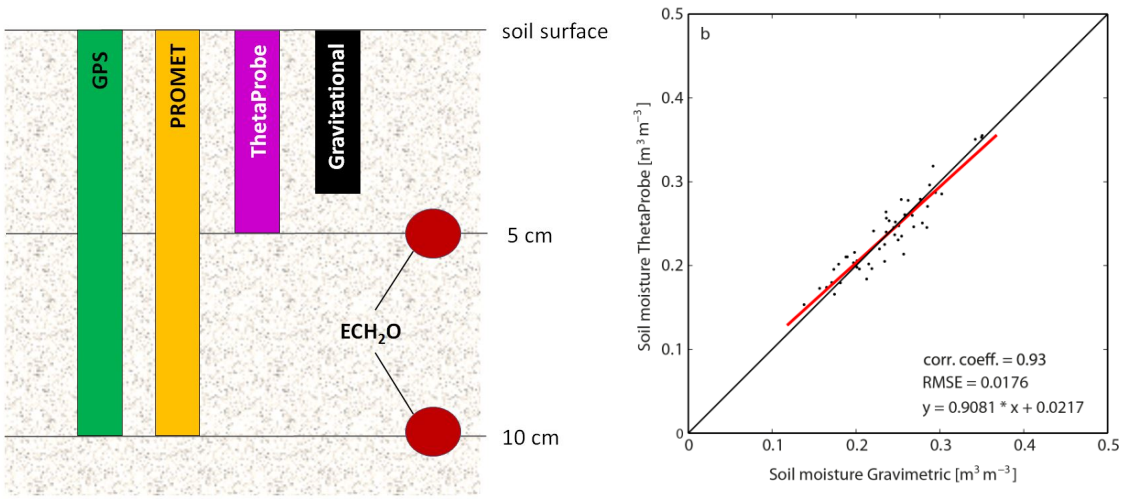

Figure 5.2: (a) Vertical location and measurements range in the soil column of the different methods to derive soil moisture. (b) Validation of ThetaProbe soil moisture readings by comparison with gravimetric measurements at the DWD test site Munich at numerous field campaigns during the measurement period January 1, 2014 - June 10, 2015.

The ECH_2O EC-5 and ECH_2O TM probes reach an estimated sampling volume of 10.5 cm^3 and of 15 cm^3, respectively [*Limsuwat et al.*, 2009]. As these sensors have a small sampling volume, they can only give valid information about the SM conditions in their direct vicinity, in this case at approximately 5 and 10 cm soil depth

as illustrated in the schematic in Figure 5.2a. The readings of the five ECH_2O sensors showed high conformity. The correlation of the sensors at a depth of 5 and 10 cm was high with a correlation coefficient of 0.96 and root mean square error (RMSE) of 0.0115 $m^{-3} \cdot m^{-3}$. In the following, the mean of all ECH_2O measurements was taken.

The prongs of the FD sensor ThetaProbe are 5 cm in length and they cover an approximate sampling volume of 50 cm^3, whereas the gravimetric measurements cover a standardized soil volume of 100 cm^3 with a sampling depth of 4 cm. Regarding the measurement depth and vertical location at the top of the soil column, ThetaProbe and the gravimetric measurements are the most similar. Therefore, we used the gravimetric measurements mainly to validate the ThetaProbe readings. As illustrated in Figure 5.2b, these two methods show high correlation with a correlation coefficient of 0.93 and a RMSE of 0.0176 $m^{-3} \cdot m^{-3}$. Therefore, further calibration of the ThetaProbe was not necessary.

The GPS technique encompasses a bulk soil column of 10 cm and is not directly comparable to the other three conventional measurement techniques. Due to the hemispherical GPS satellite coverage, the sensors capture on average a circular cone above the buried antennas. The volume of the circular cone above each antenna is variable as it depends on the SM content. Due to more pronounced refraction processes in wet soils, the path length for electromagnetic waves, especially those with oblique angles, is shortened [*Ulaby et al.*, 2014]. This may lead to a significant sampling volume reduction compared to dry soils. The volume with a GPS antenna installation depth of 10 cm and a cut-off elevation angle of 10 degrees encompasses approximately 665 cm^3 for absolutely dry soils and approximately 50 cm^3 for very wet soils, exemplarily calculated for a quite high SM content of 40 m^3 m^{-3} regarding the observed soil in this study.

The main advantage of the model PROMET is that it can calculate the SM of entire soil layers, which makes it more comparable to the GPS bulk measurements over an entire soil layer than, e.g., single ECH_2O SM measurements at specific soil depths. For this study, we used the SM modelled by PROMET from the first two layers, accounting for a soil depth of 10 cm, which is comparable to a vertical integral soil column considered by the GPS measurements.

5.3 Soil moisture derivation with GPS

5.3.1 GPS data processing

The GPS data processing to retrieve SM is quite analogous to the GPS data processing to retrieve liquid water content in snow, which was described in *Koch et al.* [2014]. In this section, we emphasise the main steps; for more details, consider *Koch et al.* [2014]. With the Fastrax IT 430 receivers, we tracked the GPS raw data of the freely available L1 C/A code at a temporal resolution of 1 s, which is broadcasd at a frequency of 1.57542 GHz. The GPS system encompasses in total 32 GPS satellites grouped in six orbits with an equatorial inclination of 55 degrees. Each satellite is seen by the DWD test site in Munich for several hours during a sidereal day (~23 h 56 min). For each time step, the hemispherical satellite coverage ranges between eight to twelve satellites. As all three GPS sensors are situated very close together, the pattern of the satellite trajectories for each sidereal day can be assumed identical.

The carrier-to-noise power density ratio (C/N_0) is included in the GPS raw data and gives information on the received signal strength of each tracked satellite [*Hofmann-Wellenhof et al.*, 2008]. In a first step, we extracted the C/N_0 received from each GPS satellite at a certain elevation and azimuth angle from the raw data for each time step. Signals below a satellite elevation of 10 degrees were masked out due to too weak signal strength and possible influences from the surrounding. As the received signal strength can vary at different azimuth and elevation angles, we defined 16 azimuth and 16 elevation classes for each of the 32 satellites according to *Koch et al.* [2014]. The reasons for this procedure are that the gain of the low-cost antennas is angle-dependant, the

signal strength might vary slightly for each satellite; furthermore, multipath patterns might occur. In a second step, we defined a sidereal reference day during dry and stable soil and atmospheric conditions. For this study, the UTC time period 13:26 16 June 2014–13:22 17 June 2014 was chosen. This period was characterized by stable and low SM conditions due to no rainfall, percolation, capillary rise and negligible condensation over the last seven days. We assume that during this reference period, the recorded C/N_0 values theoretically present the same signal strength [*Koch et al.*, 2014]; however, the recorded absolute values differ for different elevation and azimuth angles as described above. The measurement at GPS1, which is located above the soil column, corresponds to I_{m1} for each class (see Figure 5.3). To take the different azimuth and elevation patterns of each antenna into account, we scaled the reference data of GPS1 to the antenna characteristics of GPS2 and GPS3, respectively. In a last step, the measurements recorded within the soil column at GPS2 and GPS3 for each class and each time step, which correspond to $I_{m2,3}$, were set into relation to I_{m1} to calculate the signal attenuation as described in the next section. For the SM calculations, slight temporal fluctuations due to different atmospheric conditions have no decisive impact and can be neglected according to *Schmid et al.* [2015] as described for the retrieval of snow liquid water content.

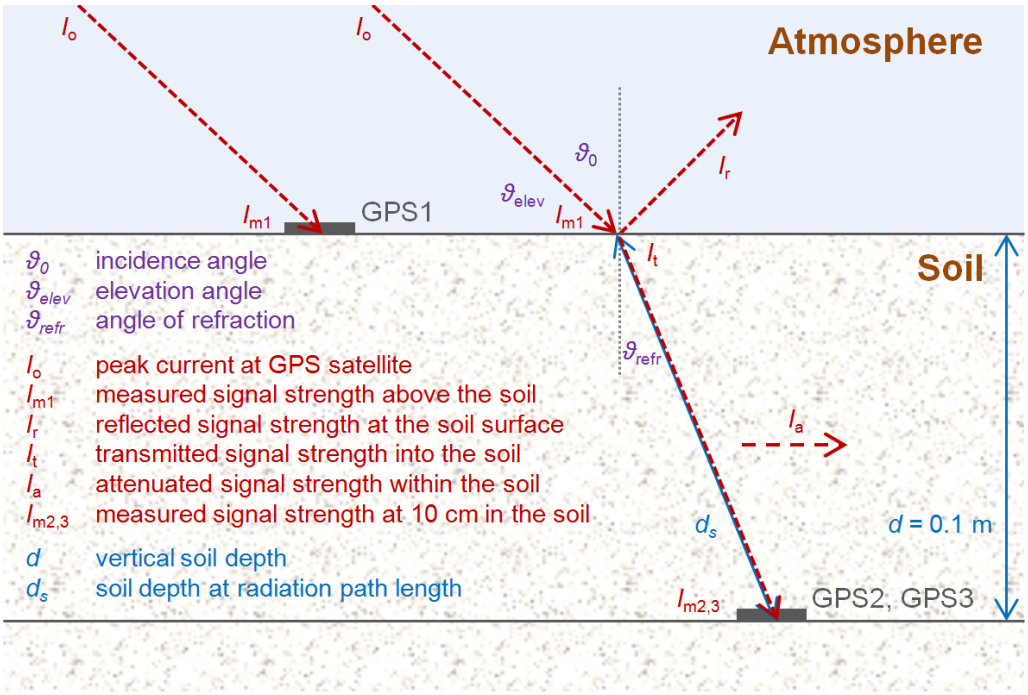

Figure 5.3: Overview of influences on the measured GPS intensity and radiation path length through the soil column, as well as the angle changes due to reflection, refraction and attenuation processes according to *Koch et al.* [2014]. Only the direct signal paths are shown for one satellite at a specific elevation (in red).

5.3.2 GPS signal strength attenuation

The calculation of the SM is based on signal strength changes according to dielectric soil properties in connection with electromagnetic waves. We considered reflection, refraction and attenuation processes quite analogous to *Koch et al.* [2014]. Instead of the input value snow depth, we used the installation depth of GPS2 and GPS3 at a soil depth of 10 cm. For this approach, we calculated the reflection and refraction for each single elevation value as already reported in *Schmid et al.* [2015], whereas in *Koch et al.* [2014], only the mean elevation angle was considered. The Equations (2.1)–(2.12) in *Koch et al.* [2014] were analogously applied for this study. However, instead of considering the complex permittivity of snow, for this approach, we considered the complex permittivity of soil, which is described in *Section 5.3.3*. The measured intensity $I_{m2,3}$ within the soil column as the mean of GPS2 and GPS3 at a soil depth d_s = 0.1 m is described by

$$I_{m2,3} = I_t - I_a = I_{m1} - I_r - I_a \tag{5.1}$$

where I_{m1} is the received intensity at GPS1 above the soil, I_t the transmitted intensity into the soil, I_a is the intensity loss due to signal attenuation within the soil, and I_r is the reflected intensity at the interface of air and soil. Figure 5.3 gives a schematic overview. The calculation of the reflection and refraction is analogous to *Koch et al.* [2014]. As the main outcome, the attenuation coefficient α is calculated by applying Beer-Lambert's law:

$$\alpha = -\frac{\ln(\frac{I_t - I_a}{I_t})}{d_s} = -\frac{\ln(\frac{I_{m2,3}}{I_{m1} - I_r})}{d_s} \tag{5.2}$$

The results for α from GPS2 and GPS3 achieved high agreement with a correlation coefficient of 0.94 and an RMSE of 0.0165 $m^{-3} \cdot m^{-3}$, which implies a high reliability of the two GPS sensors below the soil. However, slight differences might occur due to different soil textures above the single antennas. For the further data processing, the average of both antennas within the bulk soil column was taken. Multiple reflections above the soil, e.g., at small obstacles or surrounding vegetation, or within the observed soil column might occur. However, these effects are difficult or even impossible to address, and we assume that they are minor compared to the considered reflection, refraction and attenuation processes, especially considering such a flat site.

5.3.3 Dobson four-component dielectric mixing model

With dielectric models, the SM can be calculated for a specific soil based on its dielectric characteristics within a specific microwave domain. For this study we applied the Dobson four-component dielectric mixing model [*Dobson et al.*, 1985], which is based on the real ε' and imaginary part ε'' of the complex permittivity ($\varepsilon = \varepsilon' + i\,\varepsilon''$). It describes the behaviour of moist soils at frequencies between 1.4 and 18 GHz, which encompass the GPS L1-band frequency at f = 1.57542 GHz. Besides the four-component mixing model, a semi-empirical soil moisture mixing model is described in *Dobson et al.* [1985]. However, its performance for lower frequencies around 1.4 GHz is worse than the four-component dielectric mixing model [*Dobson et al.*, 1985]. It was therefore not applied in this study.

Wet soils consist of solid soil particles, air pockets and liquid water. The latter can be further divided into bound water, in a so-called Stern layer, and into bound water in a so-called Gouy layer; the former contains the first few molecular layers surrounding the soil particles; the latter is able to move in the soil medium [*Dobson et al.*, 1985]. Thereafter, the Dobson soil moisture model considers relative permittivities of the four components dry solids ε_{ds}, bound water ε_{bw}, bulk water ε_{fw} and air ε_a. The wet soil permittivity ε_{ws} is defined as

$$\varepsilon_{ws} = \frac{3\varepsilon_{ds} + 2V_{fw}(\varepsilon_{fw} - \varepsilon_{ds}) + 2V_{bw}(\varepsilon_{bw} - \varepsilon_{ds}) + 2V_a(\varepsilon_a - \varepsilon_{ds})}{3 + V_{fw}\left(\frac{\varepsilon_{ds}}{\varepsilon_{fw}} - 1\right) + V_{bw}\left(\frac{\varepsilon_{ds}}{\varepsilon_{bw}} - 1\right) + V_a\left(\frac{\varepsilon_{ds}}{\varepsilon_a} - 1\right)} \tag{5.3}$$

with V_{fw}, V_{bw} and V_a as the volume fractions of free water, bound water and air, which are dependent on the water content in the pores [*Dobson et al.*, 1985]. The entire bulk soil moisture m_v is given by

$$m_v = V_{fw} + V_{bw} \tag{5.4}$$

where V_{bw} makes up only a small part. It was calculated after *Dobson et al.* [1985] and was set to 0.191 for the soil observed in this study. The real part of the complex permittivity of dry soil ε'_{ds} is

$$\varepsilon'_{ds} = (1.01 + 0.44\rho_s)^2 - 0.062 \tag{5.5}$$

with ρ_s=2.65 $g \cdot cm^{-3}$ as the mean specific density of the soil paste [*Ulaby et al.*, 2014] whereas the measured bulk soil density ρ_b=1.3 $g \cdot cm^{-3}$. The imaginary part of dry soil is negligible. Values for ε_a, ε_{ds} and ε_{bw} are given in Table 5.1.

Table 5.1: Values for the real and imaginary part of the complex permittivity of air ε_a, dry soil ε_{ds} according to the soil properties of the observed soil and bound water ε_{bw} [*Dobson et al.*, 1985].

Permittivity of medium	real part ε'	imaginary part ε''
ε_a	1.00	0.00
ε_{ds}	2.44	~ 0.00
ε_{bw}	35.00	15.00

At a given frequency f, the complex permittivity of free bulk water ε_{fw} is assumed as a modified Debey-type relaxation [*Cole and Cole*, 1941; *Lane and Saxton*, 1952] and is due to the relaxation time of pure water τ_w and the static dielectric constant of water ε_{w0} dependent on the soil temperature. As the permittivity of wet soil is slightly temperature dependent, we took soil temperature data measured by the DWD into account. The real part is defined as

$$\varepsilon'_{fw} = \varepsilon_{w\infty} + \frac{\varepsilon_{w0} - \varepsilon_{w\infty}}{1 + (2\pi f \tau_w)^2} \tag{5.6}$$

with $\varepsilon_{w\infty}$ = 4.9 as the high frequency limit of the permittivity of water. For more information on the calculation of ε_{w0}, $\varepsilon_{w\infty}$ and τ_w, consider *Ulaby et al.* [2014] and *Lane and Saxton* [1952]. The imaginary part of the complex permittivity of free bound water is defined as

$$\varepsilon''_{fw} = \frac{2\pi f \tau_w (\varepsilon_{w0} - \varepsilon_{w\infty})}{1 + (2\pi f \tau_w)^2} + \frac{0.1\sigma_{m_v}}{2\pi\varepsilon_0 f} \tag{5.7}$$

where $\varepsilon_0 = 8.854 \times 10^{-12}$ is the permittivity of free space. It takes the effective conductivity of water σ_{m_v} [*Dobson et al.*, 1985; *Lane and Saxton*, 1952] into account, which is calculated by

$$\sigma_{m_v} = (\sigma_G + \sigma_s)\left(\frac{1 - \frac{\rho_b}{\rho_s} - \rho_b A_s d_\delta \times 10^{-4}}{m_v}\right) \tag{5.8}$$

where σ_G = 2.723 mS·cm^{-1} is the average conductivity in the Gouy layer, σ_s = 0.792 mS·cm^{-1} the conductivity of the soil paste, A_s = 49 m^2 g^{-1} the specific particle surface, which correlates with the clay content, and d_δ = 3 Å. These soil-specific values were derived by or were taken from literature [*Dobson et al.*, 1985] describing a very similar soil type with a low clay content of 8%.

Table 5.2 shows changes in the real and imaginary part of the complex permittivity of the free bulk water ε_{fw} due to different soil temperatures.

Table 5.2: Values for the real and imaginary part of the complex permittivity of free bulk water ε_{fw} at different soil temperatures.

Soil temperature	real part ε'	imaginary part ε''
0.1°C	85.57	23.81
10.0°C	82.76	19.42
20.0°C	79.47	16.55
30.0°C	76.12	14.75
40.0°C	72.95	13.61

5.3.4 Calculation of soil moisture and sensitivity

The attenuation coefficient α was described by Equation (5.2) in *Section 5.3.2*, based on GPS measurements. Moreover, the attenuation coefficient α of a medium like a wet soil can also be calculated in theory by the complex permittivity of wet soil with an emphasis on the imaginary part as:

$$\alpha = \sqrt{\frac{\mu_0}{\varepsilon'_{ws}\varepsilon_0}}\varepsilon''_{ws}\varepsilon_0 2\pi f \tag{5.9}$$

where ε'_{ws} and ε''_{ws} are calculated after Equation (5.3) considering the real and imaginary part. With a root-finding algorithm, we were able to set Equations (5.2) and (5.9) equal and could determine, as the only unknown of this approach, the soil moisture m_v under consideration of all soil specific reflection, refraction and attenuation processes for each time step. Potential temperature effects on the GPS sensors causing potential signal strength changes were not taken into account for this approach.

In general, the retrieval of SM with GPS depends on several physical soil parameters, which should be correctly investigated and determined to achieve precise results. However, to get an impression of how sensitive they are, we carried out a sensitivity analysis regarding the parameters soil density, soil texture and soil temperature. This aspect is described and discussed in *Section 5.5.3*.

5.4 Results

5.4.1 Time series of soil moisture and hydrological data

During a period of almost 1.5 years (1 January 2014–10 June 2015), the SM of the upper ten centimetres at the soil measurement field at the DWD test site in Munich was retrieved from GPS attenuation measurements and other methods (Figure 5.2a). Figure 5.4a gives an overview on the soil temperature at a soil depth of 5 cm and precipitation evolution in daily resolution, which was directly measured at the DWD test site in Munich for the entire period. Figure 5.4b illustrates the evolution of the SM derived by GPS, measured by the Decagon FD ECH_2O probes and modelled by PROMET in daily resolution. Moreover, the weekly to bi-weekly manual measurements with the Delta-T FD ThetaProbe and the gravimetric probe are shown. As described in *Section 5.2.1*, the entire winter months of December 2014 and January and February 2015 were excluded due to potential snow cover or soil frost. Moreover, percolation and soil evaporation modelled with PROMET are presented. Water infiltration into the soil and percolation are largely coupled with precipitation events. However, the daily percolation sums are lower than the daily precipitation sums as evaporation and direct surface runoff occur as well. On the one side, the evaporation rate depends on the available free water and on the other side, also on suitable temperatures. Regarding the investigated soil during the entire measuring period, capillary rise was negligible and the soil evaporation was low and was only pronounced when the temperatures were above approximately 10°C, indicating high solar radiation and when free soil water was available in the first soil layer, e.g., after a rainfall event.

In Figure 5.4a and 5.4b, regarding all methods, a direct relationship between SM increase and occurrence of percolation is obvious after precipitation events, when water infiltrated into the soil. This is especially the case after 1 July 2014. However, comparing the three continuous methods, the increase in SM of the ECH_2O probes is slightly lower, whereas for GPS more pronounced, PROMET is again in between. During periods with no or low percolation, SM declines slowly. Again, the GPS SM shows the clearest decline, followed by PROMET and then by the ECH_2O probes. The first six months of the measurement period (January–June 2014) were rather dry with only few light rainfall events. Consequently, as the temperatures started to rise in March 2014, SM declined especially in the upper four to five centimetres as the manual ThetaProbe and gravimetric measurements show.

Considerable dry periods occurred besides the first six months as well as in November 2014 and March to May 2015.

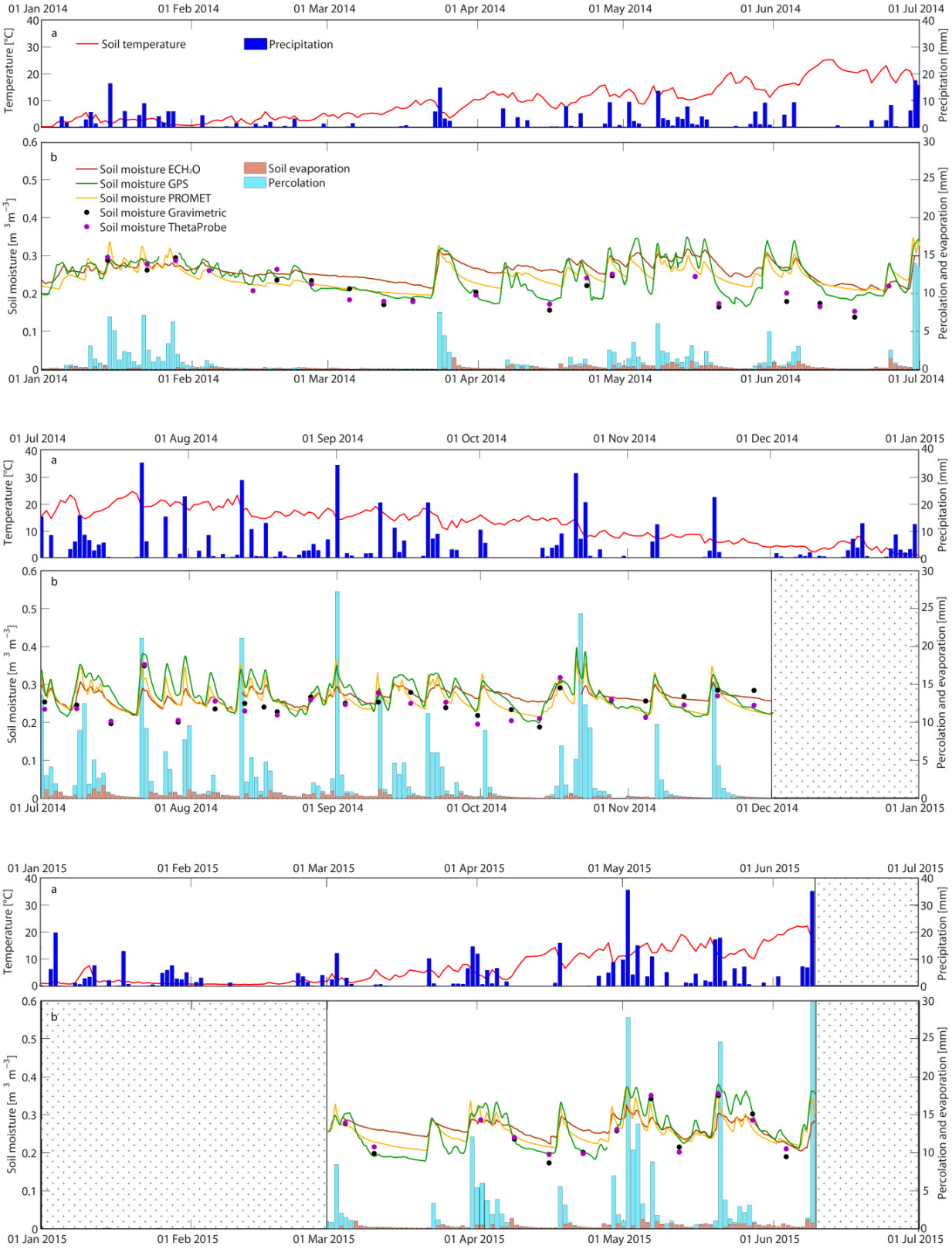

Figure 5.4: (a) Soil temperature at a soil depth of 5 cm and precipitation measured at the DWD test site Munich as well as (b) soil moisture measured by GPS, ECH_2O, ThetaProbe and gravitationally as well as modelled with PROMET at the DWD test site Munich during the measurement period January 1, 2014 - June 10, 2015. The winter time with potential snow cover and soil frost is excluded.

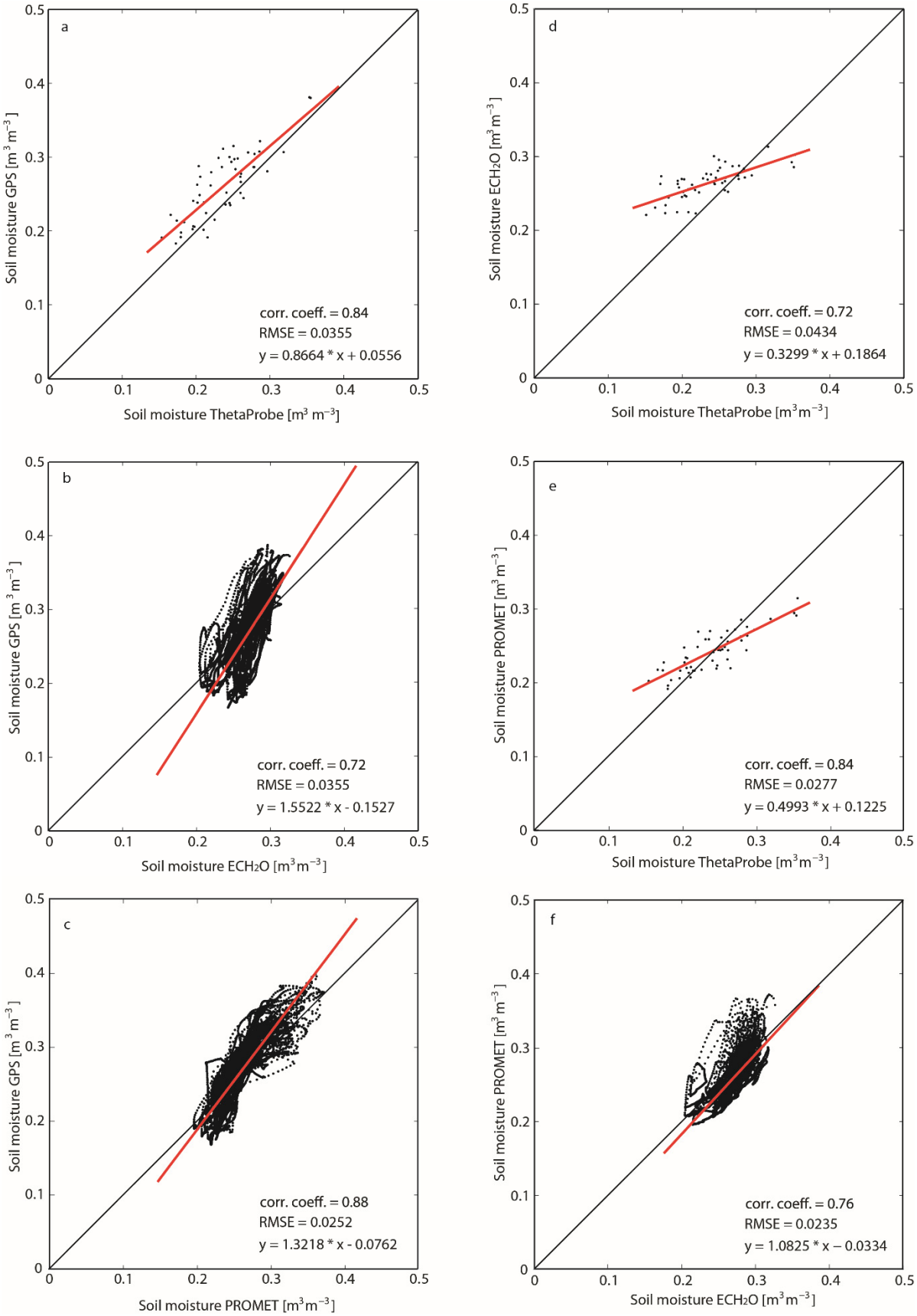

Figure 5.5: Comparison of soil moisture values (a) measured by ThetaProbe vs. measured by GPS, (b) measured by ECH_2O vs. measured by GPS, (c) modelled with PROMET vs. measured by GPS, (d) measured by ThetaProbe vs. measured by ECH_2O, (e) measured by ThetaProbe vs. modelled with PROMET and (f) measured by ECH_2O, vs. modelled with PROMET at the DWD test site Munich during the measurement period January 1, 2014 - June 10, 2015.

5.4.2 Comparison of the different soil moisture methods

During the entire period, the SM curves derived from the continuous measurements with GPS and ECH_2O probes as well as the modelled PROMET data show high conformity. The GPS SM exhibits the highest dynamic, whereas the ECH_2O SM reveals the lowest. PROMET is in between but mostly closer to the GPS SM. A statistical overview of the minimum, maximum, mean and standard deviation is given in Table 5.3 for all methods. The mean of the three continuous methods ECH_2O, GPS and PROMET is similar; however, the standard deviation is highest for the GPS values indicating a high dynamic range. The weekly to bi-weekly manual measurements with the ThetaProbe and gravimetric samples are mostly below the continuous methods, especially during dry periods. This is reflected in the lower mean and minimum values compared to the other methods. However, the two manual measurements exhibit a similar dynamic range to the GPS SM as shown in Table 5.3.

Table 5.3: Statistics overview of the soil moisture retrieval from GPS, ECH_2O, ThetaProbe and gravimetric samples as well as the modelled soil moisture with PROMET at the DWD test site Munich during the measurement period January 1, 2014 - June 10, 2015.

	mean	std	min	max
GPS	0.2565	0.0469	0.1667	0.3977
ECH_2O	0.2633	0.0216	0.2044	0.3268
PROMET	0.2522	0.0314	0.1892	0.3675
ThetaProbe	0.2382	0.0465	0.1535	0.3553
Gravimetric	0.2380	0.0482	0.1379	0.3507

Table 5.4: Statistics overview of the correlation coefficient and the RMSE comparing ThetaProbe, ECH_2O, PROMET and GPS. The upper triangular part (regular) represents the correlation coefficient and the lower triangular part (*italic*) represents the RMSE.

	ThetaProbe	ECH_2O	PROMET	GPS
ThetaProbe	-	0.72	0.84	0.84
ECH_2O	*0.0434*	-	0.76	0.72
PROMET	*0.0277*	*0.0235*	-	0.88
GPS	*0.0355*	*0.0355*	*0.0252*	-

As Figure 5.2 indicates, the manual surface SM measurements encompassing the gravimetric method and ThetaProbe show high correlation. As all comparisons with the gravimetric method and all other methods would show similar results compared to the ThetaProbe, they are therefore not explicitly shown as scatter plots in the following. The six scatter plots in Figure 5.5a–f as well as the correlation coefficient and the RMSE in Table 5.4 show all variants of comparisons between GPS, ECH_2O, PROMET and ThetaProbe SM.

Comparing GPS, ECH_2O and PROMET, the RMSE is clearly below 0.04 $m^{-3} \cdot m^{-3}$, which is considered as a very high agreement and is often the benchmark for SM retrievals from microwave remote sensing products, e.g., for the SMOS mission, and in situ measurements [*Kerr et al.*, 2001]. The same is true for comparisons of GPS and ThetaProbe SM. Only ThetaProbe SM values have a slightly higher RMSE than 0.04 $m^{-3} \cdot m^{-3}$ when compared to ECH_2O measurements Figure 5.5a shows a high conformity of the GPS measurements with ThetaProbe values; however, the positive offset of the diagonal indicates that the SM measurements undertaken with the ThetaProbe are mostly lower than those derived from the GPS. The difference between GPS and ECH_2O SM in Figure 5.5b is due to the lower dynamic range of the ECH_2O measurements. This can also be seen in Figure 5.5d by comparing ThetaProbe with ECH_2O. In Figure 5.5e, ThetaProbe has also a higher dynamic range compared to PROMET, which is, however, less so than for the comparison of ThetaProbe and ECH_2O in Figure 5.5d. Figure

5.5f gives an overview of the comparison of ECH_2O and PROMET. Especially for higher SM values, explicitly above 0.2 $m^{-3} \cdot m^{-3}$, PROMET is more dynamic than ECH_2O. GPS and PROMET reach the highest correlation with a correlation coefficient of 0.88 as shown in Figure 5.5c. The slight deviation is due to the higher dynamic range of the GPS SM measurements.

In Figure 5.6a–c, the scatterplots between GPS and the differences between GPS and ThetaProbe, GPS and ECH_2O, and GPS and PROMET are shown, which indicate a multiplicative bias between GPS and the other methods. Regarding the lower or higher SM values, the differences between all methods are most pronounced, especially comparing GPS and ECH_2O and lowest between GPS and ThetaProbe. Reaching higher SM values, PROMET shows a similar high dynamic range compared to GPS, which is indicated by the spreading of the points in the upper part of the scatter plot. Figure 5.6d–f contains scatterplots of the comparison of SM derived by GPS compared with the regression residuals between GPS and the other methods. As the correlation coefficient is lowest between GPS and the regression residuals of GPS and PROMET, indicating a random distribution, those two methods have the lowest systematic effect. Summarized, they show the highest coincidence of SM values.

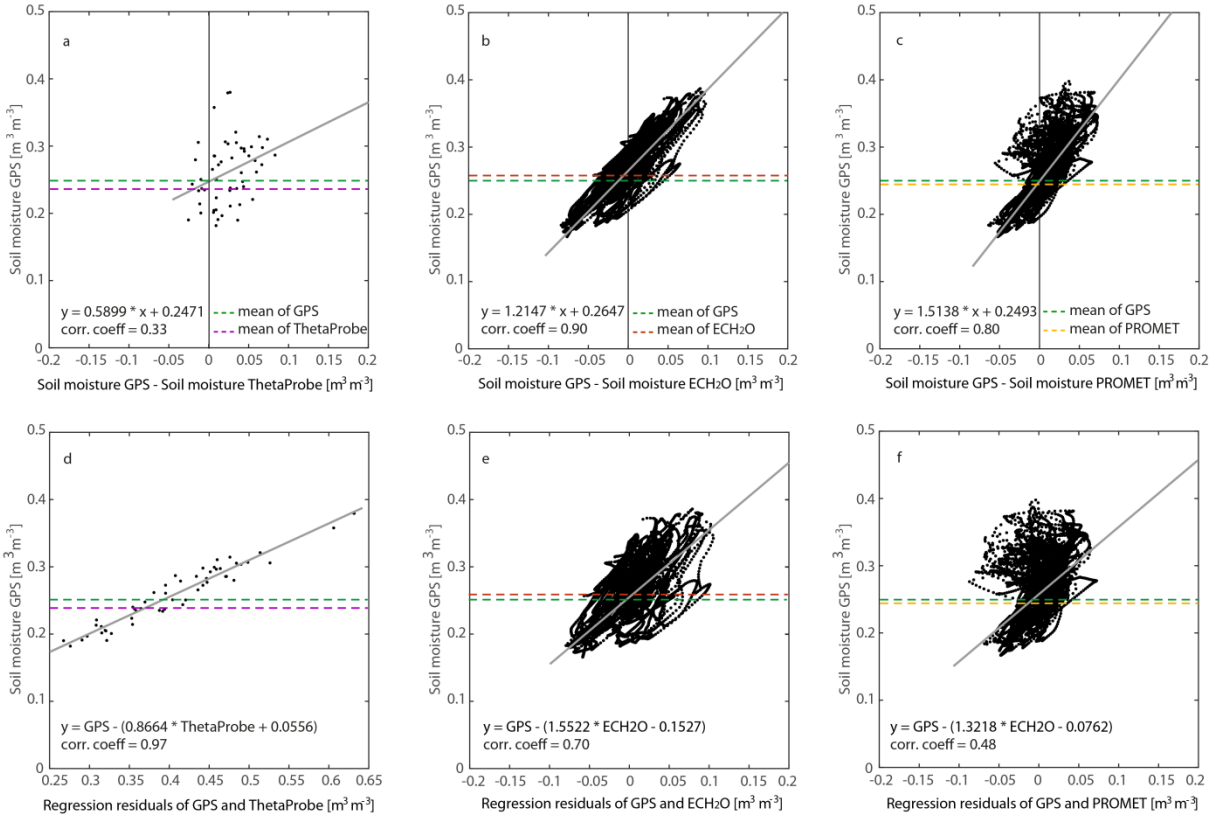

Figure 5.6: Comparison of soil moisture derived by GPS with the difference between (a) GPS and ThetaProbe, (b) GPS and ECH_2O, and (c) between GPS and PROMET as well as with the regression residuals between (d) GPS and ThetaProbe, (e) GPS and ECH_2O, and (f) between GPS and PROMET. The linear regression equations to calculate the residuals for each method compared to GPS were taken from the information given in Figure 5.5(a)-(c), respectively.

5.5 Discussion

5.5.1 Conformities and discrepancies between the different soil moisture methods

We derived SM data at the DWD test site in Munich using two continuous measurement methods; firstly, by GPS sensors, which were investigated for the first time and secondly by FD ECH_2O probes. Further, we manually measured surface SM with FD ThetaProbes and gravimetric probes in a weekly to bi-weekly basis. Moreover, we continuously modelled SM by PROMET.

The agreement of all results from the different methods is high, and all data follow the overall course of dry and wet events during the observation period of almost 1.5 years. The increase in SM after the occurrence of precipitation events with infiltration into the soil as well as long dry periods are covered by all methods. However, as described in *Section 5.2.4*, the comparability of these methods is limited due to different sampling volumes and different vertical validity ranges within the soil column. According to the results, differences in the SM readings regarding the different methods can be explained by differences in the SM conditions in the upper 10 cm. For a better understanding, the described bulk soil column of 10 cm can be divided into two layers, firstly in approximately the first 5 cm as the direct air and soil interface and secondly in a slightly deeper layer of 5 to 10 cm soil depth.

The gravimetric and ThetaProbe measurements are taken in the uppermost 4 to 5 cm. It is apparent that during dry periods, this layer dries out more than the 5 to 10 cm layer, as the latter is covered by the surrounding soil particles and has no direct exchange with the atmosphere. In the findings, it can be clearly seen that the two manual methods reach the lowest SM values compared to all other methods during these dry periods (see Figure 5.6 and Table 5.3). During wet periods they reach a similar maximum than the other methods because the water percolates quite fast from the surface to the 5 to 10 cm layer in the soil column.

The ECH_2O measurements, which were derived in a layer depth of 5 to 10 cm, show less dynamics but the highest mean value of all methods (see Table 5.3). In this vertical soil range, soil water is stored for a longer time, the SM content is more stable and influences from the atmosphere are less pronounced.

SM simulated by PROMET considers the entire 10 cm layer. The SM evolution over the entire period is highly correlated with the ECH_2O SM readings derived for the 5 to 10 cm soil depth. However, the SM dynamic range of PROMET is higher, which can be explained by the fact that PROMET also covers the highly dynamic surface processes but shows less dynamic than the manual surface measurements derived by ThetaProbe or gravimetric probes, which only consider the upper centimetres of the soil. It is therefore reasonable that the dynamics of PROMET occur between ECH_2O and the manual methods.

PROMET simulations and GPS measurements consider the same vertical range of the uppermost 10 cm and are therefore most suitable for comparison. Positively, the SM curves of GPS and PROMET fit very well, reach the highest correlation coefficient and a very low RMSE and have a similar dynamic range as well as similar minimum, maximum and mean values (see Figures 5.5 and 5.6 and Table 5.3). However, GPS is slightly more dynamic than the modelled data, especially during dry periods. One reason for this might be that the determined soil texture in the laboratory could be slightly different or inhomogeneous compared to the conditions in the soil plot, which would have an influence on the parameterisation of the PROMET model as well as the Dobson four-component model applied for the GPS approach. This in turn has an influence on the SM calculations with both methods. Secondly, as the GPS measurements undergo reflection, refraction and attenuation processes, which are non-linear, especially in case of high SM gradients within the first 10 cm, the GPS calculations might slightly under- or overestimate SM. This is the case if, e.g., the upper 5 cm are drier or wetter, than the lower 5 cm. This might be the reason why during dry periods, GPS is more similar to the ThetaProbe and gravimetric measurements. In summary, we state that the GPS sensors are more sensitive to the dynamics at the soil surface, which is positive in terms of interpreting events directly at the interface of air and soil.

5.5.2 Advantages and limitations of GPS soil moisture measurements

This study successfully demonstrates that low-cost GPS sensors are highly capable of quantitatively and continuously retrieving bulk SM of the upper soil layer in a non-destructive manner. A main advantage is that the GPS antennas are installed below the soil column of interest, in this case the upper 10 cm, which means that the soil above the antennas is unaffected by the sensors after the installation. In contrast, gravimetric measurements are accurate but they are highly destructive as for each sample, soil has to be extracted. Regarding FD and TDR probes, their prongs might influence the soil sampling volume during installation. This could cause

destruction of the soil structure that could result in an increased pore volume that can fill up with air or water or compacted soil [*Walker et al.*, 2004], which is not the case when using the GPS measurement system.

Further, soil is a quite heterogeneous medium. Soil texture, pore size distribution, the soil density, and the existence of large air and water pockets or larger heterogeneities like small rocks might vary largely even at small scales. This makes SM measurements quite difficult and explains the effect that sensors installed next to each other might possibly measure different SM values [*Walker et al.*, 2004]. As the GPS sensors cover the entire soil column above the antennas, which integrate over potential soil inhomogeneities, uncertainties are reduced due to larger sampling volumes. In contrast, most permanently installed FD or TDR sensors only have small sampling volumes at a certain soil depth.

Moreover, we assume the advantage that the GPS sensors are sensitive to the surface SM. Especially the uppermost centimetres of a soil column, at the interface between air and soil, are subject to a high dynamic in SM due to the direct influence of precipitation as well as intense radiation during dry periods. All these processes can be resolved with high sensitivity by the GPS sensor measurements.

It is also considered as an advantage that the GPS signals are broadcasted in the microwave L-band. For SM observations in general, that band is most suitable because the penetration depth of the electromagnetic waves reaches several centimetres even for moist soils. For dry soils, it can even reach several meters [*Nolan and Fatland*, 2003; *Ulaby et al.*, 2014]. As the L-band is widely and successfully used for SM retrievals from microwave measurements, e.g., from SMOS or SMAP, SM data derived by GPS use the same band and rely on a similar physical basis. Therefore, GPS-retrieved SM measurements could have a high potential as ground truth validation data for L-band microwave products. However, passive microwave systems derive SM through emission and the active microwave systems, and GNSS-R use signal reflections, and the GPS approach presented in this study is mainly based on signal strength attenuation.

As this method was only tested on a bare soil field, no quantitative statements about the SM retrieval capabilities of this GPS SM approach can be made for vegetation covered soils. However, we assume that this approach has high potential for soils covered, e.g., by agricultural crop plants like wheat, barley or even maize. In this case, an additional antenna above the vegetation would have to be installed to extract signal strength information from the plant water content, which has to be considered in the calculation in relation to the reduced signal strength at the antennas placed within the soil. Forest stands, however, might be too reductive for the GPS signals to also extract the underlying soils' SM.

Nevertheless, the vertical range of the soil column that can be investigated is limited, as at some point the GPS signal strength becomes too weak to be tracked continuously. The maximum installation depth might, however, differ for different soil textures and SM contents. For example, for high elevation angles (>70 degrees), the mean C/N_0 values received above the soil at GPS 1, reached approximately 47 dBHz. At a GPS antenna installation depth of 10 cm at GPS2 and GPS3 and for this specific soil texture, we always received strong enough GPS signals without interruption. During quite dry periods, with an SM content of 20 $m^3 \cdot m^{-3}$, the mean C/N_0 values of the high elevation angles reached approximately 36 dBHz, whereas they declined to approximately 29 dBHz during wet days, exemplarily at an SM content of 35 $m^3 \cdot m^{-3}$. However, an antenna installation depth below approximately 20 cm for this soil type, especially under wet soil conditions, makes potentially no practical sense, because the GPS signals would be attenuated excessively before reaching the GPS antennas. This could result in a reception of too weak GPS signals, which are then unreliable, or even longer signal interruptions or no signals at all. We tested this during a short experiment with an SM content of 35 $m^3 \cdot m^{-3}$ at a depth of 20 cm, where the C/N_0 declined to approximately 19 dBHz considering the high elevation angles; during even wetter conditions the signals were, however, not continuous anymore. Applying this approach potentially to vegetation-covered soils at deeper laying root-zones, it could be difficult or even impossible to derive continuous SM information regarding this specific soil type.

A further limitation regarding this measurement approach might be a too constrained hemispherical coverage, e.g., due to tall buildings and trees in the surroundings or extremely steep mountain slopes and deeply cut valleys, which could cover the direct line of sight of too many GPS satellites to the receiver. However, other than GPS positioning algorithms, our approach to measure SM does not depend on a minimum number of four satellites to find a solution. Theoretically, the signal of one single GPS satellite for each time step would be sufficient.

Last but not least, as for every retrieval algorithm, a wrong parameterization might lead to imprecise results. To obtain an impression of its sensitivity, we carried out a sensitivity analysis in the next section.

5.5.3 Sensitivity analysis of GPS soil moisture measurements

According to *Dobson et al.* [1985] and *Hallikainen et al.* [1985], we investigated the sensitivity of the retrieval algorithm for soil texture and soil temperature, which were identified as the most important physical soil parameters for this approach. In addition, we conducted a sensitivity assessment of the soil density because this parameter exhibited a rather large variability in our soil sampling. For this sensitivity analysis, we applied Equations (5.1)–(5.9) analogous to the original and correct soil parameterization.

Regarding different soil textures with different sand, silt and clay contents, the same SM values are based on different values of the complex permittivity of moist soil [*Dobson et al.*, 1985; *Hallikainen et al.*, 1985]. The soil texture is mainly represented by the physical soil parameter A_s, which was set to the value of 49 $m^2 \cdot g^{-1}$ for the observed soil at the DWD test site in Munich. Lower values for A_s represent soils with lower clay and higher sand contents, whereas higher values represent higher clay and lower sand contents. We increased and decreased A_s by ± 10 and ± 20. A_s = 29 $m^2 \cdot g^{-1}$ represents, for example, the textural class sand and A_s = 69 $m^2 \cdot g^{-1}$ silt loam. As shown in Figure 5.7a, the changes in A_s have quite a large impact on the SM results. If the soil is assumed to be too sandy, SM is underestimated, whereas if it is assumed too clayish, SM is overestimated. In case of an overestimation, the dynamic range increases and in case of an underestimation, it decreases. According to these findings, great effort should be taken to obtain reliable soil texture measurements in the laboratory.

In general, the GPS SM retrieval is based on the complex permittivity of water, which is temperature dependent in the microwave range [*Dobson et al.*, 1985; *Hallikainen et al.*, 1985] (see also Table 5.2). For this study, we used separate soil temperature measurements to correctly adapt the Dobson four-component dielectric mixing model. In case no soil temperature readings are available, uncertainties in SM calculations might occur due to wrong soil temperature assumptions. To address this, we additionally calculated for each time step the SM with a fixed soil temperature assumption of 15°C, which is approximately the average annual soil temperature at the DWD test site. Figure 5.7b illustrates the difference between the assumed fixed soil temperature and the results with the correct soil temperature. Especially during the colder winter periods, the SM curves deviate the most with a rather high overestimation of up to 8%. However, during warm periods especially in summer, the deviation, expressed as an underestimation, is negligible or less than 2.5%. In case no soil temperature data are available, we recommend an assumption of the soil temperature based on air temperature measurements, if they are available, e.g., from stations nearby. The dynamic range of the air temperature measurements at our test site was only slightly higher than of the soil temperature readings at 5 cm soil depth, which is negligible for the SM results.

To obtain an impression of how soil density variations affect the SM calculations, we decreased and increased the actual measured soil density of ρ_b = 1.3 $g \cdot cm^{-3}$ by $\pm 10\%$ leading to densities of 1.17 $g \cdot cm^{-3}$ and 1.43 $g \cdot cm^{-3}$, and $\pm 20\%$ leading to densities of 1.04 $g \cdot cm^{-3}$ and 1.56 $g \cdot cm^{-3}$. Figure 5.7c shows that these changes in soil density have no severe impact on the SM results. An increase in soil density leads to a slight increase in the SM curve, whereas a decrease in soil density leads to a slight decrease in the SM curve. Though the soil density measurements might not be absolutely accurate, it is still possible to retrieve reasonable SM values.

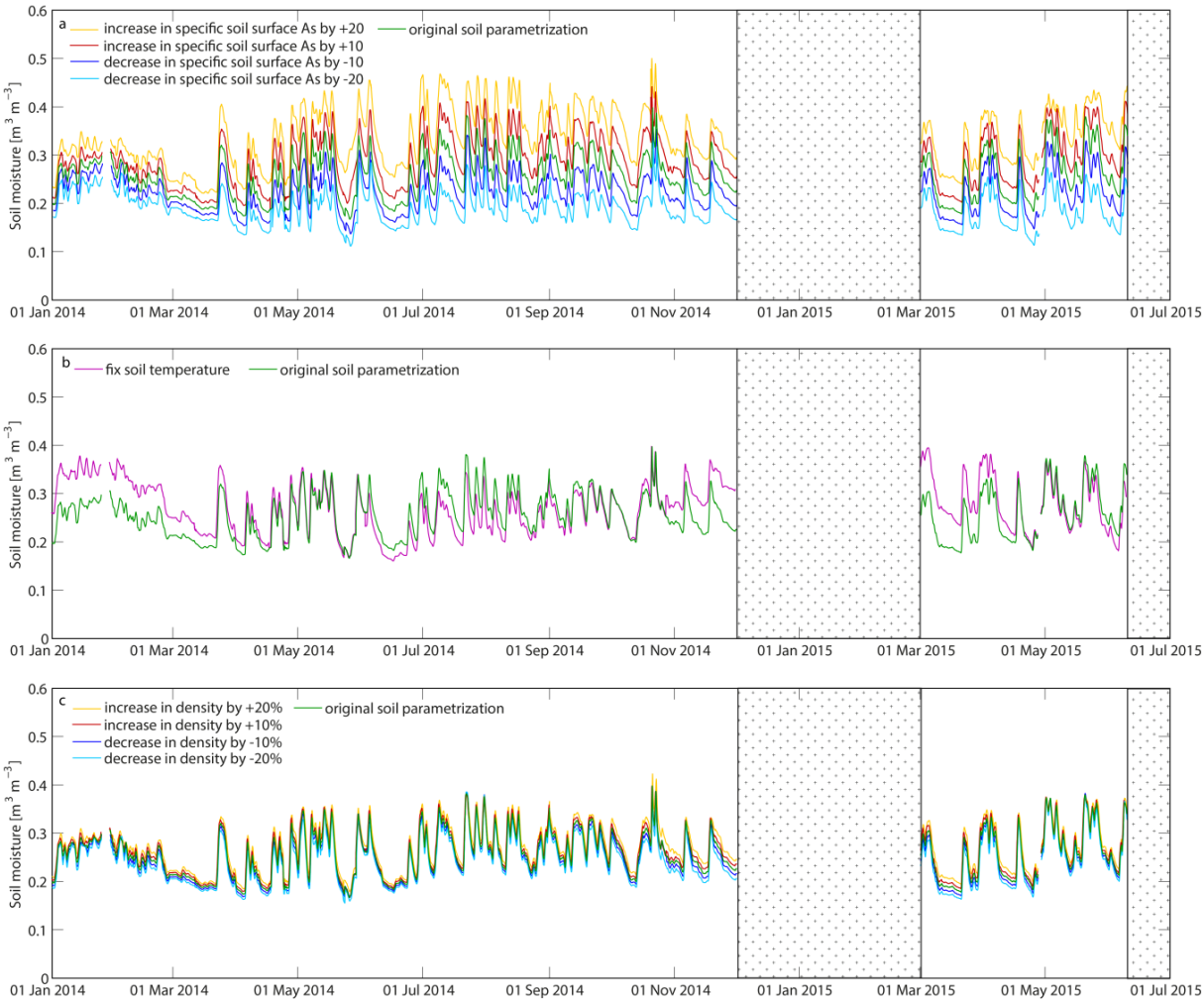

Figure 5.7: Soil moisture derived from GPS containing different assumptions on (a) an increase or decrease of the specific soil surface A_S, which is an indicator for different soil texture assumptions by ± 10 and ± 20, (b) a fix soil temperature assumption of 15°C and (c) a soil density over- and underestimation of $\pm 10\%$ and $\pm 20\%$ compared to the original parameterized calculations at the DWD test site Munich during the measurement period January 1, 2014 - June 10, 2015.

5.6 Conclusions

With this new dielectric low-cost GPS approach, we were able to continuously and non-destructively retrieve the bulk soil moisture (SM) of the first 10 cm of bare soil. Our test site was situated at the soil measurement field at the DWD test site in Munich where we installed the sensors for a time period of almost 1.5 years (1 January 2014–10 June 2015). The quantitative retrieval of SM is based on the attenuation of GPS L1-band signals and was calculated with the Dobson four-component soil moisture model based on the complex permittivity.

The temporal evolution of the SM derived by GPS was compared with high conformity to three other measurement methods, namely FD ECH_2O measurements, also in a continuous mode, and weekly to bi-weekly FD ThetaProbe and gravimetric measurements as well as SM simulations with the hydrologic land-surface model PROMET. Comparing all continuous methods, the SM derived by GPS is the most dynamic, showing the greatest minima during dry periods and the highest peaks during intense precipitation. As each method represents the SM values according to different sampling volumes and vertical ranges, their comparability has limitations. However, PROMET and GPS consider the same vertical range and also show the highest conformity. Only during periods with extreme vertical SM gradients, GPS seems to be more dynamic than PROMET. Moreover, all SM curves showed high temporal coincidence with parallel measured precipitation and modelled percolation. In addition, we carried out a sensitivity analysis to address the sensitivity of the applied

main physical soil parameters. Overall, an error in the estimation of density is less severe than errors in soil textures and temperature assumptions, especially during cold periods.

In this study, we measured the temporal evolution of SM based on GPS signal attenuation for a bare soil field with a specific soil texture and at a certain soil depth. In a next step, this approach should also be tested for other soil types and different installation depths. Further, this approach could be extended to vegetation-covered soils. For this approach, two antennas above the soil with one situated directly at the soil surface and the second one above the vegetation to extract the signal attenuation of the vegetation layer could be used. Using this extension, near-surface SM could potentially also be derived for vegetation covered soils. This approach would be similar to or could also be combined with the approach of *Koch et al.* [2014] measuring the liquid water content of snow, with antennas above and below the snow cover. As a technology transfer to hydrological monitoring, the SM and snow cover approaches derived by GPS were already successfully investigated within a thematically specific DFG project and a ESA feasibility study, and are recently under preparation for demonstration as an integrated service within the IAP Demo Project SnowSense (co-funded by ESA under the ARTES 20 program). In general, a major advantage of this approach is that the retrieval of the hydrological observable, which is in this study SM, is based on the microwave L-band. This makes it highly attractive as potential validation data for SM products generated from L-band microwave remote sensing data, like the SMOS or SMAP mission. Moreover, this could complement satellite data with a large spatial coverage but low temporal resolution to extrapolate SM data in a continuous mode at representative sites. As the GPS antennas are installed at a defined soil depth, e.g., 10 cm, the bulk SM of this first soil layer is measured rather than measuring only a small soil volume at a certain depth as is mostly done with FD or TDR sensors. As we use small low-cost and low-power GPS components, the data analysis is not time consuming and the GPS signals can be received globally, and this approach would be suitable to equip entire sensor networks in different regions worldwide. Besides serving as highly useful remote sensing ground truth data and validation data for climate and hydrology studies, SM retrieval based on GPS could also support agricultural studies.

Acknowledgements

The authors wish to acknowledge the contribution of the student Thomas Ramsauer of the University of Munich (LMU) helping with the installation and the weekly to bi-weekly in situ measurements at the German Weather Service (DWD) test site in Munich. Moreover, they would like to thank Heike Bach and Markus Muerth from Vista Remote Sensing GmbH for the numerous fruitful discussions on soil moisture model retrieval. The authors would like to thank the DWD, which kindly provided the opportunity to install our GPS sensors at their test site in Munich. Until mid-2015, Franziska Koch was supported by the German Research Foundation (DFG MA 875/12-1). Recently, Franziska Koch and Florian Appel were co-funded by the European Space Agency (ESA, 4000113149/14/NL/AD) within the ARTES-IAP Demo Project SnowSense (https://artes-apps.esa.int/projects/snowsense-dp), which is gratefully acknowledged. The authors thank two anonymous reviewers for greatly improving this manuscript with their constructive comments.

6. CONCLUSIONS AND OUTLOOK

6.1 Conclusions

As introduced in the motivation in *Section 1.1*, continuous information on the bulk snow cover properties snow height (HS), snow water equivalent (SWE) and the volumetric liquid water content in snow (LWC), as well as the soil property soil moisture (SM) are largely needed for climate and hydrological simulations. Moreover, they are important for the prediction of extreme events, avalanches and water supply, e.g., for energy and agriculture. Therefore, the superior aim of this thesis was to develop a continuous, non-destructive, and potentially globally applicable low-cost measurement system to derive information on bulk snow cover properties and soil conditions. For this purpose, a new and completely different approach compared to all other applications relying on the freely available GPS L1-band signals was developed. To perform field studies on this approach in a specific snow or soil environment, suitable robust low-cost GPS sensors and components were chosen and partly self-constructed. Since autumn 2012, the GPS measurements on the snow cover properties were running at the high Alpine SLF test site Weissfluhjoch (WFJ) near Davos in Switzerland and the GPS soil measurements were conducted at a bare soil field of the German Weather Service (DWD) in Munich (MUC) for a time period of almost 1.5 years in 2014/15.

To solve the above mentioned envisioned aims, the thesis was structured into six **research objectives** (**OJ**), defined in *Section 1.6*, which lead step by step to the answering of the three **research questions** (**RQ**), mentioned in *Section 1.1*. The research objectives encompass, e.g.: sensor construction and sensor setup at the test sites; data processing and algorithm development for the three bulk snow cover properties LWC, SWE and HS, as well as SM; the combination of different sensors and input data; data comparison and validation with meteorological and in situ reference measurements and modelling results. In the following, the conclusions and achievements summarized as **research answers** (**RA**) are described for each **RQ**:

RQ1. ***Is it possible to derive information on environmental parameters with low-cost GPS sensors by analysing GPS signals passing through a medium like snow or soil?***

RA1: At the initial point of this thesis, this novel approach of applying low-cost GPS sensors relying on the freely broadcast GPS L1-band signals passing through media like snow or soil to derive information on environmental properties was considered theoretically possible. However, it was unclear if this could actually be achieved in practice. From a pure physics perspective, the behaviour of the electromagnetic waves in different media is well established, so it was obvious that this approach should theoretically be possible. However, it was uncertain for example, if GPS signals could be tracked through all different conditions in harsh environmental surroundings though varying thickness of the media, and whether the GPS sensors would perform reliably when used in a continuous mode over several years. Now, at the end of this thesis this fundamental first research question can be answered with a clear yes. It was possible to derive snow properties and SM accurately.

RQ2. ***Which snow cover properties can be derived? Which GPS raw data information is necessary, how should the GPS sensors be located and is external information required?***

RA2.1: At the test site WFJ, one GPS sensor was installed on a pole and remained permanently above the surrounding snow cover. Two other sensors were placed at the ground level and were buried by snow during the entire snow period. As a first step, the recorded signal strength, expressed as C/N_0, was analyzed and normalized with a snow-free reference for each time step. As snow melting occurred, C/N_0 decreased markedly. Compared to that, the C/N_0 of the upper antenna remained relatively constant, which means that atmospheric influence is negligible resulting in the assessment that the upper

antenna is not mandatory for this LWC approach. Taking into account externally measured HS, a dry snow density assumption and dielectric mixing models, it was possible for the first time, to quantitatively, continuously and non-destructively derive bulk volumetric LWC with low-cost GPS sensors. The results were in high coincidence with meteorological and snow lysimeter measurements taken in parallel as well as several capacity probe measurements in snow pits (see *Chapter 2*). The GPS derived LWC data was corroborated using L-band upward-looking ground-penetrating radar (upGPR) data (supplied by a SLF research team who was independently monitoring LWC). Comparing the results of both methods, the results showed a high correlation (see *Chapter 3*).

RA2.2: Using solely time delay information of electromagnetic waves through snow, it is possible to accurately derive HS or SWE in case of dry snow, but lacks accuracy under wet-snow conditions. However, combining signal strength and time delay information, the three bulk snow properties HS, SWE and LWC can be jointly derived for dry and wet-snow conditions. This was successfully solved by combining GPS C/N_0 and the two-way travel time (TWT) measured by an upGPR. This sensor combination offers a very good solution to measure non-destructively from beneath the snowpack and could therefore be a big step towards improving avalanche forecasting, as e.g. sensors installed on poles would easily be destroyed by avalanches. The results derived by the upGPR-GPS combination were validated positively by conventional in situ methods like laser and ultrasonic HS sensors as well as snow pillow and snow scale SWE recordings (see *Chapter 3*).

RA2.3: Since autumn 2015, a second generation GPS sensor setup was installed at the test site WFJ, which made it possible to process GPS carrier phases. The antenna constellation with at least one above and one below the snow cover was the same as before. As snow reduces the velocity of electromagnetic waves, the time delay was determined using double differenced (DD) carrier phase measurements, an elevation mapping function, and the particular refraction angles being proportional to the dielectric snow properties. Using an assumption of signal wave velocity, it was possible to calculate SWE under dry-snow conditions. The results highly correlate with manual snow pit and snow pillow data (see *Chapter 4*). Under wet-snow conditions, however, further research on phase processing is needed. After a successful solution on this, additional to the time delay derived by GPS, C/N_0 should be considered to jointly derive SWE, HS and LWC solely by GPS signals. As outlined in *Section 6.2*, this approach would be similar to the upGPR-GPS combination, however, using, instead of TWT, GPS carrier phases.

RQ3. ***Is it possible to transfer the derivation of snow cover properties to soil properties?***

RA3: The GPS signal strength attenuation in wet soil behaves quite similar to the attenuation in wet snow. The GPS antennas, installed at a soil depth of 10 cm, derived the SM from the soil surface down to the depth of the installed antennas representing the entire first soil layer encompassing the direct interface between air and soil. Applying the Dobson four component dielectric mixing model, bulk SM was quantitatively derived with a high correlation with FD and gravimetric in situ methods either at the uppermost soil surface or at defined soil depths of the upper soil layer. To further corroborate the GPS measures, the SM of the 10 cm surface layer was modelled with the physically-based land-surface model PROMET, which showed very high correlation (see *Chapter 5*). This positive evaluation shows that it is possible, to adapt the methods developed for snow, to the derivation of soil properties, like SM. However, the GPS SM measurements are restricted to the soil surface as the signals would be attenuated too much in deeper soil layers, e.g. at deeper laying plant root-zones.

In summary, all **RQ**s can be answered positively and the main aims of this thesis were achieved successfully. By combining the GPS signal strength measurements with information from other sensors (e.g., laser or radar sensors), all three bulk snow cover properties were derived with high accuracy. As a further big success SM and SWE, in case of dry snow, were derived solely using GPS signals; no further sensors were necessary in these cases. However, regarding wet-snow conditions, it still requires further development with regard to a more stable carrier phase processing, which is currently investigated. A success in this work would lead in the derivation of

all three snow cover properties HS, SWE and LWC using solely GPS L1-band signals. Thereto, *Section 6.2* is an outlook on the possibility of solely using GPS for wet snow. Additionally, *Section 6.3* gives an outlook on a selection of potential improvements, extensions and further applications.

In total, this thesis encompasses important and promising steps towards the development of a new continuous, non-destructive and low-cost environmental monitoring system which could be potentially applied globally and is not affected by cloud cover. The concept on solely using GPS signals for the derivation of environmental parameters shows considerable commercial promise. Moreover, establishing networks of low-cost GPS sensors, potentially also located in remote and difficult to access areas, could help to bridge gaps in environmental monitoring.

6.2 Combination of GPS C/N_0 and carrier phase time delay for wet snow

As stated in *Chapter 4* and in the section before, GPS carrier phase tracking and processing during conditions of wet snow is much more difficult compared to such of dry snow and is still under development (as of November 2016). This is due to the significantly higher attenuation of the L1-band GPS signals passing through liquid water. In general, the C/N_0 signal strength tracking is, so to speak, more robust than phase tracking, in particular by using low-cost GPS receivers. Due to an increase in tracking losses, cycle slips, phase noise, multipath and problems of estimating integer ambiguities correctly, especially the carrier phase processing becomes difficult. However, in close cooperation with ANavS GmbH, this subject is recently investigated to be solved as soon as possible in a positive way. The aim of this current work is in getting time delay information caused by wet snow between two permanently installed antennas, similar to the approach presented in *Chapter 4*.

Under the assumption that the above mentioned work will be successful, the retrieved time delay can then be used as input for further algorithms on snow cover properties. The results of this thesis show already a direction towards a potential combination of the presented techniques in the *Chapters 2*, *3* and *4*. In general, time delay information and C/N_0 can be combined in case of wet snow, as both variables are functions of the dielectric characteristics of wet snow. Both can be used to calculate LWC when additional information such as externally measured HS is given. As demonstrated in *Chapter 3*, the snow properties HS, SWE and LWC were derived solely by combining the time delay information measured by the upGPR and the GPS signal strength. The difference between the upGPR TWT and the GPS carrier phase time delay through snow is that the former expresses HS and the latter SWE. This is due to the fact that upGPR measures the TWT of electromagnetic waves between the ground and the air-snow interface, whereas the GPS carrier phase time delay approach considers the time delay through the amount of snow particles which is independent of the snow density. However, both measurements can easily be converted as they are directly linked by the bulk density of the snowpack. So, it should generally be possible using GPS carrier phase time delay information instead of the upGPR TWT. In the following, this section points out how further steps could potentially look like.

Before processing GPS carrier phase and C/N_0 under dry or wet-snow conditions, snow-free reference data have to be processed. This encompasses the derivation of normalized C/N_0 reference values, as described in *Chapter 2*, and a fix baseline estimated with the RTK carrier phase positioning approach, as presented in *Chapter 4*. Independent whether the snow is dry or wet, information on the snow density is necessary. This value can either be assumed as a fix value (e.g. the mean of a certain region and time) [*Heilig et al.*, 2009; *Schmid et al.*, 2014] or can be estimated by meteorological and regional information, e.g., after the findings of *Meløysund et al.* [2007], *Jonas et al.* [2009] and *Sturm et al.* [2010]. Besides, further analysis on C/N_0 might deliver such plausible dry snow density estimates regarding the complex permittivity of snow [*Denoth*, 1994; *Sihvola and Tiuri*, 1986]. However, GPS C/N_0 values might be too noisy for this approach. In addition, a further possibility might be using information simulated by models, such as specific snowpack models [*Bartelt and Lehning*, 2002; *Braun*, 1993] or hydrological land-surface models, e.g., PROMET [*Mauser and Schädlich*, 1998; *Mauser and Bach*, 2009].

As a check whether the snowpack is dry or wet, the signal strength values can be categorized. If the C/N_0 values decrease by <-3dB from the standard value range (expressing a normalized C/N_0 of approximately 0.8), they are classified as wet snow, whereas values lying above this threshold are handled as dry snow [*Koch et al.*, 2014]. If the snow is classified as dry, SWE can be calculated by using the time delay derived by carrier phase residuals, as presented in *Chapter 4*. HS can then be calculated by multiplying SWE with the dry snow density.

As already mentioned, in case of wet snow, the derivation of the snow cover properties becomes more difficult. This is because liquid water in snow leads to a significant increase in the dielectric properties, expressed in the real and the imaginary part of the complex permittivity. Regarding impacts on the carrier phase time delay of wet snow compared to dry snow, two points are relevant:

- the refraction angle declines which shortens the pathway of the GPS signals through the snowpack,
- and the velocity of the GPS signals in wet snow declines.

To achieve information on all three snow cover properties, the carrier phase time delay and the normalized signal strength, have to be combined. This could potentially be solved by the following three methods:

(a) Inclusion of the carrier phase time delay processing algorithm in the C/N_0 root-finding algorithm, which was presented in *Chapter 2*, to solve the equations of the complex permittivity with more than one unknown.
(b) Usage of a priori knowledge of previously processed time steps for the currently processed time step.
(c) Calculation of carrier phase time delay for dry-snow conditions as pre-processed data, which might not be correct for wet snow. Correction by post-processing of C/N_0 values combined with the results of the pre-processed carrier phase time delay values.

In general, the implementation of option (b) and (c) are considered to be more practical than option (a). In the following, a possible implementation of option (b) is further described, whereof an example on a possible processing chain is given in Figure 6.1.

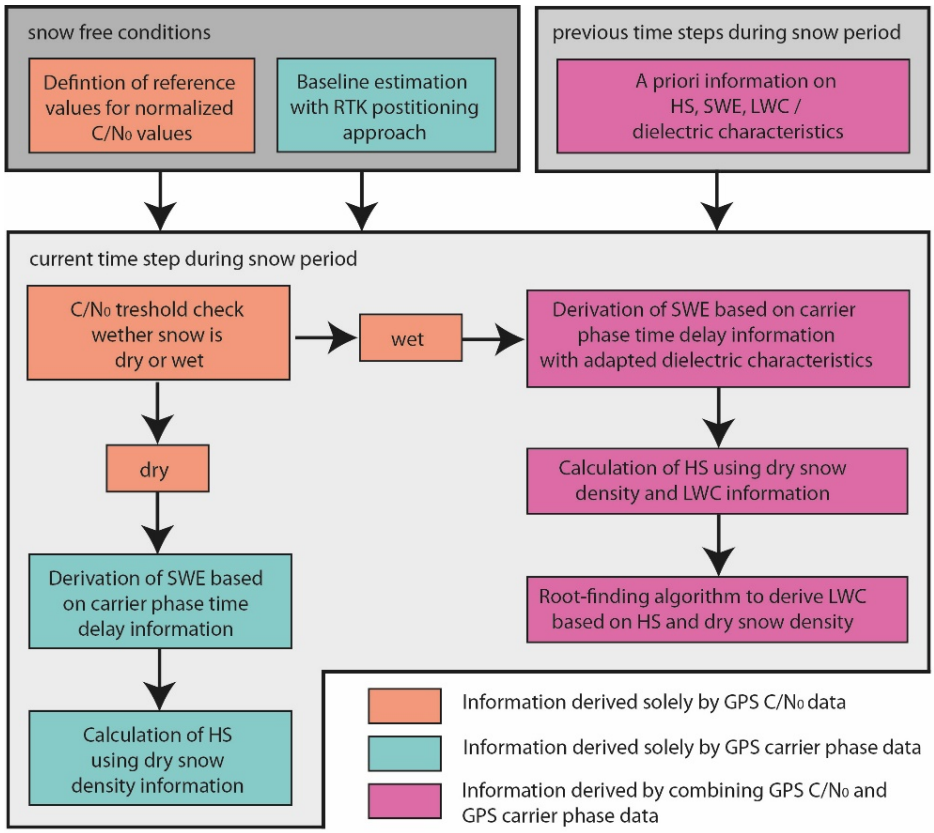

Figure 6.1: Schematic overview of a potential processing chain for dry and wet-snow conditions combining GPS C/N_0 and carrier phase. In this example a priori knowledge (option (b)) is used to solve the derivation of SWE, HS and LWC in case of wet snow.

As the current measurement time steps are one second, the snow conditions of subsequent time steps can be assumed as identical. Moreover, this could even reasonably be assumed for the mean of subsequent time steps of approximately up to 30 minutes, as the snow conditions do not change that quickly. As suggested in *Chapter 4*, additionally low-pass filtering techniques over a defined time period should be used to suppress outliers.

After deriving the time delay information through a snowpack adapted to the current wet-snow conditions by involving C/N_0, SWE can subsequently be calculated by using Equation (4.37). HS can then be calculated using the dry snow density information, as suggested above, and by including LWC information as a priori values from the previous time steps. As a last step, the calculated HS serves as input for the root-finding algorithm to solve the equations for LWC under consideration of the complex permittivity as presented in *Chapter 2*. The results of the three snow properties HS, SWE and LWC of this current time step are then again used as a priori knowledge input for the next time steps and so on.

6.3 Further research and development perspectives

Besides the further steps presented in *Section 6.2*, the following ideas and optimizations were identified as future **research and development perspectives** (**RDP**) on the basis of the findings presented in this thesis in combination with the aim to improve this new technique and to make it usable also for further applications:

RDP1. Sensor improvement

The first self-composed experimental sensor setup with the Fastrax IT430 receivers was successfully tested and applied over several years at both test sites under harsh environmental conditions. Negligible breakdowns occurred and when they did, they were attributed to power outages. However, for commercial use, this first experimental sensor system has to be improved. A first step in this direction has already been taken by using more advanced sensors since autumn 2015. As an example, in the ESA Artes-IAP demonstration project SnowSense it is foreseen to use fully autarkic in situ measurement devices including a robust power management system with solar panels and batteries, a communication interface (e.g., SatCom) and an on-time processing unit. This is currently being tested at the SnowSense project test areas in Newfoundland. The outcome of this demonstration project should lead to the production of commercially available GNSS sensor systems.

RDP2. Adaptive temporal data and energy management

For this study, the GPS data was collected and analysed at one second intervals. This amassed a large volume of data requiring storage and processing capacity. However, the raw data of each time step is not entirely necessary to derive a complete picture of the temporal evolution of the observed environmental properties. An adapted data management plan should aim to record a reduced set of raw data at adequate time steps which means that the intervals should be still sufficient to derive all necessary information on significant short-term changes, e.g., in the amount of snow, its melting stage and in- or decrease in SM. This reduction in the amount of stored and processed data can either be handled by reducing the temporal rate, e.g. from one second to several minute or to reduce the recordings, e.g. for an hourly measurement interval of a few minutes, whilst during the rest of the time the receivers turn into a sleeping mode.

This would additionally save energy. This strategy would especially be helpful or even necessary in remote areas where the sensor can only rely on solar and battery power. The derivation of an adequate solution of these aspects is also a major task in the project SnowSense.

RDP3. Combination with GNSS-R

As presented shortly in *Section 1.4.2*, interferometric GNSS reflectometry (GNSS-R) aims to derive HS with antennas installed above the snow cover. The received signal strength from line-of-sight and reflected signals contain multipath information of the varying snow cover surface compared to the fix

antenna height. HS retrieved by GNSS-R could, e.g., be used as input for the LWC signal strength model, presented in *Chapter 2*, which would replace the additionally used HS laser sensor. This approach could potentially also be combined with the approach presented in *Chapter 4* and *Section 6.2*, e.g. to deliver a better estimate of a priori information and to calculate LWC based on the GNSS-R HS information. Moreover, improved information on SWE and HS would improve information on the bulk snow density. However, this approach might be too error-prone or impossible to correctly interpret by using low-cost receivers. The latter are quite noisy and for low-cost antennas with unknown, highly different antenna patterns. Moreover, this approach needs smooth surfaces for correct interpretation of the environmental properties. Slopes or obstacles like poles might spoil the information. Until now, GNSS-R was mainly used for high-end geodetic receivers or specific left- and right-hand polarized receivers. Moreover, most approaches predominantly used L2-band which has a lower frequency, but is not civilly available. In general, the noise in the L1-band readings are higher which makes an identification for example of HS practically more difficult [*Larson*, 2016].

RDP4. Derivation of spatial information

The in situ GNSS approach, as introduced in this thesis is more or less a point measurement following a high temporal resolution. However, for many applications, regarding e.g., accurate predictions in water supply, hydropower or extreme events, spatial information is highly relevant. Region- or basin-wide networks with numerous low-cost GNSS sensors might improve spatial coverage as the parameters could be measured simultaneously at different locations, land use situations, altitudes or expositions.

Moreover, a combination of the L-band in situ GNSS measurements with microwave remote sensing data, e.g., from the active C-band senor Sentinal-1 or the passive L-band sensor SMOS, would be a big improvement towards spatial information. The point measurement of snow properties and SM could then be interpolated at the explicit overflight date for the entire remote sensing scene depending on the values of the recorded microwave remote sensing data.

Further, the measured in situ GNSS data could improve spatially distributed model results. Using them as input for, e.g., a physically-based land-surface model like PROMET, the quality of the model output of the observed snow and soil properties could be improved. Consequently, also the spatially modelled environmental properties would improve.

RDP5. Identification of heterogeneities

Based on the low-cost GPS sensors, an investigation of small scale differences within the snow cover or a soil column in its vertical and horizontal extent could be performed. The installation of sensors at defined snow heights could e.g. improve the understanding of wetting fronts during melt-onset, and on the effect of precipitation events and the respective depth of melt-freeze cycles, which occur from the top to the bottom of a snowpack. A vertical sensor arrangement in soils could track SM at different depths in parallel, as well as percolation and potential capillary rise activities.

Horizontal variations could be recorded by placing several sensors at distances of a few decimetres or meters. An investigation is currently running at the test field WFJ to establish, if LWC differs spatially within an area of 100 m². An investigation of this type has been made possible using low-cost GPS sensors.

RDP6. Applications at further locations

Regarding the derivation of the snow cover properties, this approach was tested at a high alpine region having a continuous snow cover over for a period of 8-9 months. Over this period there were several months with dry-snow conditions with no or negligible melting periods. Following the first significant wetting date in spring, the snow cover remained more or less moist. This means that the conditions did not change frequently. As a next step, test sites at lower altitudes with more frequently changing snow conditions should be tested. This issue is presently being investigated at several locations in Newfoundland and in the Alps as part of the SnowSense project.

Regarding the derivation of SM by GPS signal strength attenuation, a transfer to other locations would be useful. As until now this approach was only tested at a bare soil field with a soil texture of sandy loam, an investigation regarding different soil types or even vegetation covered soils would be highly attractive. Regarding e.g. dry prairie or desert soils, the installation depth could be extended to several decimetres or meters. Moreover, the approach could be extended also to frozen soil.

RDP7. Application of the upGPR-GPS combination in avalanche prone slopes

The combination of upGPR and GPS was successfully tested at a flat area at the test site WFJ as presented in *Chapter 3*. The main advantage of this sensor combination is that it derives the snow properties HS, SWE and LWC non-destructively without external information and without poles or stakes as all instruments are installed underneath the snow cover. This makes it largely suitable for measurements in avalanche prone slopes, and is recently tested at a slope near Davos in Switzerland. In general, direct and continuous information from avalanche prone slopes, especially of LWC and HN would be highly relevant for avalanche predictions and hazard management.

RDP8. Combination of upGPR and GPS carrier phase time delay to derive dry snow density

As presented in *Chapter 4*, it is possible to use GPS carrier phase to retrieve accurate SWE values for dry snow. As the upGPR delivers accurate measures for HS of dry snow and SWE and HS are only related by the value of the dry snow density, the latter can also be derived accurately using this sensor combination. Further, it might be possible to extend this approach also to wet-snow conditions. Knowledge on the snow density is for example an important variable in avalanche forecasting as it gives important information on snow metamorphism and compression.

RDP9. Extension to other GNSS signals

Until now, this approach was applied only for GPS signals. As an addition, other GNSS signals could be used. GNSS sensors which are able to track GLONASS and GPS satellites in parallel would be beneficial because this would improve the overall satellite availability, especially over areas with difficult satellite coverage over mountain slopes, valleys and urban areas. In the future, also additional information from the European Galileo system and the improved Chinese Beidou/COMPASS system could be used in this sense.

RDP10. Investigation of other environmental properties

Last but not least, further research regarding other environmental properties could be carried out by applying the techniques presented in this thesis. Regarding signal strength attenuation, mainly due to water content within environmental material, such as plant water content as already investigated as a first estimation by *Rodriguez-Alvarez et al.* [2012a]. Moreover, this could encompass for example observations on the plant biomass, agricultural crop growth rates and vegetation health in a continuous mode and with a fine temporal resolution. The tracking of the plant biomass evolution could, e.g., help farmers to better manage their agricultural production and yields. Further, information on plant interception water could be derived, as then additionally the droplets of water on top of the plants are detected. The signal strength would then be attenuated more strongly compared to periods without interception.

Moreover, GNSS phase measurements providing time delay data could further be applied for permanent snow cover or sea and glacier ice thickness measurements. This would be a highly promising approach regarding Polar Regions with almost dry-snow conditions.

Further, the technique with two permanently installed antennas could also be used for the detection of slightly moving objects such as soil or snow dunes or to detect soil accumulation and erosion. In case of vertical mass changes, changes in signal strength and carrier phase time delay would occur.

APPENDIX

APPENDIX A: PICTURES OF GPS SENSOR CONSTRUCTION, INSTALLATION AND REFERENCE MEASUREMENTS AT THE SLF TEST SITE WEISSFLUHJOCH……...……..... XXVII

APPENDIX B: PICTURES OF GPS SENSOR INSTALLATION AND REFERENCE MEASUREMENTS AT THE DWD TEST SITE MUNICH. ..……..……....…….…….…….... XXXI

APPENDIX C: GPS SENSOR INSTALLATION PLAN AT THE SLF TEST SITE WEISSFLUHJOCH. XXXII

APPENDIX D: OVERVIEW OF MEASURED SNOW PROPERTIES, SENSORS AND THEIR LOCATION AT THE TEST SITE WEISSFLUHJOCH. ..…….....…… XXXIII

APPENDIX E: MEASURING THE HYDROLOGICAL SNOW STORAGE IN ALPINE CATCHMENTS WITH A NEW LOW-COST GPS TECHNOLOGY. ….…….……...……..…….…..…… XXXIV

Appendix A: Pictures of GPS sensor construction, installation, and reference measurements at the SLF test site Weissfluhjoch

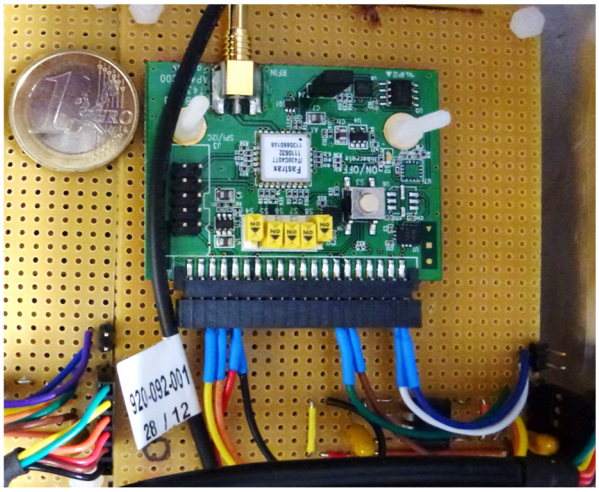

Figure A.1: FASTRAX IT430 GPS receiver (green) with self-constructed application board (orange) with voltage regulation and USB-to-serial interface.

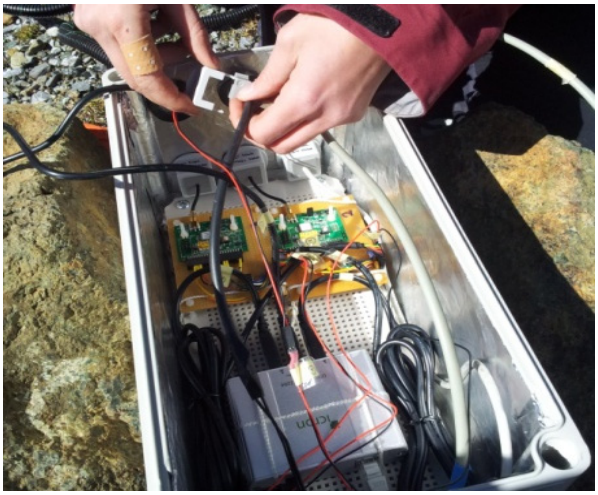

Figure A.2: Connecting cables with the GPS receivers in the big weather-proofed box on the ground level for GPS2&3.

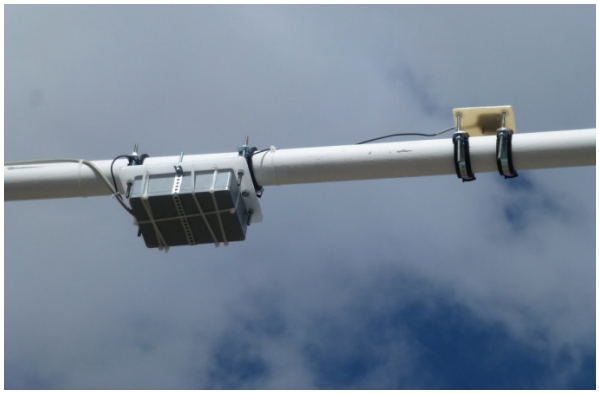

Figure A.3: GPS1 antenna and small weather-proofed box for the receiver above the snow installed for the winter season 2012/13 at the test site WFJ.

Figure A.4: Hirschmann GPS7M antenna installed for the winter season 2012/13 at the test site WFJ.

Figure A.5: Tallysman 2410 antennas with ground-planes installed since the winter season 2013/14 at the test site WFJ.

Figure A.6: Self-constructed antenna radome for GPS1 used since the winter seasons 2013/14 at the test site WFJ.

Figure A.7: Fanless mini-PC Spo-book MOVE T56N.

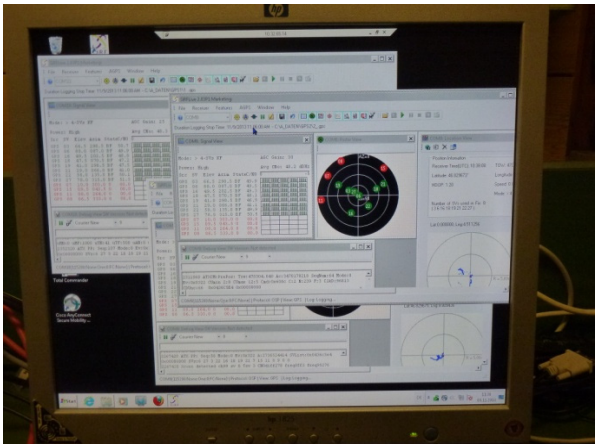

Figure A.8: PC monitor showing the active receiver specific GPS SiRFLife software.

Figure A.9: GPS reset box for the GPS receivers GPS1, GPS2 and GPS3 at the test site WFJ.

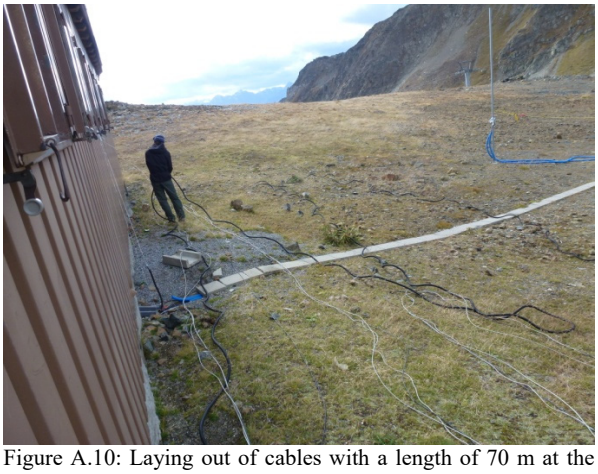

Figure A.10: Laying out of cables with a length of 70 m at the test site WFJ (25.09.2012).

Figure A.11: Suitcase with ANavS GPS sensor system encompassing a single-board computer, two antennas and two receivers (photo taken by P. Henkel).

Figure A.12: Ground and pole antenna of the ANavS GPS sensor system installed at the test site WFJ (10.10.2016).

Figure A.13: View from Parsenn II top station on the WFJ test site and the Parsenn skiing area in autumn (03.09.2013; http://www.swisswebcams.ch).

Figure A.14: View from Parsenn II top station on the WFJ test site and the Parsenn skiing area in winter (03.02.2014; http://www.swisswebcams.ch).

Figure A.15: WFJ test site in summer (23.07.2012).

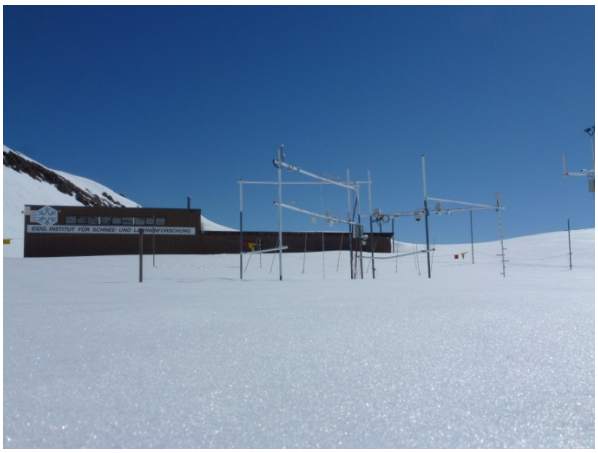

Figure A.16: WFJ test site in spring (15.04.2013).

Figure A.17: Panoramic view of Davos Parsenn skiing area, the test site WFJ and the mountain Weissfluhjoch (08.11.2013).

Figure A.18: Maintenance work of GPS sensors at the test site WFJ (08.11.2013).

Figure A.19: Snow scale at the test site WFJ.

Figure A.20: Snow pillow at the test site WFJ.

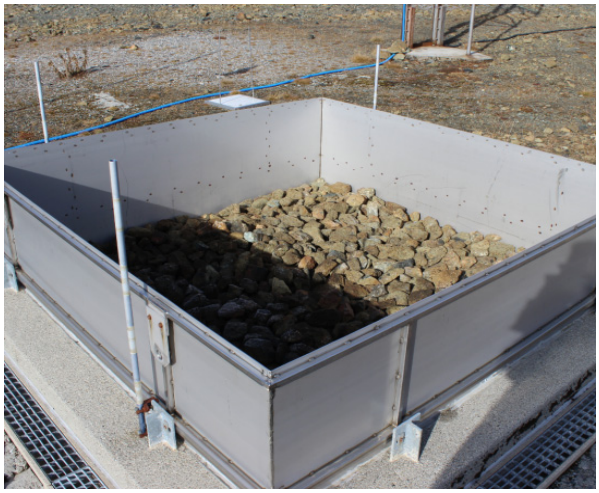

Figure A.21: Snow lysimeter at the test site WFJ.

Figure A.22: Open snow pit for bi-weekly snow profile analysis at the test site WFJ (15.04.2013).

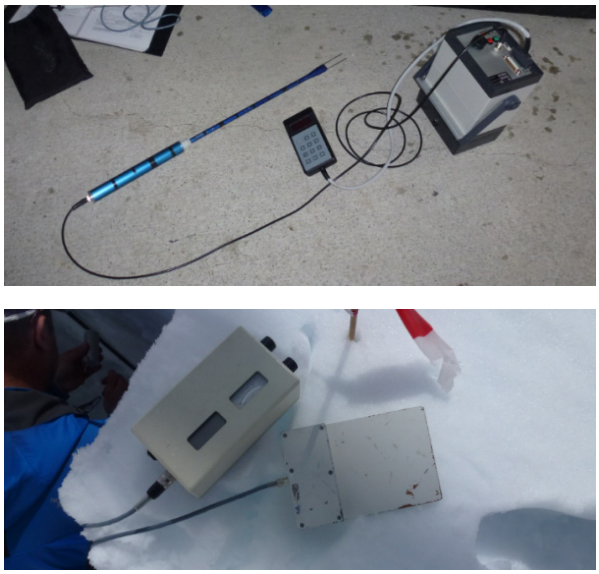

Figure A.23: SnowFork (above) and Denoth meter (below) for LWC measurements.

Figure A.24: upGPR with hoisting device (left) and installed in the ground (right) at the test field WFJ (photos taken by L. Schmid).

Appendix B: Pictures of GPS sensor installation and reference measurements at the DWD test site Munich

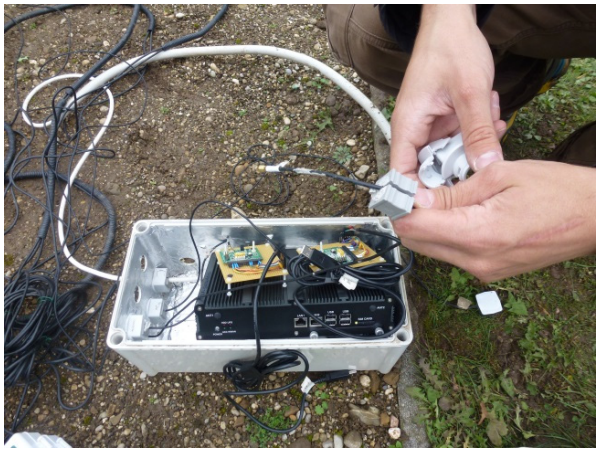

Figure B.1: Connecting cables and placement of GPS receivers in the weather-proofed box (01.10.2013).

Figure B.2: Placement of the GPS1 antenna on top of the soil (01.10.2013).

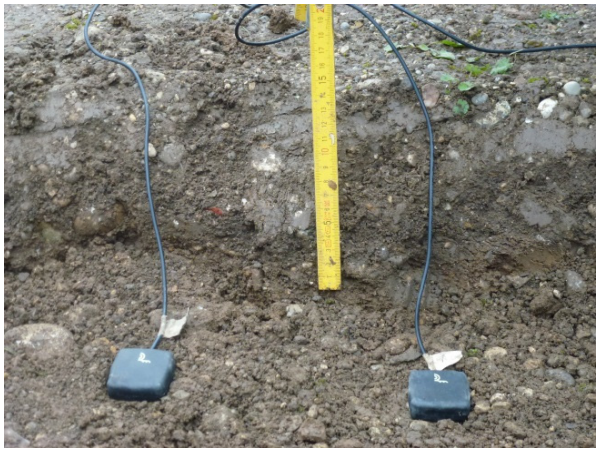

Figure B.3: Placement of the antennas of GPS2 and GPS3 at a soil depth of 10 cm (01.10.2013).

Figure B.4: ECH_20 Em50 data logger for the FD ECH_2O probes.

Figure B.5: Placement of FD ECH_2O probes at the DWD test site Munich (01.10.2013).

Figure B.6: Reference measurement with the ThetaProbe at the DWD test site (15.05.2014).

Appendix C: GPS Sensor installation plan at the test site Weissfluhjoch

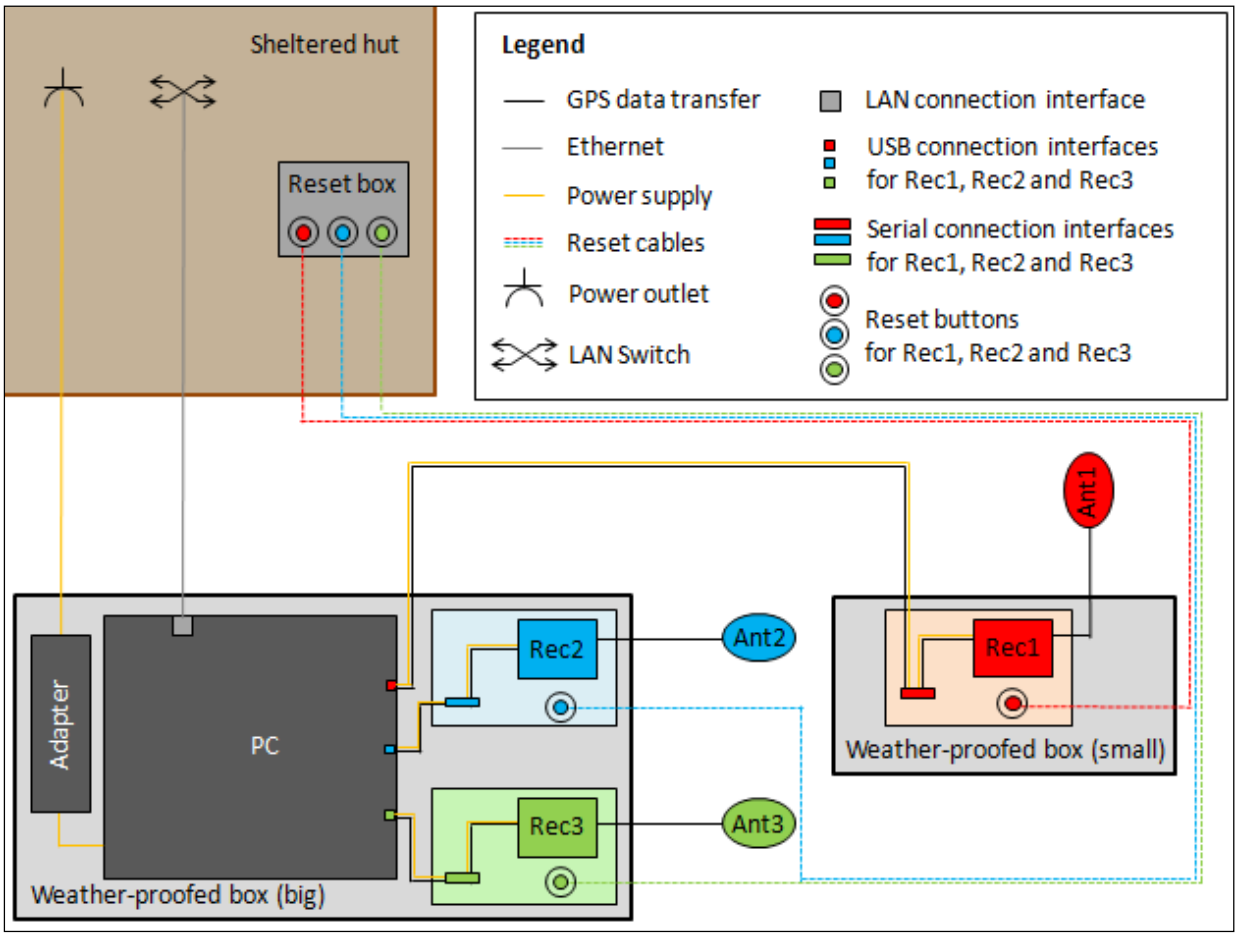

Figure C.1: Installation plan for all components of GPS1, GPS2 and GPS3 at the test site WFJ. For example, receiver Rec1 and antenna Ant1 belong to GPS1.

Appendix D: Overview of measured snow properties, sensors and their location at the test site Weissfluhjoch

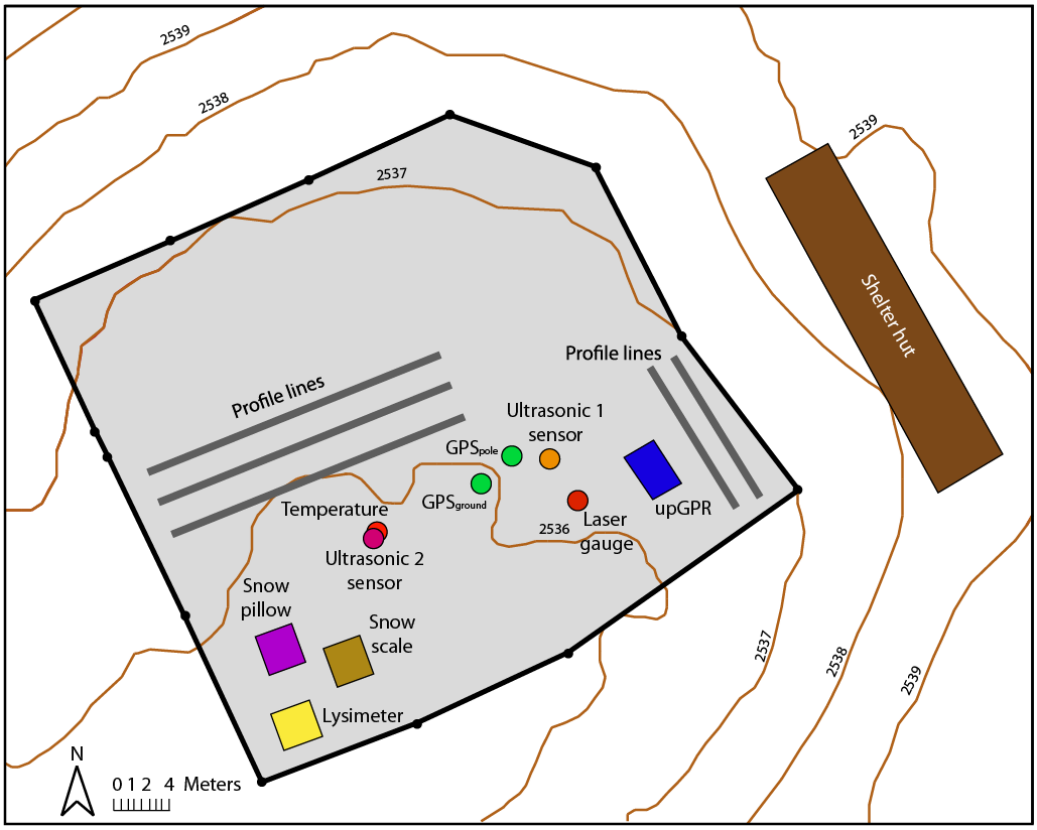

Figure D.1: Map of the test site WFJ showing all applied sensors and the snow profile lines. The green dots show the location of the GPS antennas situated either on the pole (GPS1) or on the ground level (GPS2&GPS3).

Table D.1: Measured snow properties and applied sensors or techniques at the study site WFJ.

Snow properties	**Sensor/Measurement technique**	**Units**	**Temporal resolution (aggregated)**
Air temperature (TA)	Thermistor	°C	30 min
Snow surface temperature (TSS)	Infrared	°C	30 min
Snow height (HS)	Laser sensor	cm	30 min
Snow height (HS)	Ultrasonic sensors	cm	30 min
Snow meltwater outflow	5-m² snow lysimeter	$l\ m^{-2}\ h^{-1}$	30 min
Snow height (HS), snow water equivalent (SWE), liquid water content (LWC)	GPS sensors	cm, mm, %	30 min
Snow water equivalent (SWE)	Snow pillow	mm	30 min
Snow water equivalent (SWE)	Snow scale	mm	30 min
Snow height (HS), snow water equivalent (SWE), liquid water content (LWC)	upGPR	cm, mm, %	3 h (dry snow), 30 min (wet snow)
Liquid water content (LWC)	Denoth meter	%	single days
Liquid water content (LWC)	Finnish Snow Fork	%	single days
Snow height (HS), snow water equivalent (SWE), Liquid water content (LWC), other snow properties	Manual snow profiles in snow profile lines	cm, mm, Index	single days, bi-weekly
Height of new snow (HN)	Snow board	cm	every day at 8 a.m.

Appendix E: Measuring the hydrological snow storage in Alpine catchments with a new low-cost GPS technology

This appendix is published in the ***Proceedings of the Danube Conference 2014***:

Koch, F., Prasch, M., Schmid, L., Schweizer, J. and Mauser, W. (2014): Measuring the hydrological snow storage in alpine catchments with a new-low-cost technology. Proceedings of the Danube Conference 2014, 22.-24.09.2014, Deggendorf, Germany.

Abstract

The retarded runoff from the seasonal snow cover in the Alps and its forelands plays an important role for entire watersheds like the Danube River Basin which is one of Europe's most important catchments reaching from the Eastern Alps down to the Black Sea. For hydrological purposes, information about the snow water equivalent and the amount and temporal onset of melt water release are highly important to estimate river runoff and water availability within a catchment. However, in mountainous areas it is still a problem to get these data due to no or only sparse in situ snow measurements. In general, a wider and more cost-efficient measurement network would improve e.g. low-flow and flood forecast models as well as water supply and hydropower estimates and would therefore also serve as a necessary basin-wide preparatory adaptation measure due to climate change impacts on snow which tend to cause an earlier runoff peak in spring.

The study, which will be presented, investigates a new low-cost NAVSTAR-GPS (Navigational Satellite Timing and Ranging Global Positioning System) measurement experiment to derive continuous information on snow, especially on the liquid water content. During the snow covered periods of 2012-2013 and 2013-2014 we performed non-destructive snow measurements with low-cost GPS receivers and antennas above and underneath the snowpack at a high Alpine test site in Switzerland. The freely available GPS L1-band signals (1.57542 GHz) including the carrier-to-noise power density ratio of each of the 32 GPS satellites are partly absorbed and scattered by the snowpack, especially when it becomes wet. The attenuation of the GPS signals serves therefore as a good qualitative indicator for snow wetness and daily melt-freeze cycles. The GPS-derived snow wetness data were compared to meteorological and snow-hydrological data and agreed well in their temporal occurrence. To derive the liquid water content a mixing formula for wet snow related to the GPS signal attenuation was applied. Due to its cost-efficiency and global availability, this approach could possibly have the potential to be implemented in a basin-wide snow measurement network. Preliminary results of this new measurement technology will be presented.

E.1 Introduction

The retarded runoff from the seasonal snow cover in the Alps and its forelands plays an important role for entire watersheds like the Danube River Basin which is one of Europe's most important catchments reaching from the Eastern Alps down to the Black Sea. For hydrological purposes, such as discharge forecasts for hydropower generation [*Koch et al.*, 2011b], information about the snow water equivalent and the amount and temporal onset of meltwater release are highly important to estimate river runoff and water availability within a catchment. However, in mountainous areas it is still a problem to get these data due to no or only sparse in situ snow

measurements. Therefore, this study aims to develop a reliable low-cost technique which measures snow parameters continuously and which is globally applicable.

E.2 Measurement setup

Besides other snow parameters, the liquid water content of the snowpack is a key parameter to determine e.g. wet-snow stability and the spring meltwater onset. To continuously estimate the snow wetness, a new experimental low-cost GPS measurement technique was tested recently within an alpine catchment in winter and spring 2012/13. The measurements were situated at the high Alpine SLF test site Weissfluhjoch (46°49'47" N, 9°48'34" E) near Davos in Switzerland. Three low-cost GPS receivers connected with low-cost GPS antennas were installed. One antenna was mounted at a high pole (GPS_{pole}) which was always situated above the snow cover. The GPS signals received at this antenna serve as a snow free reference indicating atmospheric influences. Before the first snow fall in winter, two redundant antennas (GPS_{ground}) were brought out on the ground at an even place and were buried underneath the snowpack during the entire snow covered period. The signal losses registered at these antennas indicate the wetness of the snowpack. A schematic overview is given in Figure E.1. For validation, meteorological and snow-hydrological data were continuously recorded at the same site.

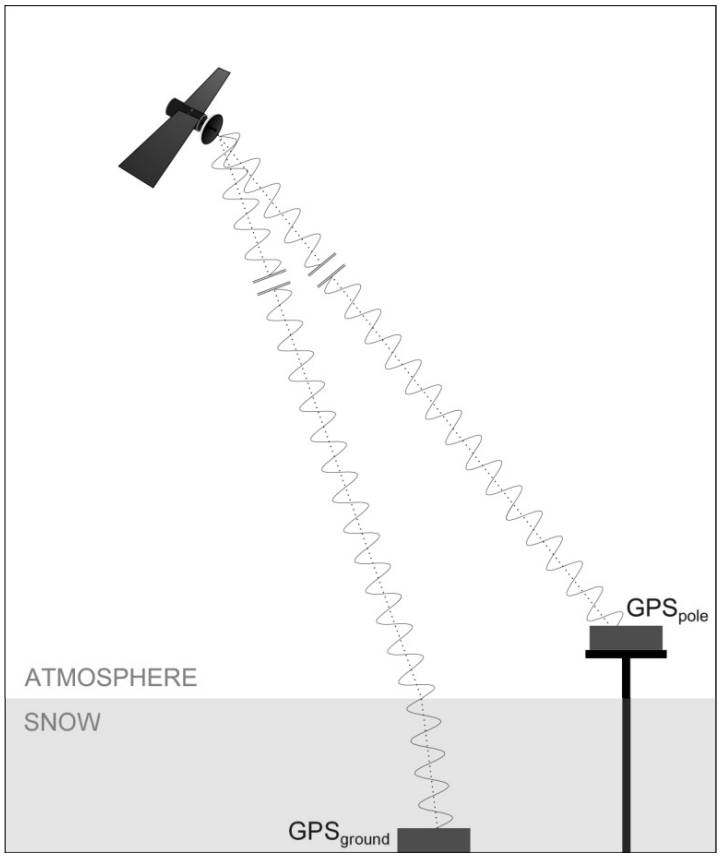

Figure E.1: Schematic of the experimental GPS measurement setup.

E.3 GPS data

The freely available GPS data are transmitted via L-band microwaves at a frequency of 1.57542 GHz. The signal strength for each of the 32 GPS satellites is expressed as carrier-to-noise-power-density ratio (C/N_0) and is continuously recorded with a temporal resolution of one second within the GPS raw data protocol. Per definition, C/N_0 is a bandwidth-independent index and is used for assessing signal quality and quantifies the signal power of the received signal of each tracked satellite [*Hofmann-Wellenhof et al.*, 2008]. The data analysis is based on normalized C/N_0 data considering a snow-free reference as well as elevation and azimuth information for each

satellite at each time step. The microwave GPS signals interact as L-band microwaves with the snowpack, especially when it becomes wet [*Bernier*, 1987; *Hofmann-Wellenhof et al.*, 2008]. Thereafter, the C/N_0 values received at GPS_{ground} indicate the degree of signal losses due to attenuation, reflection and refraction processes within the snowpack and its surface. The normalized C/N_0 values are aggregated to half-hourly data showing the evolution of the wetness of the snowpack continuously by registering changes of the snowpack in a high temporal resolution.

E.4 Start of spring snow-melt and daily melt-freeze cycles

In this study, the behavior of wet snow on the normalized GPS C/N_0 signals was analyzed. At the test site Weissfluhjoch, GPS_{ground} was permanently covered with snow from the end of October 2012 until the beginning of July 2013. Until mid-April, the snowpack was predominately dry, before the melt period started. The results cover exemplarily a period at the beginning of the spring snow melt. Figure E.2 gives an overview of the evolution of the normalized C/N_0 values recorded with the GPS receivers as well as surface temperature, precipitation and snow lysimeter meltwater outflow measured at the SLF test site Weissfluhjoch for the time period 12-28 April 2013. In general, the lower the normalized C/N_0 values, the wetter was the snowpack. The first two days of this period represented dry snow conditions without discharge at the lysimeter and constantly high normalized GPS C/N_0 values. After 15 April, the air temperature reached values above 0°C during mid-day and the first meltwater outflow was measured. In accordance to the evolution of the temperature and the meltwater outflow, the normalized GPS C/N_0 indicate with a clear decline the onset of the snow melt period as well as daily melt-freeze cycles with a minimum during mid-day and a peak during night-time. Shortly after reaching the GPS signal strength minimum, the peak discharge occurred at the lysimeter. A dry snowfall with air temperatures below 0°C led to an increase of the snow water equivalent on 19 April and interrupted the daily repeated melt-freeze pattern. During the following day no discharge at the lysimeter was recorded and the GPS C/N_0 values showed no significant decrease. Less discharge was also measured on 22 and 27 April with colder air temperature around mid-day. In sum, Figure E.2 clearly shows the coincidence of the GPS signals and the meteorological recordings. In a further step, the GPS signal strength losses due to attenuation, reflection and refraction processes will be transformed into the bulk volumetric liquid water content considering the complex permittivity, by applying e.g. *Tiuri et al.* [1984].

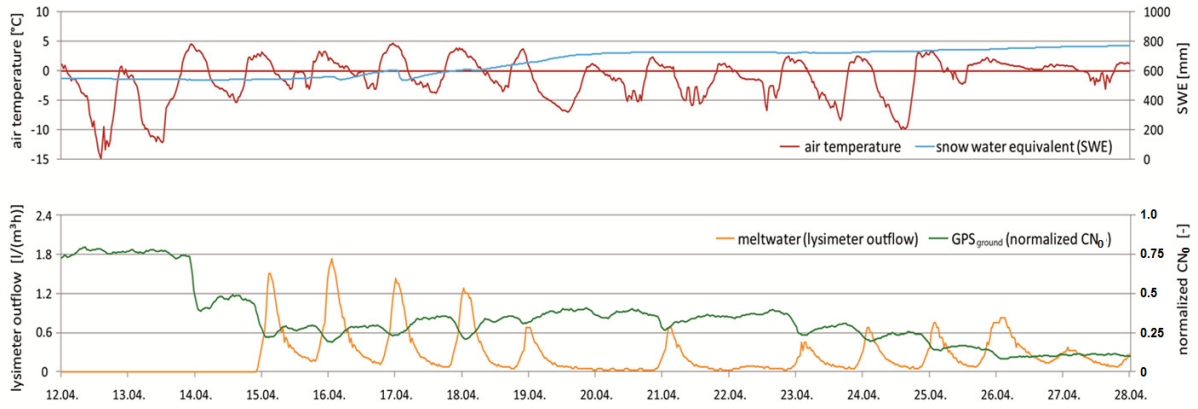

Figure E.2: Evolution of the normalized C/N_0 values recorded with GPSground as well as air temperature, snow water equivalent and meltwater outflow at a snow lysimeter measured at the SLF test site Weissfluhjoch at the start of the snow melt period in 2013 (12-28 April 2013).

E.5 Conclusions

As a low-cost, globally applicable, low power consuming and non-destructive snow measurement setup, this approach might have the potential to be implemented in a basin-wide snow measurement network aiming at

continuous data generation. Analyzing signal strength losses of GPS C/N_0 data caused by wet snow has therefore a high potential for the determination of continuous measurements of the snow wetness with a high temporal resolution in basin-wide sensor networks for different hydrological applications. In general, a wider and more cost-efficient measurement network would improve e.g. low-flow and flood forecast models as well as water supply and hydropower estimates and would therefore also serve as a necessary basin-wide preparatory adaptation measure due to climate change impacts on snow which tend to cause an earlier runoff peak in spring.

Acknowledgments

We greatly thank the German Research Foundation (DFG MA 875/12-1) for funding the project 'Kontinuierliche Messung der Schneedeckenentwicklung mit GPS-Empfangsgeräten zur Bestimmung des Schneespeichers im Hochgebirge'.

REFERENCES

Abdalati, W., and K. Steffen (1995), Passive microwave-derived snow melt regions on the Greenland Ice Sheet, *Geophysical Research Letters*, *22*(7), 787-790.

Appel, F., H. Bach, A. Loew, R. Ludwig, W. Mauser, and W. Schulz (2005), Operational monitoring of the snow cover dynamics in Southern Germany: capabilities of optical and microwave remote sensing for improved flood forecast, Proceedings of IGARSS 2005, 25-29 July 2005, Seoul, Korea.

Archer, D., and D. Stewart (1995), The installation and use of a snow pillow to monitor snow water equivalent, *Water and Environment Journal*, *9*(3), 221-230.

Artemov, V., and A. Volkov (2014), Water and ice dielectric spectra scaling at 0°C, *Ferroelectrics*, *466*(1), 158-165.

Bacchi, B., and R. Ranzi (2003), Hydrological and meteorological aspects of floods in the Alps: an overview, *Hydrology and Earth System Sciences*, *7*(6), 785-798.

Baggi, S., and J. Schweizer (2009), Characteristics of wet snow avalanche activity: 20 years of observations from a high alpine valley (Dischma, Switzerland), *Natural Hazards*, *50*(1), 97-108.

Barnett, T. P., J. C. Adam, and D. P. Lettenmaier (2005), Potential impacts of a warming climate on water availability in snow-dominated regions, *Nature*, *438*(7066), 303-309.

Barré, H. M. J. P., B. Duesmann, and Y. H. Kerr (2008), SMOS: The mission and the system, *Geoscience and Remote Sensing, IEEE Transactions on*, *46*(3), 587-593.

Bartelt, P., and M. Lehning (2002), A physical SNOWPACK model for the Swiss avalanche warning; Part I: numerical model, *Cold Regions Science and Technology*, *35*(3), 123-145.

Bartelt, P., C. Pielmeier, S. Margreth, and S. Harvey (2012), The underestimated role of the stauchwall in full-depth avalanche release, Proceedings of ISSW 2012, 16-21 September 2012, Anchorage, U.S.A.

Bartsch, A., R. A. Kidd, W. Wagner, and Z. Bartalis (2007), Temporal and spatial variability of the beginning and end of daily spring freeze/thaw cycles derived from scatterometer data, *Remote Sensing of Environment*, *106*(3), 360-374.

Baumgartner, A., and H.-J. Liebscher (1996), *General hydrology. Quantitative hydrology*, Gebrüder Borntraeger.

Bavay, M., M. Lehning, T. Jonas, and H. Löwe (2009), Simulations of future snow cover and discharge in Alpine headwater catchments, *Hydrological Processes*, *23*(1), 95-108.

Bender, M., G. Dick, M. Ge, Z. Deng, J. Wickert, H.-G. Kahle, A. Raabe, and G. Tetzlaff (2011), Development of a GNSS water vapour tomography system using algebraic reconstruction techniques, *Advances in Space Research*, *47*(10), 1704-1720.

Bernier, P. Y. (1987), Microwave remote-sensing of snowpack properties: potential and limitations, *Nordic Hydrology*, *18*(1), 1-20.

Bernier, P. Y. and J.-P. Fortin (1998), The potential of times series of C-band SAR data to monitor dry and shallow snow cover, *Geoscience and Remote Sensing, IEEE Transactions on*, *36*(1), 226-243.

Bernier,P. Y., J.-P. Fortin, Y. Gauthier, R. Gauthier, R. Roy, and P. Vincent (1999), Determination of snow water equivalent using RADARSAT SAR data in Eastern Canada, *Hydrological Processes*, *13*(18), 3041-3051.

Bircher, S., J. E. Balling, N. Skou, and Y. H. Kerr (2012), Validation of SMOS brightness temperatures during the HOBE airborne campaign, Western Denmark, *Geoscience and Remote Sensing, IEEE Transactions on*, *50*(5), 1468-1482.

Blewitt, G., W. C. Hammond, C. Kreemer, H.-P. Plag, S. Stein, and E. Okal (2009), GPS for real-time earthquake source determination and tsunami warning systems, *Journal of Geodesy*, *83*(3-4), 335-343.

Bogena, H., J. Huisman, C. Oberdörster, and H. Vereecken (2007), Evaluation of a low-cost soil water content sensor for wireless network applications, *Journal of Hydrology*, *344*(1), 32-42.

Borre, K., and G. Strang (2012), *Algorithms for Global Positioning*, Wellesley-Cambridge Press.

Bosy, J., W. Rohm, A. Borkowski, K. Kroszczynski, and M. Figurski (2010), Integration and verification of meteorological observations and NWP model data for the local GNSS tomography, *Atmospheric Research*, *96*(4), 522-530.

Botteron, N. Dawes, J. Leclere, J. Skaloud, S. V. Weijs, and P. A. Farine (2013), Soil moisture & snow properties determination with GNSS in Alpine environments: Challenges, status, and perspectives, *Remote Sensing*, *5*(7), 3516-3543.

Boyne, H., and D. Fisk (1987), A comparison of snow cover liquid water measurement techniques, *Water Resources Research*, *23*(10), 1833-1836.

Bradford, J. H., J. T. Harper, and J. Brown (2009), Complex dielectric permittivity measurements from ground-penetrating radar data to estimate snow liquid water content in the pendular regime, *Water Resources Research*, *45*, W08403.

Braun, L. N. (1993), Validation of Safran-Crocus at the basin scale and comparison with conceptual snowmelt runoff models, Note de travail N° 3 du Centre d'Etudes de la Neige, Météo-France, CNRM/CEN, Saint-Martin d'Hères, France.

Brocca, L., S. Hasenauer, T. Lacava, F. Melone, T. Moramarco, W. Wagner, W. Dorigo, P. Matgen, J. Martínez-Fernández, P. Llorens, J. Latron, C. Martin, M. Bitterli, *Remote Sensing of Environment*, 115, 3390-3408.

Brooks, R. H., and A. T. Corey (1964), Hydraulic properties of porous media and their relation to drainage design, *Transactions of the ASAE*, *7*(1), 26-0028.

Brun, E., P. David, M. Sudul, and G. Brunot (1992), A Numerical-Model to Simulate Snow-Cover Stratigraphy for Operational Avalanche Forecasting, *Journal of Glaciology*, *38*(128), 13-22.

Brun, E., E. Martin, V. Simon, C. Gendre, and C. Coleou (1989), An energy and mass model of snow cover sidtable for operational avalanche forecasting, *Journal of Glaciology*, *35*(12), 1.

Cardellach, E., F. Fabra, O. Nogués-Correig, S. Oliveras, S. Ribó, and A. Rius (2011), GNSS-R ground-based and airborne campaigns for ocean, land, ice, and snow techniques: Application to the GOLD-RTR data sets, *Radio Science*, *46*(6), RS0C04.

Carroll, S. S., and T. R. Carroll (1989), Effect of uneven snow cover on airborne snow water equivalent estimates obtained by measuring terrestrial gamma radiation, *Water Resources Research*, *25*(7), 1505-1510.

Chang, A., J. Foster, and D. Hall (1987), Nimbus-7 SMMR derived global snow cover parameters, *Annals of Glaciology*, *9*(9), 39-44.

Chaplin, M. (2016), Water and Microwaves. Available online: http://www1.lsbu.ac.uk/water/microwave_water.html (accessed on: 14.06.2016).

Chew, C., E. E. Small, and K. M. Larson (2015), An algorithm for soil moisture estimation using GPS-interferometric reflectometry for bare and vegetated soil, *GPS Solutions*, *20*(3), 1-13.

Chew, C., R. Shah, C. Zuffada, G. Hajj, D. Masters, and A. J. Mannucci (2016), Demonstrating soil moisture remote sensing with observations from the UK TechDemoSat-1 satellite mission, *Geophysical Research Letters*, *43*(7), 3317-3324.

Colbeck, S. C. (1987), History of snow-cover research, *Journal of Glaciology*, *33*(Special Issue commemorating the Fifttieth Anniversary of the Glaciological Society), 60-65.

Cole, K. S., and R. H. Cole (1941), Dispersion and absorption in dielectrics I. Alternating current characteristics, *The Journal of Chemical Physics*, *9*(4), 341-351.

Dall'Amico, J. T., F. Schlenz, A. Loew, and W. Mauser (2012), First results of SMOS soil moisture validation in the upper Danube catchment, *Geoscience and Remote Sensing, IEEE Transactions on*, *50*(5), 1507-1516.

De Rosnay, P., J.-C. Calvet, Y. Kerr, J.-P. Wigneron, F. Lemaître, M. J. Escorihuela, J. M. Sabater, K. Saleh, J. Barrié, and G. Bouhours (2006), SMOSREX: A long term field campaign experiment for soil moisture and land surface processes remote sensing, *Remote Sensing of Environment*, *102*(3), 377-389.

Deems, J. S., T. H. Painter, and D. C. Finnegan (2013), Lidar measurements of snow depth: a review, *Journal of Glaciology*, *59*(215), 467-479.

Delwart, S., C. Bouzinac, P. Wursteisen, M. Berger, M. Drinkwater, M. Martin-Neira, and Y. H. Kerr (2008), SMOS validation and the COSMOS campaigns, *Geoscience and Remote Sensing, IEEE Transactions on*, *46*(3), 695-704.

Denoth, A. (1989), Snow dielectric measurements, *Advances in Space Research*, *9*(1), 233-243.

Denoth, A. (1994), An electronic device for long-term snow wetness recording, *Annals of Glaciology*, *19*, 104-106.

Denoth, A., A. Foglar, P. Weiland, C. Mätzler, H. Aebischer, M. Tiuri, and A. Sihvola (1984), A comparative study of instruments for measuring the liquid water content of snow, *Journal of Applied Physics*, *56*(7), 2154-2160.

DeWalle, D. R., and A. Rango (2008), *Principles of snow hydrology*, Cambridge University Press.

Dirmeyer, P. A. (2000), Using a global soil wetness dataset to improve seasonal climate simulation, *Journal of Climate*, *13*(16), 2900-2922.

Dobriyal, P., A. Qureshi, R. Badola, and S. A. Hussain (2012), A review of the methods available for estimating soil moisture and its implications for water resource management, *Journal of Hydrology*, *458*, 110-117.

Dobson M. C. and F. T. Ulaby (1986), Active microwave soil moisture research, *Geoscience and Remote Sensing, IEEE Transactions on*, 23-36.

Dobson, M. C., F. T. Ulaby, M. T. Hallikainen, and M. A. El-Rayes (1985), Microwave dielectric behavior of wet soil—Part II: Dielectric mixing models, *Geoscience and Remote Sensing, IEEE Transactions on*, *23*(1), 35-46.

Dorigo, W., W. Wagner, R. Hohensinn, S. Hahn, C. Paulik, A. Xaver, A. Gruber, M. Drusch, S. Mecklenburg, and P. v. Oevelen (2011), The International Soil Moisture Network: a data hosting facility for global in situ soil moisture measurements, *Hydrology and Earth System Sciences*, *15*(5), 1675-1698.

Dozier, J., and T. H. Painter (2004), Multispectral and hyperspectral remote sensing of alpine snow properties, *Annual Review of Earth and Planetary Science*, *32*, 465-494.

Eagleman, J. R., and W. C. Lin (1976), Remote sensing of soil moisture by a 21-cm passive radiometer, *Journal of Geophysical Research*, *81*(21), 3660-3666.

Egido, A., M. Caparrini, G. Ruffini, S. Paloscia, E. Santi, L. Guerriero, N. Pierdicca, and N. Floury (2012), Global navigation satellite systems reflectometry as a remote sensing tool for agriculture, *Remote Sensing*, *4*(8), 2356-2372.

Egido, A., S. Paloscia, E. Motte, L. Guerriero, N. Pierdicca, M. Caparrini, E. Santi, G. Fontanelli, and N. Floury (2014), Airborne GNSS-R polarimetric measurements for soil moisture and above-ground biomass estimation, *Selected Topics in Applied Earth Observations and Remote Sensing, IEEE Journal of*, *7*(5), 1522-1532.

Entekhabi, D., E. G. Njoku, P. E. Neill, K. H. Kellogg, W. T. Crow, W. N. Edelstein, J. K. Entin, S. D. Goodman, T. J. Jackson, and J. Johnson (2010), The soil moisture active passive (SMAP) mission, *Proceedings of the IEEE*, *98*(5), 704-716.

Fastrax (2011), Fastrax IT430 Data Sheet. Available online: https://upverter.com/datasheet/042ba70ed2cd4485a04760b5e6864a3cad0eca96.pdf (accessed: on 4 August 2014).

Ferrazzoli, P., L. Guerriero, N. Pierdicca, and R. Rahmoune (2011), Forest biomass monitoring with GNSS-R: theoretical simulations, *Advances in Space Research*, *47*(10), 1823-1832.

Fierz, C., R. L. Armstrong, Y. Durand , P. Etchevers, E. Greene, D. M. McClung, K. Nishimura, P. K. Satyawali, and S. A. Sokratov (2009), The International Classification for Seasonal Snow on the Ground, UNESCO-IHP, Paris.

Fischer, E., S. Seneviratne, D. Lüthi, and C. Schär (2007), Contribution of land-atmosphere coupling to recent European summer heat waves, *Geophysical Research Letters*, *34*(6), L06707.

Foster, J. L. and A. Rango (1982), Snow cover conditions in the northern hemisphere during the winter of 1981, *Journal of Climatology*, *2*(2), 171-183.

Foster, C. Sun, J. P. Walker, R. Kelly, A. Chang, J. Dong, and H. Powell (2005), Quantifying the uncertainty in passive microwave snow water equivalent observations, *Remote Sensing of Environment*, *94*(2), 187-203.

Frei, A., M. Tedesco, S. Lee, J. Foster, D. K. Hall, R. Kelly, and D. A. Robinson (2012), A review of global satellite-derived snow products, *Advances in Space Research*, *50*(8), 1007-1029.

Fritzsche, A. E. (1983), *The National Weather Service gamma snow system physics and calibration*, EG & G, Energy Measurements Group.

Garstka, W. U. (1958), *Factors affecting snowmelt and streamflow. A report on the 1946-53 cooperative snow investigations at the Fraser Experimental Forest, Fraser, Colorado, Rocky Mountain Forest and Range Experiment Station (Fort Collins, Colorado)*, Washington.

GLOWA-Danube (2009), *Einzugsgebiet Obere Donau, Global Change Atlas. GLOWA-Danube-Projekt.* Department für Geographie, Ludwig-Maximilins-Universität, München.

Godfray, H. C. J., J. R. Beddington, I. R. Crute, L. Haddad, D. Lawrence, J. F. Muir, J. Pretty, S. Robinson, S. M. Thomas, and C. Toulmin (2010), Food security: the challenge of feeding 9 billion people, *Science*, *327*(5967), 812-818.

Goodison, B., P. Louie, and D. Yang (1998), The WMO solid precipitation measurement intercomparison, In: Instruments and observing methods, 67, World Meteorological Organization-Publications, TD 872.

Google Earth (2016), Deutscher Wetterdienst, Niederlassung München. Available online: https://www.google.de/intl/de/earth/ (accessed on: 15.06.2016).

Grünewald, T., M. Schirmer, R. Mott, and M. Lehning (2010), Spatial and temporal variability of snow depth and ablation rates in a small mountain catchment, *The Cryosphere*, *4*(2), 215-225.

Gubler, H., and M. Hiller (1984), The use of microwave FMCW radar in snow and avalanche research, *Cold Regions Science and Technology*, *9*(2), 109-119.

Guneriussen, T., K. A. Høgda, H. Johnsen, and I. Lauknes (2001), InSAR for estimation of changes in snow water equivalent of dry snow, *Geoscience and Remote Sensing, IEEE Transactions on*, *39*(10), 2101-2108.

Gutmann, E. D., K. M. Larson, M. W. Williams, F. G. Nievinski, and V. Zavorotny (2012), Snow measurement by GPS interferometric reflectometry: an evaluation at Niwot Ridge, Colorado, *Hydrological Processes*, *26*(19), 2951-2961.

Hall, D. K., and J. Martinec (1985), Remote sensing of snow and ice, In: Henderson F. M. and A. J. Lewis (ed.), Principles and Applications of Imaging Radar, 677-703.

Hall, R. S. Williams, K. Casey, N. E. Digirolamo, and Z. Wan (2006), Satellite-derived, melt-season surface temperature of the Greenland Ice Sheet (2000–2005) and its relationship to mass balance, *Geophysical Research Letters*, *33*(11).

Hall, J. C. Comiso, N. E. DiGirolamo, C. A. Shuman, J. E. Box, and L. S. Koenig (2013), Variability in the surface temperature and melt extent of the Greenland ice sheet from MODIS, *Geophysical Research Letters*, *40*(10), 2114-2120.

Hallikainen, M. (1984), Retrieval of snow water equivalent from Nimbus-7 SMMR data: effect of land-cover categories and weather conditions, *Oceanic Engineering, IEEE Journal of*, *9*(5), 372-376.

Hallikainen, M. (1989), Microwave radiometry of snow, *Advances in Space Research*, *9*(1), 267-275.

Hallikainen, M., P. Halme, M. Takala, and J. Pulliainen (2003), Combined active and passive microwave remote sensing of snow in Finland, Proceeding of IGARSS 2003, 21-25 July 2003, Toulouse, France.

Hallikainen, M., F. T. Ulaby, M. C. Dobson, M. A. El-Rayes, and L.-K. Wu (1985), Microwave dielectric behavior of wet soil-part 1: empirical models and experimental observations, *Geoscience and Remote Sensing, IEEE Transactions on*(1), 25-34.

Hasted, J. B. (1972), Dielectric properties of water and of aqueous solutions, In: Davies, M., *Dielectric and Related Molecular Processes: Volume 1*, The Royal Society of Chemistry 121-162.

Heilig, A., M. Schneebeli, and O. Eisen (2009), Upward-looking ground-penetrating radar for monitoring snowpack stratigraphy, *Cold Regions Science and Technology*, *59*(2-3), 152-162.

Heilig, A., O. Eisen, and M. Schneebeli (2010), Temporal observations of a seasonal snowpack using upward-looking GPR, *Hydrological Processes*, *24*(22), 3133-3145.

Henkel, P. (2015), Tightly coupled precise point positioning and attitude determination, *IEEE Transactions on Aerospace and Electronic Systems*, *51*(4), 3182-3197.

Henkel, P., and C. Günther (2010), Partial integer decorrelation: optimum trade-off between variance reduction and bias amplification, *Journal of Geodesy*, *84*(1), 51-63.

Henkel, P., and J. Cárdenas (2014), Method for Determining a Baseline between two Receivers, EP 12 199 772.0, appl. date: 28.12.2012; European patent publication No. EP2749900 (A1), publ. date 02.07.2014.

Henkel, P., and M. Iafrancesco (2014), Tightly coupled position and attitude determination with two low-cost GNSS receivers, Proceeding of 11th International Symposium on Wireless Communications Systems (ISWCS) 2014, 26-29 Aug 2014, Barcelona, Spain.

Henkel, P., U. Mittmann, and A. Iafranesco (2016a), Real-Time Kinematic Positioning with GPS and GLONASS, Proceeding of the 24th European Signal Processing Conference, Budapest, Hungary.

Henkel, P., M. Iafrancesco, and A. Sperl (2016b), The influence of thermal, hydrologic, and snow deformation mechanisms on snow water equivalent pressure sensor accuracy, Proceeding on 2016 IEEE/ION Position, Location and Navigation Symposium (PLANS), 11-16 Apr 2016, Savannah, U.S.A.

Hirschmann (2014), GPS antennas - powerful and flexibly combined. Available online: http://www.hirschmann-car.com/en/products/antenna-systems/gnss-satellite-positioning/gps/ (accessed on: 25 August 2014).

Hofmann-Wellenhof, B., H. Lichtenegger, and E. Wasle (2008), *GNSS – Global Navigation Satellite Systems: GPS, GLONASS, Galileo & more*, Springer.

Hopkinson, C., M. Sitar, L. Chasmer, and P. Treitz (2004), Mapping snowpack depth beneath forest canopies using airborne lidar, *Photogrammetric Engineering & Remote Sensing*, *70*(3), 323-330.

House, C., and C. B. Park (2009), CSR SiRFstarIV™ One Socket Protocol Interface Control Document, Issue 8, Available online: http://www.mt-system.ru/sites/default/files/docs/documents/sim18%20module%20osp%20manual%20(cs-129291-dc-8)%5B1%5D.pdf (accessed on: 16 Mar 2013).

Hsü, K. J., and U. Briegel (2013), *Geologie der Schweiz: ein Lehrbuch für den Einstieg, und eine Auseinandersetzung mit den Experten*, Springer.

ICPDR (2013), ICPDR Strategy on Adaptation to Climate Change, ICPDR (International Commission for the Protection of the Danube River) RBMEG (River Basin Management Expert Group) with support of the LMU Munich (Wolfram Mauser, Ruth Weidinger, Monika Prasch, Franziska Koch), Vienna, Austria.

Immerzeel, W. W., P. Droogers, S. De Jong, and M. Bierkens (2009), Large-scale monitoring of snow cover and runoff simulation in Himalayan river basins using remote sensing, *Remote Sensing of Environment*, *113*(1), 40-49.

Jackson, T. J., R. Bindlish, M. Cosh, and T. Zhao (2011), SMOS Soil Moisture validation with US in situ networks, Proceeding of IGARSS 2011, 24-29 July, Vancouver, Canada.

Jacobson, M. D. (2010), Inferring snow water equivalent for a snow-covered ground reflector using GPS multipath signals, *Remote Sensing*, *2*(10), 2426-2441.

Jasper, K., J. Gurtz, and H. Lang (2002), Advanced flood forecasting in Alpine watersheds by coupling meteorological observations and forecasts with a distributed hydrological model, *Journal of Hydrology*, *267*(1), 40-52.

Jin, S., and N. Najibi (2014), Sensing snow height and surface temperature variations in Greenland from GPS reflected signals, *Advances in Space Research*, *53*(11), 1623-1633.

Jin, S., G. Feng, and S. Gleason (2011), Remote sensing using GNSS signals: Current status and future directions, *Advances in Space Research*, *47*(10), 1645-1653.

Jin, S., E. Cardellach, and F. Xie (2014), GNSS Remote Sensing, Springer.

Johnson, J. B., and G. L. Schaefer (2002), The influence of thermal, hydrologic, and snow deformation mechanisms on snow water equivalent pressure sensor accuracy, *Hydrological Processes*, *16*(18), 3529-3542.

Johnson, J. B., and D. Marks (2004), The detection and correction of snow water equivalent pressure sensor errors, *Hydrological Processes*, *18*(18), 3513-3525.

Jonas, T., C. Marty, and J. Magnusson (2009), Estimating the snow water equivalent from snow depth measurements in the Swiss Alps, *Journal of Hydrology*, *378*(1), 161-167.

Jung, M., M. Reichstein, P. Ciais, S. I. Seneviratne, J. Sheffield, M. L. Goulden, G. Bonan, A. Cescatti, J. Chen, and R. De Jeu (2010), Recent decline in the global land evapotranspiration trend due to limited moisture supply, *Nature*, *467*(7318), 951-954.

Kattelmann, R. C. (1984), Snowmelt lysimeters: design and use, Proceedings of the Western Snow Conference, 17-19 Apr 1984, Sun Valley, U.S.A.

Kattelmann, R. C. (1987), Some measurements of water movement and storage in snow, Proceeding at the Davos Symposium Sep 1986 - Avalanche Formation, Movement and Effects, *IAHS Publications*, 162, 245-254.

Katzberg, S. J., O. Torres, M. S. Grant, and D. Masters (2006), Utilizing calibrated GPS reflected signals to estimate soil reflectivity and dielectric constant: results from SMEX02, *Remote Sensing of Environment*, *100*(1), 17-28.

Kerr, Y. H., P. Waldteufel, J.-P. Wigneron, J.-M. Martinuzzi, J. Font, and M. Berger (2001), Soil moisture retrieval from space: The Soil Moisture and Ocean Salinity (SMOS) mission, *Geoscience and Remote Sensing, IEEE Transactions on*, *39*(8), 1729-1735.

Kerr, Y. H., P. Waldteufel, J.-P. Wigneron, S. Delwart, F. O. Cabot, J. Boutin, M.-J. Escorihuela, J. Font, N. Reul, and C. Gruhier (2010), The SMOS mission: New tool for monitoring key elements ofthe global water cycle, *Proceedings of the IEEE*, *98*(5), 666-687.

Klenk, P. T. P. (2012), Developing ground-penetrating radar for quantitative soil hydrology. Diss., Ruprecht-Karls-Universität Heidelberg.

Koch, F., M. Prasch, L. Schmid, J. Schweizer, and W. Mauser (2014), Measuring snow liquid water content with low-cost GPS receivers, *Sensors*, *14*(11), 20975-20999.

Koch, F., H. Bach, M. Prasch, M. Weber, L. Braun, and W. Mauser (2011a), Klimawandel und Energie - Einfluss der Schnee- und Gletscherschmelze auf die Wasserkraft im Einzugsgebiet der Oberen Donau, *Korrespondenz Wasserwirtschaft*, *6*, 319-328.

Koch, F., M. Prasch, H. Bach, W. Mauser, F. Appel, and M. Weber (2011b), How will hydroelectric power generation develop under climate change scenarios? A case study in the Upper Danube basin, *Energies*, *4*(10), 1508-1541.

Koch, F., F. Schlenz, M. Prasch, F. Appel, T. Ruf, and W. Mauser (2016), Soil moisture retrieval based on GPS signal strength attenuation, *Water*, *8*(7), 276.

Komma, J., G. Blöschl, and C. Reszler (2008), Soil moisture updating by Ensemble Kalman Filtering in real-time flood forecasting, *Journal of Hydrology*, *357*(3), 228-242.

Koster, R. D., P. A. Dirmeyer, Z. Guo, G. Bonan, E. Chan, P. Cox, C. Gordon, S. Kanae, E. Kowalczyk, and D. Lawrence (2004), Regions of strong coupling between soil moisture and precipitation, *Science*, *305*(5687), 1138-1140.

Kubo, N., F. Wu, and A. Yasuda, Integral GPS and QZSS ambiguity resolution, *Transactions Japanese Society of Aerospace Space Science*, 47, 155, 38-43.

Lane, J., and J. Saxton (1952), Dielectric dispersion in pure polar liquids at very high radio-frequencies. I. Measurements on water, methyl and ethyl alcohols, *Proceedings of the Royal Society of London A: Mathematical, Physical and Engineering Sciences*, 213, 1114, 400-408.

Langlois, A., D. Barber, and B. Hwang (2007), Development of a winter snow water equivalent algorithm using in situ passive microwave radiometry over snow-covered first-year sea ice, *Remote Sensing of Environment*, *106*(1), 75-88.

Larson, K. M. (2013), A new way to detect volcanic plumes, *Geophysical Research Letters*, *40*(11), 2657-2660.

Larson, K. M. (2016), GPS interferometric reflectometry: applications to surface soil moisture, snow depth, and vegetation water content in the western United States, *Wiley Interdisciplinary Reviews: Water*, 3(6), 775-787.

Larson, K. M., and F. G. Nievinski (2013), GPS snow sensing: results from the EarthScope Plate Boundary Observatory, *GPS Solutions*, *17*(1), 41-52.

Larson, K. M., and E. E. Small (2016), Snow depth retrievals using L1 GPS signal-to-noise ratio data, *Selected Topics in Applied Earth Observations and Remote Sensing, IEEE Journal of*, in press.

Larson, K. M., E. E. Small, E. D. Gutmann, A. L. Bilich, J. J. Braun, and V. U. Zavorotny (2008), Use of GPS receivers as a soil moisture network for water cycle studies, *Geophysical Research Letters*, *35*(24), L24405.

Larson, K. M., E. D. Gutmann, V. U. Zavorotny, J. J. Braun, M. W. Williams, and F. G. Nievinski (2009), Can we measure snow depth with GPS receivers?, *Geophysical Research Letters*, *36*(17), L17502.

Lehning, M., P. Bartelt, R. L. Brown, and C. Fierz (2002a), A physical SNOWPACK model for the Swiss avalanche warning; Part III: meteorological forcing, thin layer formation and evaluation, *Cold Regions Science and Technology*, *35*(3), 169-184.

Lehning, M., P. Bartelt, R. L. Brown, C. Fierz, and P. K. Satyawali (2002b), A physical SNOWPACK model for the Swiss avalanche warning; Part II. Snow microstructure, *Cold Regions Science and Technology*, *35*(3), 147-167.

Lemke, P., J. Ren, R. B. Alley, I. Allison, J. Carrasco, G. Flato, Y. Fujii, G. Kaser, P. Mote, and R. H. Thomas (2007), Observations: Changes in snow, ice and frozen ground, Climate Change 2007: The physical science basis; summary for policymakers, technical summary and frequently asked questions. Part of the Working Group I contribution to the Fourth Assessment Report of the Intergovernmental Panel on Climate Change, In: S. Solomon, D. Qin, M. Manning, Z. Chen, M. Marquis, K. B. Averyt, M. Tignor and H. L. Miller (ed), Cambridge, UK, pp. 337-383.

Leroux, C., J. L. Deuzé, P. Goloub, C. Sergent, and M. Fily (1998), Ground measurements of the polarized bidirectional reflectance of snow in the near-infrared spectral domain: Comparisons with model results, *Journal of Geophysical Research*, *103*(D16), 19721-19731.

Limsuwat, A., T. Sakaki, and T. H. Illangasekare (2009), Experimental quantification of bulk sampling volume of ECH2O soil moisture sensors, Proceedings of the 29th Annual American Geophysical Union Hydrology Days, 25-27 Mar 2009, Fort Collins, U.S.A.

Loew, A., R. Ludwig, and W. Mauser (2002), Land use dependent snow cover retrieval using multitemporal, multisensoral SAR-images to derive operational flood forecasting models, Proceedings of EARSeL-LISSIG-Workshop Observing our Cryosphere from Space, 11-13 Mar 2002, Bern, Switzerland.

Loew, A., R. Ludwig, and W. Mauser (2006), Derivation of surface soil moisture from ENVISAT ASAR wide swath and image mode data in agricultural areas, *Geoscience and Remote Sensing, IEEE Transactions on*, *44*(4), 889-899.

Loew, A., and F. Schlenz (2011), A dynamic approach for evaluating coarse scale satellite soil moisture products, *Hydrology and Earth System Sciences*, *15*, 75-90.

Loew, A., M. Schwank, and F. Schlenz (2009a), Assimilation of an L-band microwave soil moisture proxy to compensate for uncertainties in precipitation data, *Geoscience and Remote Sensing, IEEE Transactions on*, *47*(8), 2606-2616.

Loew, A., T. Holmes, and R. de Jeu (2009b), The European heat wave 2003: Early indicators from multisensoral microwave remote sensing?, *Journal of Geophysical Research: Atmospheres*, *114*(D5), D05103.

Loth, B., G. Friedrich, and J. M. Oberhuber (1993), A snow cover model for global climatic simulations, *Journal of Geophysical Research*, *98*(D6), 10451-10464.

Ludwig, R., W. Mauser, S. Niemeyer, A. Colgan, R. Stolz, H. Escher-Vetter, M. Kuhn, M. Reichstein, J. Tenhunen, and A. Kraus (2003), Web-based modelling of energy, water and matter fluxes to support decision making in mesoscale catchments—the integrative perspective of GLOWA-Danube, *Physics and Chemistry of the Earth, Parts A/B/C*, *28*(14), 621-634.

Lundberg, A., and H. Thunehed (2000), Snow wetness influence on impulse radar snow surveys theoretical and laboratory study, *Nordic Hydrology*, *31*(2), 89-106.

Lutz, S. L. (2008), High-resolution GPS tomography in view of hydrological hazard assessment, Diss., Eidgenössische Technische Hochschule ETH Zürich.

Maaß, N., L. Kaleschke, X. Tian-Kunze, and M. Drusch (2013), Snow thickness retrieval over thick Arctic sea ice using SMOS satellite data, *The Cryosphere*, *7*(6), 1971-1989.

Mankin, J. S., D. Viviroli, D. Singh, A. Y. Hoekstra, and N. S. Diffenbaugh (2015), The potential for snow to supply human water demand in the present and future, *Environmental Research Letters*, *10*(11), 114016.

Martin-Neira, M. (1993), A passive reflectometry and interferometry system (PARIS): Application to ocean altimetry, *ESA Journal*, *17*, 331-355.

Martinec, J., and A. Rango (1986), Parameter values for snowmelt runoff modelling, *Journal of Hydrology*, *84*(3), 197-219.

Marty, C., and R. Meister (2012), Long-term snow and weather observations at Weissfluhjoch and its relation to other high-altitude observatories in the Alps, *Theoretical and Applied Climatology*, *110*(4), 573-583.

Mätzler, C. (1987), Applications of the interaction of microwaves with the natural snow cover, *Remote Sensing Reviews*, *2*(2), 259-387.

Mätzler, C. (1994), Passive microwave signatures of landscaped in winter, *Meteorology and Atmospheric Physics, 54*(1), 241-260.

Mätzler, C. (2002), COST Action 712: Microwave Radiometry, In: Marzano, F. S., and G. Visconti (ed.), Remote Sensing of Atmosphere and Ocean from Space: Models, Instruments and Techniques, Springer, 231-246.

Mätzler, C., H. Aebischer, and E. Schanda (1984), Microwave dielectric properties of surface snow, *IEEE Journal of Oceanic Engineering, OE-9*(5), 366-371.

Mätzler, C., T. Strozzi, T. Weise, D.-M. Floricioiu, and H. Rott (1997), Microwave snowpack studies made in the Austrian Alps during the SIR-C/X-SAR experiment, *International Journal of Remote Sensing*, *18*(12), 2505-2530.

Mauser, W., and S. Schädlich (1998), Modelling the spatial distribution of evapotranspiration on different scales using remote sensing data, *Journal of Hydrology*, *212*, 250-267.

Mauser, W., and H. Bach (2009), PROMET–Large scale distributed hydrological modelling to study the impact of climate change on the water flows of mountain watersheds, *Journal of Hydrology*, *376*(3), 362-377.

Mauser, W., and Prasch (2015), *Regional Assessment of Global Change Impacts: The Project GLOWA-Danube*, Springer.

Mauser, W., G. Klepper, F. Zabel, R. Delzeit, T. Hank, B. Putzenlechner, and A. Calzadilla (2015), Global biomass production potentials exceed expected future demand without the need for cropland expansion, *Nature Communications*, *6*, 8946.

McCreight, J. L., E. E. Small, and K. M. Larson (2014), Snow depth, density, and SWE estimates derived from GPS reflection data: Validation in the western US, *Water Resources Research*, *50*(8), 6892-6909.

Meløysund, V., B. Leira, K. V. Høiseth, and K. R. Lisø (2007), Predicting snow density using meteorological data, *Meteorological Applications*, *14*(4), 413-423.

Meurer, M. (1984), Höhenstufung von Klima und Vegetation: Erläutert am Beispiel der mittleren Ostalpen, *Geographische Rundschau*, *36*(8), 395-403.

Mittelbach, H., F. Casini, I. Lehner, A. J. Teuling, and S. I. Seneviratne (2011), Soil moisture monitoring for climate research: Evaluation of a low-cost sensor in the framework of the Swiss Soil Moisture Experiment (SwissSMEX) campaign, *Journal of Geophysical Research: Atmospheres*, *116*(D5), D05111.

Mitterer, C. (2012), Formation of wet-snow avalanches, Diss., Eidgenössische Technische Hochschule ETH Zürich.

Mitterer, C., H. Hirashima, and J. Schweizer (2011a), Wet-snow instabilities: Comparison of measured and modelled liquid water content and snow stratigraphy, *Annals of Glaciology*, *52*(58), 201-208.

Mitterer, C., A. Heilig, J. Schweizer, and O. Eisen (2011b), Upward-looking ground-penetrating radar for measuring wet-snow properties, *Cold Regions Science and Technology*, *69*(2-3), 129-138.

Motte, E., M. Zribi, P. Fanise, A. Egido, J. Darrozes, A. Al-Yaari, N. Baghdadi, F. Baup, S. Dayau, and R. Fieuzal (2016), GLORI: A GNSS-R Dual Polarization Airborne Instrument for Land Surface Monitoring, *Sensors*, *16*(5), 732.

Muerth, M. (2008), A soil temperature and energy balance model for integrated assessment of global change impacts at the regional scale, Diss., Ludwig-Maximilians-Universität München.

Muerth, M., and W. Mauser (2012), Rigorous evaluation of a soil heat transfer model for mesoscale climate change impact studies, *Environmental Modelling & Software*, *35*, 149-162.

Nash, J. E., and J. V. Sutcliffe (1970), River flow forecasting through conceptual models, a discussion of principles, *Journal of Hydrology*, 10, 282-290.

Nagler, T., and H. Rott (2000), Retrieval of wet snow by means of multitemporal SAR data, *Geoscience and Remote Sensing, IEEE Transactions on*, *38*(2), 754-765.

Najibi, N., and S. Jin (2013), Physical reflectivity and polarization characteristics for snow and ice-covered surfaces interacting with GPS signals, *Remote Sensing*, *5*(8), 4006-4030.

National Weather Service (2013), Snow Measurement Guidelines for National Weather Service Surface Observing Programs, edited, U.S. Department of Commerce, National Oceanic and Atmospheric Administration, National Weather Service, Office of Climate, Water and Weather Services, Silver Spring, U.S., Available online: http://www.nws.noaa.gov/om/coop/reference/ Snow_Measurement_

Guidelines.pdf. (accessed on: 14.06.2016)

Nievinski, F. G., and K. M. Larson (2014a), Inverse modeling of GPS multipath for snow depth estimation—Part I: Formulation and simulations, *Geoscience and Remote Sensing, IEEE Transactions on, 10*, *52*(10)*, 6555-6563*.

Nievinski, F. G., and K. M. Larson (2014b), Inverse modeling of GPS multipath for snow depth estimation—Part II: Application and validation, *Geoscience and Remote Sensing, IEEE Transactions on, 52*(10)*, 6564-6573.*

Niu, G. Y., K. W. Seo, Z. L. Yang, C. Wilson, H. Su, J. Chen, and M. Rodell (2007), Retrieving snow mass from GRACE terrestrial water storage change with a land surface model, *Geophysical Research Letters*, *34*(15), L15704.

Njoku, E. G., T. J. Jackson, V. Lakshmi, T. K. Chan, and S. V. Nghiem (2003), Soil moisture retrieval from AMSR-E, *Geoscience and Remote Sensing, IEEE Transactions on*, *41*(2), 215-229.

Nolan, M., and D. R. Fatland (2003), Penetration depth as a DInSAR observable and proxy for soil moisture, *Geoscience and Remote Sensing, IEEE Transactions on*, *41*(3), 532-537.

O Keefe, K., J. Stephen, G. Lachapelle, and R. A. Gonzales (2000), Effect of ice loading of a GPS antenna, *Geomatica-Ottawa*, *54*(1), 63-74.

Ohta, Y., and M. Iguchi (2015), Advective diffusion of volcanic plume captured by dense GNSS network around Sakurajima volcano: a case study of the vulcanian eruption on July 24, 2012, *Earth, Planets and Space*, *67*(1), 1-10.

Okorn, R., G. Brunnhofer, T. Platzer, A. Heilig, L. Schmid, C. Mitterer, J. Schweizer, and O. Eisen (2014), Upward-looking L-band FMCW radar for snow cover monitoring, *Cold Regions Science and Technology*, *103*, 31-40.

Otto, M. (2011), *Analytische Chemie*, John Wiley & Sons.

Ozeki, M., and K. Heki (2012), GPS snow depth meter with geometry-free linear combinations of carrier phases, *Journal of Geodesy*, *86*(3), 209-219.

Painter, T. H., K. Rittger, C. McKenzie, P. Slaughter, R. E. Davis, and J. Dozier (2009), Retrieval of subpixel snow covered area, grain size, and albedo from MODIS, *Remote Sensing of Environment*, *113*(4), 868-879.

Panciera, R., J. P. Walker, J. D. Kalma, E. J. Kim, J. M. Hacker, O. Merlin, M. Berger, and N. Skou (2008), The NAFE'05/CoSMOS data set: Toward SMOS soil moisture retrieval, downscaling, and assimilation, *Geoscience and Remote Sensing, IEEE Transactions on*, *46*(3), 736-745.

Pei, Y., R. Notarpietro, P. Savi, M. Cucca, and F. Dovis (2014), A fully software Global Navigation Satellite System reflectometry (GNSS-R) receiver for soil monitoring, *International Journal of Remote Sensing*, *35*(6), 2378-2391.

Peng, J., A. Loew, S. Zhang, J. Wang, and J. Niesel (2016), Spatial downscaling of satellite soil moisture data using a vegetation temperature condition index, *Geoscience and Remote Sensing, IEEE Transactions on*, 54(1), 558-566.

Peng, J., J. Niesel, A. Loew, S. Zhang, and J. Wang (2015), Evaluation of satellite and reanalysis soil moisture products over southwest China using ground-based measurements, *Remote Sensing*, 7(11), 15729-15747.

Perla, R. (1991), Real permittivity of snow at 1 MHz and 0°C, *Cold Regions Science and Technology*, *19*(2), 215-219.

Perla, R., and M. Martinelli (1978), Avalanche handbook, Agriculture handbook 489, USDA Forest Service, 254 pp, Fort Collins, Colorado, USA.

Philip, J.-R. (1957), The theory of infiltration: 1. The infiltration equation and its solution, *Soil Science*, *83*(5), 345-358.

Pierdicca, N., L. Guerriero, M. Caparrini, A. Egido, S. Paloscia, E. Santi, and N. Floury (2013), GNSS reflectometry as a tool to retrieve soil moisture and vegetation biomass: Experimental and theoretical activities, Proceeding of 2013 International Conference on Localization and GNSS, 25-27 Jun, 2013, Torino, Rome.

Prasch, M., W. Mauser, and M. Weber (2013), Quantifying present and future glacier melt-water contribution to runoff in a central Himalayan river basin, *The Cryosphere*, *7*(3), 889-904.

Prasch, M., T. Marke, U. Strasser, and W. Mauser (2011), Large scale integrated hydrological modelling of the impact of climate change on the water balance with DANUBIA, *Advances in Science and Research*, *7*(1), 61-70.

Privette III, C. V., A. Khalilian, W. Bridges, S. Katzberg, O. Torres, Y. J. Han, J. M. Maja, and X. Qiao (2016), Relationship of Soil Moisture and Reflected GPS Signal Strength, *Advances in Remote Sensing*, *5*(1), 18.

Prokop, A. (2008), Assessing the applicability of terrestrial laser scanning for spatial snow depth measurements, *Cold Regions Science and Technology*, *54*(3), 155-163.

Pulliainen, J., and M. Hallikainen (2001), Retrieval of regional snow water equivalent from space-borne passive microwave observations, *Remote sensing of Environment*, *75*(1), 76-85.

Rango, A. (1980), *Operational applications of satellite snow cover observations*. Wiley.

Rango, A., A. Chang, and J. Foster (1979), The utilization of spaceborne microwave radiometers for monitoring snowpack properties, *Nordic Hydrology*, *10*(1), 25-40.

Rees, W. G. (2005), *Remote sensing of Snow and Ice*, CRC Press.

Rees, C. Derksen, M. English, A. Walker, and C. Duguay (2006), Uncertainty in snow mass retrievals from satellite passive microwave data in lake-rich high-latitude environments, *Hydrological Processes*, *20*(4), 1019-1022.

Reisigl, H., and R. Keller (1987), *Alpenpflanzen im Lebensraum*. Fischer.

Ringler, C., A. Bhaduri, and R. Lawford (2013), The nexus across water, energy, land and food (WELF): potential for improved resource use efficiency?, *Current Opinion in Environmental Sustainability*, *5*(6), 617-624.

Robinson, D., C. Campbell, J. Hopmans, B. Hornbuckle, S. B. Jones, R. Knight, F. Ogden, J. Selker, and O. Wendroth (2008), Soil moisture measurement for ecological and hydrological watershed-scale observatories: A review, *Vadose Zone Journal*, *7*(1), 358-389.

Rodriguez-Alvarez, N., X. Bosch-Lluis, A. Camps, M. Vall-Llossera, E. Valencia, J. F. Marchan-Hernandez, and I. Ramos-Perez (2009), Soil moisture retrieval using GNSS-R techniques: Experimental results over a bare soil field, *Geoscience and Remote Sensing, IEEE Transactions on*, *47*(11), 3616-3624.

Rodriguez-Alvarez, N., X. Bosch-Lluis, A. Camps, I. Ramos-Perez, E. Valencia, H. Park, and M. Vall-Llossera (2012a), Vegetation water content estimation using GNSS measurements, *Geoscience and Remote Sensing Letters, IEEE*, *9*(2), 282-286.

Rodriguez-Alvarez, N., A. Aguasca, E. Valencia, X. Bosch-Lluis, A. Camps, I. Ramos-Perez, H. Park, and M. Vall-Llossera (2012b), Snow thickness monitoring using GNSS measurements, *Geoscience and Remote Sensing Letters, IEEE*, *9*(6), 1109-1113.

Rodriguez-Alvarez, N., X. Bosch-Lluis, A. Camps, A. Aguasca, M. Vall-llossera, E. Valencia, I. Ramos-Perez, and H. Park (2011), Review of crop growth and soil moisture monitoring from a ground-based instrument implementing the Interference Pattern GNSS-R Technique, *Radio Science*, *46*(6), RS0C03.

Rose, R., S. Gleason, and C. Ruf (2014), The NASA CYGNSS mission: a pathfinder for GNSS scatterometry remote sensing applications, Proceeding of SPIE Remote Sensing, International Society for Optics and Photonics, 22 Sep 2014, Amsterdam. Netherlands.

Roth, K., R. Schulin, H. Flühler, and W. Attinger (1990), Calibration of time domain reflectometry for water-content measurement using a composite dielectric approach, *Water Resources Research*, *26*(10), 2267-2273.

Rott, H., and R. E. Davis (1993), Multifrequency and polarimetric SAR observations on alpine glaciers, *Annals of Glaciology*, *17*, 98-98.

Rott, H., T. Nagler, and R. Scheiber (2003), Snow mass retrieval by means of SAR interferometry, Proceeding of 3rd FRINGE Workshop, European Space Agency, Earth Observation, 2-5 Dec 2003, Frascati, Italy.

Rötzer, K., C. Montzka, H. Bogena, W. Wagner, Y. Kerr, R. Kidd, and H. Vereecken (2014), Catchment scale validation of SMOS and ASCAT soil moisture products using hydrological modeling and temporal stability analysis, *Journal of Hydrology*, *519*, 934-946.

Salminen, M., J. Pulliainen, S. Metsämäki, A. Kontu, and H. Suokanerva (2009), The behaviour of snow and snow-free surface reflectance in boreal forests: Implications to the performance of snow covered area monitoring, *Remote Sensing of Environment*, *113*(5), 907-918.

Scheffer, F., and P. Schachtschabel (2002), *Lehrbuch der Bodenkunde*, 15 ed, Ferdinand Enke Verlag.

Schlenz, W. Mauser, and A. Loew (2012a), Analysis of SMOS brightness temperature and vegetation optical depth data with coupled land surface and radiative transfer models in Southern Germany, *Hydrology and Earth System Sciences*, *16*, 3517-3533.

Schlenz, J. T. Dall'Amico, A. Loew, and W. Mauser (2012b), Uncertainty assessment of the SMOS validation in the upper Danube catchment, *Geoscience and Remote Sensing, IEEE Transactions on*, *50*(5), 1517-1529.

Schleppe, J., and G. Lachapelle (2008), Tracking performance of a HSGPS receiver under avalanche deposited snow, *GPS Solutions*, *12*(1), 13-21.

Schmid, L., A. Heilig, C. Mitterer, J. Schweizer, H. Maurer, R. Okorn, and O. Eisen (2014), Continuous snowpack monitoring using upward-looking ground-penetrating radar technology, *Journal of Glaciology*, *60*(221), 509-525.

Schmid, L., F. Koch, A. Heilig, M. Prasch, O. Eisen, W. Mauser, and J. Schweizer (2015), A novel sensor combination (upGPR–GPS) to continuously and non-destructively derive snow cover properties, *Geophysical Research Letters, 42*(9), 3397-3405.

Schneebeli, M., C. Coléou, F. Touvier, and B. Lesaffre (1998), Measurement of density and wetness in snow using time-domain reflectometry, *Annals of Glaciology*, *26*, 69–72.

Schweizer, J., J. B. Jamieson, and M. Schneebeli (2003), Snow avalanche formation, *Reviews of Geophysics*, *41*(4), 2.

Seneviratne, S. I., T. Corti, E. L. Davin, M. Hirschi, E. B. Jaeger, I. Lehner, B. Orlowsky, and A. J. Teuling (2010), Investigating soil moisture–climate interactions in a changing climate: A review, *Earth-Science Reviews*, *99*(3), 125-161.

Shi, J., and Dozier (2000), Estimation of snow water equivalence using SIR-C/X-SAR. I. Inferring snow density and subsurface properties, *Geoscience and Remote Sensing, IEEE Transactions on*, *38*(6), 2465-2474.

Shi, J., Y. Lou, H. Zhang, Q. Zhao, J. Geng, R. Wang, R. Fang, and J. Liu (2010), Seismic deformation of the M w 8.0 Wenchuan earthquake from high-rate GPS observations, *Advances in Space Research*, *46*(2), 228-235.

Shi, J., and J. Dozier (1995), Inferring snow wetness using C-band data from SIR-C's polarimetric synthetic aperture radar, *Geoscience and Remote Sensing, IEEE Transactions on*, *33*(4), 905-914.

Shi, J., J. Dozier, and H. Rott (1994), Snow mapping in alpine regions with synthetic aperture radar, *Geoscience and Remote Sensing, IEEE Transactions on*, *32*(1), 152-158.

Sihvola, A., and Tiuri, M. (1986), Snow fork for field determination of the density and wetness profiles of a snow pack, *IEEE Transactions on Geoscience and Remote Sensing*, *24*(5), 717-721.

Sihvola, A., E. Nyfors, and M. Tiuri (1985), Mixing formulae and experimental results for the dielectric constant of snow, *Journal of Glaciology*, *31*(108), 163-170.

SLF (2015a), History of the SLF, edited, WSL Institute for Snow and Avalanche Research SLF, Available online: http://www.slf.ch/ueber/geschichte/index_EN (accessed on: 05.08.2015).

SLF (2015b), Weissfluhjoch test site, Available online: http://www.slf.ch/ueber/standorte/weissfluhjoch (accessed on: 05.08.2015).

Small, E. E., K. M. Larson, and J. J. Braun (2010), Sensing vegetation growth with reflected GPS signals, *Geophysical Research Letters*, *37*(12), L12401.

Spicher, A., A. Spicher, M. Géologue, S. Cartographe, A. Spicher, M. Geologist, and S. Cartographer (2004), *Geologische Karte der Schweiz*, Bundesamt für Wasser und Geologie.

Steppuhn, H. (1981), Snow and agriculture, In. Gray, D. M. and D. N. Male (ed.), Handbook of snow: principles, processes, management and use, 60-126, Pergamon Press.

Stewart, I. T. (2009), Changes in snowpack and snowmelt runoff for key mountain regions, *Hydrological Processes*, *23*(1), 78-94.

Stiles, W.H., and F. T. Ulaby (1980), The active and passive microwave response to snow parameters: 1. Wetness, *Journal of Geophysical Research: Oceans (1978–2012)*, *85*(C2), 1037-1044.

Stiles,W. H., and F. T. Ulaby (1982), Dielectric properties of snow, *US Army CRREL Special Report 82-18*, 91-103.

Strasser, U. and W. Mauser (2001), Modelling the spatial and temporal variations of the water balance for the Weser catchment 1965–1994, *Journal of Hydrology*, *254*(1), 199-214.

Strozzi, T., Wiesmann, A., and C. Mätzler (1997), Active microwave signatures of snow cavers at 5.3 and 35 GHz, *Radio Science*, *32*(2), 479-495.

Sturm, M., B. Taras, G. E. Liston, C. Derksen, T. Jonas, and J. Lea (2010), Estimating local to global snow water resources using snow depth data and snow climate classes, *Journal of Hydrometeorology*, *11*, 1380-1394.

Tabler, R. D., N. Berg, D. Trabant, H. Santeford, and P. Rechard (1990), Measurement and evaluation of winter precipitation, In: Ryan, W. L. and R. D. (ed.), Chrissman Cold Regions Hydrology and Hydraulics, American Society of Civil Engeneers, 9-38, New York, U.S.A.

Takala, M., J. Pulliainen, S. J. Metsämäki, and J. T. Koskinen (2009), Detection of snowmelt using spaceborne microwave radiometer data in Eurasia from 1979 to 2007, *Geoscience and Remote Sensing, IEEE Transactions on*, *47*(9), 2996-3007.

Takasu, T., and A. Yasuda (2009), Development of the low-cost RTK-GPS receiver with an open source program package RTKLIB, Proceeding of International Symposium on GPS/GNSS, International Convention Centre, Jeju, Korea.

Talbot, N. C. (1993), Centimeters in the field, a users perspective of real-time kinematic positioning in a production environment, Proceeding of the 6th Int. Techn. Meet. of Satellite Divison of the Institute of Navigation (ION GPS), 1049-1057, Salt Lake City, UT, USA.

Tallysman (2016), GPS L1 / GLONASS G1 Magnetic Mount Antenna TW 2410, Available online: http://www.tallysman.com/index.php/gnss/products/antennas-gps-l1/ (accessed on 12.04.2016).

Techel, F., and C. Pielmeier (2011), Point observations of liquid water content in wet snow-investigating methodical, spatial and temporal aspects, *The Cryosphere*, *5*(2), 405-418.

Tedesco, M. (2009), Assessment and development of snowmelt retrieval algorithms over Antarctica from K-band spaceborne brightness temperature (1979–2008), *Remote Sensing of Environment*, *113*(5), 979-997.

Tedesco, M. (2014), *Remote Sensing of the Cryosphere*, John Wiley & Sons.

Tedesco, M., and E. J. Kim (2006), Retrieval of dry-snow parameters from microwave radiometric data using a dense-medium model and genetic algorithms, *Geoscience and Remote Sensing, IEEE Transactions on*, *44*(8), 2143-2151.

Tedesco, M., and J. Miller (2007), Observations and statistical analysis of combined active–passive microwave space-borne data and snow depth at large spatial scales, *Remote Sensing of Environment*, *111*(2), 382-397.

Tedesco, M., R. Reichle, A. Loew, T. Markus, and J. L. Foster (2010), Dynamic approaches for snow depth retrieval from spaceborne microwave brightness temperature, *Geoscience and Remote Sensing, IEEE Transactions on*, *48*(4), 1955-1967.

Tedesco, M., X. Fettweis, T. Mote, J. Wahr, P. Alexander, J. Box, and B. Wouters (2013), Evidence and analysis of 2012 Greenland records from spaceborne observations, a regional climate model and reanalysis data, *The Cryosphere*, *7*, 615-630.

Teunissen, P. J. (1995a), On the double-difference ambiguities and their partial search spaces, Proceedings of the IAG Symposium Nr. 114 'Geodetic Theory Today', 39-48, 29 May – 03 June 1995, l'Aquila, Italy.

Teunissen, P. J. (1995b), The least-squares ambiguity decorrelation adjustment: a method for fast GPS integer ambiguity estimation, *Journal of Geodesy*, *70*(1-2), 65-82.

Thomson Reuters (2016), Journal Citation Report 2015, Available online: http://thomsonreuters.com/en/press-releases/2015/06/thomson-reuters-releases-40th-annual-journal-citation-reports.html (accessed on: 07.06.2016).

Tiuri, M. E., A. H. Sihvola, E. G. Nyfors, and M. T. Hallikainen (1984), The complex dielectric constant of snow at microwave frequencies, *IEEE Journal of Oceanic Engineering*, *9*(5), 377-382.

Topp, G. C., J. L. Davis, and A. P. Annan (1980), Electromagnetic determination of soil water content: Measurements in coaxial transmission lines, *Water Resources Research*, *16*(3), 574-582.

Tsang, L., Z. Chen, S. Oh, R. J. Marks, and A. Chang (1992), Inversion of snow parameters from passive microwave remote sensing measurements by a neural network trained with a multiple scattering model, *Geoscience and Remote Sensing, IEEE Transactions on*, *30*(5), 1015-1024.

u-blox (2016), ublox - Position and Time, Available online: https://www.u-blox.com/de/position-time (accessed on: 24.04.2016).

Ulaby, F. T. and U. Ravaioli (2015), *Fundamentals of Applied Electromagnetics*, 7 ed., Prentice Hall.

Ulaby, F. T., P. C. Dubois, and J. van Zyl (1996), Radar mapping of surface soil moisture, *Journal of Hydrology*, *184*(1), 57-84.

Ulaby, F. T., D. G. Long, W. J. Blackwell, C. Elachi, A. K. Fung, C. Ruf, K. Sarabandi, H. A. Zebker, and J. Van Zyl (2014), *Microwave radar and radiometric remote sensing*. The University of Michigan Press.

US Army Corps of Engineers (1956), Snow hydrology. Summary report of the snow investigations of the North Pacific Division, US Army Corps of Engineers, North Pacific Division, Portland, U.S.A.

Vachaud, D. G., J. Royer, and J. Cooper (1977), Comparison of methods of calibration of a neutron probe by gravimetry or neutron-capture model, *Journal of Hydrology*, *34*(3), 343-356.

Vaughan, D. G., J. C. Comiso, I. Allison, J. Carrasco, G. Kaser, R. Kwok, P. Mote, T. Murray, F. Paul, and J. Ren (2013), Observations: Cryosphere, *Climate Change 2013: The Physical Science Basis. Contribution of Working Group I to the Fifth Assessment Report of the Intergovernmental Panel on Climate Change*, 317-382.

Verehagen, S., and P. J. G. Teunissen (2013), The ratio test for future GNSS ambiguity resolution, *GPS solutions*, 17(4), 535-548.

Vey, S., A. Güntner, J. Wickert, T. Blume, and M. Ramatschi (2016), Long-term soil moisture dynamics derived from GNSS interferometric reflectometry: A case study for Sutherland, South Africa, *GPS Solutions*, 20(4), 641-654.

Wagner, W., G. Blöschl, P. Pampaloni, J.-C. Calvet, B. Bizzarri, J.-P. Wigneron, and Y. Kerr (2007), Operational readiness of microwave remote sensing of soil moisture for hydrologic applications, *Hydrology Research*, *38*(1), 1-20.

Waldner, P. A., C. Huebner, M. Schneebeli, A. Brandelik, and F. Rau (2001), Continuous measurement of liquid water content and density in snow using TDR., Proceeding of Second International Symposium and Workshop on Time Domain Reflectometry for Innovative Geotechnical Applications, 5-7 September 2001, Evanston, U.S.A.

Walker, J. P., G. R. Willgoose, and J. D. Kalma (2004), In situ measurement of soil moisture: a comparison of techniques, *Journal of Hydrology*, *293*(1), 85-99.

Wang, J. R., and T. J. Schmugge (1980), An empirical model for the complex dielectric permittivity of soils as a function of water content, *Geoscience and Remote Sensing, IEEE Transactions on*(4), 288-295.

Wang, J. R., J. C. Shiue, T. J. Schmugge, and E. T. Engman (1990), The L-band PBMR measurements of surface soil moisture in FIFE, *Geoscience and Remote Sensing, IEEE Transactions on*, *28*(5), 906-914.

Warscher, M., U. Strasser, G. Kraller, T. Marke, H. Franz, and H. Kunstmann (2013), Performance of complex snow cover descriptions in a distributed hydrological model system: A case study for the high Alpine terrain of the Berchtesgaden Alps, *Water Resources Research*, *49*(5), 2619-2637.

Weber, M., L. Braun, W. Mauser, and M. Prasch (2010), Contribution of rain, snow-and icemelt in the Upper Danube discharge today and in the future, *Geografia Fisica e Dinamica Quaternaria*, *33*(2), 221-230.

Weber, M., M. Bernhardt, J. W. Pomeroy, X. Fang, S. Härer, and K. Schulz (2016), Description of current and future snow processes in a small basin in the Bavarian Alps, *Environmental Earth Sciences*, 75, 1223.

Wickert, J., O. Andersen, G. Beyerle, E. Cardellach, B. Chapron, C. Gommenginger, J. Hatton, P. Høeg, A. Jäggi, and N. Jakowski (2014), Innovative remote sensing using the international space station: GNSS reflectometry with GEROS, Proceedings of the IGARSS 2014, 13-18 Jul 2014, Québec, Canada.

Wiesmann, A., T. Strozzi, C. Werner, U. Wegmüller and M. Santoro: Microwave remote sensing of Alpine snow (2007), Proceedings of the IGARSS 2007, 23-28 Jul 2007, Barcelona, Spain.

Wigneron, J.-P., J.-C. Calvet, T. Pellarin, A. Van de Griend, M. Berger, and P. Ferrazzoli (2003), Retrieving near-surface soil moisture from microwave radiometric observations: current status and future plans, *Remote Sensing of Environment*, *85*(4), 489-506.

Wigneron, J.-P., Y. Kerr, P. Waldteufel, K. Saleh, M.-J. Escorihuela, P. Richaume, P. Ferrazzoli, P. De Rosnay, R. Gurney, and J.-C. Calvet (2007), L-band Microwave Emission of the Biosphere (L-MEB) Model: Description and calibration against experimental data sets over crop fields, *Remote Sensing of Environment*, *107*(4), 639-655.

Woodhouse, I. H. (2005), *Introduction to Microwave Remote Sensing*, Taylor & Francis.

Wu, X., and S. Jin (2014), GNSS-Reflectometry: Forest canopies polarization scattering properties and modeling, *Advances in Space Research*, 54.5, 863-870.

Zavorotny, V. U., K. M. Larson, J. J. Braun, E. E. Small, E. D. Gutmann, and A. L. Bilich (2010), A physical model for GPS multipath caused by land reflections: Toward bare soil moisture retrievals, *Selected Topics in Applied Earth Observations and Remote Sensing, IEEE Journal of*, *3*(1), 100-110.

Zreda, M., D. Desilets, T. Ferré, and R. L. Scott (2008), Measuring soil moisture content non-invasively at intermediate spatial scale using cosmic-ray neutrons, *Geophysical Research Letters*, *35*(21).